R-03-21

System and safety studies of accelerator driven transmutation

Annual Report 2002

Waclaw Gudowski, Jan Wallenius, Kamil Tucek,
Marcus Eriksson, Johan Carlsson, Per Seltborg,
Jerzy Cetnar, Roumiana Chakarova, Mikael Jollkonen
and Daniel Westlén

Department of Nuclear and Reactor Physics
Royal Institute of Technology, Stockholm

June 2003

Svensk Kärnbränslehantering AB
Swedish Nuclear Fuel
and Waste Management Co
Box 5864
SE-102 40 Stockholm Sweden
Tel 08-459 84 00
+46 8 459 84 00
Fax 08-661 57 19
+46 8 661 57 19

ISSN 1402-3091
SKB Rapport R-03-21

System and safety studies of accelerator driven transmutation

Annual Report 2002

Waclaw Gudowski, Jan Wallenius, Kamil Tucek,
Marcus Eriksson, Johan Carlsson, Per Seltborg,
Jerzy Cetnar, Roumiana Chakarova, Mikael Jollkonen
and Daniel Westlén

Department of Nuclear and Reactor Physics
Royal Institute of Technology, Stockholm

June 2003

The full report including all Appendices is available as a .pdf-file on the enclosed CD-ROM-disc. The printed version contains only the main text and a list of the Appendices.

PREFACE

The research on safety of Accelerator-Driven Transmutation Systems (ADS) at the Department of Nuclear and Reactor Physics of KTH, Stockholm reported here has been focused on different aspects of safety of the Accelerator-Driven Transmutation Systems and on Transmutation research in more general terms. An overview of the topics of our research is given in the Summary which is followed by detailed reports as separate chapters or subchapters.

Som of the research topics reported in this report are referred to appendices, which have been published in the open literature. Topics, which are not yet published, are described with more details in the main part of this report.

Blue text color in a PDF version of this report implies links which can take a reader by a mouse click to the referred part of the report or to a referred Appendix.

Abbreviations and acronyms are explained in a table on pages 16-20. The appendices are submitted with the printed report on a CD-ROM.

A Summary in Swedish is given in the very early chapter called “SAMMANFATT-NING”.

SAMMANFATTNING

Forskningen om acceleratordrivna transmutationssystem (ADS) på avdelningen för Kärn- och reaktorfysik har till stor del styrts av det europeiska samarbetsprojektet inom ramen av det 5:e ramprogrammet, i vilket KTH deltar aktivt. In synnerhet:

a) ADS-härddesign och utveckling av avancerade kärnbränslen optimerade för höga transmutationsrater och höga säkerhetsegenskaper. Dessa aktiviteter innefattar även datasimuleringar av kärnbränsleproduktion. Tre olika ADS-härdkoncept undersöks:
   - Konceptuell design av Pb-Bi-kyld härd med nitridbränsle – den så kallade Sing-Sing härden som utvecklats på KTH.
   - Pb-Bi-kyld härd med oxidbränsle, den så kallade ANSALDO-designen inom det europeiska projektet PDS-XADS.
   - Gaskyld härd med oxidbränsle – en design som studeras inom det europeiska projektet PDS-XADS.

b) Analys av ADS-dynamik och fastställande av de viktigaste reaktivitetsåterkopplingarna.

c) Nödkylning i ADS-system

d) Deltagande i ADS-experiment som inkluderar tillverkningen av 1 MW spallationsstrålmål, underkritiska experiment MUSE (EA/Cadarache), YALINA underkritiska experiment i Minsk och designen av det underkritiska experimentet SAD i Dubna.

e) Materialstudier för ADS, i synnerhet teoretiska och simuleringsstudier av strålningsskador i kraftiga neutron- (och/eller proton-) flöden.

f) Datakod- och kärndatautveckling tillämpad för simulering och optimering av ADS. Särskilt arbete har tillägnats, inom ramen av EU-projektet PDS-XADS, utförandet av känslighetsstudier av olika kärndatabibliotek.

g) Studier av transmutationspotentialen hos kritiska reaktorer, i synnerhet gaskylda högtemperatur-reaktorer.

De viktigaste resultat och slutsatser från vår forskning:

ADS-härdar:

- En kraftig positiv voidkoefficient identifierades för Pb-Bi-kylda härdar (samma effekt är också tydlig för Na-kylning). Denna avsevärda voideffekt uppstår pga den höga andelen americium (60%) i bränslet. Det visades också att voidreaktivitetsökningen ökar med P/D.
- Reaktorresponsen från ett olycksscenario med ökning av acceleratoreffekten visade sig ta dubbelt så lång tid för Pb-Bi-kylning, jämfört med Na-kylning.
- En viktig säkerhetsfråga är det höga void-värdet som möjligtvis skulle kunna göra reaktorn prompt överkritisk. Detta är en osannolik händelse pga den höga kokpunkten hos Pb/Bi, men måste likväl tas i beaktande.

Transmutation av mindre aktinider i ADS:

- *Composition:* Förekomsten av 30-40% plutonium, för att åstadkomma minimal reaktivitetsswing, kombinerat med en typisk inert matrisandel (volym) högre än 50%, för att försäkra tillverkningsmöjligheterna och för att erhålla en lämplig reaktivitetsnivå.
- *Marginal till smältning:* En hög termisk konduktivitet kombinerat med hög smälttemperatur, för att erhålla hög marginal till smältning. Natriumbundet nitridbränsle har utomordentliga egenskaper i detta avseende.
- *Voidvärde:* Små tvärsnitt för inelastisk spridning kombinerat med hög termisk konduktivitet minimerar voidvärdet. Inert matris av Cr eller YN (Yttriumnitrid) ger nästan ingen inverkan av void på reaktiviteten för de undersökta konfigurationerna.
- *Sannolikhet för fission:* Hög sannolikhet för fission minimerar uppbyggnaden av curium. Hafniumnitrid ger den högsta sannolikheten för fission jämfört med ZrN eller YN.

Studier av strålningsskador i de inre delarna av en bly-vismutkyld XADS-härd:

- Den högsta bestrålningen har observerats för de inre delarna placerade över och under härden, med skademaximum nära reaktoraxeln (pga minst avstånd till centrum av härden).
- Strålningsskador i härden under en 20-årsperiod är lägre än 0.4 DPA för en lokal maxpunkt.
- Strålningsskador på ej utbytbara delar är också väl under gränsen och kan nå 0.4 DPA i en lokal maximipunkt. Minskningen av detta värde, om perifert arrangemang med Be-SS-B_4C introduceras, kan uppnå en faktor 10, till 0.04 DPA.
- Andra lösningar av härdperiferi (utan neutronmoderering) har ingen potential för att minska DPA i lokala maximipunkter.
- Den erhållna nivån av strålskador tillåter minskning av reaktordimensionerna.
- Perifera härdarrangemang har begränsad effekt på DPA-nivån i positioner nära centralaxeln och enbart neutronmoderering kan minska den med blygsamma 15%

Det passiva omedelbara bortförandet av sönderfallsvärme under allvarliga kylningsolyckor i Pb/Bi-kyld 80MW_{th} och 250MW_{th}-härdar.

- Inga struktuproblem uppkommer så länge protonstrålen stängs av omedelbart efter incidentens uppkomst.
- Ett försenande av protonstrålestoppet på 30 minuter efter en kombinerad LOHS- och LOF-olycka kan leda till temperaturökning i reaktorinneslutningen som inte orsakar allvarliga strukturproblem.

Känslighetsstudier av kärndatabibliotek för ADS-härdar.

Reaktivitetsberoende på utvärderade kärndatabibliotek är systematiserad och:

- JENDL3.2 ger ungefär 100-200 pcm högre resultat än JEF2.2
- ENDFB6.8 ger ungefär 1000 pcm högre resultat än JEF2.2

Temperaturreaktivitetskoefficienter på ungefär 700 pcm kan uppnås med alla provade kärndatabibliotek .
Korrekt fastställande av reaktivitet vid effekttemperaturer kräver införandet av temperaturberoende kärndatabibliotek.

MUSE-experiment:

Experiment med ett begränsat utbyte av natriumkylmedel mot blykylmedel som föreslagits i MUSE-experimenten leder till fördelaktiga resultat. Till exempel har vi funnit att utbytet av 22 centrala bränsleelement ökar effekten med ungefär 12%.

Bättre förståelse av strålskademekanismer:

- Förekomsten av Cr-atomer har liten effekt på de integrala kaskadegenskaperna.
- Avsevärda skillnader observeras i konfigurationen av defekter, klusteringeffekter och rörligheten av defekter

Deep Burn – heliumreaktorn kan på ett effektivt och säkert sätt bränna LWR-avfall. Den kräver, emellertid, minst en återcyklingsfas med kapslade partiklar (kan vara svårt) och två olika typer av partiklar.

SUMMARY

The research on safety of Accelerator-Driven Transmutation Systems (ADS) at the Department of Nuclear and Reactor Physics has been largely determined by the program of the European projects of the the 5th Framework Programme in which KTH is actively participating. In particular:

a) ADS core design and development of advanced nuclear fuel optimized for high transmutation rates and good safety features. This activity includes even computer modeling of nuclear fuel production. Three different ADS-core concept are being investigated:
   - Conceptual design of Pb-Bi cooled core with nitride fuel – so called Sing-Sing Core developed at KTH
   - Pb-Bi cooled core with oxide fuel – so called ANSALDO design for the European Project PDS-XADS
   - Gas cooled core with oxide fuel – a design investigated for the European Project PDS-XADS

b) analysis of ADS-dynamics and assessment of major reactivity feedbacks;

c) emergency heat removal from ADS

d) participation in ADS experiments including 1 MW spallation target manufacturing, subcrtical experiments MUSE (CEA-Cadarache), YALINA subcritical experiment in Minsk and designing of the subcritical experiment SAD in Dubna;

e) material studies for ADS, in particular theoretical and simulation studies of radiation damage in high neutron (and/or proton) fluxes ;

f) computer code and nuclear data development relevant for simulation and optimization of ADS, special efforts were put in the frame of the European Project PDS-XADS to perform sensitivity studies of the different nuclear data libraries;

g) studies of transmutation potential of critical reactors in particular High Temperature Gas Cooled Reactor.

Most important finding and conclusions from our studies:

ADS-cores:

- a strong positive void coefficient was found for lead/bismuth cooled cores (the same effect is also well pronounced for Na-cooling). This considerable void effect is attributed to a high fraction of americium (60%) in the fuel. It was found that void reactivity insertion rates increases with P/D;

- in response to the beam overpower accident the Pb/Bi-cooled core featured the twice longer grace time compared to the sodium-cooled core;

- an important safety issue is the high void worth that could possibly drive the system prompt critical. This is an improbable event due to the high boiling temperature of Pb/Bi but requires anyway attention.

Minor actinide transmutation in ADS:

- *Composition:* Presence of 30-40% plutonium, in order to achieve a minimum reactivity swing, combined with an average inert matrix volume fraction larger than 50%, in order to ensure fabricability and obtain a suitable sub-criticality level. A Tungsten matrix does not seem to fulfill this condition;
- *Margin to melt:* A high thermal conductivity combined with a high melting temperature, in order to provide a high power to melt. Sodium bonded nitride has an outstanding performance in this context;
- *Void worth:* A small cross section for in-elastic scattering combined with a high thermal conductivity minimizes void worth. Inert matrix of Cr or YN yields close to zero void worth for the configurations investigated;
- *Fission probability:* A high probability for fission of Am minimizes buildup of curium. Hafnium nitride gives the highest fission probability compared to ZrN and YN;
- Some reduction of ^{210}Po concentration can be easily obtained by introduction of reflectors and absorbers in the core periphery. Some improvement can be also obtained by moderation of the flux by beryllium. However, other means will be necessary to achieve significant ^{210}Po activity reduction satisfying radiation protection requirements.

Studies of radiation damages in the internals of the lead-bismuth cooled XADS core give:

- the highest irradiation of the internals located above and below the core with the damage peaking close to the reactor axis due to the closest distance to the core centre is observed;
- radiation damage on the core diagrid over 20 years of operations is lower than **0.4 DPA** for a local peaking point;
- radiation damage on regions of restraint plate (not replaceable) stays also well below the limit and can reach **0.4 DPA** for a local peaking point. The reduction of it if Be-SS-B_4C periphery arrangement is introduced can be by factor of 10 to 0.04 DPA;
- other solutions of core periphery (without neutron moderation) have no potential for lowering the DPA at central location;
- the limits of DPA on diagrid and core restraint plate are observed already in the reference design of LBE cooled XADS and for this purpose no action is required;
- obtained radiation damage level allows for reduction of the vessel dimensions;

- arrangements of core periphery has limited influence of DPA level at positions close to central axis and only neutron moderation can bring its reduction by modest 15%.

The passive emergency decay heat removal during severe cooling accidents in Pb/Bi-cooled 80MW$_{th}$ and 250MW$_{th}$

- no structural problems occur as long as the accelerator proton beam is switched off immediately after accident initiation.
- a delay of beam stop by 30 minutes after a combined Loss-Of-Heat-Sink and Loss-Of-Flow accident would lead to reactor vessel temperatures in the secondary creep domain, which do not cause severe structural problems.

Sensitivity studies of nuclear data libraries for ADS cores:

Reactivity dependence on evaluated nuclear data files is systematic and:

- JENDL3.2 gives about 100-200 pcm higher results that JEF2.2
- ENDFB6.8 gives about 1000 pcm higher results than JEF2.2

Temperature reactivity coefficient of about 700 pcm can be obtained with all tested cross section evaluated data files.

Proper assessment of reactivity in power temperatures requires application of temperature dependent cross section libraries.

MUSE experiment:

Experiments with a limited replacement of sodium coolant by lead coolant as suggested to MUSE-management make real sense. For example we conclude that the replacement of sodium coolant by lead coolant in 22 of the central fuel subassemblies increases the power by approximately 12 %.

Better understanding of radiation damage mechanisms:

- The presence of Cr atoms has little effect on the integral cascade properties.
- Substantial differences observed in the defect configuration, clustering and mobility.

The Deep Burn - Modular Helium Reactor can effectively and safely burn LWRs wastes. It requires, however, at minimum one reprocessing phase of coated fuel particles (may be difficult) and 2 types of fuel particles

TABLE OF CONTENTS

APPENDICES LIST

1. W. Gudowski, Accelerator-Driven Transmutation of Nuclear Wastes – an Experimental Path to a Demonstration Facility, Proc. of The Biennial Topical Meeting of the Radiation Protection and Shielding Division(RPDS) of the American Nuclear Society(ANS), Santa Fe, New Mexico, USA, 14-18 April 2002
2. J. Wallenius, Neutronic aspects of inert matrix fuels for application in ADS, Journal of Nuclear Materials, accepted for publication
3. J. Carlsson, H. Wider, Emergency Decay Heat Removal by Reactor Vessel Auxiliary Cooling System from an Accelerator-Driven System, Nuclear Technology Vol. 140, October 2002
4. J. Carlsson, H. Wider, An investigation on locating the heat-exchangers in the riser of an Accelerator-Driven System' accepted for publication in the Annals of Nuclear Energy
5. P. Seltborg, J. Wallenius, K. Tuček, W. Gudowski, Definition and Application of Proton Source Efficiency in Accelerator Driven Systems, Nucl. Sci. Eng., accepted for publication.
6. A. V. Ignatyuk, V. Lunev, Yu. Shubin, E. Gai, N. Titarenko, W. Gudowski, Neutron And Proton Cross Section Evaluations For ^{232}Th up to 150 MeV, Nuclear Science and Technology, Volume 142, Number 2, October 2002.
7. I. Gudowska, W. Gudowski, M. Kopec, Monte Carlo Evaluation of Neutron Contamination in High-Energy Photon Therapy Beams, Proc. of The Biennial Topical Meeting of the Radiation Protection and Shielding Division(RPDS) of the American Nuclear Society(ANS), Santa Fe, New Mexico, USA, 14-18 April 2002

ABBREVIATIONS AND ACRONYMS:

EUROPEAN PROJECTS:

ADOPT	"Thematic Network on Advanced Options for Partitioning and Transmutation."
BASTRA	cluster of the nuclear data related EU-projects
CONFIRM	"Collaboration On Nitride Fuel Irradiation and Modelling"– shared cost project
FUETRA	"Fuel for Transmutation" – cluster of nuclear fuel related EU-projects
FUTURE	"Fuels for transmutation of long lived radiotoxic elements"– shared cost project
ITEM	"Network - Development of multiscale modelling for simulation of radiation effects for Virtual Test Reactors (VTR).
MOST	"Network - Review and revaluation of Molten Salt Reactor technology and previous realizations or projects."
MUSE	"Experiment for Subcritical Neutronics Validation - MasUrca Subcritical Experiment"– shared cost project
PDS-XADS	"Preliminary Design Studies of an eXperimental Accelerator Driven System" – shared cost project
SPIRE	SPallation and IRradiation Effects - "Irradiation Effects in Martensitic Steels under Neutron and Proton Mixed Spectrum" – shared cost project
TECLA	"Technologies, Materials and Thermal-hydraulics and Safety for Lead Alloys" – shared cost project
TETRA	Technology for Transmutation – cluster of EU-projects

OTHER ABBREVIATIONS AND ACRONYMS

% h.a.	% of heavy atoms, a way of expressing burnup/transmutation
ADS	Accelerator Driven (Transmutation) System
ALMR	Advanced Liquid Metal cooled Reactor
ANSALDO	Italian electromechanical company, Ansaldo Nucleare is a part of this company
BA	Burnable Absorber
BCC	Body Centered Cubic - type of a crystallographic lattice

BOL	Beginning of Life
BOC	Beginning of Cycle
BR	Breeder Reactor
CAPRA	Consommation Accrue de Plutonium dans les Rapides – Enhanced Burning of Plutonium in Fast Reactors
CERCER	CERamic-CERamic – type of nuclear fuel
CERMET	CERamic-METallic – type of nuclear fuel
CFD	Computational Fluid Dynamics
CR	Control Rods
DB-MHR	Deep Burn Modular Helium Reactor
DF	Driver Fuel (for the high temperature gas cooled reactors)
DFR	The Dounreay Fast Reactor
DIF3D	The multigroup steady state neutron diffusion and transport code
DLC200	Nuclear Data Library release following the standard version of the MCNP-code
DPA	Displacement Per Atom
DPA–NRT	Displacement Per Atom calculated due to the model of Norgett, Robinson and Torrens - NRT
EAM	Embedded Atom Method
EBR	Experimental Breeder Reactor
EFPD	Effective Full Power Days
EM10	type of ferritic steel
ENDFB	Evaluated Nuclear Data File, suffix indicates a version of the file e.g. ENDFB6.8
EOC	End of Cycle
EOF	End of Life
ERMT	European Research on Materials for Transmutation Workshops
FBR	Fast Breeder Reactor
FCC	Face Centered Cubic - type of a crystallographic lattice
FFTF	Fast Flux Test Facility
FTF	Flat-to-Flat, a core design strategy
FZK	Forschungszentrum Karlsruhe

GA	General Atomics
GENEPI	High intensity neutron generator, external neutron source for MUSE experiments
GeV	Giga-electron-Volt, energy unit
GWd	GigaWatt day, energy unit
H/S	Heating per source particle (proton or neutron)
HTGR	High Temperature Gas Cooled Reactors
HM	Heavy Metal
HT-9	High quality stainless steel
H451	Symbol of the nuclear-grade graphite
I	Importance of the neutrons
ISOTX	A format of string/representing of multigroup data neutron cross-sections
ITU	Institute of Transuranium Elements, Karlsruhe
JEF	Joint Evaluated (Nuclear Data) File, suffix indicates a version of the file e.g. JEF2.2
JENDL	Japanese Evaluated Nuclear Data Library, suffix indicates a version of the file, e.g. JENDL3.2
keV	kilo-electron-Volt – energy unit
KCODE	A MCNP module for k_{eff} (eigenvalue) calculations
KMC	Kinetic Monte Carlo
LA150	Nuclear data cross section library up to 150 MeV for the MCNPX-code, standard release of the Los Alamos (LA) National Laboratory
LBE	Lead Bismuth Eutectic
LOCA	Loss of Coolant Accident
LOF	Loss of Flow
LOHS	Loss of Heat Sink
LWR	Light Water Reactor
MA	Minor Actinides
MASURCA	Fast reactor at Cadarache, hosting MUSE-experiments
MCB	Monte Carlo based computer program for burnup calculations
MCNP	Monte Carlo Neutron Photon transport code
MCNPX	Monte Carlo Neutron Photon and Light Ion transport code

MC^2	A computer program for nuclear data evaluation and multigroup structure derivation
MD	Molecular Dynamics, a computer simulation method
MeV	Mega-electron-Volt, energy unit
MHTGR	Modular High Temperature Gas Cooled Reactor
Minatom	Ministry of Atomic Energy in Russia
MOX	Mixed Oxide (fuel)
NEA	Nuclear Energy Agency
NJOY	A computer program for processing evaluated nuclear data files
P/D	Pitch to Diameter ratio
PBM	Parallel Block Methods, a simulation technique in Molecular Dynamics
pcm	per cent mille, a reactivity unit equal to 10^{-5}
PPS	Plant Protection System
PRISM	Advanced fast reactor concept
P0, P1	Approximation symbols of the nodal transport theory
RSC	reserve shutdown control rods
RSSA	neutron source file in the MCNP/MCNPX/MCB codes
RVACS	Reactor Vessel Auxiliary Cooling System
SA, S/A	SubAssembly (of the nuclear fuel)
SAS4	Reactor kinetic calculation code
SAS/DIFF-K	Reactor kinetic calculation code system
SS	Stainless Steel
SSC	Sing-Sing Core, an accelerator driven system concept of KTH
STAR-CD	Computer program for fluid dynamics problems
TF	Transmutation Fuel (for the high temperature gas cooled reactors)
TOP	Transient Overpower
TRADE	Triga Accelerator Driven Experiment, ADS-related experiment in Italy
TRISO	Triple isotropic coated fuel particles, fuel particles for gas cooled high temperature reactor
TRU	TRansUranium elements
TWODANT	A deterministic neutron transport code

UREX	URanium and fission products Extraction, nuclear fuel reprocessing technology
UTOP	Unprotected Transient Overpower
VARIANT-K	A Nodal transport and diffusion module for the DIF3D
WP	Work package
XADS	eXperimental Accelerator Driven System

1 INTRODUCTION

Primary goal of partitioning and transmutation technology is to limit radiotoxic inventory of nuclear wastes destined to geological repository. Accelerator Driven Systems, subcritical reactors supplied with neutron from an external source driven by spallation processes, are one of the important components – aside of partitioning technology - proposed for future, effective transmutation systems.

The research program in accelerator-driven nuclear transmutation at the Department of Nuclear and Reactor Physics of the Royal Institute of Technology in Stockholm is focused on safety aspects of transmutation systems. In order to cover this broad and complicated topic and to harmonize our activities with international projects in which we actively participate, our research has been structured into few major areas:

- Design of high-performance ADS-core and analysis of its parameters including dynamics of ADS, emergency cooling systems, radiation stability of materials and development of advanced fuel for ADS
- Development of simulation tools and nuclear data libraries necessary for advanced ADS-simulations
- Theoretical work aimed at better understanding of radiation damage processes
- Participation in ADS-related experiments, with a special attention to important components of ADS (e.g. construction of the spallation target)
- Revisiting potential of critical reactors for the different transmutation strategies

2 NEUTRONIC AND BURNUP STUDIES OF AN ACCELERATOR-DRIVEN, SUB-CRITICAL TRANSURANIUM BURNER (SING-SING CORE CONCEPT)

Partitioning and Transmutation require new advanced fuel cycle schemes with multiple fuel recycling and implementation of fast critical reactors and/or sub-critical, accelerator-driven systems (ADS). Accelerator-driven systems are particularly suited to work as dedicated minor actinide burners in synergy with fast and/or thermal reactors in the frame of double-strata scenario.

Reactor fuel with high content of minor actinides may, however, turn out to be too difficult to fabricate and/or reprocess the entire transuranics discharge of light-water reactors can be directly loaded into sub-critical burners. Such two-component scenario, envisioned in this study, is often foreseen by countries without developed fast reactor programme or with political proliferation concerns.

Low uranium content in the fuel of transuranium ADS burner together with hard neutron spectrum (high portion of flux above actinide resonance region) significantly deteriorates neutronic and burnup characteristics of the system, resulting in:

- Rapid reactivity loss due to burnup of fissile fuel
- Positive coolant void coefficient
- Vanishing Doppler reactivity coefficient
- Small delayed neutron fractions

These issues are addressed in the Sing-Sing Core (SSC) conceptual design of a sub-critical transuranium burner by:

- Introduction of burnable absorbers (B_4C) and enlarging core batch-wise, thus reducing the reactivity swing
- Optimized distribution of fuel and burnable absorber in individual core zones, minimizing power peaking and increasing fuel averaged linear power
- Choice of large pitches up to 2.3 pin diameters, mitigating consequences of unprotected transients; at the same time, coolant void worth becomes negative

The potential of boron carbide for mitigating reactivity losses in a sub-critical TRU burner employing nitride fuels and lead-bismuth coolant has been investigated in our previous work [1]. It was demonstrated that slow neutrons can be shielded from being captured by americium, and accordingly, build-up of the curium isotopes can be reduced. The introduction of burnable absorbers (BA), on the other hand, further deteriorates safety characteristics of the reactor, particularly coolant void reactivity and Doppler feedback. In this study, it is shown that these adverse effects of burnable absorbers can be mitigated while still maintaining favorable transmutation characteristics of the core.

2.1 DESIGN CONCEPT

For detailed discussion on choice of fuel and coolant materials as well as a pin and pellet geometry is reader advised to consult our previous papers and reports [1][2]. A brief overview of major design data of the study is given in Table 2-1.

Table 2-1. Sing-Sing Core fuel pin and pellet design parameters. A triangular pin lattice is adopted.

Fuel	(U,TRU)N
Diluent	ZrN
Pellet density (% TD)	0.85
Coolant and target material	Pb/Bi
Maximum coolant velocity (m/s)	3.0
Structural material	Fe/Cr-steel
Pin design	
Active pin length (cm)	120
Pellet inner radius (mm)	1.00
Pellet outer radius (mm)	2.40
Clad inner radius (mm)	2.49
Clad outer radius (mm)	2.94
Smear density (% TD)	0.67

Actinide mononitrides, combining good thermal stability together with compatibility with water-based reprocessing techniques, are taken as a core fuel. The thermophysical properties of the nitride fuel, however, contain large uncertainties. Experimental results indicate that vaporization of PuN is small for temperatures below 2150 K but the dissociation behavior of minor actinide nitrides (NpN, AmN, CmN) is not well known. The stability limit of AmN was thus conservatively assumed the same as its fabrication temperature 1573 K. The thermal conductivity of nitride fuel depends strongly on the porosity and decreases with increasing atomic number. It was therefore assumed that the thermal conductivity of AmN and CmN is 75% and 55% that of PuN, respectively. In order to reduce the (n,p)-production of troublesome ^{14}C, the nitrogen was enriched up to 99% of ^{15}N.

Porosity of fuel is 15% allowing fission gases and helium to escape to the gas plenum, rather than to be retained within the fuel promoting fuel swelling.

A choice of lead/bismuth as a coolant material is motivated primarily by its favorable effect on void worth. Lead-bismuth eutectic has good thermodynamical properties: low melting point (398 K) limiting problems with freezing in the system, and high boiling point (1943 K) making risks for coolant boiling and subsequent voiding rather hypothetical. Additionally, it features lower spectral gradient upon voiding than sodium. The lead-bismuth eutectic has been also chosen as a target material and serves also as a pin bond. High thermal conductivity of lead-bismuth (15 kW/m at 800 K) reduces risks

for fuel damage at elevated temperatures. On the other hand, little experience is available on the use of lead-bismuth for this purpose as well as about its compatibility with nitrides.

The steady-state temperature of 12%Cr-Si steel components has to be kept under 870 K as higher temperatures strongly exacerbate plasticity, mechanical strength, embrittlement susceptibility and creep resistance of the material. Due to the lack of relevant experimental data, the thermophysical properties of the cladding and structure materials were assumed to be as those for HT-9 ferritic stainless steel. However, mechanical properties, used to evaluate cladding failure, are those for 20% cold-worked 316-stainless steel. This requires a word of caution since the high temperature strength properties of HT-9 can be substantially lower than for 316-stainless steel.

Due to its favorable burnability in the fast reactor spectrum (in comparison to other candidates as Gd, Hf, and Eu) and relative thermal and irradiation stability, boron carbide enriched up to 90% of ^{10}B is selected as the reference absorber. The purpose of boron carbide in the system is manifold:

- absorb slow neutrons and hence block them from being captured in ^{241}Am. The decay chain of ^{242}Am is a source of helium build-up in the fuel during irradiation, which may lead to un-acceptable fuel swelling and/or pin pressurization;
- mitigate reactivity losses as fissile plutonium isotopes are burned away. The burnability of boron carbide is a disadvantage when using it in FBR control rods, but becomes useful in sub-critical cores fuelled with transuranics from LWR discharges having high Pu quality;
- enable a power distribution flattening technique independent of fuel composition and geometry;
- block neutrons to re-enter reactor core during coolant voiding.

2.2 SYSTEM GEOMETRY

In Sing Sing core concept, one relies on increasing the coolant volume fraction in the reactor lattice. Large pitches has a beneficial impact on void worth and also enhance the decay heat removal capacity of the system, increasing margins to fuel and cladding damage during accidental conditions.

Comparing to the previous study, all minor actinides have now been removed from the inner core parts, and located in fuel pins adjacent to the absorber pins in the central core zones. The core consists of three distinctive zones: the *source* multiplication zone ensuring effective multiplication of spallation neutrons, the *transmutation* zone where all minor actinides are placed and the outer *driver* supplying neutrons to heavily poisoned transmutation zones.

The core structure is immersed in a pool of lead-bismuth eutectic coolant with heat exchangers and primary pumps well elevated in order to promote natural circulation. Loop design as proposed for the sodium design reactors is not appropriate due to the high density of the Pb/Bi-coolant. The pool system, which avoids nozzles and pipes, has the benefits of extremely low probability for loss-of-coolant accidents, a large heat capacity, and reliable natural circulation. Pool designs, on the other hand, use large

vessels containing massive amounts of heavy liquid metal. The large volume and high density of the coolant may exert significant impulsive load on the vessel in the event of an earthquake excitation.

The system has four identical steam generators with four primary centrifugal pumps located in the cold pool. The vessel is filled with Pb/Bi eutectic to a prescribed level, with the remainder of the vessel being occupied by an inert cover gas. The compressibility of the cover gas permits the coolant to expand with rising temperatures. An auxiliary tank, containing enough cover gas volume, may be connected to the reactor vessel to account for nitrogen gas that might be generated by thermal dissociation of the nitride fuel. Because lead-bismuth eutectic is nearly incompressible, and the saturation temperature is high, there is no need to pressurize the primary system.

With increasing coolant mass flow, the margin and grace time to fuel damage increases. High coolant fraction reactor cores are thus more permissible in order to mitigate beam power transients. Increased coolant fractions also have favorable impact both on coolant void worth and pressure loss across the core. The obvious drawback is, however, an increase in the neutron leakage, adversely affecting neutron economy and elevating both burnup reactivity swing and initial fissile inventories.

2.3 FUEL COMPOSITION

The SSC transmutation reactor would work in symbiosis with a park of light-water reactors in the frame of a two-component strategy. Here, we investigate a start-up scenario (first cycle) assuming the composition of TRU vector as being that of light-water reactor spent fuel discharges with average burnup of 41 GWd/tHM after cooling period of 30 years. Such a delay could be a reasonable estimation of an ADS implementation into nuclear reactor parks. During this period, the relative concentration of ^{241}Am in TRU vector is more than doubled due to the beta-decay of ^{241}Pu.

2.4 CALCULATION METHODS AND TOOLS

The calculations of neutron fluxes, power densities and one-group cross sections at BOL were performed by Monte Carlo code MCNPX [3] executed in coupled proton-neutron source mode. The multiplication eigenvalue calculations of void worth and Doppler feedbacks were obtained from neutron KCODE mode simulations.

The depletion calculations were carried out by Monte Carlo code MCB integrating MCNP4C neutron transport with in-flight calculation of reaction rates and nuclide density evolution. For this purpose, the external neutron source was recorded in MCNPX on the surface of the spallation target and subsequently supplied to MCB.

As the LA150 cross-section library does not include any actinide isotopes so far, it could be for our purposes, used only along with MCNPX for analyses of the spallation reaction in the target. Subsequent simulations of the reactor system were thus based on standard JEF2.2 and ENDFB6.8 nuclear data libraries processed with NJOY in order to account for temperature dependence. For the sake of simplicity, an average steady-state operational temperature were used for individual components of the heterogeneous design – 1500 K for fuel pins, 1200 K for cladding, and 900 K for coolant and upper

plenum and upper reflector structure. The temperature of the lower axial plenum and radial reflector was assumed to be 600 K.

2.5 CORE DESIGN

For the optimized core design, the flat-to flat (FTF) of the core sub-assembly was further decreased to 9.72 cm, allowing thus finer distribution of fuel and burnable absorbers in the core. Further decrease of the duct FTF would not however be meaningful as this would lead to an excessive fraction of the construction materials in the core.

The proton beam impact window was placed 17.2 cm above the midplane of the core in order to minimize number of neutrons leaking out of the spallation target into the axial reflectors and maximizing thus the source efficiency. At the same time, it yields almost axially symmetric power distribution. The gas plenum is located in upper part of the core, reducing risks associated with positive reactivity insertion due to the gas release from ruptured cladding. The length of the upper plenum was assumed substantially large, 150 cm, sufficient to accommodate released fission gases and all helium from decayed 242Cm. The length of the active fuel column was in comparison to our previous design increased to 120 cm to further enhance the source efficiency. In this case, only 3% of the spallation neutrons escape spallation target into the axial reflector without inducing fission in the core. For the same purpose, we also set up smaller pin pitches in the source zones than in transmutation zones and driver. As the AmN is removed from the source zones, a small pitch does not at accidental conditions (i.e. a sudden increase of beam power) immediately result in fuel decomposition. Such approach is economically more favorable than using different pellet diameters in individual zones. To further improve the coolant void worth, the length of the BA pins in transmutation zones was increased to 150 cm, preventing neutrons from re-entering the core upon coolant voiding. This improves the void worth upon voiding the core, upper plenum and reflector by additional 800 pcm.

The outer radius of the spallation target is kept at 19.6 cm and the core now consists of 12 zones as illustrated in Figure 2.1. The distribution of the fuel pins and BA yielding flat power density at BOL is further summarized in Table 2-2. Four innermost zones are fuelled with uranium and plutonium, ^{238}U content ranging from 72% to 55%. The amount of MA in TRU fuel of transmutation zones is kept under 30% as pins with larger MA fractions may start to be difficult to fabricate. The volume fraction of boron carbide is kept at 25-30%. By concentrating minor actinides into poisoned fuel zones, curium build-up in the fuel is reduced and consequently pin pressurization can be limited. In the driver zones, the PuN is mixed with diluent (19 vol% ZrN) in order to compensate for excessive plutonium reactivity.

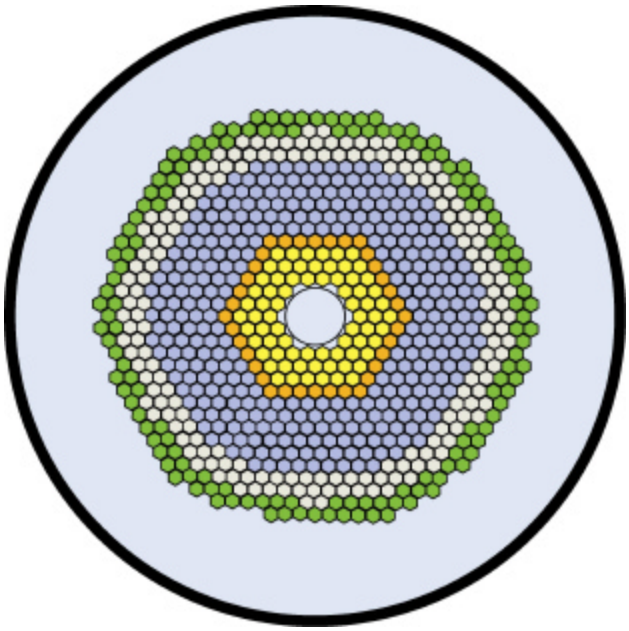

Figure 2.1: Cross-section of Sing-Sing core design. The core consists of four zones: source zone consisting of (U,Pu)N pins (depicted in yellow), buffer zone with PuN and B_4C pins (in dark orange), transmutation zone containing (Pu,MA)N and B_4C pins (in blue) and driver with (Pu,Zr)N fuel (in grey). Core enlargement zones are depicted in green.

Table 2-2. Sub-assembly design parameters for the Sing-Sing Core yielding a radial power peaking less than 1.5 at BOL

Zone	1	2	3	4	5	6	7	8	9	10	11	12
Fuel pins	61	61	61	25	26	26	27	28	29	29	37	37
B_4C pins	0	0	0	12	11	11	10	9	8	8	0	0
Pin P/D	1.83	1.83	1.83	2.33	2.33	2.33	2.33	2.33	2.33	2.33	2.33	2.33
Number S/A	18	24	30	36	42	48	54	60	66	54	96	38
U	0.72	0.68	0.62	0.45	-	-	-	-	-	-	-	-
Pu	0.28	0.32	0.38	0.55	0.70	0.70	0.70	0.70	0.70	0.70	1.00	1.00
MA	-	-	-	-	0.30	0.30	0.30	0.30	0.30	0.30	-	-

Neutronics

The neutronic characteristics of the optimized core design are summarized in Table 2-3. Heavy presence of burnable absorber in MA fuelled zones yields hard neutron spectra decreasing thus neutron capture probability in even neutron number nuclides. The distribution of fission-to-absorption probabilities of major minor actinides is displayed in Figure 2.2. We note that the fission probability of ^{241}Am reaches 24%, a factor of two higher than typical in CAPRA reactor core. The neutron spectrum remains fairly constant in transmutation zones, with median energies ranging from 300 to 400 keV,

which is to be compared to the median energies of around 200 keV in the source zones and the driver.

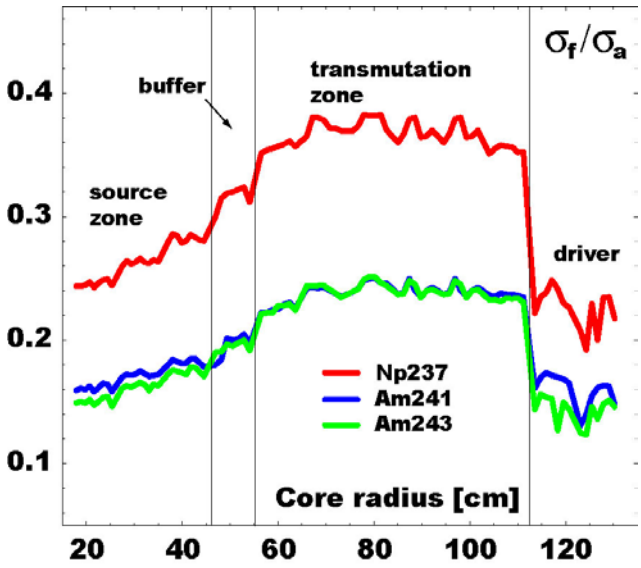

Figure 2.2: Pin-by-pin calculated radial distribution of fission probabilities. Boron carbide volume fraction in transmutation zones is kept at 25-30%, yielding maximum fission-to-absorption probabilities of ^{241}Am equal to 0.24.

The void worth was calculated by the voiding of coolant from core and upper plenum and reflector structure including spaces in-between sub-assembly hexanes. Despite of the heavy presence of burnable absorbers in the core, slightly negative void reactivity feedback (-200 pcm) could be obtained in the present design. However, voiding the core region only (corresponding e.g. to the scenario of gas release upon the pin failure, steam ingression from a heat exchanger, or fuel blockage) the void worth still remains positive.

Limited presence of fertile materials in fast transmutation cores results in a deterioration of prompt fuel temperature feedback. In very hard spectrum, hardly any neutrons reach resonances around 1 keV (2.4 keV for ^{240}Pu and 0.9 keV for ^{242}Pu) and the Doppler feedback is accordingly rather small and unreliable. The Doppler feedback was calculated by evaluating multiplication eigenvalue of the system at BOL, varying the temperature of fuel in the interval from 300 K to 1800 K.

Due to the low fractions of uranium in the fuel, the effective delayed neutron fraction β_{eff} is accordingly very small. The β_{eff} was estimated in MCNP4C code, explicitly modeling the yield and spectrum of delayed neutrons

Table 2-3. Neutronic and burnup performance parameters of the optimized core design of the Sing-Sing core.

Parameters	Unit	SSC
Power	MW_{th}	800
Proton beam energy	GeV	1
Number of batches		9
Batch length	days	110
Neutron source efficiency ϕ^* (BOL/EOL)		1.25/1.20
Average burnup	% h.a.	11.5
Reactivity loss	pcm/batch	2200
Average linear power at BOL	kW/m	34.9
Maximum linear power	kW/m	66.3
Maximum radiation damage at EOC	dpa-NRT	120
U/(U+TRU) content	%	20.1
Fissile inventory at BOL	kg	3252
Net Pu consumption	kg/y	211
Net MA consumption	kg/y	21.1
Doppler constant	10^{-5} T dk/dT	-40
BOL β_{eff}	pcm	170
Coolant void worth at BOL	pcm	-200
Coolant void worth (only core voided) at BOL	pcm	+3000

Burnup

The reactivity loss is about 1000 pcm per percent of TRU burnup and the average heavy metal burnup achieved during an irradiation period of 990 EFPD becomes 11.5%. The fuel cycle consists of nine 110-days long irradiation batches; see Figure 2.3(a). After each 330 EFPD, the reactor is shut-down for 30-day long maintenance period. During that 14 S/A are exchanged for reflector sub-assemblies in the core perimeter. At the same time, all sub-assemblies in the source zones are replaced. The length of the reactor stops in-between maintenance outages is three days assuming half a day for reactor shut-down and restart. In that case, 26 S/A are reloaded into the outer zones of the core. The fuel residence time in the core then ranges from 330 EFPD for sub-assemblies in the source zones to 990 efpd for transmutation zone and driver sub-assemblies. Zone burnup of individual sub-assemblies is displayed in Figure 2.4. Due to the power peaking constraints in the adjacent assemblies in driver, the irradiation has to be interrupted after 990 EFPD.

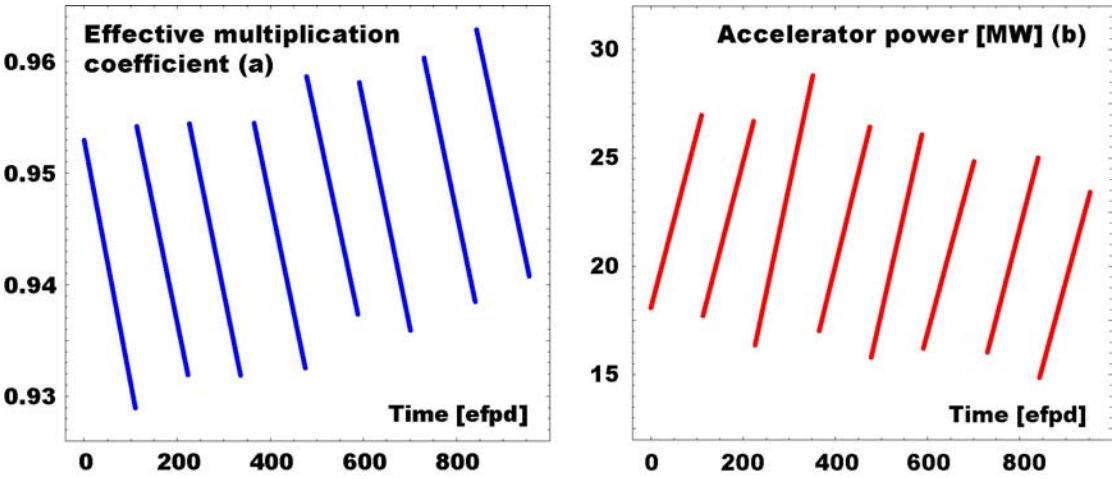

Figure 2.3: Reactivity loss (a) and accelerator power (b) of the SSC system during one irradiation cycle. The core is enlarged after each batch by sub-assemblies placed at the perimeter of the core. Additionally, during 30-days long maintenance periods, sub-assemblies in the source zones are also replaced.

The accelerator beam power needed to keep system power constant is depicted in Figure 2.3(b). The reactivity drop in the individual fuel batches is compensated by an increase in accelerator beam by less than a factor of 1.9.

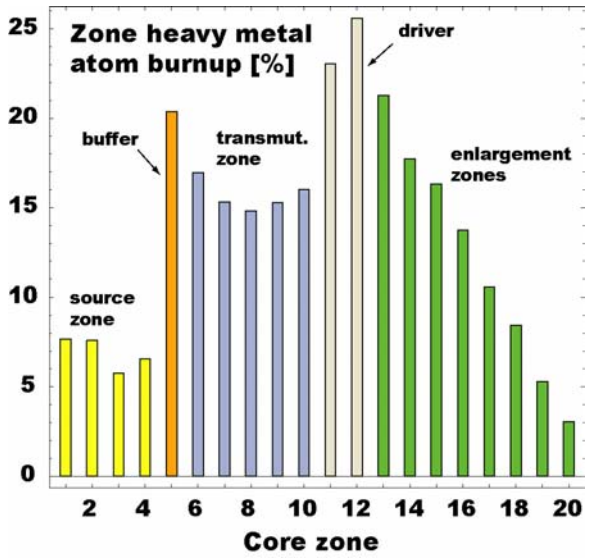

Figure 2.4: Discharged burnup rates of heavy metal atoms in individual core zones. Burnup of MA fuel pins placed in transmutation zones reaches 14%.

The radial power profile of the Sing-Sing Core at BOL is displayed in Figure 2.5. In order to increase the source multiplication, the plutonium content in (U,Pu)N mixture in source zones was increased to the maximum permissible levels with regards to thermal stripping of sub-assemblies, yielding radial power peaking factor equal to 1.5 at the BOL. At the EOL, the linear power of the most exposed pins in zone 1 reaches 66 kW/m, still leaving maximum cladding temperatures bellow 620 ^{o}C limit.

The maximum achievable burnup in the fuel pin is determined by a requirement to maintain structural integrity of the cladding. The radiation damage have been estimated using the formula suggested by Garner, relating 200 dpa-NRT damage rate to the damage neutron fluence (En > 0.1 MeV) of $4 \cdot 10^{23}$ n/cm^2. Most exposed are highly burned fuel pins placed in hard neutron spectrum of the fifth zone. There, 79% of the neutron flux is above the 100 keV, clearly illustrating beneficial effect of burnable absorbers. The average fast flux calculated in the most exposed fuel pin is $2.1 \cdot 10^{15}$ n/cm^2/s. Considering axial power peaking factor of 1.28, the maximum clad damage after 990 EFPD becomes 120 dpa-NRT, well bellow the limit of 180-200 dpa-NRT. Due to the lack of published data for ferritic steels, the material behavior of cladding was estimated by using data for austenitic SS-316.

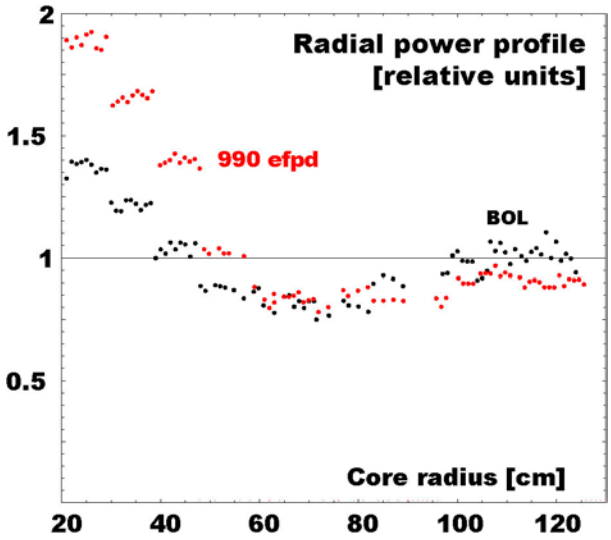

Figure 2.5: Radial power profile at BOC (in black) and EOC (in red). The maximum steady-state linear power of fuel pin remains under 70 kW/m, ensuring thermal dynamic stability of fuel.

In our simplified approach, we have additionally neglected pellet-cladding interaction and we note that both assumptions might somewhat overestimate the value of cladding burst temperature. The gas pressure in the fuel pin was calculated assuming that all fission gases and helium from ^{242}Cm decay are released from the fuel. The maximum pressure in the most exposed pin in zone 5 at EOC is 13 MPa, generating hoop stress of 65 MPa. This is well bellow 120 MPa, which is the measured ultimate tensile strength for non-irradiated rods at the temperature of 1000^{o}C.

2.6 ACCIDENT ANALYSIS

The objective of the safety study is to describe the response of the system to three representative sequences of unprotected accidents: transient overpower (TOP), loss-of-flow (LOF), and loss-of-heat-sink (LOHS). In all these scenarios we not only have an initial breakdown, such as failure in the power supply, but an additional malfunctioning of the plant protection system (PPS). Typically, the PPS is designed to detect excess

power levels, or low coolant flows, and automatically initiates measures to terminate the transient. Thus, it is only when the PPS malfunctions that an unprotected event may occur. It should be recognized that system redundancy makes the assumption of failure to shut down the accelerator highly unlikely. These accidents must be regarded as hypothetical. The accident analysis investigates the transient response in the pre-disassembly phase. The purpose is to investigate the safety characteristics and define failure mechanisms and possible ranges of safe operation.

Modeling and assumptions

Accident analysis was performed by SAS4A code. A primary system model is set-up including a detailed multi-channel model of the core, heat exchangers, pumps, compressible pool volumes, and connecting piping. Burnable absorber pins, containing boron carbide, are mocked up into the subassembly structure field in order to preserve the total heat capacity. Safety consequences are evaluated taking into consideration a set of postulated transient failure temperatures listed in Table 2-4.

Table 2-4. List of failure temperatures used in the analysis.

Component/mechanism	Failure temperature [K]
Dissociation of PuN, zones 1-4 and 11-12	2150
Dissociation of AmN, zones 5-10	1573
Cladding burst temperature	1333
Cladding corrosion	946

Space-time effects in strongly coupled cores are in general small and point kinetics theory should be adequate for the present purpose. Moreover, non-uniform changes in reactivity over the reactor are not expected as hard spectrum and long neutron mean free paths allow the spatial shape of the flux to be quickly established in a transient. In our simulations, we take into account Doppler, coolant temperature and radial core expansion reactivity feedbacks. The spatial distribution of the coolant temperature coefficient was provided in three distinctive axial segments, explicitly considering positive reactivity contribution of the coolant voiding in the core only, and strong negative reactivity contributions arising from upper plenum and reflector voiding.

Constant steam generator boundary conditions are assumed. Depending on the type of accident this corresponds to either constant (or zero) coolant temperature drop through the steam generator or constant coolant temperature at the steam generator outlet.

Unprotected TOP

The initiator for the unprotected transient overpower (TOP) accident is assumed to be a sudden increase in beam power. In this "source-jerk" type of accident the intensity of the external neutron source is promptly increased by a factor of 2.0, corresponding to the total amount of beam power available for insertion. The source intensity in an ADS will most likely be actuated by the accelerator control as well as the plant protection system, and therefore a control system failure or simply inadvertent operation of the accelerator may lead to accidental increase in source power. The response of the system

to the unprotected TOP transient is displayed in Figure 2.6. The effect of radial expansion of the core is investigated using an assumed reactivity coefficient of -5.2 Δk/k per C, corresponding to the value of the reactivity coefficient of a lead-bismuth eutectic cooled critical reactor with metal (U,Pu) fuel.

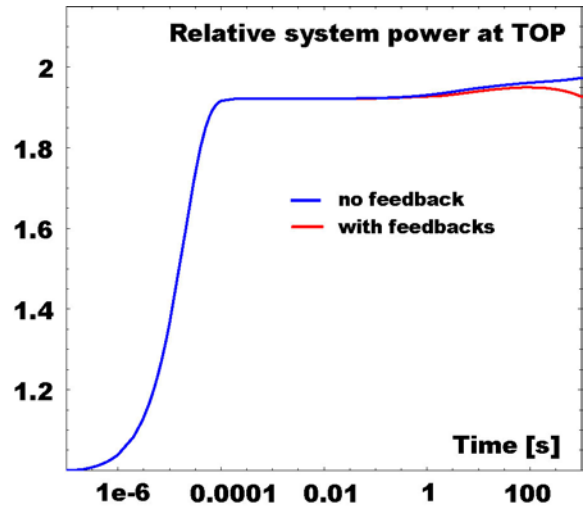

Figure 2.6: Normalised power as a function of time for unprotected transient of overpower accident following sudden increase in source intensity by a factor of two.

It has appeared, however, that reactivity feedbacks only have a minor role on the transient power response. Source dominance suppresses the effect of feedbacks and the system suffers a rapid power excursion. The power abruptly adjusts to a quasi-static level, which is close to the asymptotic level. The speed of the transition is determined by the prompt period and in the absence of any prompt negative feedback the transition occurs without any constraining mechanisms. Small effect from delayed neutrons appear at the time scale of seconds and transient behavior is governed by the response of prompt neutrons. The power eventually approaches a stationary level, which is linearly proportional to the source strength. The effect of the negative reactivity feedback due to the rise in coolant temperature can be observed after 100 s from the beginning of the transient. In Figure 2.7, the resulting peak core temperatures are displayed.

The heat transport time constants of the system are such that the power excursion pursues most of its course before any temperature changes occur in the core. The source disturbance is first noted as a rise in fuel temperatures and later by a rise in coolant temperatures. The initial rise in temperature is determined by the characteristic time constant of the fuel pin. Core temperatures arrive at a period of almost constant temperature within a few seconds. The length of this plateau is determined by the primary loop circulation time. A crucial part of the transient is completed in the first second or so. According to the calculation, transient temperatures following the initial rise do not exceed the safety limits. In the first 10 seconds of the transient, fuel temperatures in zone 5, containing AmN, reach 1452 K, leaving a margin to failure of 100 K. Cladding temperatures are well below the transient burst temperature, too. The accident thus should not result in any immediate core damage and instantaneous shut down of the beam is not a necessary requirement to prevent core damage.

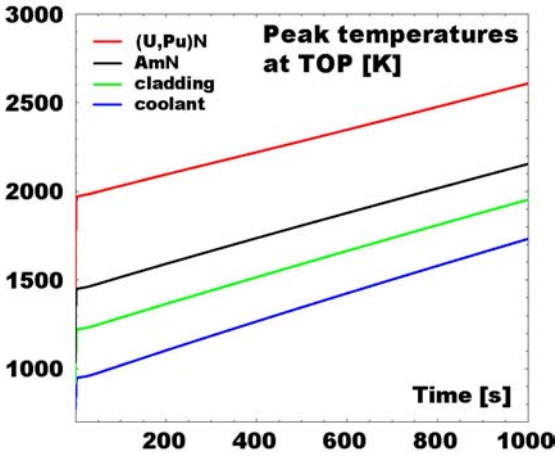

Figure 2.7: Peak fuel, cladding, and coolant temperatures in an unprotected TOP accident. Source intensity is increased by a factor of two. Constant heat rejection rate in steam generators is estimated.

In the subsequent transient course of events, there will be a mismatch between heat production and removal rate in the steam generators. The net effect of the mismatch is that the coolant inlet temperature will increase steadily as the transient proceeds and excess energy would cause the reactor core, coolant, and other components to overheat. Dissociation of americium-nitride (zone 5) is onset at approximately 175 seconds, which, in principle, offers plenty of time for a well-designed safety system to take effect. The cladding (zone 1) is expected to reach its burst temperature, 1333 K, in 160 seconds. Within that time, beam shut off would successfully terminate the transient.

The time available for the safety system to react may be thus extended from being determined by the time constant for the fuel to transport heat (~0.5 seconds) to a time constant determined by the primary loop circulation time (~30 seconds). In this case, a fast-acting safety system is not an imperative requirement to assure a protection against sudden source transients. The transient is slow enough for effective action to be taken to detect the malfunction and trip the beam before undue damage results. The initial thermal response, that follows a prompt source increase, occurs however so rapidly (<1 second) that it is unsafe to rely on a safety system to avoid such transients.

Unprotected LOF

The unprotected loss-of-flow (LOF) accident is initiated by a loss of primary pump power. It is assumed that the feed water pumps maintain normal flow and beam trip completely fails. In absence of reactivity feedback mechanisms, normal power levels are maintained throughout the transient. Following failure of the power supply to the primary pumps, the pump torque immediately drops to zero. The pump coasts down gradually at a rate determined by the inertia of the fly wheel (360 kg.m^2), the inertia within the pump, and the inertia of the coolant. These inertial forces will help to push coolant through the primary system for a substantial length of time (~100 seconds). As the pump impeller comes to rest, the flow rate has a tendency to dip before establishing

a natural circulation flow that is in equilibrium. An asymptotic flow rate of 25% of the steady-state flow is obtained in 400 seconds.

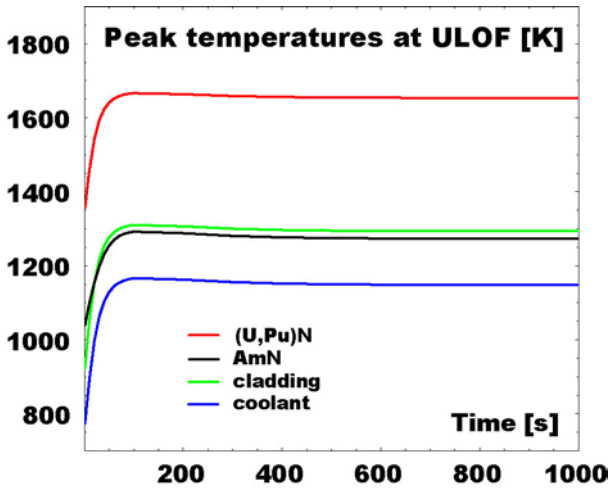

Figure 2.8: Peak fuel, cladding and coolant temperatures in an unprotected LOF accident. Primary pump power is suddenly removed. Coolant inlet temperature is constant.

As illustrated in Figure 2.8, the temperature of the coolant increases first and is a primary indication of flow reduction. As the coolant heats up, less heat is transferred from the fuel with temperature growing at a rate determined by the flow coast down. It is seen that minor core heat-up arises during the initial seconds. Within that time period, shut down of the beam would effectively terminate the transient. When the pumps have come to a complete rest, mass flow rate is at a minimum and core temperatures reach a maximum. As coolant temperature peaks, the buoyancy driven flow is given an additional push before settling in the equilibrium state. Peak temperatures in fuel, cladding, and coolant are found in zone 1, maximum AmN temperature appears in zone 5. The fuel temperature in zone 5 peaks at 1292 K, where the dissociation temperature for AmN is 1573 K, leaving a margin to dissociation of more than 250 K. The cladding temperature peaks at 1311 K, which is still below the transient burst temperature limit of 1333 K. The coolant exceeds the recommended operational temperature and the protective oxide film layer on the cladding may suffer some damage that potentially could harm the cladding in the long run.

Unprotected LOHS

The unprotected loss-of-heat-sink (LOHS) accident is assumed to start with a sudden inability of the steam generators to remove heat, with the primary pumps continuing to run. Peak temperatures following instantaneous loss of heat removal were calculated to be that shown in Figure 2.9.

The LOHS tends to be a longer-term accident than TOP and LOF. The calculations indicate that about 20 seconds are required for the loss of the heat rejection capability to have an effect on the core temperatures. After 20 seconds, the change in core temperature is caused solely by the rise in core inlet temperature, which accompanies

the loss of the primary heat sink. Unless the beam is shut down the primary system temperature will rise at a constant rate according to Figure 2.9.

The failure temperatures for the fuel (AmN in zone 5) and the cladding (zone 1) are exceeded at approximately 640 and 480 seconds, respectively. In the event of a loss-of-heat-sink accident, it is essential that the failure be sensed and a safety system terminates the transient. The fact that the times to reach core damage for LOHS are long provides a relatively long time for the safety system to trip the beam. Several options may then be used for emergency decay heat removal. It is likely that a loss-of-heat-sink accident will be in the form of impairment rather than a drastic total loss of heat rejection capability of the steam generators. More detailed calculations are expected to yield less pessimistic results.

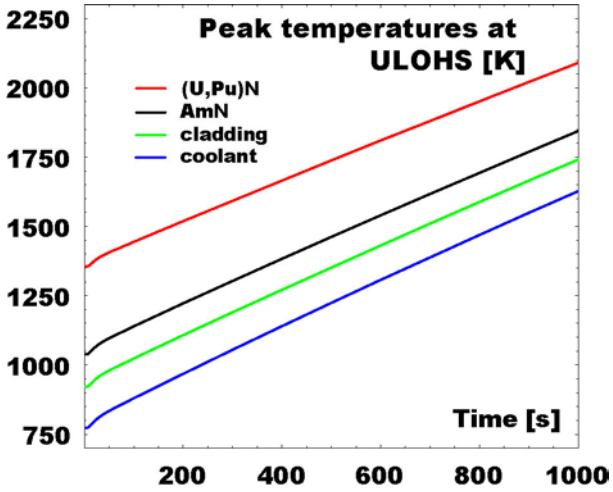

Figure 2.9: Peak fuel, cladding and coolant temperatures in unprotected LOHS accident. Complete loss of heat rejection capability of steam generators is assumed. Constant power is maintained during a whole transient.

3 ADS DYNAMICS SIMULATIONS

3.1 INTRODUCTION

In this section, recent work on reactor dynamics simulations is presented in summarized form. First is a report on the safety performance of sodium vs. lead/bismuth as primary coolant in a minor actinide burner reactor. The coolants are benchmarked for a beam overpower event and the time to core damage are compared. Neutronic investigations are performed of the void reactivity effect. Second is a progress report on the input data generation procedures applied in the preparation of advanced reactor dynamic simulations. The objective is to investigate the performance of traditional space-time kinetic methods in source-driven systems. The computational methods and procedures for generating multigroup cross sections are described.

3.2 DYNAMICS ANALYSIS OF A SODIUM-COOLED AND A PB/BI-COOLED ADS

The purpose of this study is to investigate the safety performance of a sodium-cooled and a lead/bismuth-cooled ADS in response to a beam overpower event. The systems are benchmarked for uranium-free oxide fuel. The analysis presented is a selection of work that was reported at the 3rd International Workshop on Utilisation and Reliability of High Power Proton Accelerators in Santa Fe [4].

Model and assumptions

The benchmark is performed using a common design, a common set of assumptions, and common computational methods. The continuous energy MCNP simulation code is applied to the calculation of the void coefficient. A three-dimensional pin-by-pin model is defined. Oxide fuel is adopted being diluted with zirconium dioxide. In order to flatten the power distribution, the core is subdivided into two regions with varying content of ZrO_2. We have adopted a Pu to TRU ratio of 40% at BOL since this composition minimizes reactivity losses over a large number burnup cycles [4]. The Pu/TRU ratio is kept constant. The plutonium isotopic vector corresponds to the discharge from spent MOX fuel (5% ^{238}Pu, 38% ^{239}Pu, 30% ^{240}Pu, 13% ^{241}Pu, and 14% ^{242}Pu). The americium composition consists of two thirds ^{241}Am and one third of ^{243}Am. The analysis aimed at increasing the core diameter through an increase in pin pitch while holding the pin diameter and core height constant. Pitch-to-diameter ratios are varied in the range from P/D=1.25 to 2.25 (constant D=8 mm). To compensate the reactivity loss when P/D is increased the fraction of ZrO_2 is adjusted (from core average of 30% at P/D=2.25 to 70% at P/D=1.25) in order to preserve k_{eff}=0.97. A summary of design parameters is presented in Table 3-1.

Transient analysis is performed with the aid of the SAS4A safety code [6]. A primary heat transport system is defined and represented by the core, primary pumps, the shell side of the heat exchangers, connecting piping, and compressible pool volumes with cover-gas surfaces. Coolant passage through the core is modelled by a single thermal and hydraulics channel. The feedwater system is assumed to remove heat at 100% for

Table 3-1. Design parameters

Characteristic	Value
Core power	800 MW_{th}
Average linear power	16 kW/m
Core coolant inlet temperature	573 K (Pb/Bi and Na)
Coolant flow rate	2.5 m/s (Pb/Bi) and 5.0 m/s (Na)
Fuel composition	$(Pu_{0.6}Am_{0.4})O_2 + ZrO_2$
Fuel porosity	10 %
Core height	1.0 m
Fission gas plenum height	1.50 m
Outer fuel radius	3.45 mm
Inner cladding radius	3.50 mm
Outer cladding radius	4.00 mm
P/D	Varied from 1.25 to 2.25
Doppler constant (Tdk/dT)	-38 pcm
k_{eff} (eigenvalue)	0.97
β_{eff}	0.20 %

all time. Thus, when the power increases above nominal, there is a mismatch in heat production and heat removal. The net effect is coolant inlet temperature rising with time. The point kinetics approximation is used for calculating transient power. A value of β_{eff} equal to 0.20% is assumed, a representative value for a minor actinide burner. The coolant flow rate in a lead/bismuth-cooled reactor is limited by erosion/corrosion damage of structural material. At present the flow rate of lead/bismuth is taken to be 2.5 m/s. No such limitation exists for the sodium-cooled reactor where the main concern in the past has been to limit pumping power requirement. For that reason a sodium flow rate of 5 m/s is adopted. Transient response is calculated assuming intact core geometry; i.e., fuel pins and coolant channels are well defined. Temporal and spatial void distributions are calculated. Reactivity feedbacks are modelled by coolant density changes and an assumed Doppler constant of Tdk/dT=-38 pcm. As will be seen, the Doppler coefficient has negligible influence on the operational behavior. The void reactivity coefficient and the prompt neutron lifetime are determined from static neutronic analysis. In a preliminary study, a uniform void coefficient is used. Structural reactivity feedback phenomena (e.g. radial and axial core expansion) have been excluded. Under the present conditions, structural expansion introduces reactivity changes that are small with respect to the void effect. It is recognized, however, that such reactivity feedback effects may affect the calculated performance values.

Neutronic analysis

Following coolant voiding there is hardening of the spectrum caused by a decrease in neutron scattering. Removal of coolant also results in higher neutron leakage. Hardening of the neutron spectrum and increased neutron leakage are the two dominating physical phenomena contributing to the void reactivity effect. In general, hardening of the spectrum leads to a positive reactivity component due to an increase in the number of neutrons released per neutron absorbed in the fuel while increased leakage gives rise to a reactivity loss since more neutrons may escape the core. The void reactivity effect has been calculated for the present system and is illustrated in Figure 3.1. The void coefficient is expressed as a function of pitch-to-diameter ratio. The void coefficient is obtained by calculating the k-eigenvalue at a given density and then performing a second calculation but with a coolant density corresponding to a temperature increase of 200 degrees Celsius. The density is changed uniformly over the core and the upper plenum. Figure 3.2 indicates that the negative reactivity effect associated with increased neutron leakage is not sufficient to offset the positive reactivity contribution of a harder spectrum. The spectrum effect becomes more positive as P/D increases. As a result, the void reactivity coefficient becomes increasingly positive at higher P/D. It is observed that both coolants possess a significant positive void reactivity coefficient. However, the void coefficient tends to be more positive for sodium because of higher moderating power and an influential scattering resonance in ^{23}Na at 3 keV. In the energy region above 100 keV, the fission-to-capture ratio for ^{241}Am rises more rapidly than for ^{239}Pu. For that reason, the void coefficient becomes more positive if the fraction of americium is increased and the fraction of plutonium is correspondingly decreased.

The prompt neutron lifetime was calculated using MCNP. As expected, the prompt neutron lifetime increases with increasing P/D, corresponding to a softer spectrum and longer distance travelled by neutrons up to their point of absorption. Note that the average neutron lifetime in the lead/bismuth-cooled core exceeds 1μs for high pin pitches (P/D>2.0).

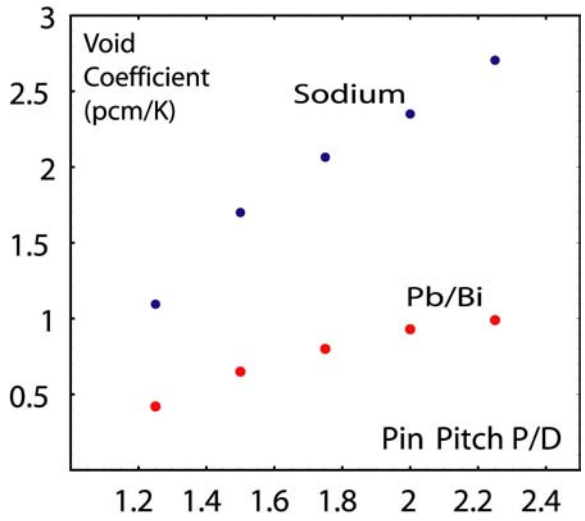

Figure 3.1: Void reactivity coefficient [pcm/K]

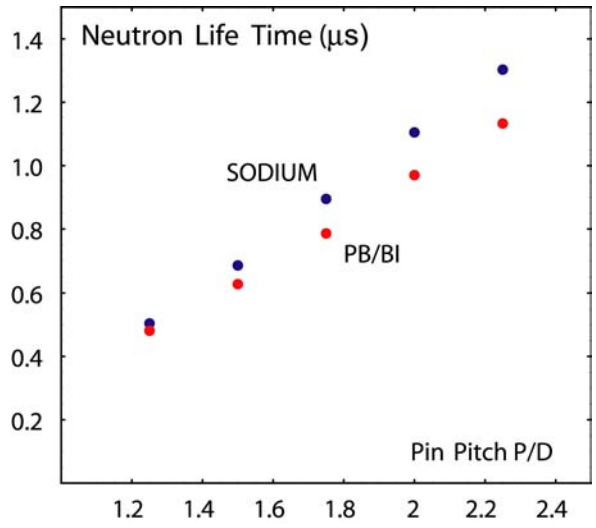

Figure 3.2: Prompt neutron lifetimes

Failure criteria

In order to determine the point of reactor damage a set of failure criteria, i.e. limiting temperature, has been postulated, those are listed in Table 3-2. Several difficulties exist in attempting to provide failure criteria for the existing system. The principal difficulty is the uncertainty in the operating performance of the fuel and structural materials. Chemical and mechanical interactions between the fuel, cladding, and coolant, as well as irradiation performance, etc. are not well known. Validation of failure criteria would require the availability of experimental test data. Preliminary safety margins are established as a first estimate to envelop worst-case conditions. The fuel is assumed to be stable up to the melting point, which is a reasonable assumption for present (sub-stoichiometric) oxide fuel. The fuel melting point as well as thermophysical properties vary with the stoichiometry. Present fuel properties correspond to an oxygen-to-metal ratio of 1.93. The failure temperature is based on the melting point of PuO_2 [7] and AmO_2 [8] together with the melting point of diluent ZrO_2, applying Vegard's law. The maximum cladding temperature is constrained by mechanical considerations. The primary cladding loading is the internal gas pressure; fuel-cladding mechanical interaction is neglected. We have assumed a maximum internal pin pressure of 10 MPa in steady-state as a result of pressure build-up by the release of fission gases. Under transient conditions the pressure may increase even further causing an increase in the loading of the cladding. Simultaneously, the cladding loses its strength at elevated temperatures. The cladding failure temperature is determined from correlations based on the calculated hoop stress and the failure temperature measured in cladding burst tests (20% cold-worked type 316 austenitic stainless steel) [9]. The transient burst temperature is representative for fast transients where the temperature is rapidly increasing until the cladding fails, providing less time for creep-type deformation.

Table 3-2. List of failure temperatures

Failure mechanism	Failure temperature	Comment
Melting of oxide fuel	2886 K	$0.11(Pu_{0.6}Am_{0.4})O_2 + 0.89ZrO_2$
Cladding burst temperature	1333 K	20% CW SS316, 5.56 °C/sec, hoop stress 100 MPa.

Transient analysis

Transient response has been examined for an unprotected transient overpower (UTOP) event. The possibility of a beam overpower accident is unique to accelerator-driven systems and it is open to debate. However, it is possible to imagine that a control system failure or inadvertent operation of the accelerator could lead to an accidental increase of beam power. The safety consequences will depend strongly on the details of the initiating circumstances, e.g.; what is the maximum beam load change that could possibly occur and at what speed can this event materialize? In the following analysis, the beam is presumed to double in strength in an instant. Reactor shutdown is disregarded. It is important to acknowledge the highly hypothetical nature of these assumptions. However, the analysis of accidents that appear incredible is an important part of the design of a safe reactor.

Transient power is displayed in Figure 3.3. For the case displayed the pitch-to-diameter ratio is 1.50. The magnitude of the initial burst is the same, independent of the coolant. The steady-state power will multiply by a factor of S/S_0 if the source strength is stepped from S_0 to S. The speed of the transition is determined by the prompt period. Delayed neutrons do not appreciably slow the response. Following the prompt jump, the power changes as a result of reactivity feedbacks. Coolant void reactivity feedbacks contribute to the course of the accident by adding reactivity. The small negative reactivity feedback associated with the Doppler effect does not influence the course of the accident. Differences in transient behaviour between lead/bismuth and sodium result primarily from the difference in boiling point and void reactivity effect. Coolant density changes provide modest changes in reactivity compared to the full void reactivity effect, which may introduce significant positive reactivity values. This causes the reactivity insertion rate to be considerable larger in the sodium-cooled core. Void generation, and thus positive reactivity insertion, is abrupt in the vicinity when boiling starts. Sodium boiling begins at the core outlet and develops axially downward. In the sodium-cooled core, the void effect adds enough reactivity to bring the reactor to a prompt critical state, with possible severe safety consequences. Prompt critical conditions are established about 400 seconds after accident initiation. Large positive reactivity insertions are potentially possible due to lead/bismuth voiding as well. However, it is seen that the high boiling temperature for lead/bismuth (1943 K) compared to sodium (1154 K) makes voiding less probable even though there are other ways of voiding the coolant besides boiling, i.e. large scale steam generator failure or possibly sudden gas release from ruptured pins. Voiding could possibly occur in severe loss of coolant accidents, such as tank rupture, however this must be regarded as extremely unlikely. It should be recognized that structural damage most likely occurs before boiling is encountered in a lead/bismuth-cooled reactor.

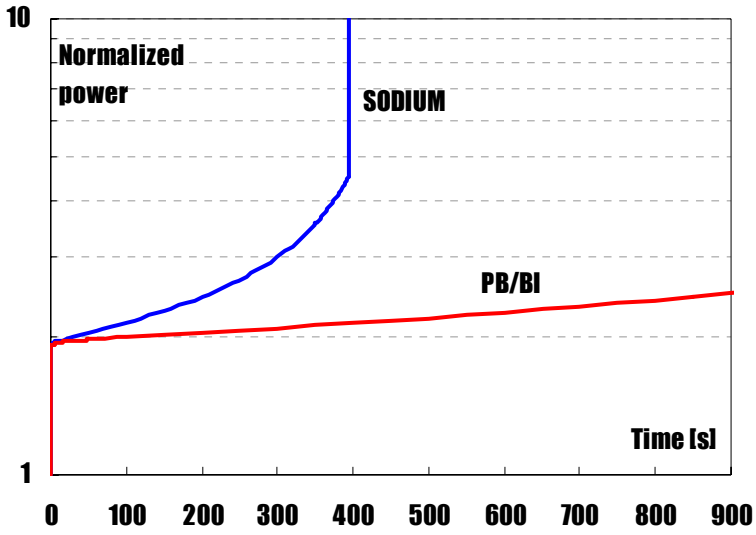

Figure 3.3: Normalized reactor power. P/D=1.50

In Figure 3.4 peak fuel and cladding temperatures are shown for the case P/D=1.50. Since no time is required for heat transport, the fuel suffers a rapid temperature rise. The amount of beam input determines whether there is immediate fuel damage or not. Subsequent heat-up occurs as a result of positive feedback from voiding and insufficient heat removal capability. The steam generators are assumed to remove heat at a rate of nominal power, resulting in increasing coolant inlet temperature as the transient proceeds. Sharp fuel temperature increase is calculated in the sodium case, as a result of a strong void reactivity insertion. The failure criterion for the fuel is exceeded in 200 seconds and the cladding is expected to reach its burst temperature in 350 seconds. The fuel fails prior to the initiation of sodium boiling (~350 sec) and this might disable the reactor before boiling and prompt criticality occurs. However, it is difficult to determine the consequences of fuel melting relocation. In the sodium case, cladding failure is predicted to occur by burnout. Cladding failure occurs simultaneously with sodium boiling. It is recognized that a substantial change in the nature of the accident may occur at the onset of fuel or cladding damage. Extrapolation of the transient beyond the actual failure points is subject to considerable uncertainty.

The assumption of constant heat rejection rate is conservative. In an overpower accident it is likely there will be some increase in the heat removal above 100%. Taking this into account would yield less pessimistic results. In reality, the feedwater system would try to maintain the correct coolant temperature returning to the core, and if it is not able to do so, the feedwater system would trip and issue reactor shutdown. It should be recognized that for both coolants considered the grace period is in the order of several minutes, which, in principle, provides considerable time for a well-designed safety system to act.

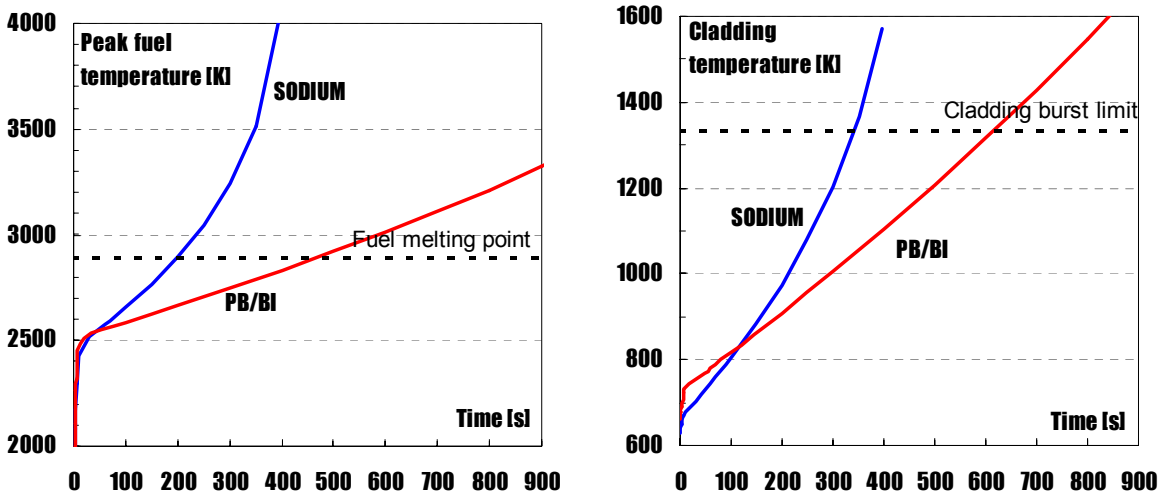

Figure 3.4: Peak fuel temperature (left) and peak cladding temperature (right). P/D=1.50.

The calculation is repeated for a range of pitch-to-diameter ratios. In Figure 3.5, the grace period is calculated for different P/D's. The grace period is measured in seconds. The grace time decreases somewhat at large pitches, a consequence of higher void coefficient for larger P/D. From the very basis of the assumptions, the choice of coolant does not change the inevitability of reaching a failure point; the timing of failure is different, however. The Pb/Bi cooled core features twice the grace time compared to the sodium-cooled core with the same P/D and power rating. The calculation revealed a small margin to prompt criticality at large pitches (sodium case). It was found that rapid sodium vaporization and expulsion occurred at the onset of boiling. Prompt criticality could possibly occur in less than 1 sec (P/D>1.50) once sodium boiling is initiated.

Oxide fuel temperatures are sensitive to linear power ratings. The allowable linear power is limited by the melting point. The low thermal conductivity of oxide fuel is compensated somewhat by a high melting point. Figure 3.6 illustrates the sensitivity of grace time on linear power. The calculation was performed for P/D=1.50. It should be recognized that different power ratings correspond to different core total powers in 0. The number of fuel pins is fixed while the steady-state linear power is varied. In the reference case the linear power is 16 kW/m corresponding to a total reactor power of 800 MW_{th}. The mode of failure differs; fuel failure dominates at high linear powers while cladding failure supersedes as the mode of failure at low linear power (<14 kW/m). The grace period provides an indication of the time available for a safety system to act. It was found that the safety performance of oxide fuel deteriorates rapidly with increasing pin power rating. At high linear power immediate fuel damage may occur, providing little time for a protection system to respond. It is possible to extend the grace period by derating the oxide fuel, but it has some obvious penalties.

The properties that have the greatest effect in the present analysis are the differences in boiling point and void coefficient. While the boiling temperature is fixed, the void coefficient can change significantly with design parameters. The void reactivity effect is the result of several physical phenomena and various methods have been proposed for reducing the void worth by design [10]. One possible way of void worth reduction is to reduce the pin size. The net result is shown in Figure 3.7, where the void worth of

lead/bismuth and sodium, respectively, is calculated as a function of P/D. The coolant void worth is determined by removing all coolant from the core and the upper plenum. The results suggest that a significant reduction in the void worth is achievable using smaller pin diameter. Reducing the void worth is an essential design objective. Large values of the void worth may present a difficulty in the licensing of minor actinide burners because of the risk for severe damage to the plant and public safety.

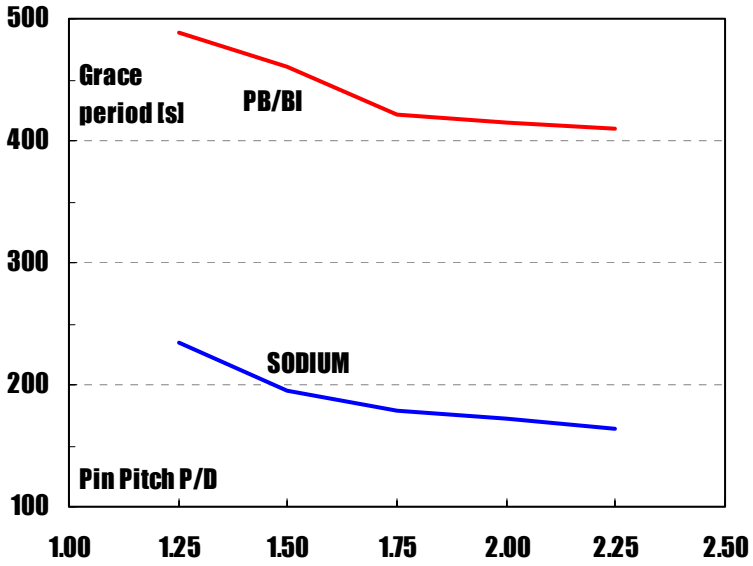

Figure 3.5 Grace period as a function of pin pitch. Linear power=16 kW/m.

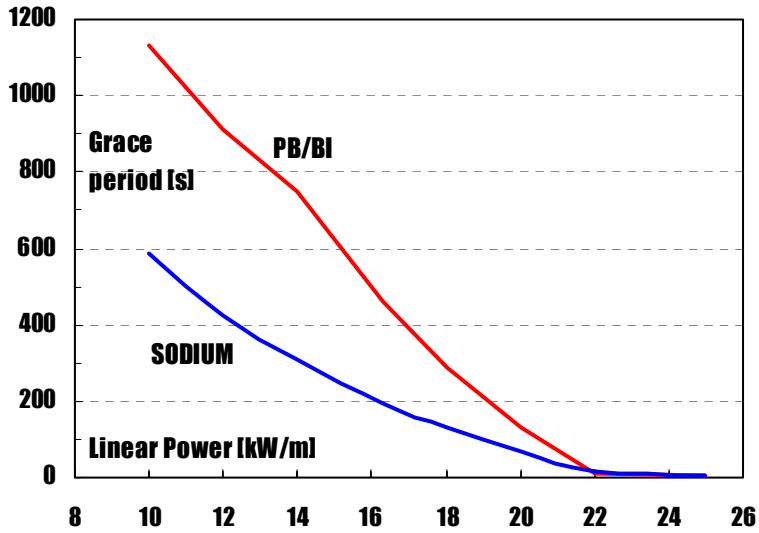

Figure 3.6 Grace period as a function of linear power rating. P/D=1.50.

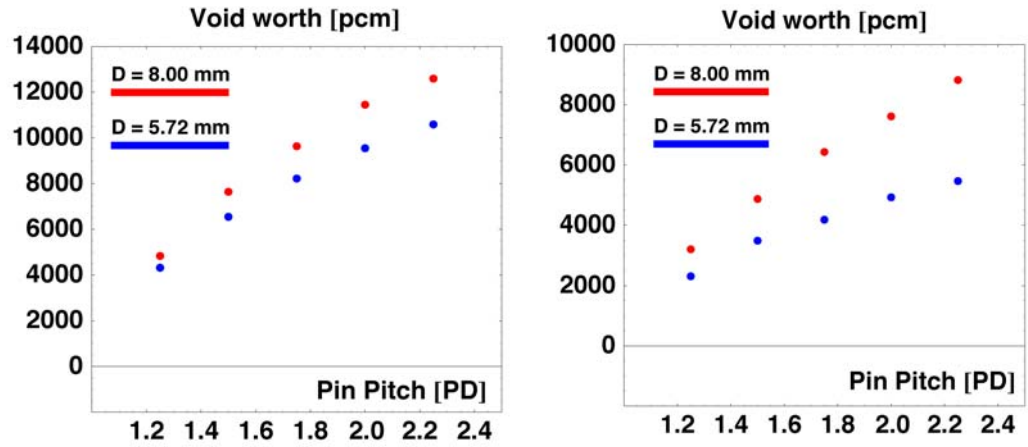

Figure 3.7 Sodium (left) and lead/bismuth (right) void worth as a function of P/D. Pin diameter is a parameter.

Conclusions

A strong positive void coefficient was found for both sodium and lead/bismuth. The considerable void effect is attributed to a high fraction of americium (60%) in the fuel. It was found that void reactivity insertion rates increases with P/D. In response to the beam overpower accident under discussion, the Pb/Bi-cooled core featured twice the grace time compared to the sodium-cooled core. The essential difference is attributed to the difference in boiling point and void reactivity contribution. An important safety issue is the high void worth that could possibly drive the system prompt critical. The problem is the result of the present fuel composition and it exists in both the sodium-cooled reactor and the lead/bismuth-cooled reactor. To some degree, this may be counter-balanced with proper core design, e.g. smaller pitch and pin diameter. For improved safety features, the general objective is to reduce the coolant void reactivity effect. The sodium-cooled core was found to have a smaller safety margin to prompt criticality. The high boiling temperature of lead/bismuth makes voiding less probable. The low effective thermal conductivity of oxide fuel results in high fuel temperatures and imposes constraints on the allowable linear power. Derating the oxide fuel could enhance the safety performance, but it has some obvious penalties.

3.3 GENERATION OF GROUP CONSTANTS FOR SPACE-TIME KINETIC ANALYSIS

An issue that arises in transient analysis is the need to apply appropriate kinetics methods. The applicability of traditional kinetics methods in driven systems is a topic of discussion. It was recently highlighted in theoretical work by D. G. Cacuci [11]. Traditional kinetic methods are based essentially on the schemes developed for critical system analyses. The experience in source-driven transient analyses is significantly less explored to that one existing for critical reactors. Verification of the existing computational tools is therefore important. That is why a corresponding benchmark has been initiated at KTH. Traditional kinetic models are compared to improve the understanding of their performance in source-driven systems. Agreement between simplified models and more general schemes may add to the validation. Comparison

between different models may also give a better understanding of neutron kinetics phenomena in ADS.

Modeling the space- and time kinetic analysis and the associated reactor dynamic phenomena requires considerable amount of input data preparation. Different procedures are applied in the various laboratories and countries. In this section, a short review of the computational methods and input data generation procedures being used at KTH, in the analysis of ADS, are described. In Figure 3.8, an overview of the work flow is presented.

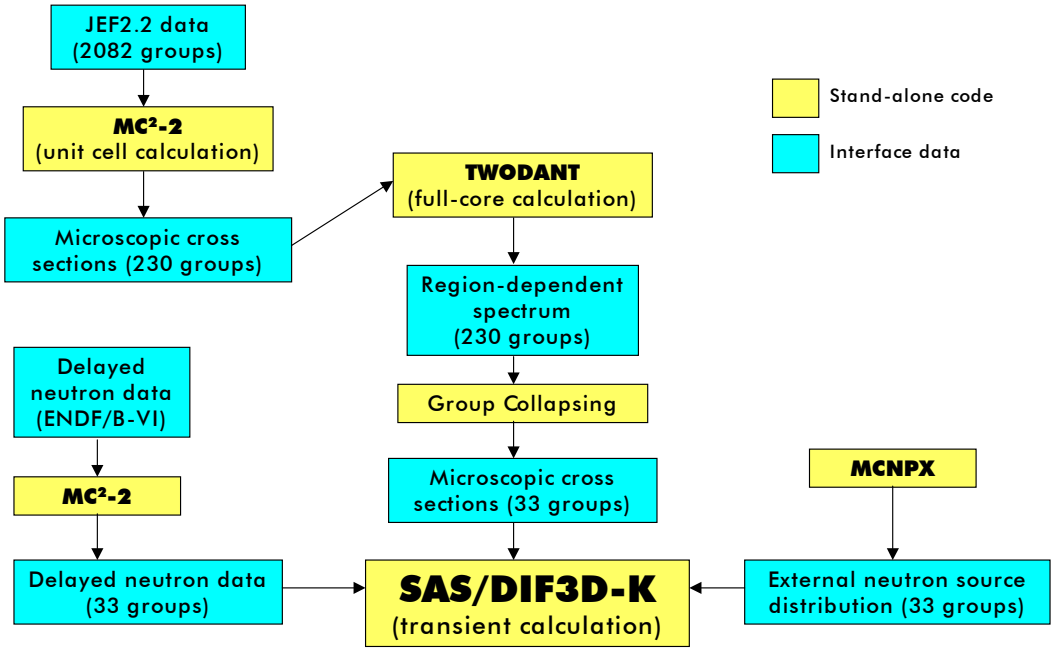

Figure 3.8: Work flow for preparing space-time neutronics analysis in SAS/DIF3D-K

MC^2-2 code

The starting point is the generation of multigroup cross sections for the reactor materials. Multigroup cross sections are derived from one of the evaluated nuclear data libraries (ENDF/B, JEF, JENDL, etc.). Such data files represent very detailed information on the cross sections. Neutronic calculations usually don't utilize these data directly. Instead, the multigroup approach is a common technique applied to manage the data in a less detailed manner.

Several group constant generation schemes have been devised to act as an interface between the master data files and a typical neutronics calculation. The two primary methods are the Bondarenko (or self-shielding factor) method and the Argonne method (MC^2), [12]. The Bondarenko method is implemented in the popular computer code called NJOY, which is the starting point for several self-shielding factor generation schemes. The Argonne method is a fundamentally different approach developed at Argonne National Laboratory and applied in the MC^2 computer codes. These methods proceed along two different paths, with somewhat different merits:

While the Bondarenko method[1] is a simplified technique, it is more widely used since it produces fairly widely applicable cross sections that are essentially independent of reactor composition and geometry. The calculation of effective cross sections involves interpolation in the generalized cross section library to fit a particular reactor composition, geometry, and temperature.

The Argonne method[2] applies a more rigorous approach, however, the output cross sections are composition dependent. Therefore, each time a new composition is desired, a new calculation must be performed. This may be impractical for design calculations.

At KTH, the MC^2-2 code is applied to the generation of cross sections based on JEF2.2 data for use in multigroup reactor dynamics calculations. The MC^2-2 code collapses the cross sections based on an ultra-fine group (2082 groups), zero-dimensional spectrum calculation (infinite medium calculation). The individual material microscopic cross sections are reduced to the fine group level (230 groups) by averaging the ultra-fine-group data over the flux and current spectra. TWODANT is then used to perform spatial cross section collapsing to a broad group level (33 groups for each region). The function of TWODANT is to take into account the reactor geometry and leakage in the fine group spectrum that is used to collapse the cross sections down to 33 groups with a regional dependence, that is different sets of multigroup cross sections for different reactor zones. The broad group data are written in the ISOTXS formats. The output cross sections are then ready for use in subsequent dynamics calculations in SAS/DIF3D-K. Multigroup cross section sets are generated at 4 different fuel temperatures. SAS/DIF3D-K interpolates the fuel capture and fission cross sections locally as the calculation proceeds.

SAS/DIF3D-K code

The SAS/DIF3D-K code couples reactor thermal hydraulics treatment with a 3D neutron spatial kinetics treatment. The code is designed to perform deterministic safety analysis of transients in liquid metal cooled reactors. The code may use sodium, lead, or lead/bismuth as coolant. The thermal/hydraulics treatment in SAS/DIF3D-K calculates detailed 3-dimensional temperatures and material densities. The code uses multiple channels (the term “channel” is used to denote collectively the fuel pin, cladding, associated coolant, and structure) to model a whole-core representation. Heat transfer in each pin is modeled with a two-dimensional (r/z) heat conduction equation. The core assembly thermal hydraulics treatment in SASSYS-DIF3DK includes the calculation of fuel, cladding, and structure temperatures, as well as coolant flow rates and pressure distributions in each channel.

---

[1] *The main difference is that the Bondarenko method assumes a within group spectra (e.g. 1/E), which greatly simplifies the problem. The emphasis of the Bondarenko method focuses on the flexibility allowed by this assumption. In general, with the Bondarenko method, one cross section set is applicable for any composition.*

[2] *The Argonne method was developed out of the conviction that an assumed within-group weighting spectrum is inaccurate. Instead, MC^2-2 explicitly calculates the within group spectral effects. The analysis necessitates a large number of energy groups that leads to an ultra-fine group slowing-down calculation (2082 groups). The calculation depends on the actual reactor composition and the cross section set becomes problem dependent. The methodology was originally developed for fast fission reactors.*

Neutron distributions are calculated using either transport theory or diffusion theory. The DIF3D-K module solves the multigroup neutron diffusion equation in both Cartesian X-Y-Z and hexagonal-Z geometries, using assembly-sized radial nodes. The VARIANT-K module solves the time-dependent multigroup neutron transport equation in two- and three-dimensional Cartesian and hexagonal geometries using variational nodal methods. The neutronic model solves the time-dependent neutron balance equations with or without external neutron source. Two major time discretization methods are available, the theta method (or direct method), and space-time factorization method (IQS, adiabatic, or point kinetics). Macroscopic cross sections are updated with respect to density and temperature variations.

Preliminary neutronic results

The newly generated cross sections have so far been applied in static neutronic calculations in SAS/DIF3D-K and TWODANT. Example problem and material compositions were taken from an OECD/NEA benchmark specification for an accelerator-driven reactor [13]. The benchmark design is based on the Advanced Liquid Metal Reactor (ALMR) design. The sodium coolant was replaced with liquid Pb/Bi, and the fuel material was replaced with zirconium containing minor actinides and plutonium in the form of mononitrides.

For the results reported here, see Table 3-3, nodal diffusion theory results were obtained with DIF3D-K, and nodal P1 transport theory results were obtained with VARIANT-K. DIF3D calculates the diffusion coefficients using the transport cross sections (i.e., P0 cross section corrected by P1 scattering.) TWODANT uses discrete ordinates method (Sn=4), and r-z geometry. Integral results from eigenvalue calculations at the steady-state are given in 0. The results were obtained on the first steady-state iterations, when the fuel temperature is at 980 K and the coolant density is uniform corresponding to the reactor inlet coolant temperature (573 K). The results are in agreement with expectations, i.e. the P0 calculation shows a large deviation from the P1 results, and the P1 correction in diffusion theory gives a result very close to the consistent P1 transport result. The difference between TWODANT and VARIANT for P0 scattering is due to different transport correction. The 33 group eigenvalue is very close to the 230 group k_{eff}. The collapsing procedure conserves the reaction rates, and hence k_{eff}. The preliminary results appear to be consistent with results contributed by the participants in the original benchmark exercise. However, the calculations are still in the process of verification. The next step is to proceed with the transient calculations.

Table 3-3. Comparison of k_{eff} calculations

	33 groups		
	TWODANT*	SAS (DIF3D-K)	SAS (VARIANT-K)
P0	0.9872	-	1.0003
P1	0.9659	0.9666	0.9664
	230 groups		
P0	0.9870	-	-
P1	0.9655	0.9669	-

4 ADS SAFETY MECHANISMS - EMERGENCY HEAT REMOVAL

4.1 OVERVIEW

The doctoral dissertation called 'Passive and Inherent Safety Mechanisms applied on a Pb/Bi-cooled Accelerator-Driven System' has been finally put together during year 2002. The defence of the thesis took place in early May 2003.

Two papers have been written describing main results of the safety studies. A paper called 'Emergency Decay Heat Removal by Reactor Vessel Auxiliary Cooling System from an Accelerator-Driven System' was published in Nuclear Technology Vol. 140 in October 2002 - see Appendix 3, and an article 'An investigation on locating the heat-exchangers in the riser of an Accelerator-Driven System' has been submitted to the Annals of Nuclear Energy – see Appendix 4.

4.2 RESULTS

Passive Emergency Decay Heat Removal

The passive emergency decay heat removal during severe cooling accidents in Pb/Bi-cooled 80 MW_{th} and 250 MW_{th} Accelerator-Driven System designs was investigated with the CFD code STAR-CD. For the 80 MW_{th} design, the calculations show that no structural problems occur as long as the accelerator proton beam is switched off immediately after accident initiation. A delay of beam stop by 30 minutes after a combined Loss-Of-Heat-Sink and Loss-Of-Flow accident would lead to reactor vessel temperatures in the secondary creep domain, which do not cause severe structural problems. By using a melt-rupture disc on the vacuum pipe of the accelerator proton beam to interrupt the beam at elevated temperatures in a passive manner the grace time before beam stop is necessary is increased from 30 minutes to 6 hours. An emergency decay heat removal design which would prevent radioactive release to the atmosphere even more reliably than the PRISM design was also investigated. For an ADS of 250 MW_{th} power with the same vessel as the 80MW_{th} ADS examined, the maximum wall temperature reaches 745 K after an immediate beam stop. This does not cause any structural problems either. The grace time until a beam stop becomes necessary for the 250 MW_{th} system was found to be about 12 minutes. To reduce elevated vessel temperatures more rapidly after a beam stop alternative cooling methods were investigated, for example filling of the gap between the reactor and the guard vessel with liquid metal and the simultaneous use of water spray cooling on the outside of the guard vessel. This decreases the coolant temperatures already within minutes after switching off the proton beam. The use of chimneys on the Reactor Vessel Auxiliary Cooling System, which increase the air flow rate, lowers the maximum reactor vessel wall temperature only by about 20 K. It can be concluded that the critical parameter for the emergency cooling of an ADS is the time delay in switching off the accelerator after accident initiation.

An Investigation on locating the Heat-Exchangers in the Riser of an Accelerator-Driven System

A safety investigation was made concerning the location of heat exchangers in the risers of a Pb/Bi cooled accelerator-driven system. In a pool type design with a simple flow path and gas lift pumps, this approach will have advantages regarding heat exchanger tube failures, particularly if water is used as the secondary fluid. The safety implications on the primary system were investigated for the case of locating the heat-exchangers in the risers of a 200 MW_{th} and an 800 MW_{th} ADS. The results were then compared to an ADS with heat-exchangers in the downcomers. Apart from temperatures and velocities at normal operation, the accident scenarios of loss-of-flow, loss-of-heat-sink, and a total-loss-of-power were examined. Assuming an immediate beam-stop after a loss-of-flow accident for a 200 MW_{th} system, the core outlet temperature increases within two minutes to 1070 K. A minute thereafter the temperature decreases to 1020 K. After a loss-of-heat-sink the grace period before the accelerator proton beam has to be shut off was found to be ~4 minutes. A total-loss-of-power accident results in a temperature peak of 664 K after nearly 10 hours. The investigations on the 800 MW_{th} system were performed in a larger vessel of 17 m height. The design with the heat-exchangers in the risers showed elevated temperatures after a loss-of-flow accident, which would severely damage the core. On the other hand, the case with heat exchangers in the downcomer showed acceptable results. The computational fluid dynamics code STAR-CD was used in all calculations.

5 PROTON SOURCE EFFICIENCY

In order to study the beam power amplification of an accelerator driven system, a new parameter, the proton source efficiency (ψ^*) is introduced. ψ^* represents the number of neutrons produced by fission in the core, relative to the eigenmode production, and is closely related to the neutron source efficiency (φ^*), which is frequently used in the ADS field. The main advantage with using ψ^* instead of φ^* is that the way of defining the source efficiency is unique.

Numerical simulations have been performed with the Monte Carlo code MCNPX in order to study ψ^* as a function of different design parameters. It was found that, in order to maximize ψ^*, a target radius as small as possible should be chosen. For target radii smaller than about 30 cm, lead-bismuth is a better choice of coolant material than sodium, while for larger target radii the two materials are equally good. The optimal axial proton beam impact was found to be located approximately 20 cm above the core center. Varying the proton energy, ψ^*/E_p was found to have a maximum for proton energies between 1200 and 1400 MeV. Increasing the americium content in the fuel decreases ψ^* considerably, in particular when the target radius is large.

Details of this study are presented in Appendix 5: "Definition and Application of Proton Source Efficiency in Accelerator Driven Systems" by Per Seltborg, Jan Wallenius, Kamil Tucek and Waclaw Gudowski

6 PROGRESS IN EUROPEAN PROJECTS

6.1 NEUTRONIC CALCULATIONS FOR FUTURE AND CONFIRM

Neutronic design and safety calculations for minor actinide burners were made for the CONFIRM and FUTURE projects. Below, the following properties pertaining to potential fuel types will be discussed:

- Reactivity evolution
- Void worth
- Expansion coefficients
- Linear rating
- Limits to burnup
- Equilibrium composition

The calculations were made for a model core with properties listed in Table 6-1.

Table 6-1. Parameters of the ADS model used for the CONFIRM /FUTURE calculations

Core power	800 MW_{th}
Spallation target	LBE
Target radius	20 cm
Core height	100 cm
Pu/Am	40/60
k-eigenvalue	0.97

Reactivity evolution

The small Doppler feedback in conjunction with a low fraction of delayed neutrons makes sub-critical operation of cores with americium based fuel imperative. The sub-critical state however limits the potential of control rods for reactivity management. Conceivable reactivity insertions may result in failure of core components due to increased heat production. Let us illustrate this with an example. If one would operate the ADS at k-source equal to 0.97, a reactivity insertion of 1500 pcm in the absence of beam shut-down would lead to an instantaneous increase in heat production of 100%. A fuel with a low thermal conductivity (2-3 W/m*K) operating at a rating of a few tens of kW/m then fails within milliseconds due to centerline melting, in spite of the core still being sub-critical. In any case, the control rod bank worth must be less than the sub-criticality margin. An accidental insertion of 100% proton beam power would have similar consequences [14].

Hence, it is highly desired that the reactivity swing should be minimized, subject to the overall P&T condition of maximizing burnup. Irrespective of whether one chooses to regulate the swing by means of control rods or proton beam power, one finds that the upper limit for Δk during a full irradiation cycle should be less than about 3000 pcm. In order to reach 20% actinide burnup without measures like fuel shuffling or core resizing, plutonium must be added to the fuel, to compensate for the increase in reactivity resulting from irradiation of americium. The appropriate fraction of plutonium is dependent on spectrum as well as plutonium quality. Table 6-2 exemplifies how the reactivity loss depends on neutron spectrum for a start-up core with oxide fuel in a Cr-matrix. The plutonium vector was taken to be that of spent MOX fuel after seven years of cooling.

Table 6-2. Reactivity losses per percent burnup in LBE cooled start-up cores with Pu/Am = 40/60. The average neutron energy differs due to different fuel density, matrix fraction and pin diameter. JEF2.2 cross section data were used.

Fuel density	Cr fraction	Di/Do [mm]	P/Do	En [keV]	En(f) [keV]	$\Delta k/\Delta M$ [pcm/%]
0.90 TD	49%	5.0/5.7	1.50	225	565	-250
0.95 TD	56%	6.0/6.8	1.50	195	515	-160
0.95 TD	49%	6.0/6.8	1.75	190	505	-120

A harder spectrum yields larger reactivity loss, as the probability for fission of americium is raised. Considering possible variations in core parameters and feed vectors, a Pu fraction between 30 and 40 percent appears to yield a sufficiently small reactivity swing [20]. Precaution must be taken for a large discrepancy in the predicted swing obtained with different evaluations of the cross section for fission of ^{242}Cm. ENDF/B-VI data gives almost two times higher reactivity losses for start up cores than data from JEF2.2 and JENDL3.2 [17].

Void worth

The lack of a significant Doppler effect in ADS fuels implies that core configurations yielding prompt super-criticality should be avoided. The combination of MA-bearing fuel and liquid metal cooling will typically yield a positive coolant void worth. The choice of coolant, as well as the fuel design however have a significant impact on the magnitude of the void worth. A parameter study made for an 800 MW_{th} core with a Pu/Am ratio equal to 40/60, has shown that the void worth may differ by up to 5 000 pcm for different ceramic matrices, and by up to 10 000 pcm for different coolants [21]. Figure 6.1 shows sodium and LBE void worth as function of P/D for an oxide CERCER (zirconia) and an oxide CERMET (chromium) fuel. As in the case of fast reactors, the void worth is lower for fuels having a high thermal conductivity. The reason for this is that a higher linear rating corresponds to a fewer number of fuel pins in the core and consequently a higher radial leakage in the voided state. The drastic difference in void worth between sodium and LBE is due to the large amount of americium in the fuel.

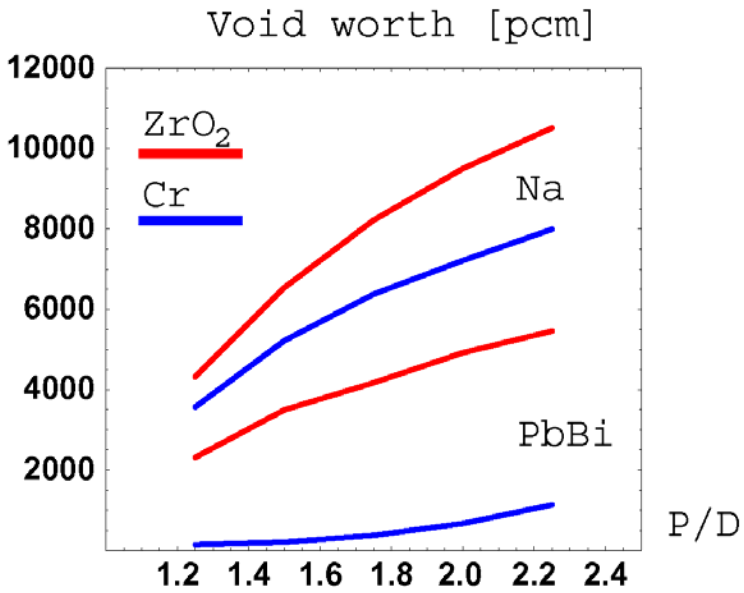

Figure 6.1: Void worth for single zone cores as function of P/D. An inner clad diameter of 5.0 mm was assumed. The Pu/Am ratio was kept constant at 40/60, and a k-eigenvalue equal to 0.97 was obtained by adjusting the fraction of inert matrix. The linear ratings were assumed to be 15 and 35 kW/m for zirconia and Cr matrices, respectively.

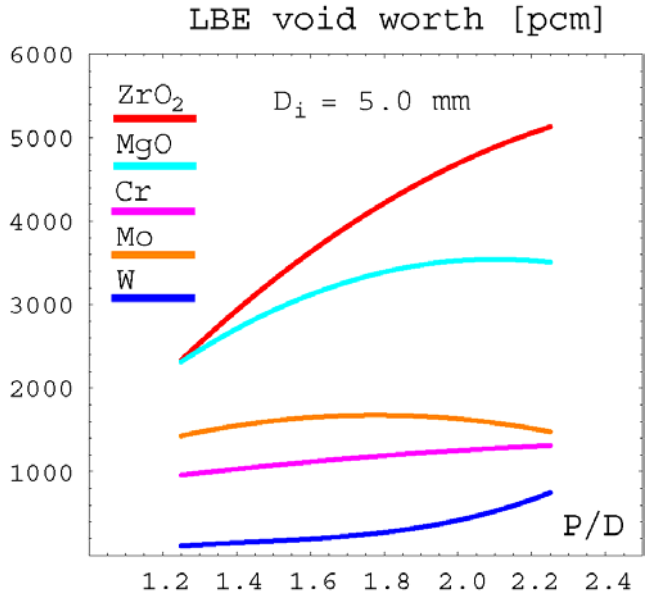

Figure 6.2: Void worth as function of P/D for oxide fuels. The linear rating assumed for the fuels was 35 kW/m for the CERMETs, 25 kW/m for the CERCER with MgO matrix, and 15 kW/m for the zirconia matrix.

In Figure 6.2 and Figure 6.3, the LBE void worth for oxide fuels is compared to that of nitride solid solutions. Note that matrices based on Chromium and Yttrium offer an advantage in terms of a low void worth. The explanation is that ^{52}Cr and ^{89}Y are nuclides with a full neutron shell, thus providing a threshold for in-elastic scattering above 1 MeV. Nuclides without a full neutron shell typically have thresholds for

inelastic scattering located at about 0.5 MeV. Hence, a larger fraction of newly born fission neutrons will be prone to loose half an MeV kinetic energy or more in a single collision with neutronically non-inert nuclides, which in combination with inelastic scattering in the coolant quickly brings the neutrons below the fast fission threshold of americium. Loss of coolant then leads to a shift in the neutron spectrum to energies above the fast fission threshold, and a positive contribution to the void worth. Chromium and Yttrium on the other hand are inelastically transparent for about half of the newly born fission neutrons, yielding not only a harder spectrum, but also a smaller shift of spectrum during coolant voiding.

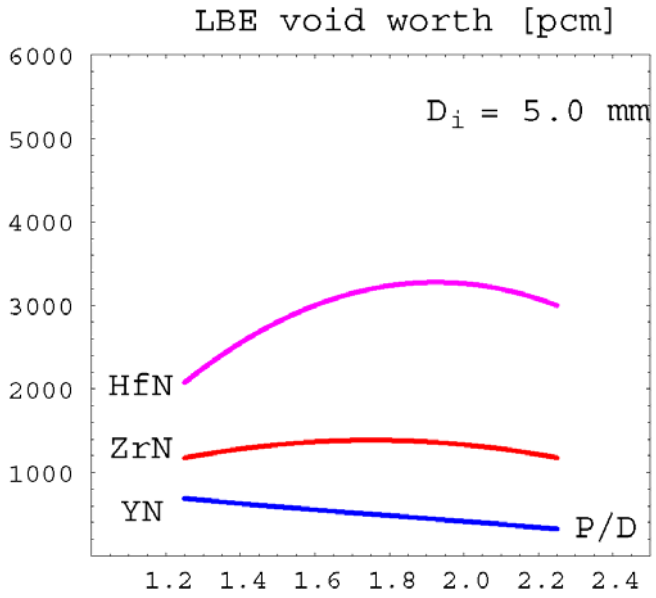

Figure 6.3: Void worth as function of P/D for nitride fuels. The linear rating assumed was 35 kW/m .

Expansion coefficients

While significant temperature feedbacks are not required for normal operation, negative feedbacks remain useful for minimizing fluctuations in core power. For liquid metal coolants, the temperature coefficient will typically be positive. Figure 6.4 shows the LBE temperature coefficient at normal operating temperature, for different oxide fuels as function of pin pitch.

Note that the coefficient remains below +1.0 pcm/K for a wide range of core parameters. Axial expansion of CERMET fuels, as well as metallic and nitride fuels, is a prompt negative feedback mechanism that may compensate for the positive temperature coefficient of the coolant. In Table 6-3 the temperature coefficients of a core with oxide fuel in a Cr-matrix and P/D = 1.50 are displayed.

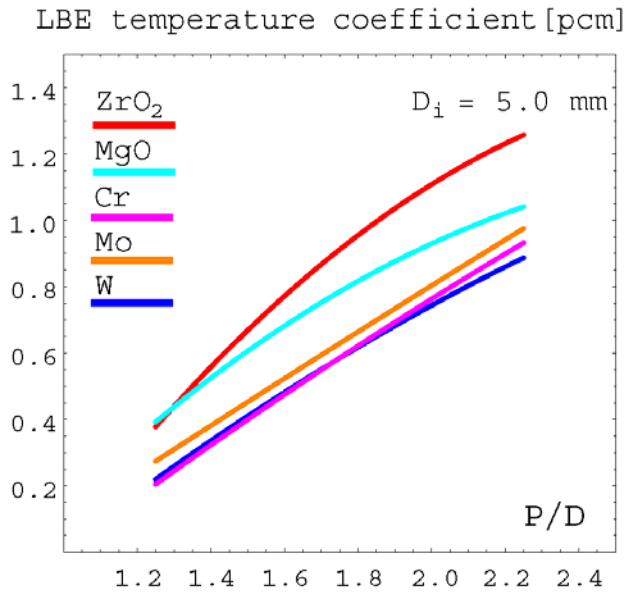

Figure 6.4: Lead-bismuth temperature coefficient as function of P/D.

Table 6-3. Temperature coefficients of an 800 MW_{th} ADS with oxide fuel in a Cr-matrix.

Mechanism	Temperature coefficient
Coolant expansion (LBE)	+0.4 pcm/K
Coolant expansion (Na)	+1.5 pcm/K
Fuel axial expansion	- 0.4 pcm/K
Radial grid expansion	- 0.3 pcm/K
Doppler broadening	- 0.05 pcm/K

Note how the LBE and fuel axial expansion coefficients cancel each other. The Doppler coefficient is negligible, as expected. Expansion of the radial grid contributes negatively to reactivity, but is a delayed feedback with a response time of about 0.1 seconds. Sodium cooling would yield a higher void coefficient, even when taking into account that the core may be designed with a smaller pin pitch. Hence the interest in introducing heavy liquid metals or helium gas as coolant for minor actinide burning ADS.

Linear rating

The lack of Doppler feedback inevitably leads to a larger vulnerability to overpower accidents in the ADS. Such accidents can be initiated by either insertion of accelerator current margin, control rod withdrawal, or incorrect fuel loading. The 15% overpower margin required for FBR licensing, is likely to increase significantly for ADS.

In addition, the poorer thermal conductivity of coolant (LBE or He) and fuel (TRU-compounds) leads to new restrictions on linear rating already during normal operation. Roughly speaking (neglecting feedbacks), the linear rating is set by the condition that

the temperature margin to fuel (cladding) failure must be larger than the temperature gradient over the fuel (coolant), in order to cope with a 100% overpower accident. Consequently, a high thermal conductivity of the fuel is desired. A high thermal conductivity (high rating) of the fuel is also beneficial for the coolant void coefficient, as explained in the previous paragraph.

Presently three major fuel compositions are planned to be irradiation tested: metals (US), nitrides (Japan, US & Europe) and oxides (Europe). Out of these, metals and nitrides must be alloyed with/dissolved in an inert matrix in order to guarantee high temperature stability, while oxides must be fabricated with a certain degree of substoichiometry. While zirconium and its nitride/oxide compounds is foreseen as matrix for the first irradiation testing of prototypic ADS fuels, their poor conductivity is a clear incentive to investigate alternatives.

Metals fuels must be fabricated with a liquid metal bond to enable operating temperatures below the melting point. Nitrides may be used with either a helium or a liquid metal bond, while oxides are incompatible with at least sodium.

An estimation of the power to melt at BOL is displayed in Table 6-4 for each candidate. A core inlet temperature of 600 K was adopted, and it was assumed that a linear power of 30 kW/m yields a temperature increase in the coolant channel of 220 K. A main approximation is that the radial clad-fuel gap was fixed to 50 microns for the helium bonded fuels. In the case of nitrides and metals, no data for the thermal conductivity of americium was available, and hence the conductivity of Pu and PuN was used. As can be seen, sodium bonded nitride fuel holds a distinct advantage over any other fuel/matrix candidate. Other choices yield acceptable ratings, with the exception of oxide fuel in solid solution with zirconia. In order to survive a 100% overpower accident, the zirconia fuel would have to be operated at less than 20 kW/m. The quoted power to melt for the sodium bonded nitride fuel is partly of academic character, since sodium boiling takes place at about 75 kW/m. Lead bonding might be a possibility to use the full potential of nitride fuels.

Burnup limits

In fast neutron reactors, swelling of fuel cladding and wrapper tubes has been identified as the ultimate limitation to fuel burnup. Steels developed for the purpose of being swelling resistant have enabled to reach doses ranging from 150 DPA (austenitic steels) to 200 DPA (ferritic steels). In order to achieve high burnup of the ADS fuel, the design should provide a high ratio between fission and DPA rates. Since the minor actinides present in the fuel are fissionable by neutrons with energy above 1 MeV, it is of interest to minimize the presence of nuclides with large cross section for inelastic scattering in the fuel while simultaneously suppressing the flux that causes damage (neutrons with $E > 0.1$ MeV).

Table 6-4. Fuel temperature gradient for c = 30 kW/m and power to melt at BOL. The inert matrix volume fraction was set to 60%. Sodium bonded fuels have a surface temperature of 850 K at c = 30 kW/m, helium bonded 1400 K. The porosity of oxide fuels was taken to be 5%, nitride fuels 15%.

Fuel	Matrix	Bond	DT_{fuel} [K]	T_{center} [K]	T_{melt} [K]	P_{melt} [kW/m]
Metal	Zr	Na	155	1005	1370	60
Nitride	ZrN	Na	190	1040	2770	159
Nitride	ZrN	He	190	1590	2770	67
Oxide	Cr	He	105	1505	2180	54
Oxide	Mo	He	60	1460	2650	69
Oxide	W	He	55	1455	2650	70
Oxide	ZrO2	He	1010	2410	2650	38
Oxide	MgO	He	540	1940	2550	52

A simple estimation of the burnup potential B_p of a fuel can be found from the formula

$$B_p = 1 - e^{-\sigma_f \varphi \tau_{\max}} \qquad (6.1)$$

where σ_f is the average fission cross section of fissionable nuclides, φ is the neutron flux, and τ_{max} is given by

$$\varphi_{fast} \tau_{\max} = \Phi_{\max} \qquad (6.2)$$

Here, φ_{fast} is the flux of neutrons with energies above 0.1 MeV, i.e. the flux capable of causing radiation damage in the clad, and Φ_{max} is the fast fluence limit. For ferritic steels 200 DPA roughly corresponds to $\Phi_{max} = 4.0*10^{23}$ n/cm^2 [15]. The fuel averaged fission cross section and the corresponding burnup potential for the ADS fuel candidates here studied are listed in Table 6-5. These numbers may be compared to the average fission cross section of standard FBR oxide fuel, being 0.33 barns, yielding a burnup potential of 20%, if estimated by formula (5.1). The good agreement with the actual burnup limit may be coincidental, since equation (5.1) contains a bare minimum of physical information. However, the relative burnup potential of different fuels should be possible to predict using this approach.

Due to the comparatively low fission cross section of americium, the burnup potential does not increase in proportion to the fraction of removed ^{238}U. Note that the burnup potential for the fuels with an MgO matrix is higher than for the other fuels. In general, it appears as the inert matrix fuels here studied have a burnup potential ranging from 30 to 33%, which of course only may be realized in full extent if core management succeeds in leveling out power peaking factors.

Table 6-5. Fuel and spectrum averaged fission cross section and burnup potential for the fuels here investigated. Values are given for LBE coolant, P/D = 1.75 and an inner clad diameter of 5.0 mm.

Fuel/Matrix	σ_f [b]	B_p [%]
Oxide/ZrO2	0.64	32
Oxide/MgO	0.66	33
Oxide/W	0.63	30
Oxide/Mo	0.64	30
Oxide/Cr	0.65	31
Nitride/ZrN	0.66	31
Nitride/HfN	0.67	30

Equilibrium composition

The plutonium present in the spent fuel of minor actinide burning ADS features a large fraction of ^{238}Pu, and hence should be recycled in ADS. Considering that the first core loads would consist of americium mixed with Pu from spent MOX fuel, with only a marginal fraction of curium, it will take 7 - 8 recycles before a near equilibrium fuel composition is obtained. Thus the first generation ADS would operate with non-equilibrium fuel for most of its lifetime. Nevertheless, equilibrium analysis is important, in order to assess long term costs for fuel fabrication and reprocessing, which are likely to be driven by curium inventories.

The equilibrium fuel composition is a function not only of neutron spectrum, but also of cooling time and neutron flux magnitude. A longer cooling time allows for out-of-pile decay of ^{241}Pu and ^{244}Cm, increasing the fraction of their decay products in the reprocessed ADS fuel. Similarly, low flux intensity increases the probability for in-pile decay of ^{242}Cm.

Preliminary calculations of the equilibrium composition for an ADS with oxide fuel in a Cr-matrix have been performed with the JEF2.2 cross section data library. The actinide vectors for the start up core and the for the 7th reload are given in Table 6-6. The inert matrix fraction was kept constant at 56 volume percent and the pin pitch adopted was 1.50 times the pin diameter. In the first reload, the top-up required to obtain a k-eigenvalue of 0.97 was 10% Pu and 90% Am. Starting from the 2nd reload, only americium was added to the reprocessed ADS fuel. The average linear power was set to 35 kW/m. The irradiation scheme was taken to be two times 300 days irradiation + 65 days of in-pile cooling, followed by seven years out-of pile cooling. During the two years in-pile an average burnup of 17% is achieved.

Note that the plutonium fraction remains approximately constant over the 60 year campaign. Curium is built up from americium, but the concentration of the troublesome alpha and neutron emitter ^{244}Cm remains below nine percent.

Table 6-6. Example of near-equilibrium composition for TRU fuel recycled in an ADS with oxide fuel in a Cr-matrix. 17% burnup and seven years of cooling time was used in the calculation.

Nuclide	Start-up	Cycle 8
^{238}Pu	0.020	0.132
^{239}Pu	0.152	0.027
^{240}Pu	0.121	0.150
^{241}Pu	0.053	0.011
^{242}Pu	0.054	0.082
Total Pu	**0.400**	**0.402**
^{241}Am	0.400	0.288
^{242m} Am	-	0.023
^{243}Am	0.200	0.185
Total Am	**0.600**	**0.496**
^{243}Cm	-	0.001
^{244}Cm	-	0.081
^{245}Cm	-	0.016
^{246}Cm	-	0.003
Total Cm	**-**	**0.101**

The neutron spectrum of FBRs varies only marginally from one design to another, due to restrictions set by breeding and neutron economy. In ADS, one has a larger parameter space available for fuel matrix and core design. The less restrictive neutron economy allows for introduction of absorbing matrices, yielding a harder spectrum, or alternatively larger pin pitches, softening the spectrum. Table 6-7 shows effective cross sections and fission probability for ^{241}Am as function of fuel matrix. Note that the use of

Table 6-7. Spectrum averaged cross sections and fission probabilities for ^{241}Am for the fuels here investigated. Values are given for LBE coolant, P/D = 1.75 and an inner clad diameter of 5.0 mm.

Fuel/Matrix	σ_f [b]	σ_c [b]	$\sigma_f/(\sigma_f + \sigma_c)$
Oxide/ZrO_2	0.31	1.34	0.19
Oxide/MgO	0.33	1.37	0.20
Oxide/W	0.33	1.10	0.23
Oxide/Mo	0.34	1.09	0.24
Oxide/Cr	0.34	1.17	0.22
Nitride/ZrN	0.35	1.18	0.23
Nitride/HfN	0.38	0.97	0.28

an oxide matrix results in a comparatively soft spectrum, and higher production rates of curium. Heavy metal absorbers, like molybdenum, tungsten and hafnium, provide low

energy neutron capture, and thus the effective capture cross section of the minor actinides is suppressed. Hafnium is more transparent to fast neutrons and provides the highest fission probability of the matrices investigated. Consequently, one may expect that using Hf or HfN as matrix material, that the corresponding equilibrium fuel will feature a smaller amount of ^{244}Cm. A penalty in form of higher reactivity losses would have to be paid.

Conclusions

From the neutronic viewpoint the following, sometimes contradictive properties would be beneficial for fuel used for minor actinide transmutation in ADS

- *Composition:* Presence of 30-40% plutonium, in order to achieve a minimum reactivity swing, combined with an average inert matrix volume fraction larger than 50%, in order to ensure fabricability and obtain a suitable sub-criticality level. A Tungsten matrix does not seem to fulfill this condition.
- *Margin to melt:* A high thermal conductivity combined with a high melting temperature, in order to provide a high power to melt. Sodium bonded nitride has an outstanding performance in this context.
- *Void worth:* A small cross section for in-elastic scattering combined with a high thermal conductivity minimizes void worth. Cr and Yt yield close to zero void worth for the configurations investigated.
- *Fission probability:* A high probability for fission minimizes buildup of curium. Hafnium nitride gives the highest fission probability.

6.2 SPIRE PROJECT - MOLECULAR DYNAMICS STUDY OF RADIATION DAMAGE IN FE-CR ALLOYS

Background

The decisive factor limiting the fuel burnup in fast neutron reactors is swelling of the cladding material. The discovery of this phenomenon was made in 1969 in the Dounray Fast Reactor. Since then a large experimental effort has been devoted to finding steel compositions more resistant to radiation. Consequently, the incubation threshold for onset of accelerated swelling has been increased from the 20 DPA limit of SS316, up to 100 DPA for austenitic steels like 15-15Ti, and up to 200 DPA for certain ferritic steels, with the 9Cr-1Mo composition (EM10) providing the best performance seen up to date.

Theoretical understanding of the mechanisms responsible for swelling of neutron irradiated steels has however remained on a qualitative level. The Production Bias Model (PBM) originally suggested by Woo and Singh has been able to reproduce swelling rates FCC-copper irradiated up to 1 DPA [27], [31]. In this model it is assumed that aggregation of interstitial clusters during the recoil cascade, and their subsequent one-dimensional migration to grain boundaries is the main driver for swelling. The well known difference in swelling rates between FCC- and BCC-crystals, has so far not been possible to explain within the PBM framework. A number of molecular dynamics simulations of interstitial cluster formation has been performed for pure BCC-iron

[23][29]indicating differences in cluster size and formation rate with respect to FCC-copper but not being able to explain experimental findings. The conclusion is strongly dependent on the validity of the effective interaction potential adopted in the simulations. A potential of Finnis-Sinclair type, further developed at Liverpool University [23], was used in all of the above listed references. This potential should be able to correctly describe the initial phase of the recoil cascade, but the long range behavior is more uncertain, especially when comparing to the EAM potential for BCC-Fe developed by Simonelli and Farkas [28]. It thus appears important to improve the quality of the existing potentials.

There is still an uncertainty in the behavior of pure iron subject to high energy recoil cascades, e.g. the measured swelling rate varies from 0.03% per DPA up to 0.5% per DPA at the same temperature [24]. A more consistent experimental picture has emerged for FeCr alloys. Irradiation of FeCr alloys with varying fractions of Cr has been made in EBR-II, FFTF, DFR and BR-10 [26]. At doses below 15 DPA (where impact of He generation would be possible to neglect), the data exhibit maximum swelling rates for Cr concentrations ranging from 9 to 12 percent. The DFR and BR-10 irradiation further show that adding 2-6 percent of Cr leads to a pronounced decrease in swelling as compared to pure Fe.

Therefore, the implementation of a Fe-Cr potential in the MD simulations may give us important information on basic mechanisms responsible for swelling that would be difficult to elucidate in pure Fe. In what follows, we will describe the work made at KTH on the development of an EAM potential for Fe-Cr, and its impact on the formation probability of interstitial clusters in high energy recoil cascades. Special attention is devoted to the fact that the bulk modulus of Fe-Cr exhibits a sharp minimum at 6-7% of Cr concentration, coinciding with the minimum in swelling seen in the low dose irradiation experiments.

General concept and structure of the Fe-Cr potential

The Embedded Atom Method (EAM) has its roots in the density functional theory where the energy of the system of atoms is given by the functional of its electronic density. The atom energy is expressed as a sum of a pairwise (electrostatic) $\swarrow(r)$ interaction,, depending on the scalar distance between the atoms and a many $F(\uparrow)$ body term,, representing the quantum mechanical energy to embed the atom into a homogeneous electron gas of a certain local density. The complete EAM energy expression in the case of the Fe-Cr binary alloy requires definitions for the Fe and Cr pair potentials, the mixed Fe-Cr pair potential, and for the embedding functions for Fe and Cr [30].

At large distances, i.e. around and after the first neighbor distance the pair interaction for Fe and Cr as well as the mixed Fe-Cr pair interaction are described by the long range potentials developed by Simonelli and Farkas [28],[25]. The free parameters of the Fe pair potential are calculated to fit experimental data such as the lattice constant, the unrelaxed vacancy formation energy and the elastic constants. The same approach is used for the Cr pair potential. However, due to the negative value of the Cauchi pressure the reproduction of the elastic constants for this material is very complicated. The Fe-Cr alloys of interest here are with relative low Cr content (up to 20%) and we have assumed that the exact fitting to the elastic constants of pure Cr is not significant. The parameters of the mixed pair potential are fitted to thermodynamic measurements of

heat of mixing of Fe-Cr alloys and to predicted variation of the lattice parameter with the Cr concentration.

These pair potentials can not be directly used to simulate radiation induced cascades since they can not describe interactions inside the nearest neighbor distances. Therefore, we have modified the Simonelli potential by smoothly transforming it into the Born-Mayer potential, which reproduces sensible values for the displacement threshold energy [23], and to the screened Coulomb potential. The modification affects the shape of the potentials at short distances and does not change their properties at large distances listed above.

The embedding functions are calculated by fitting the cohesive energy to the Rose universal expression, which gives the state of expanded or compressed perfect crystal as a function of the interatomic separation. The bulk modulus is an important parameter in the equation. When performing simulations for Fe-Cr alloys with a low Cr content, it is reasonable to fit the Cr embedding function to the alloy bulk modulus for the actual Cr content instead to a pure Cr. According to the experimental results, the bulk modulus value is a non monotonic function of the Cr concentration in the FeCr alloy, having a well pronounced minimum around 6-7% Cr (Figure 6.5). The location of this minimum coincides with the region of Cr content where the Fe-Cr alloys show minimum swelling. Therefore it is important to investigate how sensitive is the embedding function, and consequently the defect properties, to the bulk modulus value. The cascade simulations in the FeCr alloy reported in the ext section correspond to 7% Cr content in the alloy.

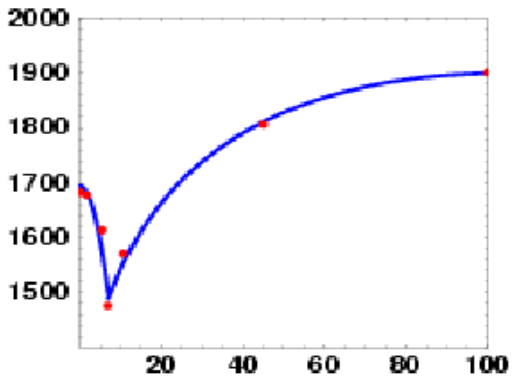

Figure 6.5: Bulk modulus [kbar] vs Cr concentration [%]

Implementation of the Fe-Cr potential to molecular dynamics simulations.

It has been found that the integral characteristics of the radiation damage such as the total number of the defects and displacements support the power law empirical formula [22] and the previous published results based on the modified N-body potential of Finnis and Sinclair. The presence of Cr atoms has little effect on the integral cascade properties. The potential favor <111> structures which is in agreement with earlier investigations relating the <111> defect orientations to the long range of the potential. In contrast to the conclusion above, substantial differences have been observed in the defect configuration, clustering and mobility. For pure iron, the new potential predicts a

formation of more extended defects (e.g. crowdions or larger structures), enhanced clustering and 1D collective motion of large sets of parallel crowdions. In general, the mobility is high with no direct relation to the size of the parallel structures. The individual crowdions jump almost independently but keep the compact arrangement.

The vacancies remain immobile during the period of investigation. The 1D motion involves dumbbell-crowdion transformation. Crowdions close to <111> orientation may rotate and join a parallel set of <111> crowdions when passing close to it. No such clustering and aggregation of defects have been observed in the Fe-7Cr alloy. An intriguing tendency of increasing of the Cr content in the defect structures with the time has been recorded. Typical cascade development for 5 keV recoil is illustrated in Figure 6.6. Only displaced atoms are shown. The blue, read and yellow balls denote a vacancy,

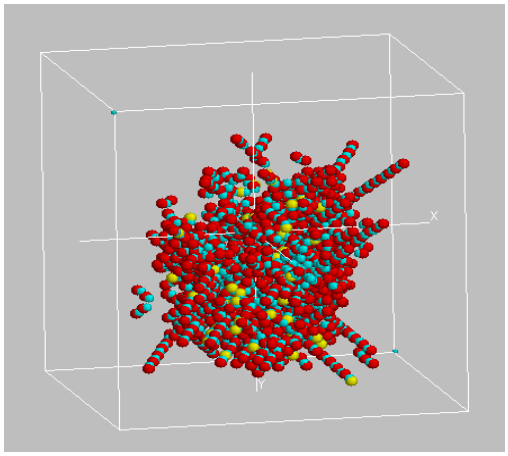

Figure 6.6: Snapshot of the defect structure in Fe-7Cr alloy at 0.4 ps after the generation of 5 keV Fe recoil in the central region of the box.

Fe or Cr interstitial atom, respectively. The damage region is expanding and rows of displaced atoms are created along the close packed directions. About 7% of the displaced atoms are Cr atoms reflecting the original Cr content in the alloy. With the time most of the atoms return to their original sites. The recombination of Fe atoms is stronger which increases the fraction of the Cr atoms in the SIAs clusters of the alloy (Figure 6.7).

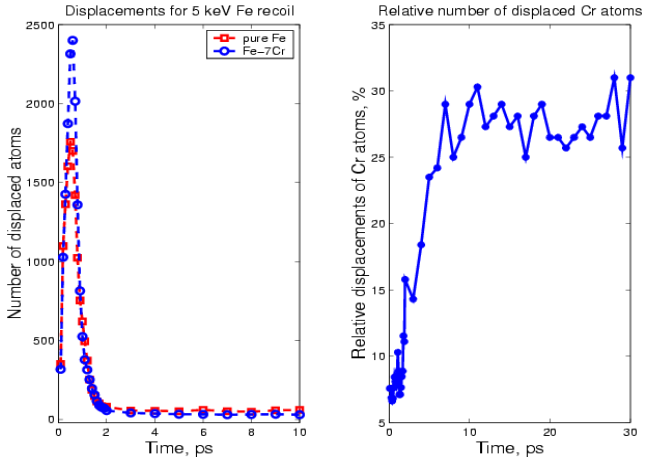

Figure 6.7: Time evolution of the Cr content in the displacements for Fe-7Cr alloy.

Future work

The future work includes further improvement of the potential parameters and their fitting to alloy properties such as heat of mixing as a function of the Cr content obtained from *ab initio* methods. The MD simulations will focus on calculations of migration barriers, cluster binding energies and other data needed to describe defect evolution and to approach methods like PBM (Parallel Block Method) or KMC (Kinetic Monte Carlo). A special attention will be devoted to simulations of cascade development in a non perfect lattice, e.g. including dislocations.

6.3 MUSE PROJECT - TIME DETECTOR RESPONSE IN MUSE-4

Introduction

The dynamic behavior of the multiplying medium, such as the time response in a detector after a neutron pulse, is studied for different sub-criticality levels. These kinds of investigations, which will be performed experimentally in MUSE-4, are important for the reactivity determination of a sub-critical system. In the last section, the sodium coolant in 22 fuel subassemblies has been replaced by lead, and the properties, in terms of k_{eff}, source efficiency and time response, of the two configurations have been compared.

Time detector Response

The techniques to monitor the sub-criticality level during operation in an accelerator driven system are under development. With the introduction of GENEPI into MASURCA it is now possible to perform accurate dynamic measurements of the sub-critical core, which allows for experimental reactivity determination of the sub-critical multiplying medium. The dynamic measurements are based on the pulsed mode operation of GENEPI and consist in registering the response as a function of time in a detector after a neutron pulse insertion. When the multiplying medium is sub-critical the neutron density will decay exponentially and the pulse will quickly disappear.

The decay process after a neutron pulse in a sub-critical medium is governed by the following relation:

$$N(t) = N_0 e^{-\alpha t} \tag{6.3}$$

where

$$\alpha = \frac{1 - k_{prompt}}{\Lambda} \quad \text{and} \quad \Lambda = \text{Neutron generation time} \tag{6.4}$$

Hence, α is the slope of the decaying curve and it is directly related to the reactivity. Eq. (5.3) is derived from the reactor kinetics equation, not taking the delayed neutrons into account. Within this time scale there is no contribution from the delayed neutrons, which is the reason why the slope of the curve (α) is directly proportional to the prompt reactivity and not to the effective reactivity.

In MUSE-4, the "Pulsed Neutron Method" will mainly be used for the experimental reactivity determination of the sub-critical core. The procedure consists in, after having registered the neutron intensity decay after a neutron pulse, determining the slope of the curve (α) and then determine $k_{prompt,}$ according to

$$k_{prompt} = 1 - \alpha \cdot \Lambda \tag{6.5}$$

The neutron generation time Λ first has to be calculated (e.g. with MCNP) and does not change much with reactivity. In order to obtain the effective reactivity you also need to determine the effective delayed neutron fraction, ($k_{eff} = k_{prompt} + \beta_{eff}$).

The time response in one of the detectors in MASURCA has been calculated for a GENEPI generated (d,t)-neutron source pulse for the three sub-critical states Sc0, Sc2 and Sc3 of the MUSE-4 experiments. The generation time Λ was found to be approximately 0.60 microseconds. The results computed by MCNP are plotted in Figure 6.8.

It is clear from the figure that the more sub-critical the core is, the faster is the prompt decay rate. The α-values corresponding to the sub-critical states (determined graphically from the plotted curves) are for Sc0: $\alpha_0 \approx 1 \cdot 10^4$ ($k_{prompt,0} \approx 0.995$), for Sc2: $\alpha_2 \approx 5 \cdot 10^4$ ($k_{prompt,2} \approx 0.97$) and for Sc3: $\alpha_3 \approx 8 \cdot 10^4$ ($k_{prompt,3} \approx 0.95$). The results are in good agreement with Eq. (5.3)

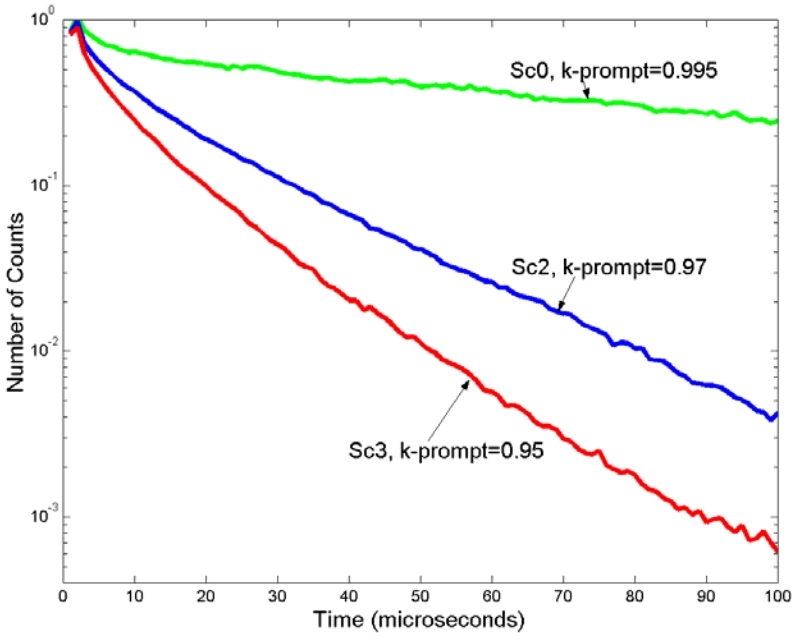

Figure 6.8: Time detector response after a (d,t)-source pulse for the three different sub-critical configurations in MUSE-4 - Sc0, Sc2 and Sc3.

Replacement of sodium coolant by lead coolant

It has recently been decided to include in the MUSE experiments a new configuration, where 22 of the central sodium cooled fuel subassemblies have been replaced by lead cooled subassemblies (with the limit marked by the black line in Figure 6.9)

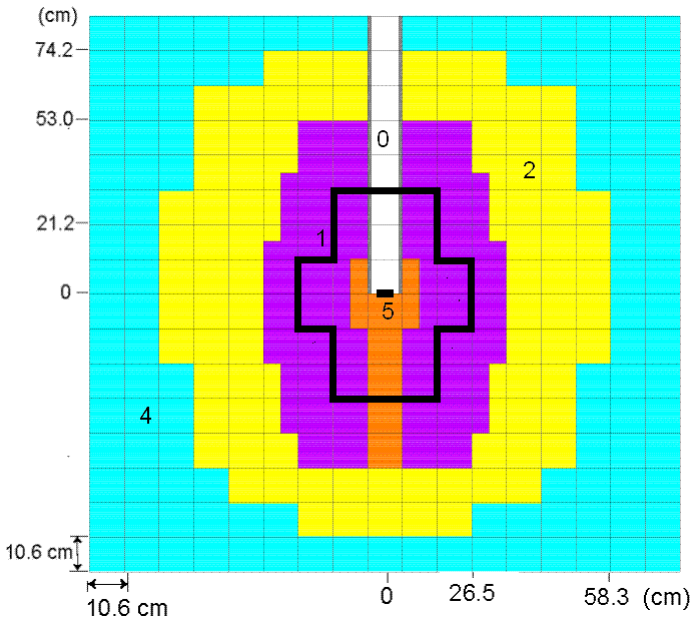

Figure 6.9: Configuration where 22 of the sodium cooled subassemblies have been replaced by lead cooled subassemblies (the limit of the lead cooled subassemblies is marked by the black line).

Three parameters, k_{eff} , the source efficiency φ* and the time detector response, have been studied for this centrally lead cooled configuration. The results have been compared with the results for the original sodium cooled configuration. The neutron source in this study was the GENEPI generated (d,t)-source.

When calculating k_{eff} for the new lead cooled configuration, it was found that it increases with about 1600 pcm. The reason for this is that there is less absorption in lead and that the energy spectrum is different. In order to maintain the same reactivity for the two configurations, which is particularly important for the time response comparison, some of the peripheral fuel subassemblies were removed. k_{eff} was about 0.974 in both cases.

Source Efficiency

The results from the comparison of the source efficiency parameter φ* for the two configurations are listed in Table 6-8. As is shown there, the value for the lead cooled configuration is significantly higher than for the sodium-cooled configuration, 2.39 compared to 2.13.

Table 6-8. Source Efficiency φ*		
Configuration	**k_{eff}**	**φ***
Sodium cooled	0.97428 (± 20 pcm)	**2.13** (± 0.02)
Centrally lead cooled	0.97382 (± 27 pcm)	**2.39** (± 0.03)

The reason for this difference is again the (n,2n)-multiplicative effect in lead, the same effect that caused the large difference in φ* between the (d,d)- and the (d,t)-source. Since there is more lead in the central part of the core in the centrally lead cooled configuration, where there are still many neutrons with energy higher than about 7 MeV, there is more (n,2n)-reactions which amplify the neutron multiplication and φ*.

Since the source efficiency relates the source intensity to the power produced by the system, we conclude that the replacement of sodium coolant by lead coolant in 22 of the central fuel subassemblies increases the power by approximately 12 %.

Time Detector Response

Finally, the time detector response from a pulse insertion from the (d,t)-source has been calculated and it is seen in Figure 6.10 that the intensity is a little higher (in average 15 %) for the lead cooled configuration. The explanation for this is the same as for the difference in source efficiency, namely the multiplicative effect of the (n,2n)-reactions in the lead. Since the neutron multiplication is higher in the second case, the intensity registered by the detector will also be higher.

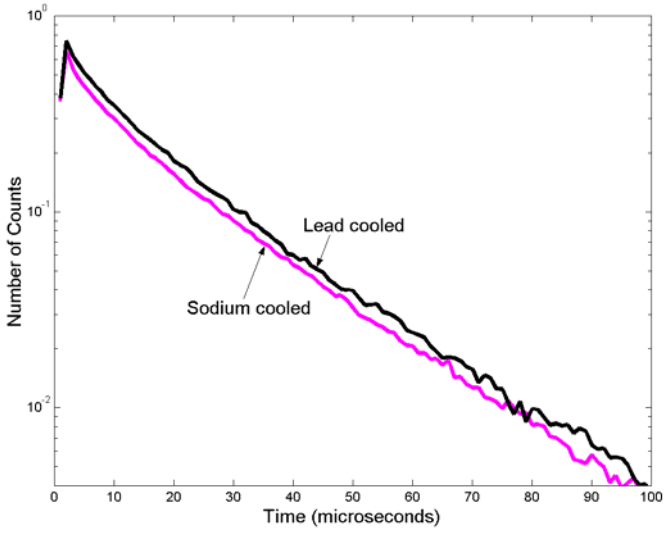

Figure 6.10: Time response in detector F

We also observe that the prompt decay rate is more or less the same for the two systems. The neutron generation time Λ, calculated by MCNP, changes very little and since k_{eff} is the same, the alpha-value and the decay rate must also be the same.

Conclusions

The Pulsed Neutron Method and the technique of experimental reactivity determination have been described and the time detector response has been computed for the three sub-critical states of MUSE-4. The plotted results show the expected behavior that the more sub-critical the core is, the faster is the prompt decay rate.

The simulations of the replacement of sodium coolant by lead coolant in 22 of the central subassemblies gave three main results: k_{eff} increased with about 1600 pcm, the source efficiency φ^* and the intensity of the time detector response increased by about 12 % and 15 % respectively, due to the same effect, namely the (n,2n)-multiplication in the lead.

6.4 XADS – PROJECT - NUCLEAR DESIGN OF EXPERIMENTAL ACCELERATOR DRIVEN SYSTEM

Evaluation of Uncertainty of the Nuclear Design

Introduction

The work was performed on the basis of using the MCNP reactor core model of the XADS project, which is considered a reference design of LBE cooled XADS prepared by ANSALDO, as a part of task of method and data verification undertaken in one of the workpackages (WP4.1) of PDS-XADS project.

Temperature Treatment

Most of the cross section libraries contain neutron cross-sections evaluated for room temperature. Simulations of the reactor core and coolant in operation, i.e. in nominal temperature require a proper treatment of the cross-sections. Three possible approaches have been investigated with the MCNP code:

- Temperature dependent cross-section libraries have been applied on material cards corresponding to the cell with specified temperature. If the specified temperature did not correspond exactly to the temperature of the cross-section library, the TMP parameter has been used in order the adjust the model through a free gas treatment. This approach has been labeled as **Power A**. Intuitively it is considered to be the most proper treatment.
- **Power B** corresponds to the situation as above but no free gas adjustment has been applied.
- **Power C** corresponds to the room temperature cross sections applied on material cards and free gas treatment applied (TMP option) on the cell cards. This treatment is the only option for the users not having temperature dependent cross section libraries and it implies disregarding the effects of Doppler broadening.

Configuration of Geometry

Two geometries have been used in our calculations:

a) A refueling case: no target inside, absorbers close to the active core
b) An operational case (room and power temperature): target inside, absorbers far from to the active core

Neutron Multiplication Factors

The neutron multiplication factor of en external source $\mathbf{k_s}$ is more ambiguous and can be defined in a few ways. We apply here a definition that is the closest to the definition of k_{eff}, as follows.

$$k_s = \frac{N_f}{1 + N_f}$$

Where N_f is the total number of fission neutrons born in the system per the source neutron.

Results

The results of k_{eff} calculations with different libraries and codes are presented on Figure 6.11 and Table 6-9. The values of k_{eff} obtained with different applied codes but the same cross section library and temperature treatment are fully consistent. That was expected since every tools used here is based on the same model and with applying the same source code. It proves that no major mistakes were introduced to the codes in their independent development.

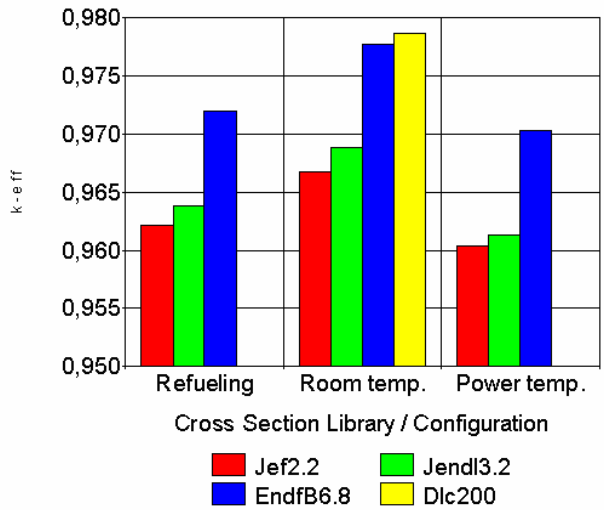

Figure 6.11: Results of k_{eff} calculations in LBE-XADS. MCB1C precision of results ~50pcm

Reactivity dependence on evaluated nuclear data files is systematic with the temperature change where the difference in results is as follows:

- JENDL3.2 gives about 100-200 pcm higher results that JEF2.2
- ENDFB6.8 gives about 1000 pcm higher results than JEF2.2
- DLC200 gives results close to ENDFB6.8 but cannot be applied to higher temperatures

Table 6-9. k_{eff} in different configuration (precision of 50 [pcm])

Case	Code	Cross section library			
		Jef2.2	Jendl3.2	Endfb6.8	DLC200
Refueling 300K	MCB1C	0.9622	0.9639	0.9720	-
Target in 300K	MCB1C	0.9668	0.9687	0.9777	0.9786
	MCB1C	0.9599	0.9612	0.9702	
Power A	MNCP4C3	0.9599	0.9613		
	MCNPX			0.9700	
	MCB1C	0.9604	0.9615	0.9703	
Power B	MNCP4C3	0.9602	0.9614		
	MCNPX			0.9692	
Power C	MCB1C	0.9679	0.9687	0.9775	0.9790

Proper assessment of reactivity in power temperatures requires application of temperature dependent cross section libraries.

Free gas treatment of cross section in MCNP – based codes gives improper results (Power C case). The magnitude of cross correction due to free gas treatment remains in the range of calculation precision (below 50 pcm) while in the cases with cross section resonance broadened with NJOY due to Doppler effect (Power A and B cases) reactivity coefficient is about 700 pcm. The application of free gas treatment in the systems with materials having resonance cross section is meaningless and can only elude the user that he applied a temperature correction to cross sections.

Calculations in the source mode are summarized in Table 6-10.

Obtained $k_s = 0.9742$ is slightly bigger than $k_{eff} = 0.9700$ that means the applied source effectiveness for fission neutron generation is slightly higher than in the eigenstate under assumed definitions of neutron source. The precision of calculation is at the level of criticality calculations.

Table 6-10. Neutron multiplication and k-s factor in Power Case (MCNPX + ENDFB6.8)	
Source neutrons per proton	15.2 ± 0.15
Total number of neutrons per proton	600 ± 10
Fission neutrons per proton	574 ± 10
Fission neutrons per source neutron	37.8 ± 0.7
Neutron multiplication factor k_s	0.9742 ± 0.0005

Conclusions

Results obtained with different applied codes but the same cross section library and temperature treatment are fully consistent.

Reactivity dependence on evaluated nuclear data files is systematic and:

- JENDL3.2 gives about 100-200 pcm higher results than JEF2.2
- ENDFB6.8 gives about 1000 pcm higher results than JEF2.2

Temperature reactivity coefficient of about 700 pcm can be obtained with all tested cross section evaluated data files.

Proper assessment of reactivity in power temperatures requires application of temperature dependent cross section libraries.

Obtained $\mathbf{k_s}$ = 0.9742 is slightly bigger than $\mathbf{k_{eff}}$ = 0.970

Assessment of the Possibility to Adopt Neutron Absorbing/ Reflecting Elements at Core Periphery (oriented to DPA reduction)

Introduction

Neutrons leaking from the core or the target cause radiation damage of vessel internals. This damage is dominated by displacement of the structure atoms by the deposition of the particles energy and is described quantitatively by the number of displacements per atoms (DPA) over a certain period of time. The level of DPA depends on the level of the particle flux as well as on the flux spectrum since the damage energy cross section is energy dependent. Generally for fission neutrons the harder spectrum means the higher DPA. An arrangement of the core periphery can lower the level of DPA if it lowers the neutron flux or softens its spectrum at the locations of sensitive construction materials. Analysis of the DPA on two major components of the internal vessel is performed – upper restraint plate and the core diagrid. Few cases of periphery arrangement are investigated for the level of possible reduction of the DPA. The DPA values after one year of irradiation are presented for few possible arrangements.

Method of DPA Calculation

Calculation of DPA was preformed by using MCB code (which incorporates neutron transport modules of MCNP4C) in a heterogeneous model of XADS reactor using damage energy cross section present in the neutron transport cross-section libraries of the MCB system. Cross section libraries from evaluated data files JEF2.2 supported for lacking nuclides of lead from JENDL3.2 were used in calculations. Cross section tables at power temperatures were applied. For assessing DPA values a conservative approach was applied where:

$DPA = E_a / 2E_d$

where:

E_a is available damage energy calculated from damage energy cross section

E_d is threshold displacement energy of 40 eV for main steel components: Fe, Cr, Ni.

Conservative approach in calculation of DPA was employed here due to neglecting in current assessment the damage effects that occur due to recoil of atoms in case of their alpha decay which process can add about 15 % to DPA obtained from recoils after direct kinetic interaction with neutrons.

The lack of axial reflectors resulting in the damage peaking of the reactor restrain plate and the reactor diagrid close to the reactor axis require accurate modeling of neutron leakage along the reactor axis. Fuel assembly extensions, upper and lower, form axial channels after orientation of the subassemblies. Since LBE is much less absorptive than the subassembly structure materials the process of neutron transport leads mainly through axial channels of LBE coolant while absorption take part mostly in the assembly walls. An accurate simulation of the neutron leakage through axial channels requires its simulation in a heterogonous geometry model of MCNP.

The MCNP model was prepared based on references [32] and specifications of deliverable D2. The geometry model is generally heterogeneous with minor geometry simplifications introduced to keep the model reasonably simple. The irradiation period of one year with 95% time availability with $80MW_{th}$ power were assumed.

Due to the thickness of restraint plate equal to 50 mm and that of the diagrid equal to 150 mm, DPA distribution across its thickness is not uniform and average values will be lower than the peak values of DPA, which will occur on the side facing the core. The Profiles of DPA deposited on core restraint plate and diagrid are presented on Figure 6.12 and Figure 6.13. It can be noticed that for the most important inner locations (close to reactor axis) DPA peak to average ratio reaches value about 1.5 for core restraint plate outer locations (not replaceable part position), and about 1.9 for the core diagrid at inner location peaking. Neutrons reflecting for LBE cause observed rise of the profiles at the far edges.

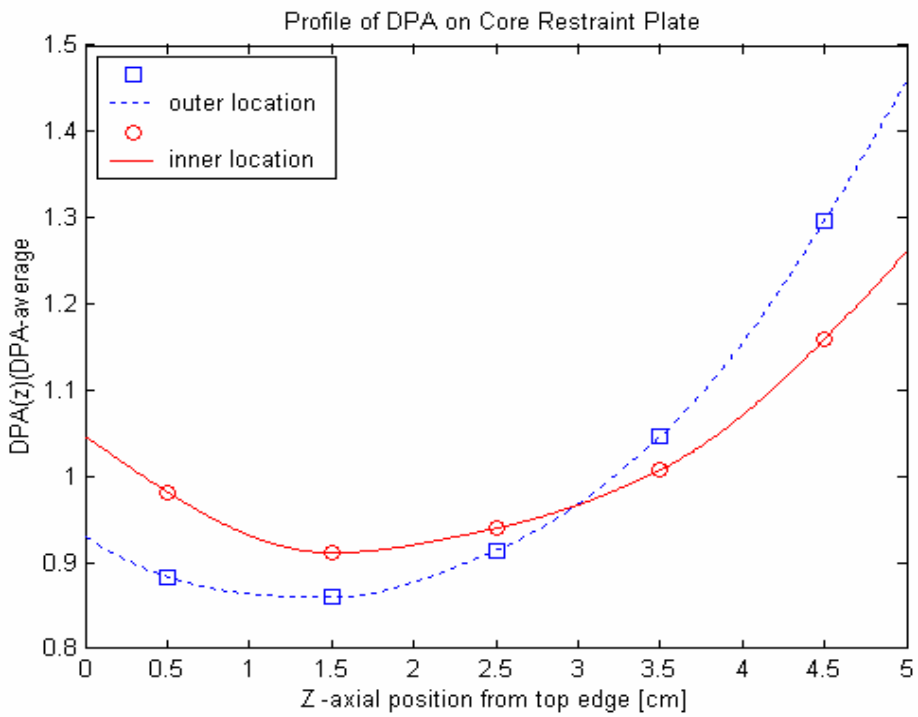

Figure 6.12: DPA across thickness of the core restraint plate normalized to the average DPA calculated for LBE cooled XADS - reference configuration.

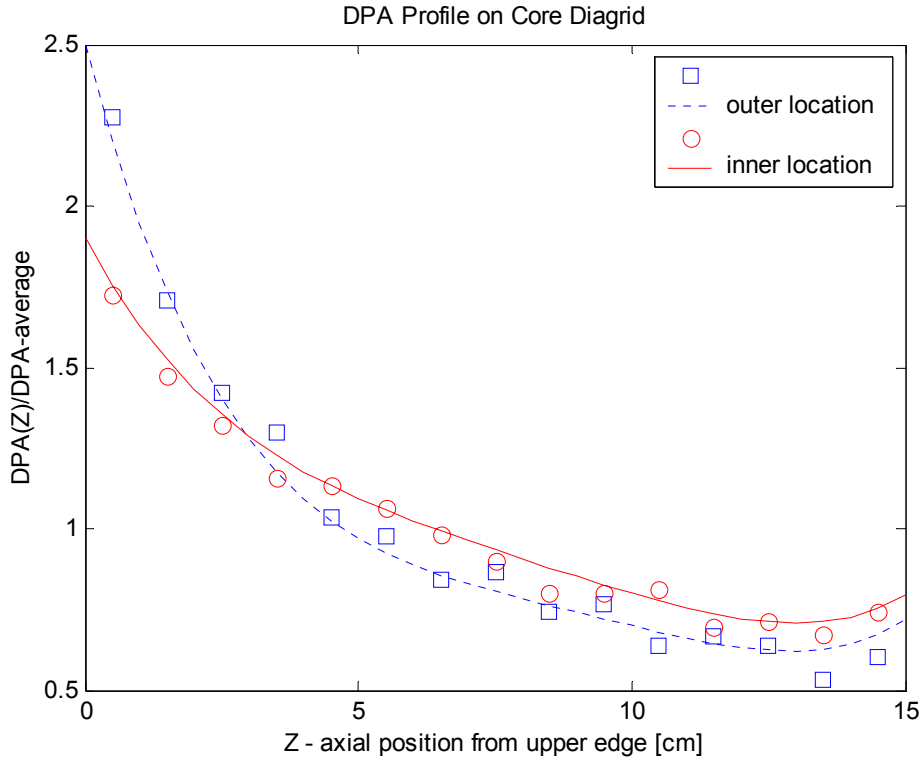

Figure 6.13: DPA across thickness of the core diagrid normalized to the average DPA calculated for LBE cooled XADS - reference configuration.

Possibilities of DPA Reduction through Core Periphery Arrangement

The level of DPA depends on the level of the particle flux as well as on the flux spectrum since the damage energy cross section is energy dependent. Generally for fission neutrons the harder spectrum means the higher DPA. An arrangement of the core periphery can lower the level of DPA if it lowers the neutron flux or softens its spectrum at the locations of sensitive construction materials. For the constrained total system power the reduction of the flux level at the reactor structure can be obtained by introduction of reflectors or absorbers in the core periphery. It should be noted that so far the reference specification for fuel subassembly of LBE cooled XADS does not include introduction of axial reflectors or absorbers thus only radial periphery is concerned in the current study. The lack of axial reflectors will result in highest irradiation of the internals located above and below the core with the damage peaking at regains close to the reactor axis due to the closest distance to the core centre.

The reference core design [33] is free from reflectors or absorbers so in this case the core leaking neutrons will be reflected only by the coolant LBE and absorbed in subassembly wrapper tubes thus keeping contribute to DPA on the construction elements higher than in cases with additional absorbers. Introduction of reflectors or absorbers can lower this contribution to DPA but influence on the main term that comes directly from the core is rather limited and can be obtained actually only by neutron flux moderation. Few cases of periphery arrangement are investigated for the level of possible reduction of the DPA. The DPA values after one year of irradiation are presented for few possible arrangements.

Following arrangements of the core periphery were investigated:

- No reflectors nor absorbers only LBE coolant (reference core)
- LBE+SS+B_4C:
    - LBE dummy subassemblies of one SA row play a role of primary reflector.
    - Stainless steal reflector of two rows of SA was placed after LBE.
    - B_4C absorber blocks fill up the rest of core periphery
- SS+B_4C:
    - Stainless steal reflector of three rows of SA was placed directly after the active core.
    - B_4C absorber blocks fill up the rest of periphery.
- Be+SS+B_4C:
    - Beryllium blocks of one SA row play a role of primary reflector.
    - Stainless steal reflector of two rows of SA was placed after first row.
    - B_4C absorber blocks fill up the rest of core periphery

Comparison of Results of DPA Calculations

Results of DPA obtained in eigenmode of neutron transport calculations for investigated cases are presented in Table 6-11. These results are the first approximations since

Table 6-11. Selected Parameters in Different Core Periphery Arrangements

Arrangement of Core Periphery	LBE (reference)	LBE+SS+B_4C	SS+B_4C	Be+SS+B_4C
k_{eff}	0.961	0.932	0.902	0.954
Inner F/A clad flux	$7.8 \cdot 10^{14}$	$7.8 \cdot 10^{14}$	$7.8 \cdot 10^{14}$	$6.4 \cdot 10^{14}$
Inner F/A clad DPA/year	6.7	6.75	6.8	5.51
DPA /year on diagrid (most inner locations)	$9.6 \cdot 10^{-3}$	$7.8 \cdot 10^{-3}$	$9.4 \cdot 10^{-3}$	$6.2 \cdot 10^{-3}$
DPA/year on core restraint plate at r = 130 cm	$1.4 \cdot 10^{-2}$	$7.4 \cdot 10^{-3}$	$7.2 \cdot 10^{-3}$	$6.1 \cdot 10^{-3}$

applied eigenflux distribution does not contain the source neutron term originated from LBE target. In all cases the flux is normalized to the level giving the nominal thermal power thus avoiding possible problems with level of criticality or the neutron source importance that have different values in considered cases.

Apart from DPA on the construction structure also the DPA values on cladding are presented. DPA on cladding is axially averaged for pins in the most inner fuel subassembly while DPA on the construction elements are averages across plate thickness.

It is noticeable that obtained damage levels both on the core diagrid and not replaceable core restraint plate elements are well below the limit of 2 DPA over 20 years of lifetime in every considered case. The results of above comparisons show:

- Introduction of an absorber in the core periphery can reduce DPA on diagrid central locations by about 15 % and on core restraint plate by half.
- Introduction of a steel reflector deteriorates the neutron reflection as compared with LBE case erasing the reduction of DPA on the diagrid central locations.
- Replacement of LBE reflector by beryllium further reduces DPA both on diagrid and core restraint plate.

The best conditions for reducing DPA occur in core periphery arrangement with beryllium reflector. An excellent neutron multiplication feature combined with moderation properties result in flux moderation and lowers the number of axially leaking neutrons.

Further investigation of DPA distributions using fixed source mode with consideration of target neutrons were performed for the reference core and the core with Be+SS+B_4C periphery. Radial distributions of DPA were calculated for diagrid and core restraint plate locations.

Radial distributions of thickness average DPA on the restraint plate in the reference case and the case with beryllium reflector are compared in Figure 6.14. To obtain peak values one should multiply the average one by the appropriate DPA profile value, which at center location equals 1.25. Average values of damage varies from 0.15 DPA/year at the most inner part of the restraint plate location down to 0.016 DPA at outer location of not replaceable external part can be observed for the reference core.

Reduction of the damage in case of Be-SS-B_4C periphery by value of about 0.02 DPA/year can be obtained as compared with referenced core due to suppression of radial streaming of core neutrons. For the not replaceable external part of restraint plate the damage level is lower than 0.003 DPA/year.

Radial distribution of DPA on the core diagrid presented on Figure 6.15 shows its large margin to the permissible limit (below 20% for the peak value) already for the reference core.

Additional 15 % of reduction can be obtained in a configuration with Be-SS-B_4C periphery.

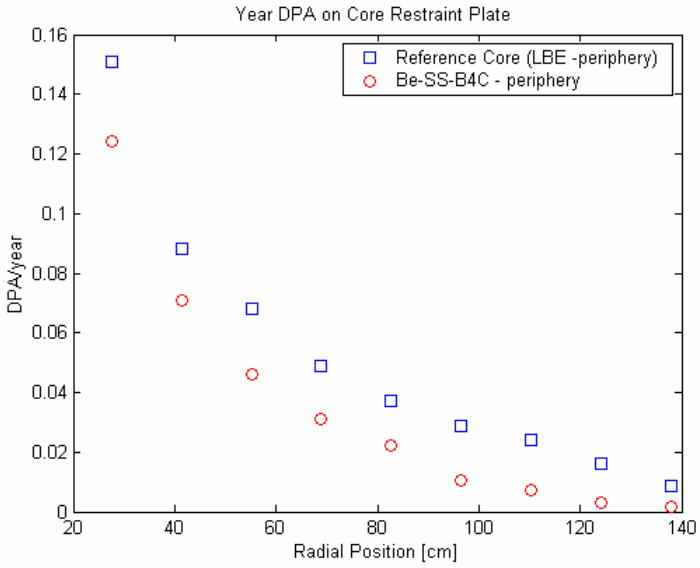

Figure 6.14: Radial distribution of average DPA on the core restraint plate calculated for LBE cooled XADS with contribution of source neutrons.

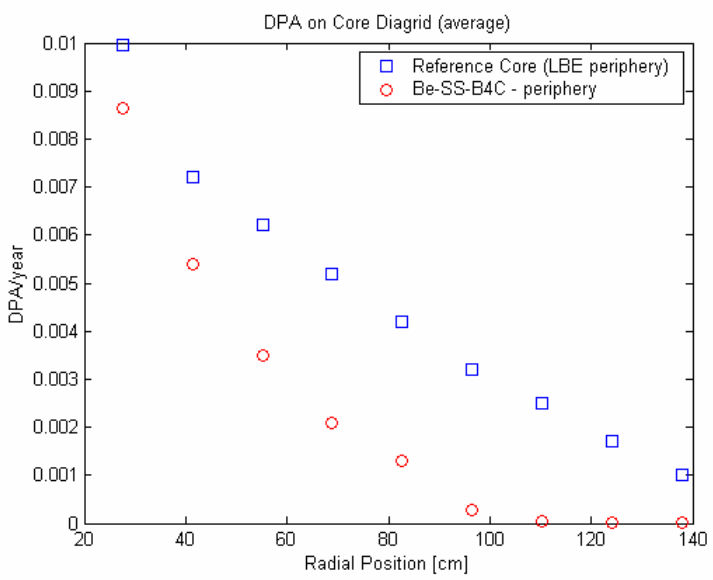

Figure 6.15: Radial distribution of average DPA on the core diagrid calculated for LBE cooled XADS with consideration of target neutrons contribution.

The difference between DPA obtained for upper and lower structures is caused mainly by the different distance from the core midplane, which is 1320 mm for the upper one while 1680 mm for the lower one. Presented distributions were obtained in external source mode of MCNP transport modules with neutron source prepared using bare target model with MCNPX code. The surface neutron source obtained this way collects neutron of every energy therefore the damage calculations includes the core neutrons and target leaking neutrons even with energy above 20 MeV. In reality the fraction of high-energy neutrons at considered locations is bellow computer accuracy. It is also the case of the damage due to high-energy protons that have no actual chance to reach these locations and was not considered in this evaluation. Also it should be noticed that power normalization to 80MW of energy deposited in the system as initiated by target leaking neutrons is assumed. Decay heat that can stand for about 7% of total heat is also neglected in power normalization. For such assumptions following values were obtained for most inner fuel assembly:

Neutron flux at fuel pins	$8.82 \cdot 10^{14}$ n/cm^2 s
Atom displacement on fuel pins	10 DPA/year
Atom displacement on fuel clad	8.5 DPA/year

Conclusions

- The highest irradiation of the internals located above and below the core with the damage peaking close to the reactor axis due to the closest distance to the core centre is observed.
- Radiation damage on the core diagrid over 20 years of operations is lower than **0.4 DPA** for a local peaking point. It can be reduced modestly – by 15 % if Be-SS-B_4C periphery arrangement is introduced.

- Radiation damage on regions of restraint plate (not replaceable) stays also well below the limit and can reach **0.4 DPA** for a local peaking point. The reduction of it if Be-SS-B_4C periphery arrangement is introduced can be by factor of 10 to 0.04 DPA.
- Other solutions of core periphery (without neutron moderation) have no potential for lowering the DPA at central location.
- The limits of DPA on diagrid and core restraint plate are observed already in the reference design of LBE cooled XADS and for this purpose no action is required.
- Obtained radiation damage level allows for reduction of the vessel dimensions.
- Arrangement of core periphery has limited influence of DPA level at positions close to central axis and only neutron moderation can bring its reduction by modest 15%.

Assessment of the Possibility to Adopt Neutron Absorbing Elements oriented to Po reduction

Introduction

^{210}Po accumulation in LBE -Cooled XADS results from neutron capture in lead and bismuth nuclides. Part of the ^{210}Po accumulation occurs while high-energy particles interact with the LBE in the spallation target; the other part is simply a neutron absorption in the LBE coolant (this process is driven by "regular" fission neutrons). The accumulation in the spallation target is a few orders of magnitude smaller than the activation of the coolant and has not been investigated at this moment.

The reference core [32] is free from reflectors or absorbers thus the core leaking neutrons will contribute greatly to polonium accumulation. Introduction of any absorbent or reflector will positively influence reduction of polonium production. Two cases of core periphery arrangement were analysed here and compared with reference case for accumulation of ^{210}Po over period of one year.

Calculation Method of ^{210}Po build-up

Calculation of polonium build-up was preformed by using MCB code in heterogeneous model of XADS reactor with three options of core periphery arrangements:

- No reflectors nor absorbers only LBE coolant (reference core)
- LBE+SS+B_4C:
    - LBE dummy subassemblies of one SA row plays a role of primary reflector)
    - Stainless steel reflector of two rows of SA was placed after LBE

- B_4C absorber blocks fill up rest of the periphery

- Be+SS+B_4C:
  - Beryllium blocks of one SA row plays a role of primary reflector
  - Stainless steel reflector of two rows of SA was placed after first row.
  - B_4C absorber blocks fill up rest of the periphery

The MCNP model was prepared based on reference [32] and the specifications of deliverable D2 [33]. The geometry model is generally heterogeneous while minor geometry simplifications were introduced to keep the model reasonably simple.

Transmutation modules of MCB take into account both production and destruction of polonium nuclides as well as transmutation of neighbouring isotopes. The final level of ^{210}Po after one year or irradiation with 80MW thermal power is calculated for few LBE zones and compared with results obtained in different configurations.

Calculations were performed using code MCB1C with cross section libraries JEF2.2 supported for lacking nuclides of Pb from JENDL3.2. The cross sections have been used for temperature corresponding to full power operation.

Results

Obtained results show very high level of polonium accumulation for the reference case. This is a result of neutron leakage from the core and absorption in surrounding LBE. Introduction of absorbers can reduce the level of ^{210}Po by 50 % mainly due to reduction of absorption at core periphery and outside of the core.

Further reduction is possible if beryllium is introduced for a reflector. This is due to moderation effect that reduces polonium production also in the active core part.

Table 6-12. Results of ^{210}Po accumulation in LBE zones due to core neutrons after one year of 80MW_{th} irradiation

Arrangement of Core Periphery		LBE (reference)	LBE+SS+B_4C	Be+SS+B_4C
LBE Volume [m^3]		222.1	209.6	208.0
LBE Mass [10^3 kg]		2.2793	2.1515	2.1351
^{210}Po Mass [kg]		1.1955	0.6551	0.4250
^{210}Po Activity [10^6 Ci]	Target	0.36547	0.38527	0.29331
	Active Core	1.7119	1.6622	1.3111
	Core Periphery	2.1267	0.7254	0.2271
	Rest of Vessel	1.1794	0.1772	0.0824
	Total	5.3834	2.9501	1.9139

^{210}Po Transmutation Analysis

Level of accumulated ^{210}Po after one year of irradiation depends on two factors: first is its production rate dominated by transmutation of ^{209}Bi while the second is its alpha decay into ^{206}Pb with half-life of 0.378 years. Since ^{210}Po decay half-life is smaller than reference period of irradiation the destruction rate of ^{210}Po at the end of the period will be close to its production rate and integral destruction over one-year period will be significant factor reducing the level of ^{210}Po accumulation.

As far as the reactor core neutrons are taken into account the production of ^{210}Po is dominated by transmutation chain that starts with neutron capture in ^{209}Bi that is the only stable isotope of bismuth. In the analyzed system the highest neutron flux is present at fuel subassemblies where a neutron flux level of $6.8 \cdot 10^{14}$ gives ^{209}Bi transmutation half-life of 5470 years where transmutation daughters of following branching rations are formed:

^{210}Bi	5.220E-01
^{210m}Bi	3.846E-01
^{208}Bi	9.321E-02
^{207}Bi	1.832E-04
^{208}Pb	1.018E-05
^{209}Pb	6.178E-06
^{206}Pb	4.617E-10
^{206}Tl	1.542E-05
^{205}Tl	9.264E-06

For assumed truncation threshold of 10^{-12} there are only two transmutation paths leading to ^{210}Po with strong domination of the first one:

1) **^{209}Bi** (n,γ) ;{b=52.2%; $T_{1/2}$ = 5470 years} – **^{210} Bi** (β-decay) {b ~100%; $T_{1/2}$ = 5 days} - **^{210}Po**

2) **^{209}Bi** (n,γ) ;{b=38.46%; $T_{1/2}$ = 5470 years} - **^{210m} Bi** (IT) ;{b=0.26%; $T_{1/2}$ = 7830 years} - **^{210}Bi** (β-decay) {b ~100%; $T_{1/2}$ = 5 days} - **^{210}Po**

Transmutation transitions defined as a net production of a product nuclide (production minus destruction) per one source nuclide over irradiation time in our case as follows:

$$Tr_1 = 3.01 \cdot 10^{-5}$$
$$Tr_2 = 3.22 \cdot 10^{-12}$$

The domination of the first path is overwhelming by seven orders of magnitude. Other possible path of transmutation leading to ^{210}Po starts with lead isotopes but here only one transmutation trajectory can produce ^{210}Po above assumed truncation threshold:

3) **^{208}Pb** (n,γ);{b=40.25%; $T_{1/2}$ = 2880 years} - **^{209}Pb** (β-decay); {b=0.26%; $T_{1/2}$ = 3.25 hours} - **^{209}Bi** (n,γ) ;{b=52.2%; $T_{1/2}$ = 5470 years} - **^{210}Bi** (β-decay) {b ~100%; $T_{1/2}$ = 5 days} - **^{210}Po**;

where transmutation transition: $Tr_3 = 1.27 \cdot 10^{-10}$

Produced atoms of ^{210}Po undergo destruction process that is predominated by α-decay into ^{206}Pb whereas all radiation-induced transmutations give branching ratio of $7.6 \cdot 10^{-6}$. Obtained destruction of ^{210}Po due to decay integrated over referenced period is following:

$D_1 = 3.47 \cdot 10^{-5}$

Destruction is in our case higher than accumulation or net production due to almost three times higher irradiation time than the half-life of decay. Sum of net production and destruction gives us production term as follows:

$P_1 = 6.41 \cdot 10^{-5} =$ **2.13** Tr_1

In order to calculate production terms in other cells of the reactor the ratio of production term to net production of **2.13** can be used since it is very weakly dependent on the neutron flux level. This will give us total production rate of ^{210}Po over the whole reactor of **2.55 kg/year**.

Conclusions

Reduction of ^{210}Po content by a factor 2÷3 can be relatively easily obtained by introduction of reflectors and absorbers in the core periphery. Also moderation of the flux by beryllium gives some positive results. This however can negatively influence buildup of actinides and should be checked out carefully in burnup calculation of fuel materials.

Estimated reduction of the ^{210}Po concentration is, nevertheless, not sufficient from the point of view radiation protection and some other means ensuring removal of ^{210}Po from the coolant will be most probably necessary.

Neutronic Calculations for Core Design of Gas-Cooled XADS

Introduction

A neutronic calculation of a nuclear power system with Monte Carlo codes like: MCNP, MCNPX or MCB, requires preparation of the system model, consisting of geometry, material and physical condition specification. The main part of the model is its geometry description, which also includes material densities and depends on the physical constraints of the system. The main dependence is on the thermal temperature but there is also dependence on the fuel burn-up, which in addition to changing the nuclide composition, also changes the fuel pellet dimensions. Thus the system model is case dependent. The main model that is a base for other models and will be called here "the base model" represents the system at beginning of life (BOL) at room temperature with geometry dimensions taken from the technical specification of the Gas Cooled XADS.

Consideration of the temperature and burn-up influence on system geometry and material density is important in calculations of some quantities such as reactivity or reactivity coefficients, while it has limited importance on other quantities that are normalized to the total system power. To account for the above effects the base model is converted into a temperature dependent model at BOL – "the power BOL model" and later will be modified due to changing burn-up conditions as "the burn-up models"

along with design development of the project. Special items like assessment of beam penetration options, dedicated neutron absorbing elements or others require *ad hoc* modifications of prepared models by changing the core arrangement or material density while generally preserving the integrity of the reactor model parts such as the target, vessel and subassemblies.

MCB Model Preparation

The geometry model is generally heterogeneous while minor geometry simplifications were introduced to keep the model reasonably simple. The active core is surrounded by axial and radial reflectors followed by neutron absorbers in order to increase the reactivity of the bare core and reduce radiation damage to the primary system structure.

Fuel used in the model was $(U,Pu+MA)O_2$. Table 6-13 gives the fuel pins composition taken form LBE XADS core model with 23.25%$(Pu+MA)O_2$ + 76.75%UO_2 (depleted uranium - 0.52% ^{235}U content)

Table 6-13. Content of fuel in grams per sub-assembly

Isotope/element	Mass (gram)
^{234}U	1.7
^{235}U	192.9
^{236}U	2.0
U238	37070
U	***37267***
^{238}Pu	30.6
^{239}Pu	7794
^{240}Pu	2754
^{241}Pu	287.1
^{242}Pu	145.0
Pu	***11019***
^{237}Np	2.4
^{241}Am	268.2
Total	***48554***

Power BoL Model.

Conversion of the base model into the power BOL model requires the following modifications:

- Changes in reactor primary system dimensions due to its thermal expansion.
- Changes of material densities due to thermal expansion of materials.
- Changes in cross-section libraries temperature specification.

The values in Table 6-14 of linear expansions were obtained for the important primary system elements assuming the high temperature expansion model:

Table 6-14. Linear expansion for the important primary system elements

Elements	Material	Coefficient	Temperature	Expansion
Fuel Pellets	MOX	(formula)	1500K	**1.01290**
Cladding S/A wrappers	PE16	$1.618\ 10^{-5}$	900K	**1.00971**
Pin Lattice	EM10	$1.24\ 10^{-5}$	600K	**1.00381**
Diagrid, S/A Lattice				
Vessel, Target	316L	$1.80\ 10^{-5}$	600K	**1.00553**

By the conservative model – low temperature expansion - the values in Table 6-15 were obtained:

Table 6-15. Linear expansion for the important primary system elements for the conservative model

Elements	Material	Coefficient	Temperature	Expansion
Fuel Pellets	MOX	(formula)	1200K	**1.00923**
Cladding S/A wrappers	PE16	$1.618\ 10^{-5}$	770K	**1.00777**
Pin Lattice	EM10	$1.24\ 10^{-5}$	600K	**1.00325**
Diagrid, S/A Lattice				
Vessel, Target	316L	$1.80\ 10^{-5}$	470K	**1.00324**

At BOL the fuel-cladding gap is almost four times greater than the reduction of the gap due to small differences in the linear expansions of the fuel pin and the cladding. Therefore, axial expansion of the fuel pins is independent of expansion of the cladding. This situation can be changed only after burn-up, when fuel swelling will close the gap, but even then the actual expansion model will have limited importance because of the close linear expansions of clad and fuel.

Core Design

In order to assess the required reactor core parameters, the Monte Carlo method of neutron transport was applied using the MCNP based codes MCNPX and MCB1C, with temperature dependent cross section libraries of the MCB system. Two modes of calculations were applied: Firstly, the fixed source mode of MCNPX in a bare target system to produce the neutron source for core calculations in MCB, to obtain core

power distribution and radiation damage. Secondly, KCODE mode to calculate the effective neutron multiplication factor, $k_{eff,}$ of the core in several arrangements in order to assess reactivity coefficients. In general, the JEF2.2 cross section libraries were used in the current calculations, whereas for nuclides of lead that are missing from JEF2.2 the JENDL3.2 data were used.

Results of Criticality Calculations

Cores in the following arrangements and assumed conditions were considered in criticality calculations (calculation uncertainties of one standard deviation are given in brackets):

a) Reactor at room temperature

The entire reactor, except for the LBE in the target, is at room temperature (300K). Control rods are placed far from the active core while their secure locations are occupied by neutron reflector subassemblies. The pure base model case is applied.

k_{eff} = 0.96786 (0.00024)

b) Reactor at room temperature, control rods in secure positions

As above except for the control rods.

k_{eff} = 0.93455 (0.00055)

c) Reactor in power conditions – fully operational – high temperature expansion (fuel 1500K, clad 900K)

The reactor is in power conditions with expanded dimensions and diluted densities according to the temperature specification. Control rods are placed far from the active core while their secure locations are occupied by neutron reflector subassemblies. Pure power BOL model is applied.

k_{eff} = 0.95034 (0.00017)

d) Reactor in power conditions – lower temperature expansion (fuel 1200K, clad 790K)

k_{eff} = 0.95393 (0.00022)

Discussion

The obtained values, though lower than the target level of 0.97 defined in Deliverable 3 [32], are close enough to it as for the reference model that is subject to changes after detailed analysis. One should be also aware that the JEF2.2 library applied here gives over 1000 pcm lower values of k_{eff} than while applying the ENDFB6.8 library. The current level of criticality is closer to the desired level of its average over the fuel irradiation cycle what makes the model more representative for the whole cycle.

The calculated change of reactivity due to all effects associated with changing from room temperature to the power operating conditions is given by the formula:

$$\Delta\rho = \rho_2 - \rho_1 = \frac{k_2 - 1}{k_2} - \frac{k_1 - 1}{k_1} = \frac{1}{k_1} - \frac{1}{k_2} \quad (6)$$

For the high temperature model this gives:

Δρ = - 1904 pcm (30pcm)

For the lower temperature model:

Δρ = - 1502 pcm (32pcm)

Core Power Distribution

For a constrained thermal power of the reactor of 80 MW_{th}, the linear power ratings were calculated using the fixed source mode of the MCNPX code and the MCB code. The ratings are the subassembly averages given for four positions of fuel subassembly, starting from the first row of fuel S/A up to the fourth row of fuel S/A – see Table 6-16. In the axial direction the ratings are averaged in fifteen 10 cm long bins.

Table 6-16. Linear power ratings [kW/m] (uncertainty 1%)

	Fuel S/A row			
Axial bin	1	2	3	4
1 (top)	11.5	10.4	9.0	8.0
2	14.3	12.9	11.2	9.5
3	17.3	15.8	13.5	11.3
4	20.0	18.2	15.5	12.9
5	22.4	20.0	17.0	14.1
6	24.0	21.6	18.1	14.9
7	24.7	22.1	18.8	15.4
8	24.5	22.0	18.8	15.5
9	23.4	21.2	18.2	15.1
10	21.7	19.9	17.2	14.1
11	19.8	18.2	15.6	13.1
12	17.4	16.1	13.9	11.7
13	15.0	13.8	12.0	10.1
14	12.4	11.4	9.8	8.4
15	10.0	9.1	7.9	7.0
Average:	**18.6**	**16.9**	**14.5**	**12.1**

For the core average linear power of 16 kW/m a radial form factor (peak to average ratio) of 1.16 can be observed. A relatively flat radial power distribution is obtained due to the steel reflector. The gradient of power ratings within one S/A is also quite flat in the first row. The following axially averaged values for most inner, middle and most outer pins, respectively, were obtained in the first S/A row:

18.85 18.65 18.36 [kW/m]

Preliminary results of initial safety analysis

The initial safety analysis covers calculations of reactivity coefficients, subassembly reactivity worth and radiation damage calculations.

A. SUBASSEMBLY REACTIVITY WORTH CALCULATIONS.

The reactivity worth of subassemblies was assessed in the room temperature model for the following locations:

Fuel S/A 1st row	$\Delta\rho$ = 730 pcm (60)
Fuel S/A 2nd row	$\Delta\rho$ = 660 pcm (60)
Fuel S/A 3rd row	$\Delta\rho$ = 630 pcm (65)
Fuel S/A 4th row	$\Delta\rho$ = 490 pcm (65)
Reflector S/A 1st row	$\Delta\rho$ = 140 pcm (30)

B. REACTIVITY COEFFICIENTS.

i) Doppler effects

The change in reactivity due to Doppler effects was calculated by using the thermally expanded models with varying cross section library temperatures. The Doppler constant is defined as:

$$\alpha = T\, d\rho / dT \tag{7}$$

It can be calculated from reactivity values obtained for two different temperatures of the library cross sections according to equation (8) which can be easily obtained from integration of (7) assuming that α is constant over the interval of integration:

$$\alpha(T_{mat}) = \frac{\rho_2 - \rho_1}{\ln T_2 - \ln T_1} \tag{8}$$

To check the α dependence on the temperature, it was calculated for three temperature points of material expansion (density and dimensions) with the following three pairs of sampled fuel temperatures, T_1 and T_2, used for the calculation in equation (8):

T_{mat}	T_1	T_2
300K	300K	600K
1200K	900K	1500K
1500K	1200K	1800K

The results obtained, presented in Figure 6.16, show that α is not a constant but changes by 50% over the applied temperature range. At high temperature (1500K) the coefficient reaches a value of -720 (±60) [pcm]. The correction due to the temperature dependence changes this value by about –10 pcm to –730 pcm.

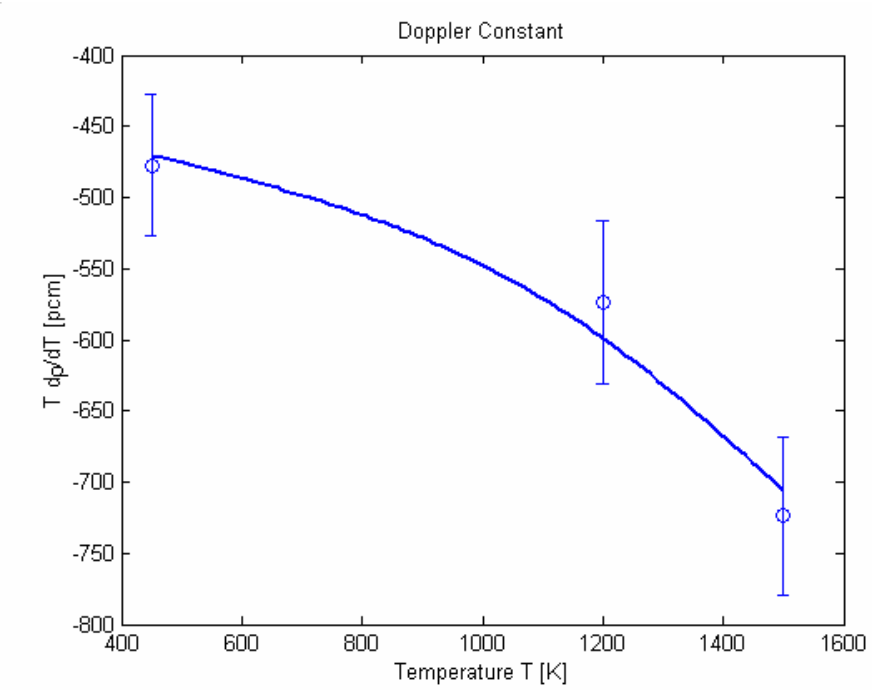

Figure 6.16: Doppler constant: α = T dρ /dT in Gas Cooled XADS obtained by MCNP sampling.

ii) Core expansion effects

Core expansion effects were calculated using cross section libraries with room temperatures applied to both the room temperature model and the thermally expanded models. The combination of reactivity values obtained in these cases gives the following values for reactivity change due to core expansion and material density dilution:

a) high temperature model:

$$\Delta\rho_{exp} = -1010 \text{ pcm} \quad (25)$$

b) lower temperature model:

$$\Delta\rho_{exp} = -686 \text{ pcm (25)}$$

iii) Coolant voiding

In the calculation model the helium pressure in the reactor vessel drops from 60 bars to 1 bar. Obtained helium coolant voiding has a slightly positive reactivity coefficient equal to:

$$\Delta\rho_{He} = +130 \text{ pcm (25)}$$

This slightly positive void coefficient for coolant voiding is overshadowed by the factor of 15 larger negative temperature coefficient coming from Doppler and core expansion effects. It should not become a safety issue.

iv) Ingress of LBE into beam tube after window failure

This value was calculated in the room temperature model since window failure will ultimately shut down the power.

$$\Delta\rho_{tube} = +140 \text{ pcm (30)}$$

This slightly positive coefficient is a result of the LBE closure of the beam line vacuum in the target decreasing the core neutron leakage and increasing the reactivity. In case of this type of accident taking place during power on, the margin to criticality is larger by 1500 pcm than in room temperature. The possible risk would occur only in room temperature, or eventually after switching-off the beam and cooling down the core. The obtained value is the limit for all considered scenarios and should not pose any major safety concern. Limit to criticality will be high enough to accommodate this positive reactivity effect.

Preliminary damage information

The DPA values were obtained under the assumption that the operation time covers 90% of real time for one year of operation. The core actual thermal power consists of direct radiation heating, including neutron KERMA heating and gamma heating, as well as decay heating – mostly from decays of short lived fission products. In our case the decay heating accounts for 3.4 MW_{th} while the remaining 76.6 MW_{th} comes from prompt radiation interaction with matter.

The presented values are the maximum obtained values for the considered component but averaged over a certain volume due to the dimensions of the geometry cells. In the case of the fuel elements, the axial bin was 10 cm and the local peak DPA at the center can be only 2% higher than the presented value. In the case of remote parts, the flux gradient is higher at the lower flux level so the local peak DPA can be up to 20% larger than the average. Radiation damage values in terms of DPA were obtained in the fixed source mode of the calculations with the source obtained from MCNPX simulation of the bare target. The DPA for the core elements obtained in this approach combines the damage from the fission neutrons and the source neutrons whereas for the target elements the DPA contributions from primary neutrons (priori to leaving the target) are

not included. To have the complete DPA values for the target elements one should run a neutron transport calculation in the MCNPX with the bare target model.

i) Fuel pellet cladding (uncertainty <1%):

Fuel S/A 1st row	**10.7 DPA/year**
Fuel S/A 2nd row	**9.79 DPA/year**
Fuel S/A 3rd row	**8.03 DPA/year**
Fuel S/A 4th row	**5.67 DPA/year**

ii) Upper part of diagrid (uncertainty ~5%):

At thimble guide	**0.020 DPA/year**
At Fuel S/A 1st row	**0.020 DPA/year**
At Fuel S/A 2nd row	**0.021 DPA/year**
At Fuel S/A 3rd row	**0.016 DPA/year**
At Fuel S/A 4th row	**0.012 DPA/year**

iii) S/A elements

Wrappers (uncertainty ~1%):

Fuel S/A 1st row	**8.6 DPA/year**
Fuel S/A 2nd row	**8.0 DPA/year**
Fuel S/A 3rd row	**6.6 DPA/year**
Fuel S/A 4th row	**4.55 DPA/year**
S/A Spike1st row	**3.6e-2 DPA/year**
S/A Head1st row	**2.3e-3 DPA/year**

iv) Target elements due to core neutrons (uncertainty ~2%):

Window	**4.7 DPA/year**
Hot channel	**5.2 DPA/year**
Thimble	**6.6 DPA/year**
Thimble guide	**0.20 DPA/year**

v) Vessel (uncertainty ~5% -20%):

Inner vessel	**3.8e-5 DPA/year**
Support plate	**2.1e-5 DPA/year**
Vessel wall	1.**7e-5 DPA/year**
Bottom head	**3.3e-6 DPA/year**
Shield plate	**1.7e-5 DPA/year**
Cover Head	8.**0e-7 DPA/year**

Assessment of the adoption of reflector/moderating materials at the core periphery

Unlike the LBE cooled reactor, introduction of a reflector to the core is a necessity in order to reduce the neutron leakage and maintain reactivity at the desired level. Without a radial reflector the reactor would have a neutron multiplication factor k_{eff} = 0.777, equivalent to a 25% loss of reactivity. This large reactivity loss is characteristic of small reactors with large surface-to-volume ratios. The reflector adopted in the reference model consists mainly of steel, making it a hard spectrum reflector that uses the neutron inelastic scattering process in a high energy range without significant neutron moderation. This main feature of the reflector is in line with the general characteristic of fast spectrum gas cooled reactors but we should consider the difference that emerges in ADS systems due to the neutron source driver.

The adoption of moderator at the core periphery will not affect the spectrum of neutrons coming from the target and then multiplied in the central zone but will introduce into the outer region, reflected and moderated neutrons that will enhance the fission reaction rate by exploiting the high fission cross sections of fissionable plutonium in the lower energy range. The approach of mixing spectra in an ADS reactor was previously studied by Stone et al. [35] where a so called dual spectra core was proposed with two separated regions: inner – fast and outer – thermal, in order to reduce the reactivity swing. In the case of XADS, the core is too small to adopt separated regions but introduction of moderating reflector can help, the same way as in the dual spectra concept, to reduce the reactivity swing. It also enhances the possibility of adopting burnable absorbers in the reflector region since the reflector starts to play an important role in maintaining the reactor criticality level.

To investigate the possibilities, a few candidates for moderating reflector can be considered as follows: aluminum, ^{11}B, various hydrides e.g. ZrH, or graphite. An excellent candidate from the neutronic point of view is beryllium but it has been decided not to consider this because it is both expensive and hazardous [36]. For the initial analysis, aluminum and graphite were assessed for their potential to raise core reactivity. In the MCNP calculation model (BOL at power, conservative expansion) the steel rods of the radial reflector were replaced by aluminum or graphite rods. The following results were obtained:

Reflector	k_{eff}
Steel	0.9539
Aluminium	0.9309
Graphite	0.9903

Whilst the aluminium reflector is inferior to the steel, the graphite looks very promising since it can raise reactivity by about 3600 [pcm] by enhancing the fission process at the outer active core region. A reactivity increment of that scale creates new possibilities for optimizing the cores design for important design goals *e.g.* reactivity swing reduction or adoption of lower enrichment fuel from SPX. Regarding SPX fuel, the reactivity drop associated with its adoption in the gas cooled XADS should be about 2000 [pcm], which is eestablished on the basis of comparative calculations, and could be balanced by introduction of the graphite reflector. Issues concerning reactivity swing

reduction are discussed in the next section. An additional advantage of adopting moderating reflector is a flattening of the radial power distribution. In the case of the graphite reflector, a halving of the radial power distribution gradient can be obtained and an even better reduction may be possible through an optimisation process.

Assessment of the possibility to adopt neutron absorbing elements

The adoption of neutron absorbing elements into the XADS core is considered mainly for the purpose of compensating for burn-up reactivity loss in case of insufficient fuel conversion from fertile materials. This, if successful, could reduce the reactivity swing and extend the fuel residence time in the reactor. The possibility of adopting a burnable poison only exists if the system can afford to have excess reactivity at the beginning of irradiation, thus compensating for the neutron loss to the absorbers. This means that the fuel for the initial loading must have a higher enrichment unless other means for increasing the reactivity, such as better reflectors, are introduced. These issues can be addressed in detail through the burn-up optimisation process that will be undertaken during the fuel cycle task. Here we can only point out some general guidelines and possibilities

The idea of using burnable absorbers is simple in principle in that, along with the fuel burn-up, neutron-absorbing material is also being burned, thus reducing the neutron loss term with burn-up. In general, extra absorption introduced into the system does not necessarily mean that neutron production is increased since the system power is constrained. To keep production and loss terms in balance the trade can occur between different elements of the loss term, thus the leakage term can be reduced to allow en enlargement of the absorption term. If we assume that the boundary conditions are not changed, the only way to reduce neutron leakage is to reduce the flux at the boundary, which in turn means increasing the flux in the inner region, thus necessitating the adoption of a multi-region core with different fuel enrichments. This obviously conflicts with the application of absorbing elements to maintain a satisfactory power form factor.

Absorbing elements could be used to improve the power distribution if they are introduced into regions of power peaking but one can see that this option would oppose the above described reactivity swing control feature. With additional absorbers and an enriched fuel introduced into central region we will have the source efficiency lowered. Reactivity swing will be reduced but on the expense of the proton beam which need to be raised to compensate for the efficiency loss. In other words, burnable absorbers in the core can reduce the reactivity swing while increasing the flux gradients what reduces the neutron leakage but increases the power form factors. An attempt to reduce the form factors will adversely affect the reactivity swing reduction. Moreover, one should notice that reactivity swing reduction or power distribution flattening obtained along with reduction of the neutron source effectiveness is not an option since the penalty in higher proton current requirements will offset all possible advantages. Therefore introducing burnable absorbers into the central core region, close to the target unit, will have limited potential for improving the design and should be exercised carefully.

As was already pointed out in the preceding section, the situation can be solved if one applies moderating reflectors. Introduction of burnable absorbers into the moderator will control the neutron flux at the active core boundary thus relaxing the constraints for neutron flux distributions that led to the conflict between power radial distribution and

the reactivity swing reduction. To prove the above-described physical phenomenon, comparative burn-up calculations were performed for the core with steel reflector and the core with graphite reflector with added thin films of B_4C, in the form of a wrapper around the reflecting rods. The burn-up calculations were done in three radial zones and 5 axial zones. The results are presented in Table 6-17.

Table 6-17. Burn-up Comparison of the Core with Burnable Absorbers and the Reference Core.

	Reference Core	Burnable Absorber Core
Reflector	Steel	Graphite
Absorber	-	B_4C wrappers, thickness 0.2 mm
Reactivity loss/1st year	1220 pcm	790 pcm
Reactivity loss/2nd year	1370 pcm	800 pcm
Inner/Outer zone power ratio at BoL	1.473	1.301
Inner/Outer zone power ratio after 2 years	1.456	1.23

These results show the great potential of moderating reflectors combined with burnable absorbers for reducing reactivity swing, already by 30% in the above unutilised designed, with simultaneous reduction of the radial power form factor. The design presented is a first guess and there is probably room for further improvements, since the absorbing elements need to be optimised so that the burn-up process would almost completely reduce their concentration over the period of one fuel cycle.

The optimum shuffling strategy strongly depends on the cycle analysis and the adopted core design. From a fuel management point of view, as well as safety, the best condition occurs when one type of fuel is used, and after one cycle all fuel S/A are replaced by fresh fuel. This provides the simplest situation but the fuel burn-up level at the time of discharge from the reactor may be quite low. Increasing the reactor residence time of the fuel increases its burn-up but at the expense of the optimal power distribution. Although the power from factor improves with burn-up due to a higher fuel depletion in the central region, the flatten power distribution decreases the neutron source efficiency. To compensate for it the shuffling between the outer and inner regions can be undertaken. In the case of the XADS design, the situation is complicated by the small size of the core and the low power, which limits the possibility of introducing a multi-zone core.

Burnup modeling with MCB for XADS with SNR300 fuel

Introduction

Although a burn-up simulation with the Monte-Carlo method MCB system can be performed on a high level of geometry complexity, the main goal in the current stage of analysis is to produce results in a relatively simple model in order to allow for their replication in a deterministic approach in order to compare different burn-up simulation methods. The model simplifications concern the system geometry and the definition of a

spallation neutron source. The neutron source definition influences the physical meaning of the neutron multiplication factor - k_s as calculated in the fixed source mode, thus different ways of the source definition in MCB and in a deterministic model can impose differences in the obtained values of k_s.

Calculation Model and Methods

A. THE MODEL

The burn-up calculation was preformed by using the MCB code in a geometry model of XADS reactor using the adapted version of core model (called "co01") prepared by FZK [37] as follows:

a) The basic model consists of a target, a beam pipe, a multiplying region with 2 types of assemblies (called C1_MAG and C2_LWR) and a reflector. The homogeneous representation of the assemblies has been used in the MCB model.

b) The target has been represented by a homogenised mixture of LBE and the structure steel outside of a separately modelled vacuum of the beam pipe.

c) The neutron source has been represented by a surface neutron source file (called RSSA) that was obtained by a collection of all neutrons leaking the LBE target during an MCNPX simulation of a 600MeV proton beam interaction with the target in a standalone bare target model, thus avoiding an overlapping of core neutrons contributions.

d) The core has been divided into 24 burnable zones: 3 radial sections times 8 axial sections.

The axial sections consist of eight central core zones filled with the MOX fuel and two outer blanket zones filled with UO_2. The radial division goes with the rows of hexagonal lattice while the axial column is divided into 5 sections as shown in Table 6-18:

Table 6-18. Description of the XADS model

Zone	Segment	Material	height [cm]
1	upper blanket	UO_2	40
2-7	core	MOX	6 x 15.833
8	lower blanket	UO_2	40

B. THE METHOD

In order to assess the required reactor core parameters, the Monte Carlo method of neutron transport was applied using the MCNP based codes MCNPX and MCB1C, with temperature dependent cross section libraries of the MCB system [38]. Two modes of calculations were applied: Firstly, the fixed source mode of MCNPX in a bare target system to produce the neutron source for burn-up calculations in MCB, to obtain core power distribution and radiation damage. Secondly, the burn-up mode of MCB to calculate the system evolution with time over 3 years of the $80MW_{th}$ thermal power

irradiation. In general, the JEF2.2 cross section libraries were used in the current calculations, whereas for nuclides of lead that are missing from JEF2.2 the JENDL3.2 data were used. The cross section at power temperatures 1200K for fuel and 900K for target were used.

For the calculation of $\boldsymbol{k_s}$ an integral approach has been applied that is based on the comparison of the number of fission neutrons produced in the fixed source mode the external neutron source mode with that number produced in the eigenmode or fundamental mode. This leads us to following definition:

$$k_s = \frac{N_f}{N_f + 1}$$

where N_f is the number of fission neutrons generated per one external source neutron.

For the source effectiveness the following formula was applied:

$$I = \frac{(1 - k_{eff}) \cdot k_s}{(1 - k_s) \cdot k_{eff}}$$

C. POWER NORMALIZATION

MCB calculates the thermal power released per one source particle and adjusts the source intensity to keep power at the user specified level. The core actual thermal power consists of direct radiation heating, including neutron KERMA heating and gamma heating, as well as decay heating – mostly from decays of short lived fission products. In our case the decay heating accounts for about **3.0 $\mathbf{MW_{th}}$** while the remaining **77.0 $\mathbf{MW_{th}}$** comes from prompt radiation interaction with matter. The total power, however, neglects the energy release into the target in the high-energy particle transport.

Results

The results obtained in the MCB burn-up calculation presented in Table 6-19 summarize the burn-up performance of XADS code with SNR300 fuel. For the purpose of a comparison with calculation systems that are normalized to fission energy we have assessed the energy release per one fission event by dividing the total heating by the number of fission events as follows:

Heating per source neutron	1.692GeV
Fissions per source neutron	7.817
Energy/number of fissions	**216.5MeV**

The obtained value should not be understood as the energy of one fission event since it includes all energy releasing processes taking places in the system.

The external source multiplication factor – $\boldsymbol{k_s}$ is slightly higher than the actual reactivity or effective neutron multiplication factor - $\boldsymbol{k_{eff}}$ implying the source effectiveness greater than one. The time evolution of the criticality is presented in Figure 6.17.

Table 6-19. Summary of LBE cooled XADS with SNR300 fuel

Time [year]	Power [MW]	Source Strength [1/s]	k_{eff}	k_s	H/S[3] [MeV]	I	Decay Heat [W]
BOL	80	3.04E+17	0.9592	0.9613	1642.93	1.0549	2.94E+06
0.25	80	3.29E+17	0.9523	0.9547	1515.12	1.0549	2.97E+06
0.50	80	3.71E+17	0.9471	0.9496	1346.43	1.0537	2.97E+06
0.75	80	4.15E+17	0.9408	0.9446	1201.79	1.0732	2.97E+06
1.00	80	4.58E+17	0.9350	0.9378	1090.56	1.0492	2.97E+06
1.25	80	5.04E+17	0.9292	0.9325	989.53	1.0534	2.97E+06
1.50	80	5.54E+17	0.9233	0.9273	900.64	1.0590	2.97E+06
1.75	80	6.16E+17	0.9168	0.9211	810.07	1.0584	2.97E+06
2.00	80	6.43E+17	0.9111	0.9164	775.79	1.0697	2.97E+06
2.25	80	6.90E+17	0.9061	0.9116	723.26	1.0694	2.97E+06
2.50	80	7.48E+17	0.9000	0.9059	667.16	1.0696	2.97E+06
2.75	80	7.70E+17	0.8946	0.9014	648.18	1.0773	2.97E+06
3.00	0.038	0	0.8891	0.8954	0	1.0687	3.76E+04

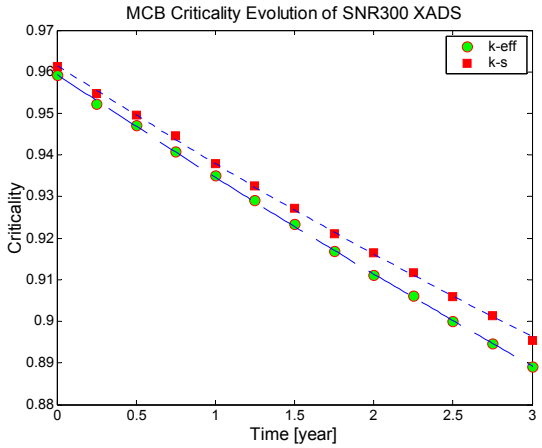

Figure 6.17: Time evolution of criticality and the external source multiplication factor in the MCB simulation of XADS with SNR300 fuel.

In order to explain possible differences in the burn-up evolution obtained with different simulation methods one need to compare the evolution of the nuclide densities as well

[3] H/S is an abbreviation for Heat per Source particle

as their influence on the system criticality. Plots of transmuted mass of those nuclides, presented in Figure 6.18, show that nuclides that are being reduced in mass are ^{238}U, ^{239}Pu, ^{235}U and ^{241}Am. Other nuclides of plutonium are being build-up affecting, to some extent, the pace of the reactivity swing. The next two Figure 6.19 and Figure 6.20 show the comparison of the depletion rates of the major actinides and their change with burn-up. Analysis of these data can shed some light on how the transmutation changes the nuclides contributions to the reactivity. The presented data concern the most inner zone in which the transmutation process has the highest rate. The main fertile nuclide – ^{238}U undergoes the fission with the density greater than those for ^{240}Pu and it does not change significantly with its depletion. The density of the main fissionable nuclide – ^{239}Pu is being reduced mainly by fission but also due to the neutron capture what leads to the build-up of the heavier nuclides. The pace of ^{239}Pu destruction is slowed down by its production term from ^{238} U that is represented by the difference between the total depletion rate and the depletion due to fission. With the burn-up the fission density of ^{239}Pu decreases the most out of the all nuclides for the favor of the heavier plutonium nuclides – ^{240}Pu and ^{241}Pu. It shows that those nuclides partially reduce the reactivity swing since their density and contribution to the fission grow with the burn-up.

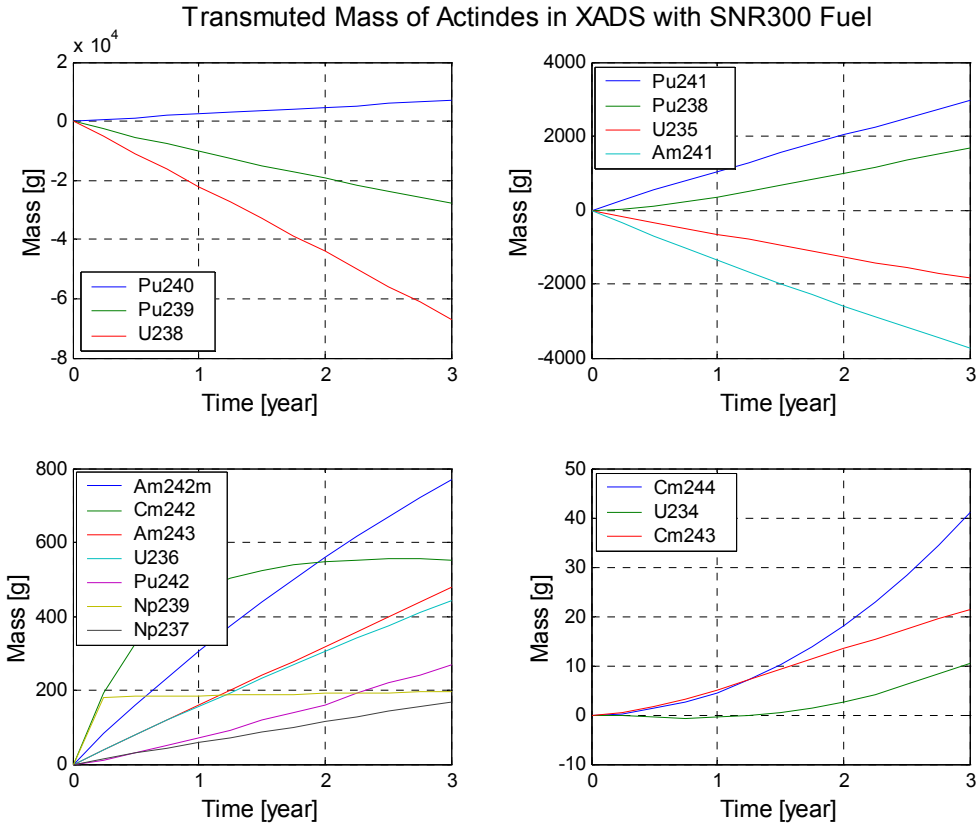

Figure 6.18: Transmuted mass of actinides in the whole XADS reactor with SNR300 fuel as obtained in the MCB burn-up simulation

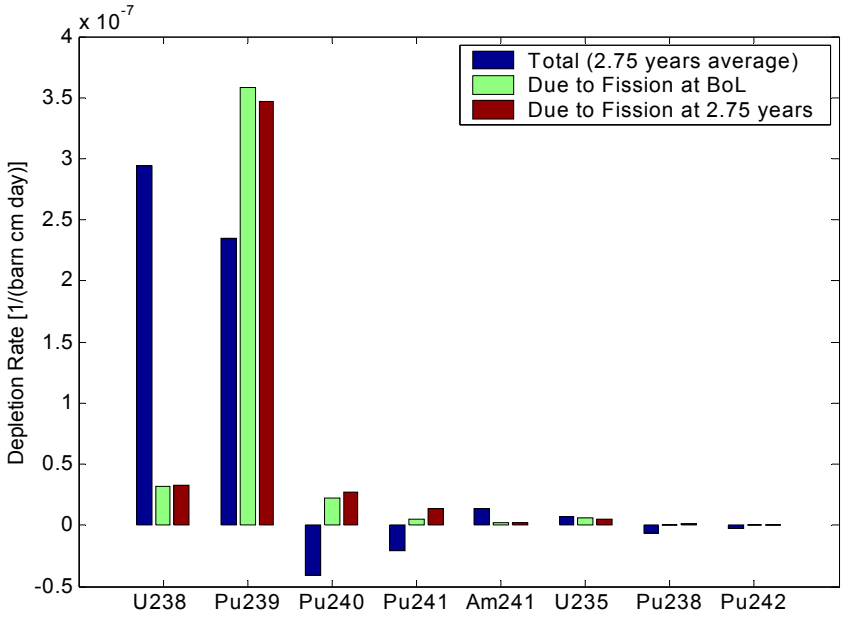

Figure 6.19: Comparison of the depletion rate of the actinides at the most central zone of XADS reactor with SNR300 fuel as obtained in the MCB burn-up simulation

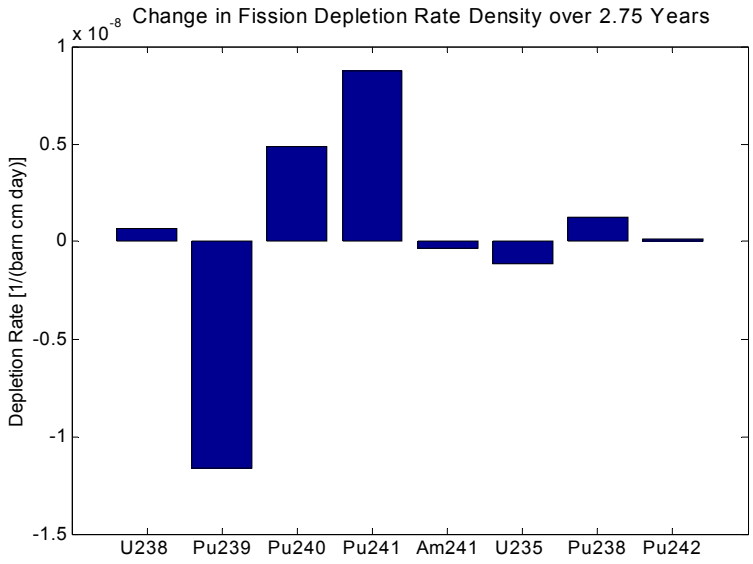

Figure 6.20: Change in depletion rate of the major nuclides in the central zone of XADS reactor with SNR300 fuel after 2.75 years of 80MW power burn-up.

Finally, Figure 6.21 summarizes mass evolution of the nuclides that strongest influence the criticality in the eight axial zones of the most inner radial subassembly row at the BoL and after 3 years of burn-up.

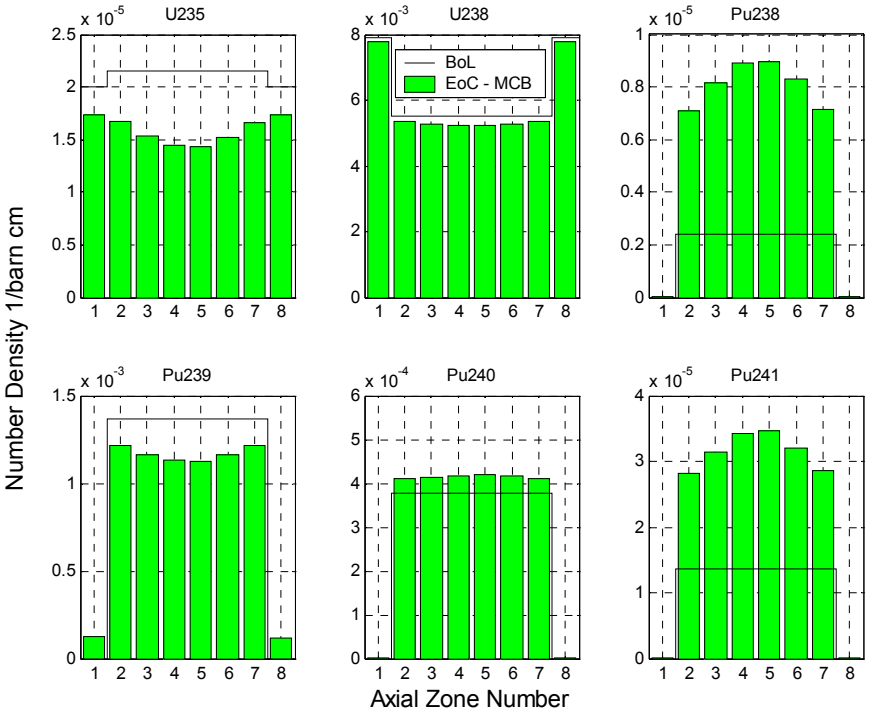

Figure 6.21: Number density of the nuclides that strongest influence the criticality in the eight axial zones of the most inner radial subassembly row at the BoL and after 3 years of burn-up.

7 TRANSMUTATION CAPABILITIES OF THE DEEP BURN MODULAR HELIUM REACTOR

7.1 INTRODUCTION

In order to broaden our understanding of transmutation potential of subcritical systems we have also studied an option of transmutation using critical reactors. In particular we aimed to verify and quantify the high burnup performance of the Deep Burn Modular Helium Reactor (DB-MHR) [39]-[46]. A typical plant layout of a DB-MHR nuclear facility uses 4 modules of 600 MW [43] to destroy Pu from Light Water Reactors and, at the same time, to produce electricity or generate high temperature process heat for the production of Hydrogen or other purposes. Each module consists of a gas-cooled graphite-moderated DB-MHR. The modular arrangement and small size are aimed at reducing the core power density, so that the complication of the security devices decreases, as well as the power excursion during an accident. The attractive features of the DB-MHR are:

- Constructional costs lower than in an ordinary LWR [46].
- Clear passive safety mechanism.
- High energy conversion efficiency (about 50% [8]), which also reduces the thermal impact on the natural environment.
- Well-developed nuclear technology both for the core and the fuel structure.
- Resistant barriers protecting the environment from dispersion of residual waste.
- High burnup, up to 700000 MWd/t [8], with better than 90% destruction of selected actinides (including ^{239}Pu).
- Great flexibility in the choice of the fuel type: fertile and non-fertile cores (e.g. Th, U or Pu).

Several factors contribute in the passive safety mechanism of the DB-MHR: negative temperature coefficient of reactivity, helium coolant (which is inert, operates in a gas single phase and it is almost transparent to neutrons), H451 graphite core (which provides high heat capacity and structural stability), low power density, about 2.1 MW/m^3 over the whole reactor core and 6 MW/m^3 in the power generating volume, triple isotropic (TRISO) coated fuel particles (which retain fission products even under a severe accident scenario), operational temperature of graphite above 270^{o}C (which facilitates the reallocation of interstitial atoms and lacunas in the lattice and avoids the Wigner effect). The low power density of the DB-MHR is a benefit from the safety point of view but also a drawback concerning electricity production. The H451 nuclear-grade graphite used in the DB-MHR is a special type of graphite that differs from normal graphite in several aspects [44]:

- it inhibits exothermic oxidation reactions (graphite fires),
- it contains a low concentration of impurities (which catalyze the oxidation reaction),
- it has a high density (which reduces porosity and inhibits oxidation),

- it has a high thermal conductivity and specific heat, it does not create (when it burns) the external porous ash layer (which would allow oxygen to pass through) and methane (which would react exothermically).

The main objective of the DB-MHR design has been the extended destruction of ^{239}Pu, one of the major contributors to long lasting radiotoxicity and the major proliferation concern. Because of the radiological importance of several minor actinides in the geologic repository [43], we have also focused our attention also on the transmutation of Minor Actinides (MA).

Before fueling the DB-MHR, LWRs waste is reprocessed by uranium and fission products extraction (UREX). The final products of the LWRs spent fuel reprocessing are $NpPuO_{1.7}$ and $AmCmO_{1.7}$; the first material constitutes the Driver Fuel (DF). The DF is the primary nuclear fuel for the DB-MHR and it sustains the fission chain reaction, mainly by ^{239}Pu. Spent DF is mixed after discharge from the reactor core with the $AmCmO_{1.7}$, which was set-aside after UREX, to build fresh Transmutation Fuel (TF). After irradiation, spent TF is sent into the repository. ^{239}Pu plays a key role in the operation of the DB-MHR, because it is the most abundant fissile isotope in LWR spent fuel after UREX, and therefore provides most of the reactivity of the DF. We can note in Figure 7.1 [47] that ^{239}Pu exhibits a particularly undesirable neutronic behavior in the neutron energy range of 0.25-1 eV, where resonances of fission and capture cross sections of ^{239}Pu set a positive temperature reactivity feedback, since the capture to fission ratio (the alpha ratio) decreases with the increase of temperature. Also production of xenon contributes in the positive reactivity feedback because of the low ^{239}Pu Doppler coefficient [48]. Usually, the undesired behavior of ^{239}Pu in the neutron energy range above 0.25 eV is mitigated by adding ^{167}Er as burnable poison (Figure 7.2) [39]-[43]. Nevertheless, in graphite moderated reactors, ^{167}Er can be replaced by ^{241}Am, ^{237}Np and ^{240}Pu, which are abundant in the TF. These actinide isotopes have resonances in the right energy range to compensate for the increased reactivity of ^{239}Pu; they need to be transmuted and are also fertile. Therefore in the DB-MHR, they can replace the parasitic rare earth burnable poisons to great advantage. The graphite–moderated DB-MHR is well suited to use some of the MA in this way, because graphite exhibits a gradual slowing down of the fission neutrons: in fact, the neutron average energy lost per collision is 14.6% for graphite and 60.1% for water. Therefore, graphite allows the effective use of the resonance absorption for ^{241}Am, ^{237}Np and ^{240}Pu to counteract the reactivity feedback of ^{239}Pu, since the neutron during its slowing down samples the energy space with much smaller steps and hits resonance energy regions more frequently than in e.g. LWRs.

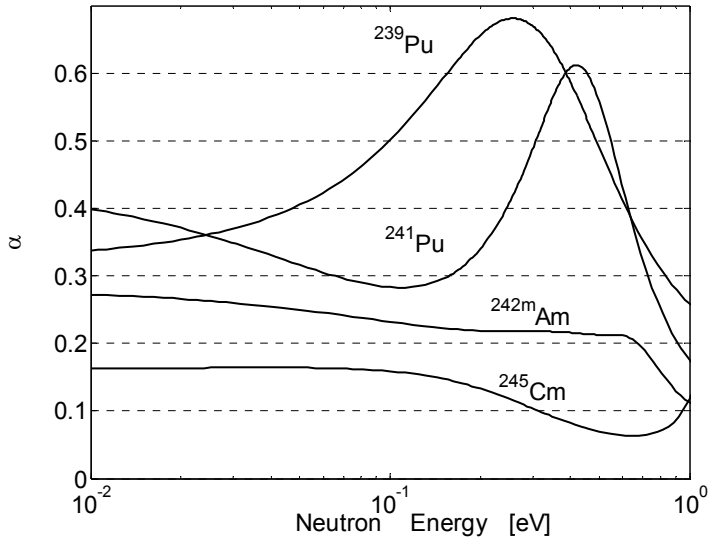

Figure 7.1: Capture to Fission Ratio of ^{239}Pu and fissile MA

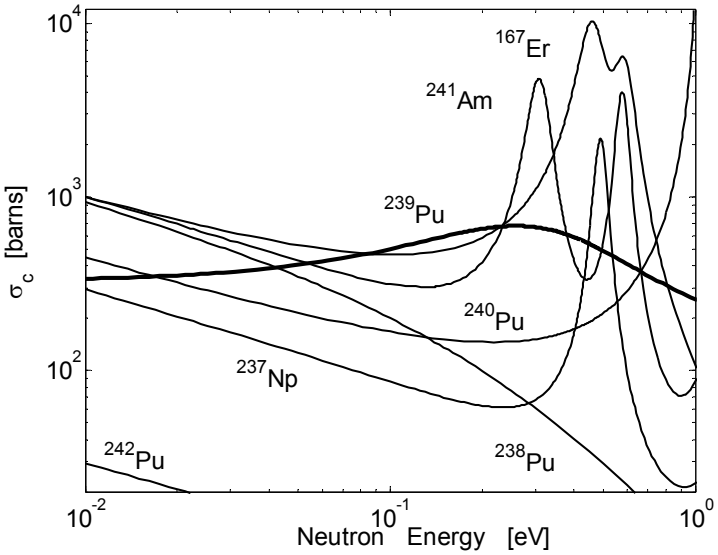

Figure 7.2: Capture Cross Section of non-fissile MA and Capture to Fission Ratio of ^{239}Pu

7.2 THE DB-MHR DESCRIPTION

Figure 7.3 describes the General Atomic – Minatom DB-MHR [40]. The core is composed by a matrix of hexagonal blocks, which contain: the inner replaceable reflectors, the outer replaceable reflectors and three rings of fuel. The space between two hexagonal blocks is 0.1016 cm. The reactor has 48 operational control rods, which are filled with boron carbide spheres. 18 control rods are located both in fuel blocks and 30 control rods in the outer replaceable reflectors. The fuel blocks are equipped with further 18 reserve shutdown control rods (RSC). The matrix of hexagonal blocks of the

core is surrounded by a permanent reflector, which, on the outer border, is filled with borated steel pins. Nevertheless, in the model we used for numerical simulations, we neglected the presence of control rods and the space between two blocks of graphite. Since we estimated a low variation of k_{eff} during the operation at equilibrium, we retain the neglecting of control rods a valid approximation.

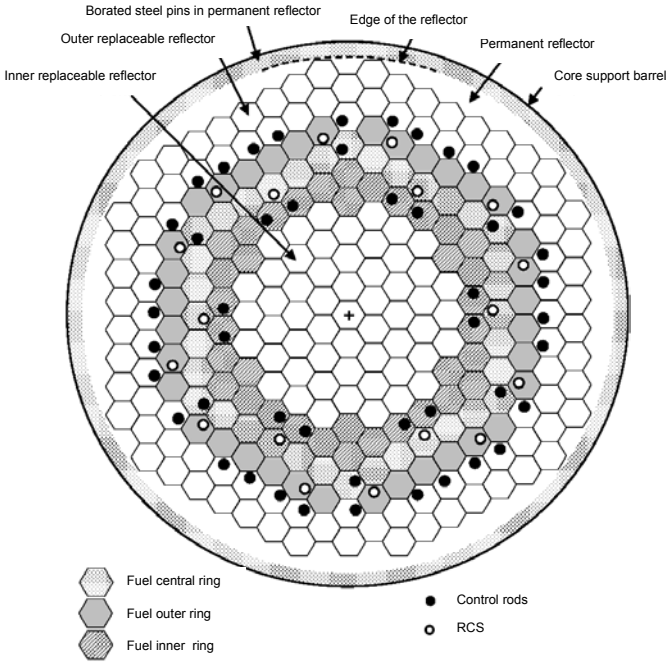

Figure 7.3: Horizontal section of the core of the General Atomic – Minatom DB-MHR

The DB-MHR has been modeled in numerical calculations as a cylinder, with a radius of 4 m and a height of 10 m, filled by hexagonal blocks of graphite (density 1.74 g/cm3) and fuel. Namely, the fuel is disposed along three concentric rings each of 36 hexagonal blocks Figure 7.4 [43]. Fuel covers just 7.93 m of the height of a hexagonal block; the remaining 2.07 m, 1.035 m at top and at bottom, are filled with graphite, which acts as blanket - Figure 7.5

The side of the hexagonal blocks is 20.8 cm. In each fuel block there are 108 cooling helium channels, 144 DF pins and 72 TF pins - Figure 7.4. Therefore, the ratio between DF pins and TF ones, as well as their volume ratio, is 2:1. The cooling channels have a radius of 0.797 cm, whereas the driver and transmutation pins have a radius of 0.622 cm. A further cooling channel, with an external radius of 0.635 cm, surrounds each driver and transmutation pin. Helium enters the cooling channels from the bottom of the reactor at 490^{o}C, with a pressure of 7 MPa, and it exits at the top with a temperature of 850^{o}C. Table 7-1 summarizes the most important parameters of the model used in numerical simulations by MCB to represent the DB-MHR. Table 7-2 gives detailed description of the TRISO particles.

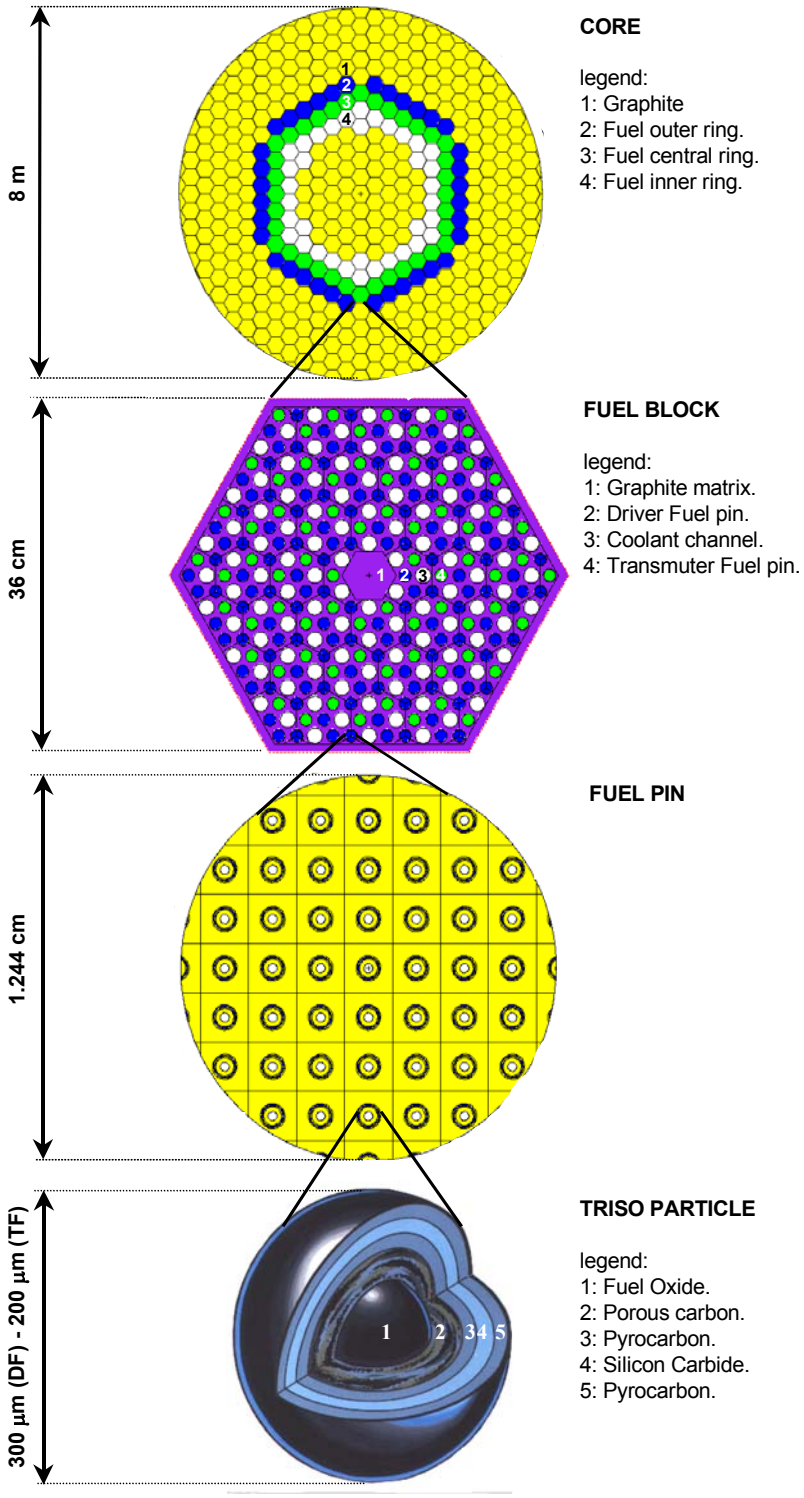

Figure 7.4: The model of the DB-MHR used in simulations

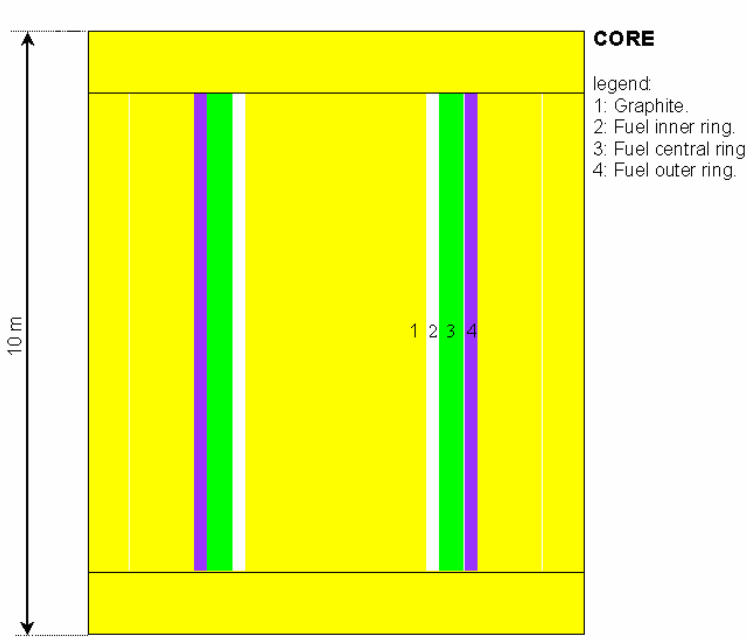

Figure 7.5: Vertical section of the core of the DB-MHR used in simulations

Table 7-1. Core design parameters for the numerical simulations of the DB-MHR	
Core Power [MW_{th}]	600
Core radius [cm]	400
Core height [cm]	1000
Side of an hexagonal block (m)	20.8
Fuel blocks	36x3
DF pins in a fuel block	144
TF pins in a fuel block	72
Coolant channels in a fuel block	108
Radius of a fuel pin [cm]	0.622
Height of a fuel pin [cm]	793
Radius of coolant channel surrounding a fuel pin [cm]	0.635
Radius of a coolant channel [cm]	0.797
Distance between DF TRISO particles in the fuel pin [cm]	0.0794138
Distance between TF TRISO particles in the fuel pin [cm]	0.0529425

Table 7-2. Structure of a TRISO particle. The density of TF is the value at the beginning of the 6th year (see Fuel Strategy). The values of density for TF refer to the inner ring at the 4th and at the 12th year.

Material	External radius [μm]	Initial Density [g/cm^3]
DF – (TF_4 ; TF_{12})	150 – 100	10.2 – (10.5 ; 15.7)
Porous Carbon Layer	300 – 250	1
Pyrocarbon	335 – 285	1.85
Silicon Carbide	370 – 320	3.2
Pyrocarbon	410 – 360	1.85

Both the driver and transmutation pins consist of a graphite matrix (fuel compact) filled with TRISO fuel particles (Figure 7.4). We set the packing ratio (the fraction of the TRISO particles volume over the total volume of the fuel pin) to 14.41% for DF and to 32.92% for TF. Whereas the packing ratio of the fuel central sphere (kernel) (the fraction of the fuel volume over the total volume of the fuel pin) of TRISO particles is 0.7% both for driver and transmutation fuel; therefore, the volume ratio between DF and TF is 2:1, since the number of DF pins is twice as that one of TF.

The kernel of a TRISO particle consists of fuel oxide, whereas the three surrounding concentric spherical layers are made by :

- Porous carbon, which provides the volume for the expansion of fission gases and attenuates fission recoils;
- Pyrocarbon (inner layer), which sets the substrate for the SiC layer;
- SiC, which retains the gas and metal fission products and provides the mechanical resistance;
- Pyrocarbon (outer layer), which sets a bonding surface for compacting and acts as fission products barrier in particles with defective SiC.

Since the mean free path of neutrons, in the resonance region 0.2-0.4 eV, is 10-100 μm, we fixed a radius of 150 μm for the DF and of 100 μm for the TF. In order to enhance the resonance capture, and therefore the transmutation of the non-fissile actinides, the radius of a TF particle is smaller than that one of a DF particle. The greater radius of DF decreases the effective capture-to-fission ratio for ^{239}Pu (averaged on the whole kernel), therefore improving the fission performance of the DF and reducing the buildup of higher actinides.

TRISO particles have proven to retain fission products up to 1600°C [49]-[52]. After this threshold, several factors can degrade their integrity: manufacture defects, internal pressure of the gas fission products, failure of the Pyrocarbon layer due to neutron-induced embrittlement, Amoeba effect (which is the migration of the kernel into the surrounding layers), failure of SiC due to chemical interaction with fission products and dissociation of SiC, which occurs at 2000 °C. During manufacture, a more isotropic and porous pyrocarbon layer, can improve by a factor 1000 the gas release under irradiation [53],[54].Recent studies have suggested that replacement SiC with ZrC improves the performance of TRISO fuel, since ZrC TRISO particles show no failure up to 1800°C [55][56][57]. We have not considered ZrC coatings in our models.

In the case of an accident, TRISO particles can stay intact for 3 hours at 1500°C [57]. During this interval of time the reactor will most probably be depressurized (10 bar/min [58]) and air may penetrate the vessel. When the air enters the reactor, TRISO particles loose integrity because of the gasification of the fuel graphite matrix by the oxidation of the pyrocarbon. In this scenario, the DB-MHR exhibits a passive security mechanism because heat conduction (in graphite), thermal radiation and natural convection (from graphite to air), coupled to a low power density (2.1 MW/m3), can keep the temperature excursion of fuel lower than 1600°C [59]. In fact, the nuclear-grade graphite H451 is not subjected to the red glow, which occurs when the heat removed by air convention is smaller than heat produced by exothermic reaction of graphite with oxygen [44].

In a repository environment, spent TRISO particles should maintain their integrity for millions of years, even if they would permanently be flooded with groundwater [61][62]. By contrast, the Nuclear America Society (NAS) estimated that, in the Yucca Mountain repository of the, Zircaloy cladding of ordinary spent fuel would retain the radiotoxic nuclides for only a few thousand years at best [63].

The initial composition of the DF is showed in Table 7-3, where the relative abundance of the Actinides reflects the inventory of LWRs spent fuel.

Table 7-3. Initial composition of the fresh DF.

Isotope	Atomic percentage %	Mass [Kg]
^{237}Np	1.91	16.49
^{238}Pu	0.56	4.849
^{239}Pu	21.11	184
^{240}Pu	8.5	74.36
^{241}Pu	3.09	27.16
^{242}Pu	1.87	16.49
^{16}O	62.96	36.70

7.3 FUEL SHUFFLING STRATEGY

The Deep Burn concept is based on the use of Driver Fuel, rich in fissile actinides (^{239}Pu) and Transmutation Fuel, rich in non-fissile actinides. The DF provides the excess reactivity to drive the power production and sustain large effective transmutation rates. The TF provides burnable poison and reactivity control.

In the DB-MHR, the hexagonal fuel blocks are disposed along three rings; in addition, each fuel block is divided into 10 sub-blocks along the z-axis. The shuffling strategy moves hexagonal fuel blocks both radially and axially. Namely, the fresher fuel is loaded in the internal rings and it is shuffled outwardly in the radial direction after 330 days, at the same time the 10 axial subblocks of fuel are shuffled from [1 2 3 4 5 6 7 8 9 10] into [5 4 3 2 1 10 9 8 7 6]. Nevertheless, in the present studies, we considered only the radial shuffling. While the fresh DF is fixed in composition, the fresh TF is in part made of irradiated (spent) DF; therefore, the TF composition changes with time and it

reaches the equilibrium according to the specific reactor refueling strategy. From a starting point with only DF, in order to arrive at equilibrium conditions with representative mass flows for both driver and transmutation fuels, we adopted a 12-year "fuel strategy" consisting of periodic refueling and shuffling. At the end of the 12th year the reactor is at equilibrium and meaningful mass flow balances can be calculated.

At the startup of operations (year 1), the fresh DF is loaded into the inner ring of 36 hexagonal fuel blocks (white ring on Figure 7.4). Each block is loaded with 10 kg of DF, in the form of $NpPuO_{1.7}$; therefore, the total initial mass of DF is 360 kg. As a consequence of the isotopic ratios in LWRs spent fuel, the set-aside amount of $AmCmO_{1.7}$ after UREX, is 40 kg (Table 7-4).

Table 7-4: Composition of the 40 kg of set-aside $AmCmO_{1.7}$ from UREX which are added to spent DF in the manufacture of the fresh TF.

Isotope	***Atomic percentage %***
^{241}Am	30.35
^{242}Am	0.11
^{243}Am	5.45
^{244}Cm	1.06
^{245}Cm	0.07
^{16}O	62.96

During the first year, the reactor operates just by the inner ring (white ring on Figure 7.4). After the first year, the DF is shuffled into the central ring (gray ring on Figure 7.4) and fresh DF is loaded again into the inner one. During the second year the reactor operates with the 2 internal rings loaded with DF. After the second year, the DF from central ring is moved into the most outer ring (dark-gray ring on Figure 7.4) and the fuel from inner ring takes its place; fresh DF is loaded into the inner ring. Finally, during the third year, the DF fills all the three rings. Each year consists of 330 days of full power operation (600 MW_{th}) and 35 days of outage at zero power, in order to allow the necessary time for refueling and shuffling. At the end of the third year, the spent DF from the outermost ring is reprocessed (Pu and MA extraction) and mixed with the set-aside $AmCmO_{1.7}$ from the initial UREX process to build the fresh TF. At the beginning of the fourth year, both fresh Driver and Transmutation Fuel fill the inner ring, with the ratio of 2 DF pins for each TF pin; the DF, irradiated in the inner ring during the previous year, fills now the central ring; the DF, previously irradiated in the central ring, moves into the outermost ring. Therefore, during the fourth year, the DF is present in all the three rings and the TF just in the inner one. The remaining two years follow the radial shuffling policy of second and third year for both for DF and TF, with the constraint of loading the inner ring with fresh DF and TF.
After the initial 6 years, DF and TF fill all the three rings and the shuffling/refueling scheme is continued, with DF irradiated for three years and reprocessed to produce fresh TF, which ends its life after three years of irradiation. In the present work we limited our studies to the first 12 years since at the 12th year fuel composition reaches the equilibrium.

7.4 APPROACH TO EQUILIBRIUM

During approach to equilibrium, the reactor satisfies the constraints for k_{eff} for most of the time and the equilibrium operation has sufficient reactivity margins (Figure 7.6). Year 5 and 6 show a slight reactivity deficit at the end of the refueling cycle. This can be easily overcome with modifications of the fuel feed or altered refueling strategy.

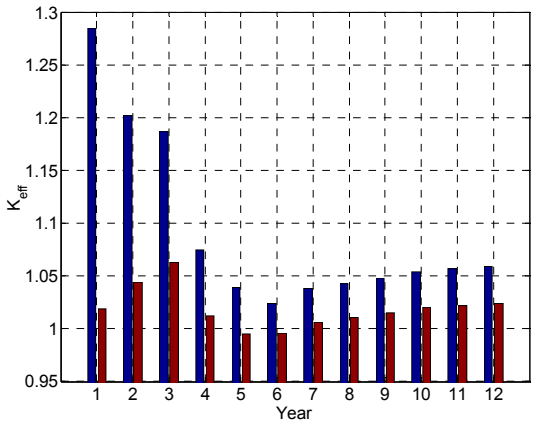

Figure 7.6: Values of k_{eff} at beginning (left columns) and at the end (right columns) of each year. All values have a RSD smaller than 0.04%.

The sharp decrease of the initial k_{eff}, during the first 6 years is due to the net increase of the total amount of capturing isotopes (e.g. fission products, ^{240}Pu, ^{242}Pu and ^{241}Am), since the total amount of irradiated fuel accumulates in the core. At beginning of the fourth year, the initial k_{eff} drops further because TF starts to fuel the reactor.

The increase of the k_{eff} final values, during the first three years, is explained by the loading and shuffling policy. The reactor operates at a constant power, 600 MW; therefore, the power density and flux intensity are very high during the first two years (during the first year all power is generated only in one ring, and during the second year in two rings, which leads to high fluxes). The flux decreases year by year as more rings are fuelled and generate power, therefore decreasing the fuel pin power density. As a consequence of the higher flux, during the first three years we can observe a higher consumption of ^{239}Pu in the DF (Figure 7.7, Figure 7.9 and Figure 7.11). This effect decreases when DF fills all the three rings.

Figure 7.7 shows the evolution of DF concentration in the first ring, Figure 7.8 shows the simultaneous evolution of the TF in the same ring. Similarly, Figure 7.9 and Figure 7.10 illustrate the evolution of driver and transmutation fuel in the central ring, and Figure 7.11 - Figure 7.12 in the external ring.

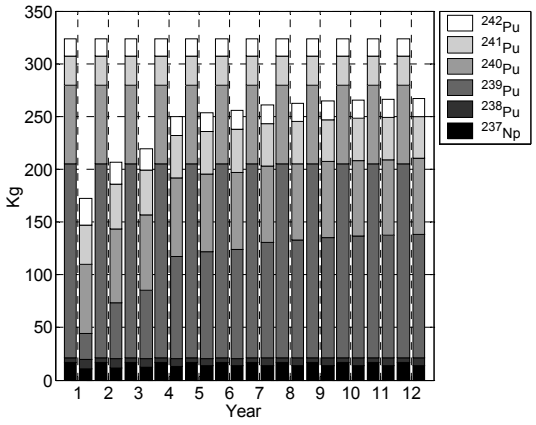

Figure 7.7: Initial (left columns) and final (right columns) mass of Actinides of DF in the inner ring.

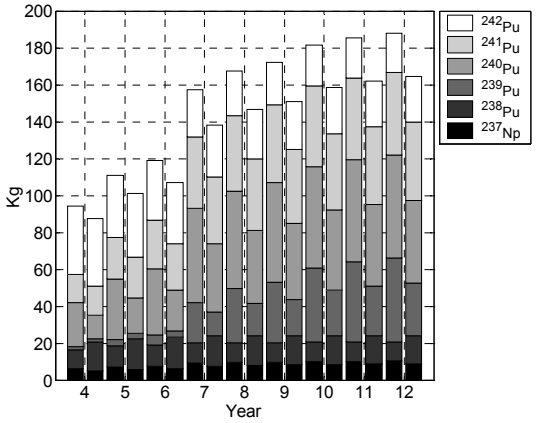

Figure 7.8: Initial (left columns) and final (right columns) mass of Actinides of TF in the inner ring

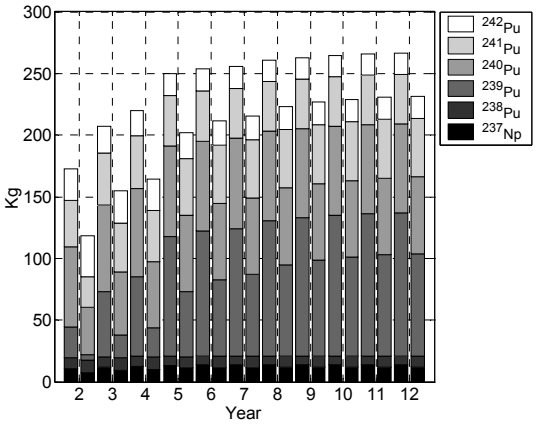

Figure 7.9: Initial (left columns) and final (right columns) mass of Actinides of DF in the central ring.

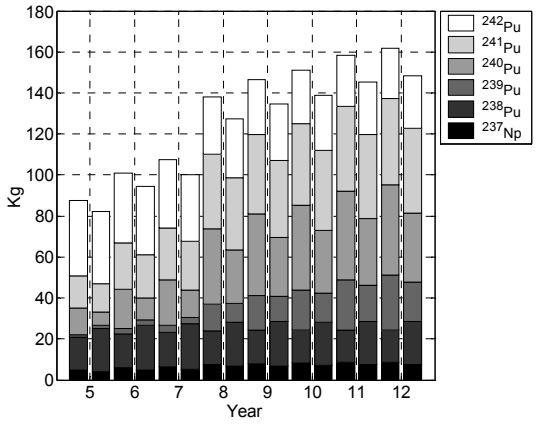

Figure 7.10: Initial (left columns) and final (right columns) mass of Actinides of TF in the central ring.

By comparing Figure 7.8 and Figure 7.9 we see how DF approaches equilibrium at the 6th year whereas the TF does it at the 10th year. For the central ring the equilibrium occurs at the 8th year for DF and at the 11th year for TF, whereas the external ring does at the 10th year for DF. At the end of the 12th year TF composition is not exactly at equilibrium but is quite close. The internal ring approaches faster the equilibrium because its initial composition is constant during all the 12 years, whereas the central and outer rings reach equilibrium at a later stage. The TF is introduced in the reactor only after the 3rd year and it is produced from the spent DF, so it reaches equilibrium with considerable delay comparing to the DF.

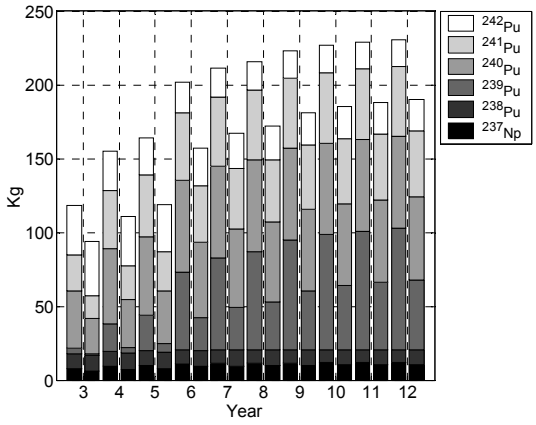

Figure 7.11: Initial (left columns) and final (right columns) mass of Actinides of DF in the outer ring

^{239}Pu is the most abundant isotope of DF just in the inner ring and in the central ring, because in the third ring ^{240}Pu dominates. This remark suggests moving the spent DF first into the outer ring (for one year) and then into the central ring (whereas the policy of the present work moves spent DF first into the central ring and then in the outer one). In fact, with this new policy the neutron flux would be more flatten, since ^{239}Pu would be distributed more homogeneously in the reactor; in fact, at the beginning of the third year the two rings more rich in ^{239}Pu would not be adjacent.

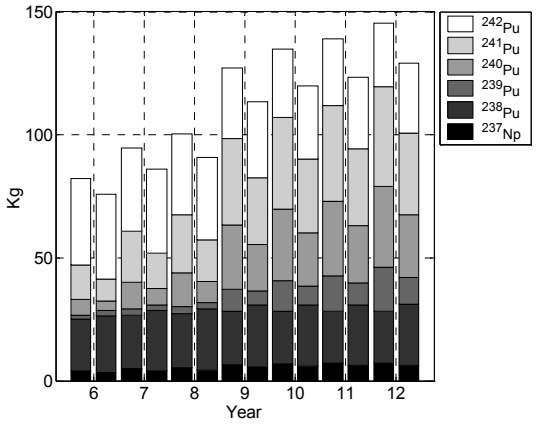

Figure 7.12: Initial (left columns) and final (right columns) mass of Actinides of TF in the outer ring.

A real approach to equilibrium may differ from our studies because of three factors. First, we neglected the representation of the control rods, which may affect the shape of the axial and radial flux profiles as well as the flux spectrum. Second, at the beginning of the 12th year, the TF initial density reached the value of 15.7 g/cm^3 which is much higher than the value for DF (10.2 g/cm^3) Third, we neglected the axial shuffling, which can jeopardize the curvature of neutron flux along the axial direction.

7.5 OPERATION AT EQUILIBRIUM

During equilibrium operation, the yearly balance mass involves: the mass of fresh DF in the inner ring at the beginning of the year, the set-aside Am-Cm after UREX, the mass of fresh TF in the inner ring at the beginning of the year, the mass of spent DF in the outer ring at the end of the year (after three years of irradiation), the mass of spent TF in the outer ring at the end of the year (after three years of irradiation) and the mass of fission products extracted from processing of spent DF.

If we focus our attention to the 12th year, when fuel composition has reached the equilibrium in all the three rings, 74% of ^{239}Pu and 41% of all Pu in the input feed (fresh DF) have been destroyed (fissioned) in the DF irradiation. In the subsequent irradiation of the TF (produced from spent DF) destruction levels are pushed to 94% for ^{239}Pu and 61% for all Pu isotopes. Results compare very favorably with the performance of pure Pu fueled LWRs, which can transmute 93% of ^{239}Pu in 4 years [65].

Figure 7.13 illustrates the destruction of the Pu isotopes at equilibrium. The 3 columns for each isotope describe respectively the amount of the isotopes in fresh DF (input to the reactor), in the spent DF or equivalently in the fresh TF, and in the spent TF, the final residual waste discharged from the reactor. The effective destruction performance at equilibrium is therefore the ratio of the third to the first column for each isotope. The behavior of ^{241}Pu in Figure 7.13 is anomalous, since it accumulates in DF whereas it is burned in TF. In fact, ^{241}Pu of fresh TF is three year old and it starts decaying since it has a half life of 14.3 y. We can note in Figure 7.13 that ^{238}Pu and ^{242}Pu accumulate

instead of decreasing; these are low cross section isotopes. However ^{241}Pu and ^{238}Pu are "short lived" ($T_{1/2}$ = 14.3 and 87.7 years, resp.) from the perspective of long term performance of the geological repository.

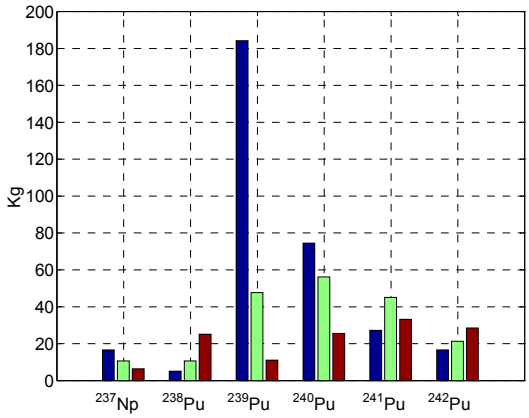

Figure 7.13: Mass of the isotopes in the fresh DF in the inner ring at the beginning of the 12th year (left columns), in the spent DF in the outer ring at the end of the 11th year (middle columns) and residual mass in the spent TF in the outer ring at the end of the 12th year (right columns).

Figure 7.14 describes the mass balance of TF and shows that the concentration of Cm increases. In fact, fresh TF contains 2.7 kg of Cm, whereas the spent TF contains 13.5 kg. ^{244}Cm accumulates due to double absorption of neutrons into ^{242}Pu.None of the Cm isotopes has long-half life and therefore they do pose risk to the geological repository performance especially if they are immobilized in the TRISO-particle fuel. However, Cm may pose problems with reprocessing of spent Driver Fuel and the manufacturing of TF.

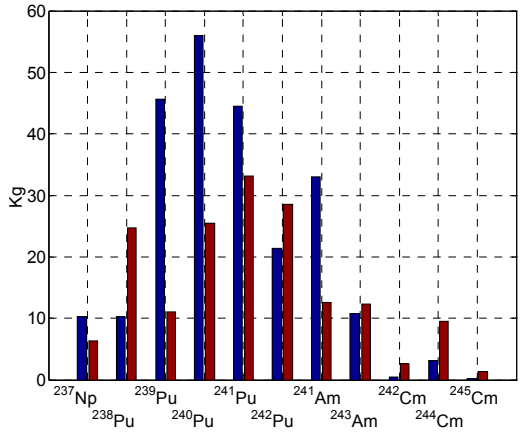

Figure 7.14: Mass of the isotopes in the fresh TF in the inner ring at the beginning of the 12th year (left columns) and residual mass in the spent TF in the outer ring at the end of the 12th year (right columns).

The values of the middle columns in *Figure 7.13* correspond to the left columns of Figure 7.14, since the spent DF in the outer ring at the end of the 11th year is processed to build fresh TF in the inner ring at the beginning of the 12th year.

Figure 7.15 graphically illustrates the overall equilibrium mass balance. From 359 kg of Actinides loaded as fresh DF and set aside Am-Cm, we obtain 180 kg of fission products and 169 kg of Actinides (53% destruction rate), including only 11 kg of ^{239}Pu, mixed with other Pu-isotopes in a composition unusable for nuclear weapons purposes.

The value of the initial mass of fresh TF in Figure 7.15 it is 236 kg; this value is 2 kg lower than the sum of the mass of spent DF in the outer ring at the end of the 12th year (202 kg) and the set aside Am-Cm (36 kg). This discrepancy is explained by the fact that fresh TF in the inner ring at the beginning of the 12th year comes from spent DF in the outer ring at the end of the 11th year (which is 2 kg lower than the mass of spent TF in the outer ring at the end of the 12th year). In fact, Figure 7.12 shows that the mass of spent DF in the outer ring at the end of the 11th year is lower than that one at the 12th year.

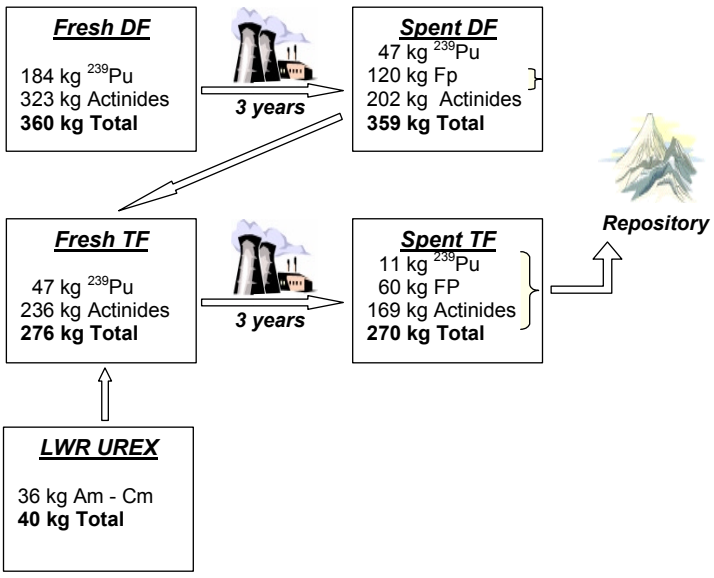

Figure 7.15: Yearly mass flow of one module of the DB-MHR during the 12th year. The total mass takes into account also Oxygen.

7.6 CONCLUSIONS

A detailed simulation of the Deep Burn - Modular Helium Reactor has been performed using 3D Monte Carlo techniques with advanced burnup capabilities. The operation of this reactor was modeled for deep burn of nuclear fuel manufactured from the LWR waste. Deep burn operation requires the use of driver and transmutation fuels. Starting with a fresh reactor core loaded with Actinides coming from the LWR waste, a strategy of reactor refueling and shuffling was simulated until equilibrium was established. We

analyzed in detail the approach to equilibrium and equilibrium operation, which sets after 12 years.

The results of the analysis confirm the viability of the Deep Burn concept for effective destruction of LWRs wastes. k_{eff} evolution with 1 year refueling intervals should guarantee reactor operation with sufficient reactivity margins. Year 5 and 6 indicate a temporary slight shortage of reactivity that can easily be overcome with external means (e.g. slight modification of feed fuel - TF or DF). Equilibrium destruction rates for ^{239}Pu, overall Pu and all Actinides are respectively: 94%, 61% and 53%. The residual waste contains Pu in isotopic composition that does not raise proliferation concerns. Moreover, Am and Np content is significantly reduced by more than 50%. This performance depends on the chosen refueling intervals, and can be significantly improved, if desired. Buildup of ^{238}Pu ($T_{1/2}$ = 87.7 years) and ^{244}Cm ($T_{1/2}$ = 18.1 years) was observed, which requires further studies to investigate if it is necessary an intermediate storage of the spent TF. These are relatively short-lived isotopes that do not contribute to degradation of repository performance and are effectively immobilized within the TRISO-particle residual waste.

8 COMPUTER MODELING OF NUCLEAR FUEL PRODUCTION – PROJECT ALCHYMY

While the industry has over 50 years of experience in the manufacture of fuels for traditional nuclear reactors, there is some controversy over what type of fuel to use in reactors dedicated to transmutation of plutonium and minor actinides. The fuel needs to be possible to manufacture in large quantity, it must exhibit an acceptable degree of chemical, thermal and mechanical stability, it should have good heat conductivity and suitable neutronics, and it should not form significant amounts of activation products.

The choice of material and of manufacturing technology is complicated by the fact that little is known about the chemistry of minor actinides and their compounds, especially at elevated temperatures. It is also hard to produce such data: for instance americium can only be handled in small quantities in highly specialized facilities, with much preparation before the experiment and careful disposal of the products afterwards. To perform a series of experiments on americium, or just plutonium, while systematically varying the conditions is a tremendously complicated task compared to doing the same with common, non-radiotoxic substances.

Some further complications are that the purity of the actinide compounds sometimes is questionable or varies from one experiment to another, and that the tiny scale of the experiment makes measurements inexact. All in all, it is slow, cumbersome, expensive and potentially dangerous work to try out a large number of formulas and conditions in order to arrive at the best method for producing a certain type of minor-actinide fuel.

For these reasons it would be very helpful with a computer model that can give reasonably accurate predictions regarding reactions and products under varying conditions. It would be too optimistic to expect complete correspondence between the model and reality since even a very complex model could not take into consideration all the non-ideal properties of a real system, but even if the model would serve only to weed out the least promising experimental setups, or to hint in what region to look for an optimum, it would save large amounts of work, time and money.

The work was started as early as October 2000 by Marco Streit of PSI, Switzerland. The model was to be run in the thermochemical software package Thermo-Calc (<http://www.thermocalc.se/>) and took the form of a "database", or a library of the relevant thermochemical properties of a large number of compounds. One central element is the Gibbs energy as a function of temperature, for each compound in (ideally) each of its stable phases, expressed as a polynom and written in a specific notation. The initial selection of compounds was centered on modelling of the carbo-reduction of the dioxides in a nitrogen atmosphere, forming plutonium nitride in solid solution with zirconium nitride.

There are a few public and many commercial databases available for use with Thermo-Calc. They are often specialized for particular fields of study, like metallurgy, semiconductors or aqueous chemistry, and there even exist databases for conventional nuclear materials, but those lack data on nitrides and minor actinides and therefore were of no use for us. Apart from that, and apparently for business reasons, the functions in

the commercial databases tend to lack references and thus it is hard to estimate their reliability. They are also known to contain rare but large errors.

The principle of Thermo-Calc is to calculate the state that yields the lowest Gibbs free energy for the entire system. The types and amounts of chemicals including the atmosphere in the system, the starting temperature, and optionally the amount heat added to the system, are defined, whereupon the software takes apart all molecules into their constituent atoms, figuratively speaking, and finds the energetically most favorable way to put them together again. This composition and the corresponding temperature are reported as the conditions at equilibrium.

The objective of this project is to develop the simulation program and the corresponding data basis to easily usable and reliable format. All functions were calculated anew from published data or critically evaluated and selected from public compilations. Special care was taken to eliminate the discontinuities at transition temperatures that sometimes prevented the calculations from converging. The library of functions was enlarged with new elements and compounds. Many of the new compounds were introduced only to provide possible contaminants or by-products; the computer model can not predict the unwanted or unexpected formation of a substance that isn't described in the database.

The hydrogen-methane-ammonia system (with possible by-products) was included to enable calculations on models including a decarburization step. The formation of compound phases remains largely ignored and all compounds in solid and liquid solutions are assumed to have the same activity as they would have as a pure substance, which obviously is a simplification.

After half a year of development, in its present incarnation under the name "ALCHYMY", v.1.0, the database includes all the data necessary to model the production of nitride fuels containing not only zirconium and plutonium, but also neptunium and americium. It appears quite stable and yields unambiguous results for any reasonable combination of starting parameters.

The database is, in itself, not sufficient to answer questions about fuel production. It contains the universally valid thermochemical properties of the components, but not the particular properties of the system under study. The system can be defined by manually entering every parameter - the chemical species involved, amounts, temperature, restrictions, output format et c - but since one rarely varies all properties at once, it is much more convenient to define most of the system in an executable script and have the software prompt for the one or two variables, which often are the temperature and/or the added enthalpy (heat).

Two main types of models have been used, defined in two types of scripts: sealed vessel ("bottle") or gas-flow furnace ("pipe"). The "bottle" model is by far the simplest, with a fixed content and no gas-exchange but unrestricted heat-exchange with the surroundings (the system remains at a pre-defined temperature). Gas exchange can be simulated in this model by making the gas phase very large, leading to a high degree of dilution of gaseous reaction products. An advantage of this model is that one can keep tally of exactly what is formed during the reaction, even the smallest trace amounts, since all material is retained.

The "pipe" model utilizes the undeservedly forgotten REACTOR module for Thermo-Calc (http://www.thermocalc.se/download/pdf/TC-PI-Matlab.pdf) that was developed

in 2000 but never released in a quite finished version or used for anything except demonstration. (Despite its name, this module has nothing to do with nuclear reactors, but is intended to emulate a chemical reactor.) "Pipe" is a relatively complicated, iterative model where the materials are carried through a number of stages (in our experiments typically ten) under sequential addition of heat and optionally addition and/or removal of gasses. New thermochemical equilibrium is calculated at each stage, whereupon the products move on to the next stage, with or without exchange of the gas phase. This rather well simulates the conditions in a furnace with a flow of hot gas through it, such as is used in the nitride experiments at e.g. PSI. The "pipe" model is the more realistic one from many viewpoints: it allows the temperature to increase gradually, it prevents the back-reaction of previously formed carbon oxides to form carbides, it illustrates the loss by evaporation of volatile actinides, especially americium, and it keeps the composition of the gas phase constant.

We plan to publish the database together with a number of calculations, performed both as a demonstration of the method and for their practical value. These calculations are in progress and should be finished before the end of January. As an example, preliminary results suggest that it is quite possible, from a thermochemical viewpoint, to produce a Zr-Pu-Np-Am nitride of extreme (100 %) purity with insignificant evaporation (0.04 %) of americium and an overall yield of 99.98 %.

One must of course keep in mind that we never can expect full match of results in reality, because of imperfect contact between graphite and oxide particles, limited diffusion of gas into solids, finite reaction times, solution and inclusion of one material in another, losses in transfer between vessels, the tendency of many actinide compounds towards non-stoichiometric composition, side reactions with container materials et c, but the results from the computer model show what is thermodynamically possible. In the above-mentioned case, it indicates that the often observed problems with incomplete reduction of oxides and formation of carbon/carbide contaminants aren't "necessary", that they could probably, or at least in theory, be overcome by using finer powders, longer reaction times or otherwise improved methods. If, in some other case, the model reports that a contaminant appears at certain conditions, or that the reaction doesn't go to completion, it may be pointless to try to refine the method by such measures, since, assuming that the model is correct, it is thermodynamically impossible to arrive at the desired result. The difference between these two cases is of great interest to the practical experimenter.

9 NUCLEAR DATA LIBRARIES FOR ADS CALCULATIONS

The nuclear data libraries for Monte Carlo stationary and MCB-burnup calculations have been updated during 2002. To the existing, temperature dependent data libraries created at KTH:

- ENDF/B6 version 8
- JENDL version 3.2
- JEF version 2.2
- EAF version 99

Two other libraries have been added:

- JENDL version 3.3
- JEF version 3.0

This vast amount of data gives a unique opportunity for the users to perform state-of-the art simulations both for k_{eff} calculations and burnup evolution.

Neutron and proton cross-section evaluations for ^{232}Th, ^{238}U and ^{239}Pu for energy range up to 150 MeV prepared at KTH in collaboration with IPPE in Obninsk have been also updated – see Appendix 6. Other isotopes of plutonium and amercium data files are under preparation.

10 SEMINARS, CONFERENCES AND INTERNATIONAL INTERACTIONS

Waclaw Gudowski participated in

- European meetings:
  - Meeting of the Contact Expert Group on Transmutation Projects, Karlsruhe, (February 2002)
  - MUSE project meetings in Brussels (March 2002) and Cadarache (May 2002)
  - ADOPT network meeting in Obrigheim (September 2002) and in Brussels (December 2002)
  - BASTRA cluster meeting in Uppsala (September 2002)
  - MOST network, Karlsruhe (September 2002)
  - XADS – meeting in Paris (September 2002)
- The Biennial Topical Meeting of the Radiation Protection and Shielding Division(RPDS) of the American Nuclear Society(ANS), Santa Fe, New Mexico, USA, 14-18 April 2002 (invited)
- SAD experiment meeting in Dubna (April 2002)
- The 21st Conference of the Israel Nuclear Societies, May 22-23, 2002—Haifa, Israel (invited speaker)
- Technical University of Prague, lecturing (May 2002)
- Trade-project proposal meeting, Rome (June, 2002)
- Spallation Target #559 meeting in Las Vegas (July 2002)
- Frederic Joliot Otto Hahn Summer School in Reactor Physics and Transmutation – lecturer, Cadarache (August 2002)

Janne Wallenius:

- EU meetings:
  - SPIRE-meeting in Paris (February, 2002)
  - CONFIRM-meeting at Paul Scherer Institute, (April, 2002)
  - FUTURE- meeting in Cadarache (May 2002)
  - SPIRE-meeting in Mol (June 2002)
  - TETRA-meeting in Karlsruhe, FZK, (September 2002)
  - FUETRA-meeting in Obrigheim, (September 2002)
  - ERMT-conference in Karlsruhe (invited speaker) (September 2002)
  - SPIRE-meeting at PSI (October 2002)
  - CONFIRM-meeting in Cadarache (November 2002)
- NEA-conference at Jeju, Korea, (November 2002)

- IMF-conference im Tokaimura, Japan, (November 2002)

Jerzy Cetnar:

- XADS – meeting in Paris (September 2002)
- XADS – meeting in Cadarache (October 2002)

Mikael Jolkkonen:

- Collaborative meeting, PSI, Villingen (June 2002)
- Visit at Minor Actinide Lab. at ITU (September 2002)
- ERMT-II seminar , ITU (September 2002)
- Confirm meeting in Cadarache (October 2002)

Marcus Ericsson:

- Study visit at Forschungszentrum Karlsruhe (January, 2002)

Per Seltborg

- Frederic Joliot Otto Hahn Summer School in Reactor Physcis and Transmutation – lecturer, Cadarache (August 2002)

Daniel Westlén

- Frederic Joliot Otto Hahn Summer School in Reactor Physcis and Transmutation – lecturer, Cadarache (August 2002)
- High Temperature Reactor Course, Cadarache, (November 2002)
- MCNPX Training course, Mol, Belgium (November 2002)

Guest researchers and scientific exchange:

Dr. A. Polanski, JINR-Dubna, March 2002. Seminars on SAD-project

Prof. Karel Matejka, Jan Rataj and Dusan Kobylka, Technical University of Prague. Seminar: "Czech Republic and Nuclear Energy"

Prof. E. Avrorin, Russian Federal Nuclear Center-VNIITF, September 2002.
Seminars:
"New aspects of non-proliferation policy of the Russian Republic. From political decisions to technical verifications",
"A role of ISTC in transformation of Russian weapon research and development into civilian activities. Future of nuclear power in Russia"

J. Lepponen, graduate student at VTI-Finland, reading transmutation course and comparison studies of burnup code.

Drs Greg van Tuyle and Kemal Pasamehmetoglu from Los Alamos National Laboratory. February 2001.

Dr. Alexander Polanski, Joint Institute of Nuclear Research. February-March 2001

Dr. Nikolai Sobolevski, Russian Academy of Sciences, April 2001.

11 REFERENCES

[1] Wallenius J., et al.: Application of burnable absorbers in an accelerator driven system, Nuclear Science and Engineering 137 (2001) 96

[2] Gudowski W., et al.: System and safety studies of accelerator driven transmutation, SKB Annual report 2001, R-02-25, 2002

[3] Laurie S. Waters, Editor, MCNPX Users's Manual, TPO-E83-G-UG-X-00001, LANL, 1999.

[4] M. Eriksson, J. Wallenius, J. E. Cahalan, K. Tucek, and W. Gudowski, "Safety Analysis of Na and Pb-Bi Coolants in Response to Beam Instabilities," 3rd Int. Workshop on Utilisation and Reliability of High Power Proton Accelerators, Santa Fe, May 12-16, 2002.

[5] T. Takizuka et al., Studies on accelerator-driven transmutation systems, Proc. 5th information exchange meeting on actinide and fission product partitioning and transmutation, EUR 18898 EN, OECD/NEA 1998.

[6] J. E. Cahalan, A. M. Tentner, and E. E. Morris, "Advanced LMR Safety Anlaysis Capabilities in the SASSYS-1 and SAS4A Computer Codes," Proc. of the International Topical Meeting on Advanced Reactors Safety, Pittsburgh, April 17-21, 1994.

[7] E. H. P. Cordfunke, R. J. M. Konings, G. Prins, P. E. Potter, and M. H. Rand, "Thermochemical Data for Reactor Materials and Fission Products," Elsevier Science, Amsterdam, 1990.

[8] J. J. Katz, G. T. Seaborg, L. R. Morss, The Chemistry of actinide elements, 2nd Ed., Vol. 1 and 2, Chapman and Hall, London, 1986.

[9] Hunter, C. W., Fish, R. L., Holmes, J. J., 1975. Mechanical properties of unirradiated fast reactor cladding during simulated overpower transients. *Nucl. Technol.* 27(3), pp. 376-388 (Nov 1975).

[10] H. S. Khalil and R. N. Hill, "Evaluation of Liquid-Metal Reactor Design Options for Reduction of Sodium Void Worth," *Nucl. Sci. Eng*., 109, 221-266 (1991).

[11] D. G. Cacuci, "On Perturbation Theory and Reactor Kinetics: From Wigner's Pile Period to Accelerator Driven Ssystems," PHYSOR 2002, Seoul, Korea, Oct. 7-10, 2002.

[12] H. Henryson II, B. J. Toppel, and C. G. Stenberg, "MC^2-2: A Code to Calculate Fast Neutron Spectra and Multigroup Cross Sections," ANL-8144, Argonne National Laboratory (1976).

[13] B. C. Na, P. Wydler, and H. Takano, "Comparison Calculations for an Accelerator-driven Minor Actinide Burner," OECD/NEA, NEA/NSC/DOC(2001)13.

[14] M. Eriksson et al, Proc. 3rd Int. Workshop on Utilisation and Reliability of High Power Proton Accelerators, Santa Fe, 2002.

[15] F. Garner, M.B. Toloczko and B.H. Sencer, J. Nuc. Mat. 276 (2000) 123.

[16] H. Murata and T. Mukaiyama, Atomkernergie-Kerntechnik 45 (1984) 23.

[17] NEA/NSC/DOC(2001)13, OECD/NEA (2001).

[18] M. Salvatores, Nucl. Inst. Meth. A 414 (1997) 5.

[19] P. Seltborg et al, submitted to Nucl. Sci. Eng. (2002).

[20] T. Takizuka et al, Proc. 5th IEM, EUR 18898 EN, page 383, OECD/NEA (1999).

[21] J. Wallenius, J. Nucl. Mat., accepted for publication (2002).

[22] D.J.Bacon, A.F.Calder and F.Gao, J. Nucl. Mat. 251 (1997) 1

[23] A. F.Calder and D.J Bacon, J. Nucl. Mat. 207 (1993) 25

[24] E. Little and D. Stow, J. Nucl. Mat. , 25 (1979)

[25] D. Farkas, C.G.Schon, M.S.F.de Lima and H. Goldstein, Acta mater. 44 (1996) 409

[26] F. A. Garner, M. B. Toloczko and B. H. Senser, J. Nucl. Mat. 283-287 (2000) 168

[27] S. I. Golubov, B. N. Singh and T. Trinkaus, J. Nucl. Mat. 276 (2000) 78

[28] G. Simonelli, R. Pasianot and E.J.Savino, Mat.Res.Soc.Symp.Proc 291 (1993) 567

[29] R. E. Stoller, G. R. Odette, B. D. Wirth, J. Nucl. Mat. 251 (1997) 49

[30] A.F. Voter in Intermetalic Compounds, vol 1, Principles, Editors J.H.Westbrook and R.L. Fleisher, John Wiley & Sons, 1995

[31] C.H.Woo and B.N.Singh, Phil. Mag. A65 (1992) 889

[32] R D W Bestwick, R E Sunderland, G Rimpault, P T Leon "Specification of the core and fuel element design for the gas-cooled XADS, PDS-XADS Work Package 4.2 Deliverable D3"

[33] "Gas cooled system Remontage (Status 04/02)" Min 02/136, FANP-SAS

[34] ANSALDO ADS 1 SIFX 0500 "XADS Pb-Bi Cooled Experimental Accelerator Driven System – Reference Configuration: Summary Report".

[35] N. Stone et al., "A Dual Spectrum Core for ATW-Preliminary Feasibility Study", PHYSOR 2000.

[36] "WP 4.2 Minutes of Technical Meeting" held in Paris on 1st October 2002, identified MIN 02/160

[37] C. H. M. Broeders, private communication.

[38] J. Cetnar, W. Gudowski and J. Wallenius, " MCB: A continuous energy Monte Carlo Burnup simulation code", In "Actinide and Fission Product Partitioning and Transmutation", EUR 18898 EN, OECD/NEA (1999) 523.

[39] A. Baxter, C. Rodriguez and F. Venneri., Deep burn MHR/A-based transmutation of nuclear waste, Framatom presentation, Paris, 2001.

[40] A. Baxter and M. Fikani, Reactor-based transmutation – physics studies of the gas-cooled graphite-moderated deep burn reactor, GA-501-0-TRT-000140, 2002.

[41] K. Ohashi, F. Okamoto and H. Hayakawa, Modular High temperature reactor contributing the global environmental protection, Progress in Nuclear Energy 37, pp. 307-312, 2000.

[42] A.I. Kiryushin, N.G. Kodochigov, N.G. Kouzavkov et al., Project of the GT-MHR high temperature helium reactor with gas turbine, Nuclear Engineering 173, pp.119-129, 1997.

[43] A. Baxter and C. Rodriguez, The application of gas-cooled reactor technologies to the transmutation of nuclear waste, Progress in Nuclear Energy 38, pp. 81-105, 2001.

[44] M.B. Richards, A preferred RAPD-based strategy for permanent disposal of commercial LWR spent nuclear fuel, Energy 20, pp. 811-822, 1995.

[45] A. Chudin, Potential for power utilization of weapons-grade plutonium in GT-MHR nuclear reactors, OECD meeting on Survey on basic studies in the field of high temperature engineering, Paris, pp. 79-88, 1999.

[46] M.P. Labar and W.A. Simon, Comparative economics of the GT-MHR and power generation alternatives, GA-A 21722, General Atomics, 1994.

[47] IANIS version 1.0. Jef-2.2.

[48] Nakagawa, Saikusa and Kunitomi, Development of a simulation model and safety evaluation for a depressurization accident without SCRAM in an advanced HTGR, Nuclear Technology 133, 2001.

[49] H. Nabielek, W. Schenk, W. Heit, A.W. Mehner and D.T. Goodin, The performance of HTR fuel particles at extreme temperatures, Nuclear Technology 84, pp. 62-81, 1989.

[50] H. Nickel, H. Nabielek et al., Long time experience with the development of HTR fuel elements in Germany, Nuclear Engineering 217, pp. 141-151, 2002.

[51] K. Fukuda, S, Kashimura, T. Tobita and T. Kikuchi, Irradiation behavior of HTGR coated particle fuel at abnormally high temperature, Nuclear Engineering and Design 157, pp. 221-230, 1995.

[52] K. Minato, T. Ogawa et al., Release behavior of metallic fission products from HTGR fuel particles at 1600 and 1900 oC, Jurnal of Nuclear Materials 202, pp.47-53, 1993.

[53] K. Minato, K. Sawa et al., Fission product release behaviour of individual coated fuel particles for HTGR, Nuclear Technology 131, 2000.

[54] D.A. Petti, J. Buongiorno, J.T. Maki and G.K. Miller, Key differences in the fabrication of US and German TRISO-coated particle fuel, and their implications on fuel performances, Conference on HTGR, Petten, Netherlands, 2002.

[55] G.K. Miller, D.A. Petti, D.J. Varacalle and J.T. Maki, Consideration of the effects on fuel particle behavior from shrinkage cracks in the inner pyrocarbon layer, Journal of Nuclear Materials 295, pp.205-212, 2001.

[56] K. Minato, T. Ogawa, K. Fukuda, H. Sekino, I. Kitagawa and N. Mita, Fission product release from Zr-coated fuel particles during post-irradiation heating at 1800 and 2000 oC, Journal of Nuclear Materials 249, pp.

[57] W. Fröhling, Courses and limitations of damage with air ingress accidents in HTR modules, OECD meeting on Survey on basic studies in the field of high temperature engineering, Paris, pp. 173-181, 1999.

[58] K. Kugeler and P.W. Phlippen, Aspects of inherent safety of future high temperature reactors, OECD meeting on Survey on basic studies in the field of high temperature engineering, Paris, pp. 29-39, 1999.

[59] W. Schenk, W. Fröhling, R. Moormann, H. Nabielek, Simulation of air ingress with irradiated fuel samples, Meeting on validation of predictive methods for fuel and fisson product behavior in gas-cooled reactors, Tokai, JAERI, 1994.

[60] S. Nakagawa, A. Saikusa and K. Kunitomi, Development of a simulation model and safety evaluation for a depresurization accident without reactor scram in an advanced HTGR, Nuclear Technology, 133, 2001.

[61] W.J. Gray, Radioactive Waste Management and the Nuclear Fuel Cycle 3, 137, 1982.

[62] V. Knobloch and L. Nachmilner, High level radioactive waste management, Annual conference of the ANS, 1994.

[63] US National Accademy of Sciences, Technical basis for Yucca mountain standards, National Academy Press, Washington, DC, 1995.

[64] http://nucleardata.nuclear.lu.se/nucleardata/toi.

[65] J.M. Paratte and R. Chawla, On the feasibility of LWR plutonium fuels without uranium, Annals of Nuclear Energy 22, pp. 471-481, 1995.

APPENDICES

APPENDIX 1

W. Gudowski, Accelerator-Driven Transmutation of Nuclear Wastes – an Experimental Path to a Demonstration Facility, Proc. of The Biennial Topical Meeting of the Radiation Protection and Shielding Division(RPDS) of the American Nuclear Society(ANS), Santa Fe, New Mexico, USA, 14-18 April 2002

Accelerator-Driven Transmutation of Nuclear Wastes – an Experimental Path to a Demonstration Facility

Waclaw Gudowski
Dept. Nuclear and Reactor Physics,
Royal Institute of Technology
Stockholm Center for Physics, Astronomy and Biotechnology
S - 106 91 Stockholm
Sweden
tel. +46 8 55 37 82 00
E-mail: wacek@neutron.kth.se

SUMMARY

Last 10 year of research on Accelerator-Driven Transmutation of Nuclear Wastes (ATW) waked up expectations to design a nuclear system capable to effectively "burn" or "incinerate" most of the radiotoxic isotopes in spent nuclear fuel and thereby reducing burden to underground repositories. A subcritical mode of operation of ATW gives more control and flexibility in the design and operation compared to dedicated critical burner reactors. However, coupling a high power accelerator with a subcritical nuclear reactor opens a whole new class of difficult scientific and engineering problems, which have to be resolved before a commercial ATW facility can be constructed. To address these problems it is necessary to develop simulation tools and to perform series of basic and integral experiments proving the feasibility of ATW-ideas. This paper reviews some projects focused on development and benchmarking of simulation tools integrating high-energy particle transport, neutron transport and burnup calculations. A possible experimental path leading to construction of an ATW demonstration facility is also sketched in this paper.

I. BACKGROUND

There is no "universal " ATW system, the choice of specific mission for ATW and consequently technical solutions depend very strongly on the nuclear fuel cycle into which ATW system should be incorporated. A very different role for ATW has been envisioned in the nuclear fuel cycle with Pu-recycling like French and Japanese "double-strata" fuel cycle compared to ATW incorporated into originally "once-through" fuel cycle. For a modified "once-through" fuel cycle a concept of "Single-" or "Dual-Tier" approach is now commonly used.

In the transmutation scenario there are two options. The waste can either be recycled and transmuted in available conventional critical reactors (homogenous fuel recycle option, with no separation of plutonium and minor actinides), or in dedicated burner reactors or sub-critical ATWs. This option is envisioned in a Single-Tier approach. In the double strata or "Dual-Tier" fuel cycle option, plutonium is kept separated from the minor actinides and 5 to 20% of dedicated burner reactors in the reactor "park" would be required. If plutonium and the minor actinides are kept together, the fraction of dedicated burner reactors would be approximately 20%.

Sub-critical ATWs are not the only option for dedicated transmutation systems. Critical reactors may also be designed and constructed as transmuters (burners, incinerators). Critical reactors, however, loaded with dedicated transmutation fuel containing large amounts of Minor Actinides (MA) pose significant safety problems caused by unfavourable reactivity coefficients and small delayed neutron fraction. In this context ATWs have clearly advantages over critical reactors allowing accommodation of fuel with high concentration of MA, relaxing requirements on safety margins determined by delayed neutron fraction and use of uranium free fuels ensuring the highest possible incineration of transuranium isotopes. ATWs bring, however, new problems into the nuclear technologies related to coupling of an accelerator with a subcritical reactor – the spallation target window becomes one of the most critical constructional problems and instability of an accelerator beam become an important disadvantage.

Important activities relevant for development of ATW ideas are going on or are planned in Europe including many projects in Russia, USA, Japan, and Korea.

European activities supported and coordinated in most cases in the frame of research framework

program of European Union (so called 5th FP) involve more than 50 organisations with a total budget of 50 M€ over the years 2000-2003. Those projects cover a large field important for ATW – from basic nuclear and material data, Pb/Bi technology, spallation target design, reprocessing chemistry, integral experiments and finally designing a demonstration ATW facility (in Europe more popular acronym for Accelerator Driven Systems is ADS, in principle a full synonym of ATW). European Commission is responsible for co-funding of these projects and is conducting a very active policy to harmonize the projects. An independent from European Commission group of experts organized in so called European Technical Working Group on ADS prepared a report "A European Roadmap for Developing Accelerator Accelerator Driven Systems (ADS) for Nuclear Waste Incineration" [3] sketching an optimal path to build an ADS experimental facility within 12 -15 years. A final goal of the Roadmap was to identify possible synergies that ADS development could have within the scientific community, indicate potential spin-offs and to show how competence can be maintained in the currently stagnating field of nuclear energy research.

In Russia, International Science and Technology Centre (ISTC) is funding and supervising a number of ATW-related projects covering also a broad spectrum of activities from a large number of nuclear data projects, through a high power spallation target construction to integral subcritical experiments.

In Japan a project carried out jointly by JAERI and KEK for a high intensity proton accelerator construction has been approved. In six years a 400 MeV linear accelerator, a 3 GeV proton synchrotron with a power rating of 1 MW, a 50 GeV proton synchrotron with a power rating of 0.75

MW, and a 1 MW spallation neutron source facility will be constructed. In the second phase an ATW facility is foreseen with the linear accelerator as a driver.

The US ATW program will be hopefully presented in details during this conference. It is however worth to note that ATW activities, which re-started in USA for about 13 years ago have evolved from "accelerator-driven" focus to more "an advanced nuclear fuel cycle" oriented activities.

It not an ambition of this paper to describe or review all the important ATW projects conducted all over the world. In the next chapter there will be given a leading thread through a selected number of projects and activities which may push forward the ATW-development.

II. COMPONENTS OF ATW

Even if there is no "universal" ATW system, each design has to provide solutions for the "universal" components of ATW:

Accelerator
Spallation target
Subcrtical core with a specified fuel/coolant system
Reprocessing chemistry

Moreover, some basic nuclear and material data have to be provided and validated in order to have a reliable and cost effective conceptual design of ATW demonstrator.

A. Accelerator

Linear or cyclotron accelerators have been proposed for ATW. In spite of a vivid discussion in the accelerator community [4] the final choice of an accelerator type will depend on an intercomparison and complex optimisation of the whole ATW including economical constraints and probably also local traditions of research groups, which will succeed to build the first demonstration facility. The optimal parameters of the accelerator are relatively easy to estimate, there are driven by two physical parameters: i) the neutron yield rate per proton and per unit of energy in the target and ii) the fraction of beam energy deposited in the entrance window of the target. For optimal neutron production proton energy should be equal to or higher than 1 GeV. The second parameter, for proton energies lower than few GeV, is a rapidly decreasing function of the beam energy. Proton current would depend on desired beam power, which for a demonstration facility would be in the limit of 5 – 10 MW, corresponding to 5 – 10 mA of protons.

However, it may be of economical interest to choose for the first demonstration facility an accelerator design from the "shelf" and consider proton energies between 400 to 800 MeV.

For the time being there is no specifically large efforts to design and construct a dedicated accelerator for ATW and particularly after a closure of the US APT project the ATW community has to rely on synergetic efforts together with neutron scattering and particle physics communities. It may however require significant compromises concerning the mode the accelerator operation (continuous vs pulsed) and its reliability.

The Korean ATW project is partially driven by the linear accelerator development – a KOMAC-project [5].
In Europe, an accelerator development package has been incorporated into the EU-project XADS with the following objectives:

- Choice of the accelerator type and beam transport line up to the spallation target based on the specific ATW requirements.
- Definition of the ATW-class accelerator characteristics such as reliability, availability, stability and reproducibility of power control and maintainability.
- Assessment of R&D needed for performance and cost optimisation on accelerator components critical to the ADS-class characteristics.
- The choice for a reference accelerator and the beam transport including the medium to long-term extrapolation from a demonstrator to an industrial machine.

In spite of a traditional European interest in cyclotron accelerators it seems now that the European accelerator research community is more interested in developing a linear accelerator for ADS rather than to find an acceptable and economical design for a cyclotron.
It is also interesting to note that in the Belgian Myrrha project – hopefully reported on this conference – a combined ATW demonstrator and commercial isotope producer it is foreseen to use an "almost" commercial cyclotron delivering 350 MeV, 5 mA of protons.

B. Spallation target

A very significant progress has been achieved in the last few years in the field of the high power spallation target technology.
1 MW liquid Pb/Bi eutectic spallation target project - see Figures 1 and 2, funded by the ISTC in Moscow, has been manufactured at the Institute of Physics and Power Engineering in Obninsk, Russia and successfully passed extensive thermal hydraulic tests. The original idea was that this target, when manufactured and transported to USA, should be irradiated at the Los Alamos accelerator beam stop. To fit to the geometrical constraints of the LANSCE beam stop the design was rather odd and difficult with a drainage tank above the spallation target module and wit a very tight thermal hydraulic circuits [6].

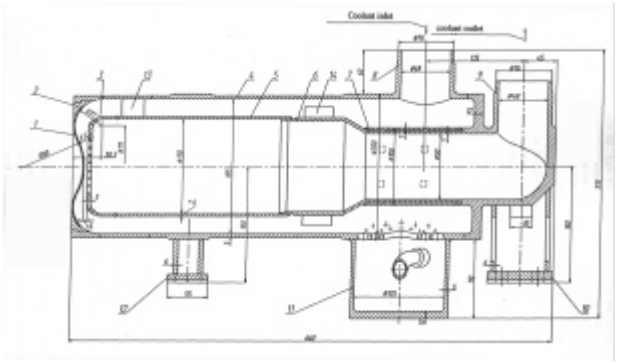

Figure 1. The 1 MW spallation target module. Main components of the target: 1 - window, 2 - window support, 3 - diffuser plate, 4 - target hull, 5 - inner channel.

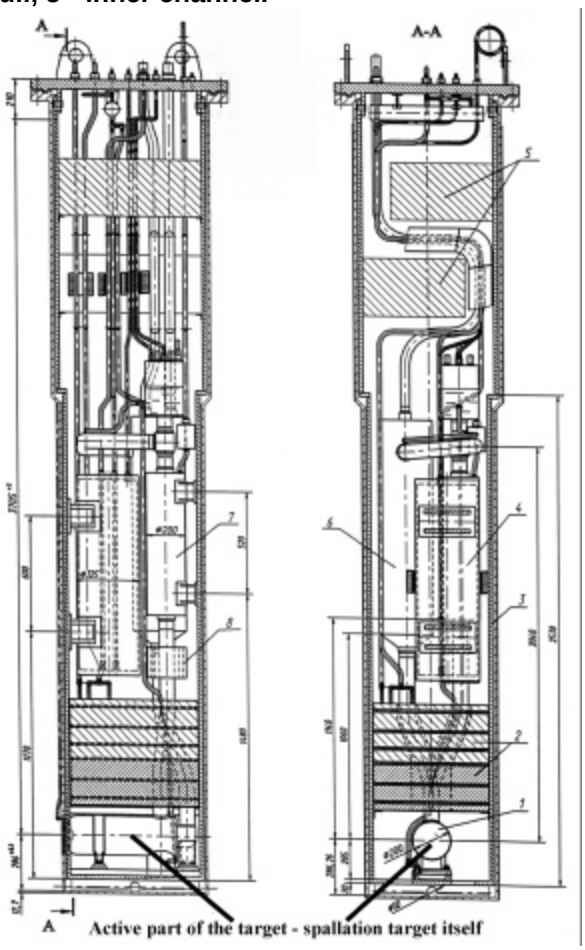

Figure 2. The whole 4m high setup of the 1 MW spallation target with all the auxiliary equipment: 1 - spallation target itself, 2 - radiation shielding, 3 – steel containment, 4 - drainage tank, 5 -support structure, 6 - heat exchanger, 7 - MHD-pump, 8 - flow rate meter.

Unfortunately, Los Alamos Laboratory is not able today to ensure funds and licensing of the target irradiation experiment and the first 1 MW liquid metal spallation target ever fabricated is waiting for its final destiny.
In spite of an unclear future for this target, it has to be stated that this project played an important role in dissemination of know-how in liquid heavy metal technology and stimulated very visibly interest for liquid Pb/Bi as a coolant as well as the spallation medium.
The European project MEGAPIE (Megawatt Pilot Experiment) carried out by a partnership of laboratories interested in ATW technology, will construct a Pb-Bi target to be irradiated as a pure spallation source by the 590 MeV, 1.8 mA proton beam of the Paul Scherer Institute.The target design uses a window for which the highest irradiation dose will be of the order of 10 dpa in the 6 months of the actual experiment planned for 2005.
The MYRRHA project, conducts an experimental program developing a windowless Pb-Bi spallation target. This challenging windowless design had been chosen a consequence of the 350 MeV accelerator choice. At this proton energy a spallation target window would be exposed to extreme and hardly manageable radiation damages.

ATW projects will definitely benefit from the experiences of the mercury spallation target development for the Spallation Neutron Source – SNS.

C. Subcrtical core with a specified fuel/coolant system

While many research groups are working on the optimal choices of the fuel/coolant for the subcritical cores few experiments have been already launched in order to examine in details physics of the subcritical systems. In absence of the suitable accelerators at the sites licensed for experiments with multiplying piles, some interesting experiment with subcritical systems driven with en intense neutron generator are being performed.

1. MUSE experiment.

In MUSE experiment at CEA/Cadarache [7] the high intensity pulsed neutron generator GENEPI [8] was coupled with a subcritical configuration of the MASURCA reactor – Figures 3 and 4.. A 250 keV deuteron beam impinging either a deuterium target or a tritium target, creates a neutron source with two different neutron spectra.
The main goals of the MUSE experiments are to:

- define sub-critical experimental configurations of interest in terms of fuel, coolant, geometric arrangement, external source type and operating modes (pseudo-continuous and/or pulsed modes);
- experimentally characterise these configurations, in terms of neutron flux level and neutron spectra, by integral experiments

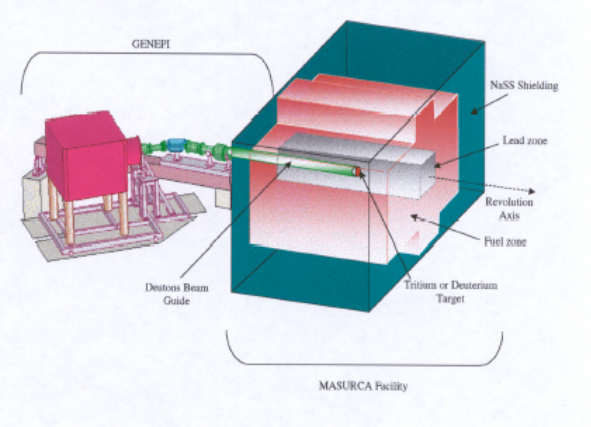

Figure 3. Schematic view of MUSE - the GENEPI-MASURCA coupling.

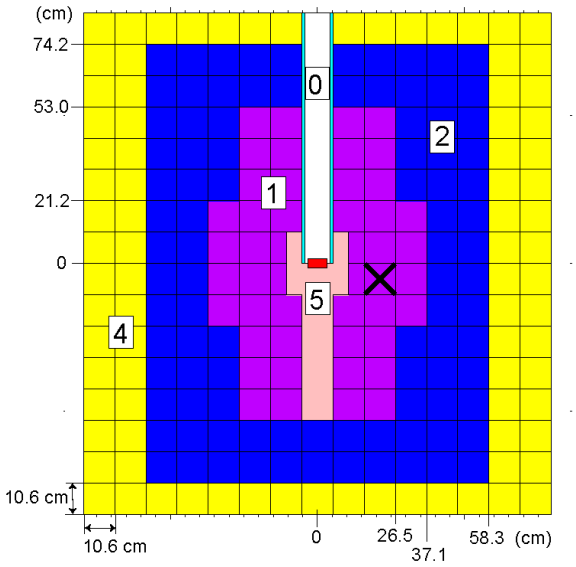

Figure 4. x-y cross-sectional view of the calculational model of the MUSE-4 sub-critical configuration. 0 - Accelerator Tube; 1 – Subcritical Core (MOX fuel with 72% ^{238}U, 21% ^{239}Pu and 5% ^{240}Pu plus small amounts of some other actinides); 2 - Na/SS Reflector; 4 – shielding; 5 – Pb diffuser with a D/T target on the top.

using standard or new experimental techniques;

- develop new specific experimental techniques mainly in support to the operation of sub-critical systems, but also for standard integral parameters to obtain a wide range of experimental results to define accurate experimental uncertainties;
- analyse these experimental results by use of different nuclear data files and calculation methods (deterministic and Monte-Carlo tools);
- define a reference calculation route (including nuclear data and calculation tools) for the neutronic predictions of an ADS;
- associate to this reference route a set of residual uncertainties to be compared to the equivalent set for equivalent fast critical system.

In the end of year 2001 MUSE-4 was licensed for performing planned experiments with Na-rodlets (simulation of Na-coolant). These experiments are now underway.

Figure 5 shows an example of Monte – Carlo simulation results of the neutron spectra at the centre of MUSE-core for different external neutron sources [10].

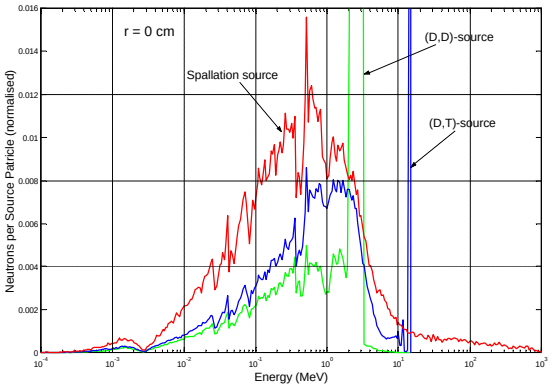

Figure 5. Neutron energy spectra in the MUSE model at position r = 0 for D-D, D-T neutron sources and hypothetical 1 GeV spallation neutron source [10].

2. Yalina experiment [11]

Subcritical thermal neutron set-up called Yalina is another interesting integral experiment very complementary to the MUSE-facility. A subcritical thermal neutron assembly is a uranium-polyethylene multiplying system with maximal multiplication factor k_{src} < 0,98 in a well of a stack composed of high purity graphite bricks) serving as a lateral reflector. The assembly is driven by an intense neutron generator wit a D or T target located OUTSIDE the subcritical core (see Fig. 6) The assembly is mounted on the movable platform which allows to shift the assembly in two directions with respect to the ion beam axis. A rectangular lattice has a pitch equal to 20 mm. Fuel pins consist of 10% enriched U.

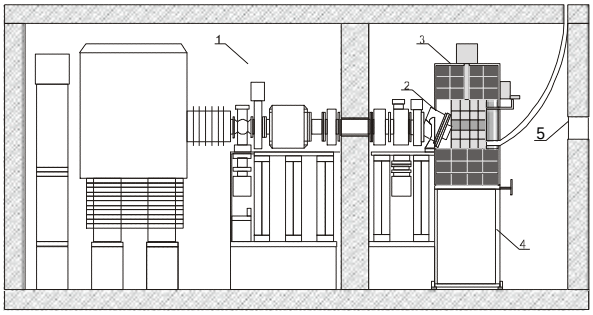

Figure 6. The subcritical facility Yalina in Minsk. 1 - neutron generator, 2 - Ti-^{3}H target system, 3 - subcritical assembly, 4 - movable platform, 5 - collimator.

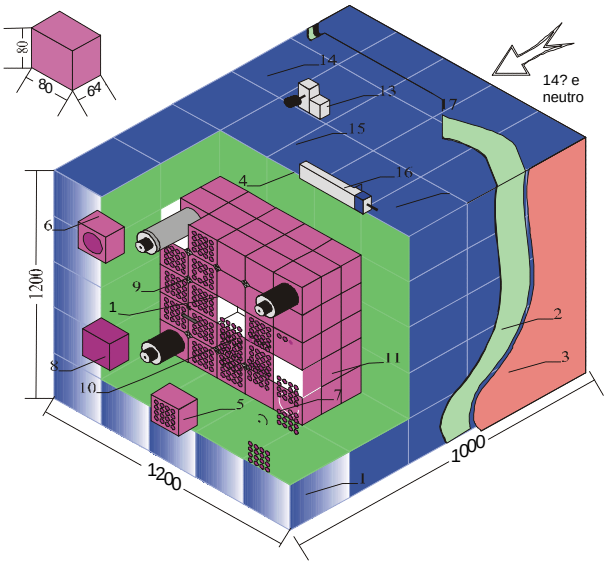

Figure 7. A detailed view of the Yalina facility [11].

Experiments on the Yalina facility are focused on:

- investigation of physics of the subcritical systems driven by a neutron generator,
- measurements of transmutation rates of the fission products and minor actinides,
- investigation of spatial kinetics of the subcritical systems with the external neutron sources,

- validation of the experimental techniques for subcriticality monitoring, neutron spectra measurement etc.

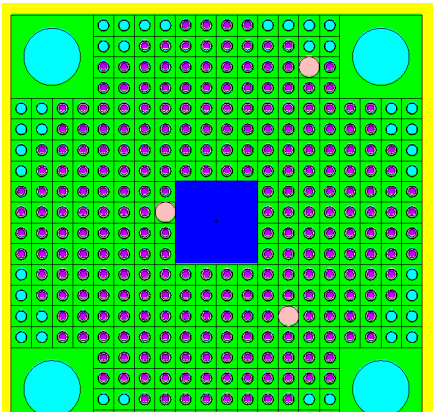

Figure 8. A core model of Yalina-benchmark IAEA benchmark. Nuclear data sensitivity studies for k_{eff} gave the following results:
ENDFB6.6 JEF2.2 JENDL3.2
0.9651+/-.0008 0.9675+/- 0.0007 0.967+/-.0007

- investigation of dynamics characteristics of the subcritical systems with the external neutron sources in pulse mode of the neutron generator operation.

2. SAD project

Joint Institute for Nuclear Research in Dubna together with foreign collaborators from KTH-Stockholm, CEA-Cadarache, CIEMAT-Madrid, nad FZK-Karlsruhe has proposed a project to develop and construct a Subritical Assembly in Dubna (**SAD**) driven by the existing phasotron accelerator of protons with energy 660 MeV. A subcritical core will be fuelled with MOX fuel elements containing a mixture uranium and weapon grade plutonium oxides.

The conceptual design of the SAD facility is based on a subcritical MOX core with a nominal thermal power of 20 kW. This corresponds to the multiplication coefficient keff = 0.95 for the accelerator beam power of 1kW.

A design of the SAD installation – see Figures 9 an 10 - includes:

- The proton accelerator with energy 660 MeV and maximum power of 2.1 kW;
- Beam transport line;
- Replaceable targets of various length and material: Pb, W, Pb/Bi;
- Subcritical core with fuel elements of a BN-600 type;
- Reflector and radiation shielding;
- Systems of air-cooling of target and blanket;
- Safety and monitoring systems.

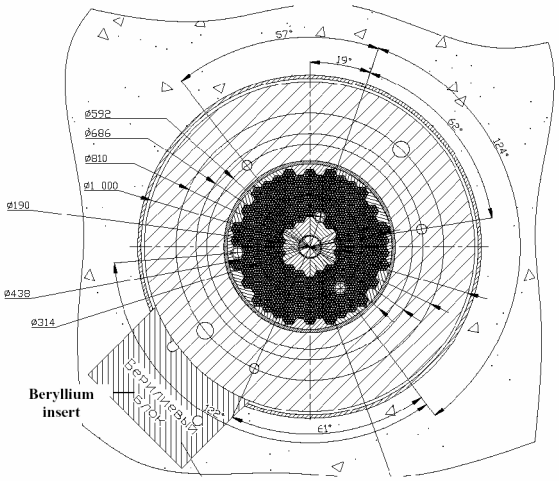

Figure 9. A predesign of a SAD-core with experimental channels and lead and beryllium inserts.

The proton beam will impinge on the target placed in a steel tube. Surrounding subcritical core will be set up with MOX fuel placed in a stainless steel vessel. The lead reflector will surround the subcritical core. A small beryllium insert with experimental channels will be placed behind the lead reflector in order to perform additional studies with moderated neutrons and to increase experimental flexibility of this assembly.

The installation will be placed in accelerator hall surrounded with a concrete wall with thickness of about 2 meters.

A standard fuel batch used in a BN-600 fast reactor has been considered for the SAD-coer. The distance between fuel batch centres has been 96 mm. The fuel designed for the fast breeder BN-600 reactor will be adopted for the core of the SAD-facility. The 127 fuel elements will be located in a hexagonal stainless steel fuel batch. Fuel elements contain the fuel pallets with 27%PuO_2 + 73%UO_2 of average density of 10 g/cm^3. The content of ^{239}Pu in PuO_2 is not less than 95%. Uranium in oxide is depleted to 0.4% of ^{235}U.

The following research topics are foreseen for SAD experiments:

- Studies of the coupling between a spallation target and a subcritical assembly, development of techniques for measurement and control of physical parameters of the facility (e.g. reactivity and subcriticality level)
- Measurement of k_{eff} and absolute value of a power gain of installation;

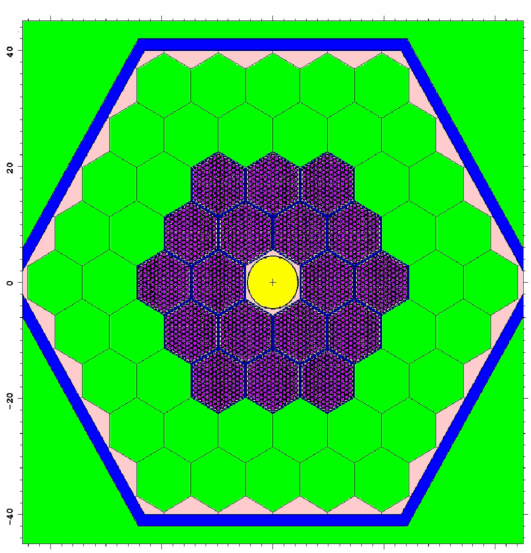

Figure 10. A computational model of the SAD subcritical assembly as simulated for different set-up. (green - lead, violet - fuel elements, blue – stainless steel, yellow-spallation target (Pb,Pb-Bi or W), rose – vacuum.

- Studies of the spallation target including spallation neutron yields and spectra for:
  - Different target materials (Pb, W, Pb-Bi)
  - Different target sizes
  - Different shapes of a target interface surface and optimization of the target shape.
  - Different position of the target in the subcritical assembly. Investigations of the spallation neutron source importance and the resulting consequence on the global energy gain of the ADS. All targets will be instrumented for monitoring neutron and proton fields. Post irradiation analysis of the targets is foreseen.
- Validation of the codes and nuclear data spporting development of ADS
- Specific properties of systems using fuels that include Pu with very large fraction of ^{239}Pu.
- The measurement of the contribution of high-energy (E >10 MeV) neutrons and protons in particular studies of neutron shielding for a high energy neutron tail.
- Post-mortem analysis of the spallation target and special samples (transuranic isotopes) including radiochemical analysis

SAD project is now under the ISTC evaluation process and if approved in the nearest months the setup will be rasy for experiments in about 2 – 3 years.

It is worth to mentioned that a number of interesting experiments have been already performed in a frame of SAD project preparation and those experiments are linked and coordinated with the mentioned above European MUSE-project. See for example references [12][13].

D. Reprocessing chemistry

More detail description of the activities related to ATW reprocessing chemistry is beyond the scope of this paper and beyond the interest of this conference. It is however worth to mention that the the reprocessing chemistry is intimately dependent on the choice of the ATW fuel and its place in the general nuclear fuel cycle. The development of new fuels and associated fuel technologies is a very length and costly process. That is why the future demonstration ATW facility will for sure use an available conventional oxide fuel with cladding compatible with the choice of the coolant material.

The choice for the advanced fuel is not obvious at present. Oxides and nitrides are considered the most promising fuel materials, oxides (either as mixed transuranium oxide or as inert matrix oxide) being the primary candidate. Oxide phases have the advantage of high chemical stability and thus relative simple handling and fabrication, which is very important for MA containing materials. However, the relatively low thermal conductivity of oxide materials will lead to a high operating temperature. Composites (ceramic-metal or ceramic-ceramic) may help to improve this. Nitride fuel, on the other hand, has much better thermal properties and, hence, a low(er) operating temperature but is more difficult to fabricate.

ATW activities have reinvigorate interest in nonconventional fuels and reprocessing technologies.

Some interesting advanced ATW core designs including new fuel cycle schems have been proposed and published, see for example [15][16]

III. ATW SIMULATION TOOLS

To simulate properly ATW-systems minimum few categories of computer codes are necessary:

- Steady state (equilibrium) codes including high energy particle transport modules, necessary for estimation of k_{eff}, steady state particle fluxes, etc.

- Kinetic codes – necessary for simulation short time transients. Very important for safety assessments
- Burn-up codes calculating long time behaviour of ATW.
- Thermal hydraulic codes necessary for a design of thermal hydraulics of ATW system and for safety assessments. Necessary coupling to the kinetic codes.

A. Steady state codes

ATW development and Accelerator Production of Tritium project in USA have stimulated development of a new class of Monte Carlo codes - mergers of the standard particle transport codes (mainly neutrons, photons and electrons) with the High Energy Transport (HET) codes (mainly charged particles of energies above few MeV).
A merger of a broadly used MCNP code with the LAHET code became the MCNPX [17]. A merger of FLUKA [18] with new modules for low energy neutron transport and burnup modules became EA-MC code [19] [20].
A lot of benchmarks and tests have been performed on the steady state simulations both in the high energy region and the "reactor" range of particle energies. From the ATW point of view one can summarize the status of simulation codes as follows:
For the high energy modules:

- Neutron Yield
  - Some differences between different codes may be seen, however the total yields has a tendency to "smear" out the differences particularly for thick targets.. Neutron yield is a very important parameter for ATW efficiency and should be always estimated with the highest possible accuracy
  - Proton multiplicities show the significant differences reflecting different treatments of barrier penetrability. Could be important for radiation damage assessment in the target vicinity
- Spallation Product Yields. This is a very important physical parameter which may have a big impact on design and licensing spallation targets alone and integral ATW-systems
  - Shows big discrepancies between different codes and experimental results, sometimes reaching few orders of magnitude. It has a "devastating" impact on radiotoxic inventory calculations and results of transmutation.
  - Good experimental data exists now and should contribute to improvement of the nuclear models used in the codes.
- Energy Deposition is a critical result for spallation target designs, particularly target window designs. Needs validation and benchmark supported with good experiments.
- Intermediate energy cross-section libraries should match low-energy libraries in their content.

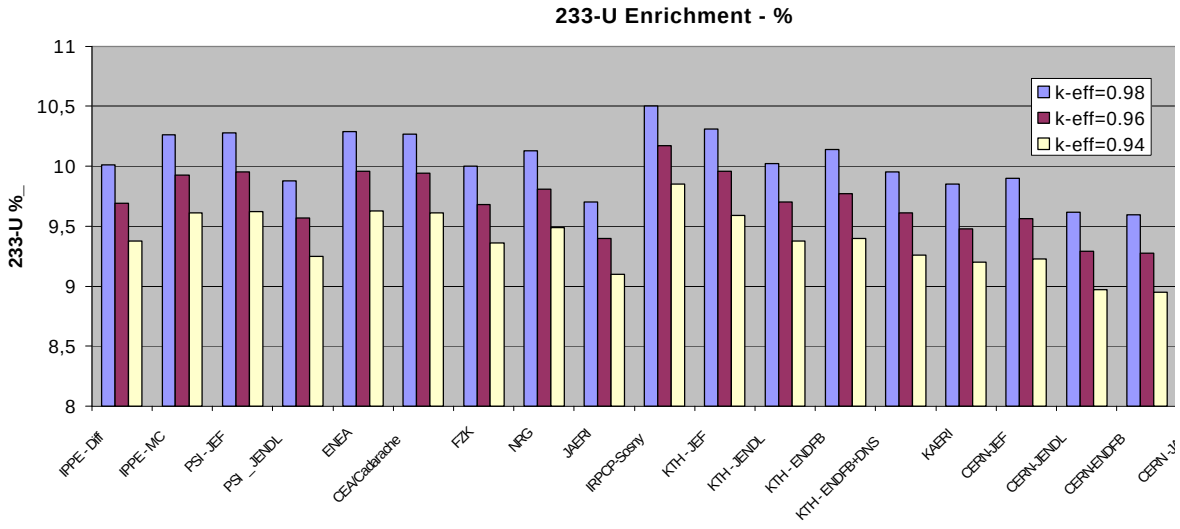

Figure 11. Dispersion of the results of ^{233}U enrichment calculations for different IAEA benchmark participants [21]

For low-energy modules:

- Subcriticality must be well understood by the code-users while calculating k_{eff} and/or k_{source}. Specially, impact of (n,xn) reactions must be properly taken into account for non-egeinvalue calculations, particularly for fast spectrum systems. See discrepancies – Figure 11 - between different codes and users for IAEA benchmark [21]
- Low-energy cross-section libraries should be improved, particularly for those isotopes which were not extensively scrutinized (Pb, Th etc.).

B. Kinetic codes

Several dynamic features are characteristic and important for the ATW. Inherent reactivity feedbacks have proven to be excellent means for achieving passive safety in traditional reactors that operate in the critical mode. However, it is shown that the course of design-basis accidents in an ATW is relatively insensitive to the values of individual reactivity coefficients. The usually desirable negative Doppler effect is an important safety mechanism in a critical reactor, but the effect is vanishing small in accelerator-driven systems employing dedicated fuels (free from fertile fuel isotopes such as uranium or thorium).
In spite of the importance of kinetic behavior of ATW there are really very few simulation tools adapted for these needs [22]. One of the codes tailored for specific ATW needs is the SAS4A safety code [23]. The thermal, hydraulic,

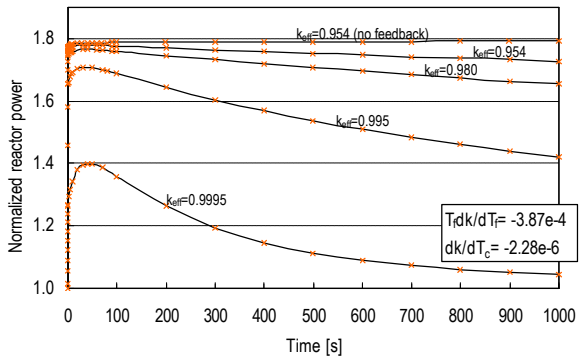

Figure 12. Impact of reactivity feedbacks in a source-driven system. Accident initiator by sudden increase in source intensity (S=1.8*S0). Subcriticality is a parameter.

neutronic, and mechanical models employed in the SAS4A computer code were developed in the U.S. liquid metal reactor development program. These models have been extensively validated with different experimental test data. The coolant thermophysical property database used in SAS4A has been extended to include the properties of lead-bismuth eutectic (LBE), based on evaluations of available U.S. and Russian experimental data [24][25]. The combination of experimentally based coolant thermophysical property data with the already validated, first-principles coolant thermal-hydraulics models in SAS4A provides a satisfactory basis for conceptual design basis analysis. A sample of the analysis performed with SAS4A is given of Figure 12.

C. Burnup codes

A very original contribution of ATW activities combined with a progress in computer technology is development of Monte-Carlo based burnup codes. In difference to a simple coupling of Monte Carlo to "Origen" like burnup codes [26], two original Monte-Carlo burnup codes emerged in the last few years. The EA-MC code [19][20] simulates steady state particle transport and perform burnup calculations starting from the initial impinging high-energy protons, the MCB code performs for today burnup calculations only starting from the neutron source supplied from the separate high-energy transport calculations or from the inherent neutron source obtained from criticality calculations.
MCB code is fully compatible with MCNP (version 4C) and complete burnup calculations can be done in a single run that requires preparation of a single input file with a very few more data lines compared to a regular MCNP input. A continuous or batch fuel feed/extraction can be simulated including a possibility of reloading and shuffling of the fuel elements. The code uses extensive data libraries that covers nuclide decay schemes, continuous energy transport and reaction cross-sections, isomer state formation ratios, incident energy and target nucleus dependent fission product yield, and radioactive hazard indexes. This novel and advanced numerical tool can be used for a design of various nuclear systems, particularly for simulations of the accelerator driven systems. The extensive tests on the system were performed on IAEA [21] and NEA ADS-benchmark [28] data covering both, time evolution of keff and transmutation of ^{99}Tc. Even if we consider that those benchmarks – see Figure 13 - show a very good performance of the MCB code one should conclude that burnup calculations with different codes and methods show very large discrepancies at the end of simulated burnup periods.

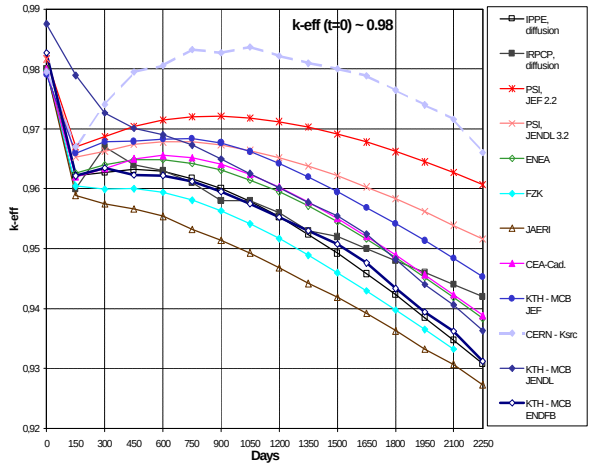

Figure 13. Evolution of k_{eff} in time for an initial k_{eff} ~0.98. CERN group evolution with the EA-MC code is based on k_{source} approach and therefore very different [21]

This is a sign of significant deficiencies in some codes simulating burnup processes and accumulation of the errors in fission product treatment. Consequently both burnup codes and data applied for simulations of ATW require a rigorous scrutiny and further benchmark activities in order to reach precision expected and required for simulation of nuclear systems.

IV. CONCLUSIONS

Parallel to different roadmapping activities and and long term program proposals for ATW development in some countries a network of interesting experiments and benchmark activities have been developed which already now establish good foundations for further progress in transmutation related research. First subcritical facilities, even if not yet driven by real spallation sources, are already now delivering experimental data. The first spallation driven experiments are also in sight. ATW stimulated very interesting development of Monte Carlo computer codes covering physics of intermediate and low energy particle transport, kinetics and burnup processes. Also nuclear data projects - not mentioned in this paper – got a real stimulus from transmutation activities. Moreover, transmutation projects reinvigorated very significantly nuclear technology field in many countries.

However, there is a long way from basic physics experiments to construction of the realistic transmutation facility. Some of the required experiments may take very long time like for example development and validation of the nuclear fuels for transmutation systems. Also development of accelerators with required reliability may pose problems.

REFERENCES

[1] H. Murata and T. Mukaiyama, Fission reactor studies in view of reactor waste programs. Atomenergie-Kerntechnik 45 (1984) 23.

[2] M. Salvatores et al, Long-Lived Radioactive waste transmutation and the role of accelerator driven (hybrid) systems. Nucl. Inst. Meth. A, 414 (1997) 5.

[3] Hill, R.N., T.A. Taiwo, J.A.Stillman, D.J. Graziano, D.R. Bennett, H.Trellue, M. Todosow, W.G. Halsey, and A. Baxter, “Multiple Tier Fuel Cycle Studies for Waste Transmutation,” ProceedingsTenth International Conference on Nuclear Engineering, April 14-18, 2002, Arlington, Virginia.

[4] C. Rubbia, editor, “A European A European Roadmap for Developing Roadmap for Developing Accelerator Accelerator Driven Driven Systems (ADS) Systems (ADS) for Nuclear Waste Incineration for Nuclear Waste Incineration”

[5] NEA/OECD Workshop on Utilisation and Reliability of High Power Accelerators,Aix-en-Provence, France, 2-24 November 1999

[6] E. Yefimov et al., "Development of Molten Lead-Bismuth Target Complex TC-1 for LANSCE Accelerator", Proc. Accelerator Applications 2001 and ADTTA 2001 “Nuclear Applications in the New Millennium”, Reno (USA). ANS (2001)

[7] J. Carlsson, MSc thesis, Dep. of Nuclear and Reactor Physics, Royal Institute of Technology, January 1997

[8] W. Assal, C.A. Bompas and R. Soule, "Geometrical and physical data for the MUSE 4 experiment", CEA/Cadarache (1999).

[9] J.M. De Conto, “GENEPI: A high intensity deuteron accelerator for pulsed neutron production”, Institut des Sciences Nucléaires de Grenoble.

[10] W. Gudowski, J. Wallenius, K. Tucek, M. Eriksson, J. Carlsson, P. Seltborg, J. Cetnar and R. Chakarova, “System and safety studies of accelerator driven transmutation” Annual Report 2001, Report of the Swedish Nuclear Fuel and Waste Management – SKB, in print.

[11] S. Chigrinov, A. Kievitskaja, ISTC Project B70 – Progress Reports and private information.

[12] W. Gudowski, A. Polanski, I. V. Puzynin, V. Shvetsov, "Monte Carlo Modeling of a Sub-Critical Assembly Driven with the Existing 660 Mev Jinr Protons Accelerator", Proc. Accelerator Applications 2001 and ADTTA 2001 "Nuclear Applications in the New Millennium", Reno (USA). ANS (2001)

[13] Bamblevski V.P., Krylov A.R., Polanski A. Timoshenko G.N. Shvecov V.N. The investigation of the Radiation Field Around the Thick Lead Target Irradiated By The 660 MeV Protons.Part.1.The neutron spectra measurement around the target. JINR Preprint E1-2000-307, Dubna, 2000.

[14] Bamblevski V.P., Krylov A.R., Polanski A. Timoshenko G.N. Shvecov V.N. The investigation of the Radiation Field Around the Thick Lead Target Irradiated By The 660 MeV Protons.Part.2.The measurements of the angular and spatial distributions of the hadron's yeld from the target. JINR Preprint E1-2000-308, Dubna.

[15] Wallenius J., et al.: Application of burnable absorbers in an accelerator driven system, Nuclear Science and Engineering 137 (2001) 96

[16] Wallenius J., et al.: The Sing Sing core: A sub-critical TRU burner with low production of curium, Proc. Accelerator Applications 2001 and ADTTA 2001 "Nuclear Applications in the New Millennium", Reno (USA). ANS (2001)

[17] Laurie S. Waters, Editor, MCNPX Users's Manual, TPO-E83-G-UG-X-00001, LANL, 1999.

[18] A. Fassó, A. Ferrari, J. Ranft, P.R. Sala, G.R. Stevenson And J.M. Zazula, Nuclear Instruments and Methods A, 332, 459 (1993)

[19] C. Rubbia et al, "Conceptual Design of a Fast Neutron Operated High Power Energy Amplifier", CERN Divisional Report CERN/AT/95-44 (ET), 29th September 1995. See also C. Rubbia, "A High Gain Energy Amplifier Operated with Fast Neutrons", AIP Conference Proceedings 346, International Conference on Accelerator-Driven Transmutation Technologies and Applications, Las Vegas, July 1994.

[20] F. Carminati and Y. Kadi, CERN/ET/ Internal Note 98-005

[21] W. Gudowski et al. "IAEA Benchmark On Accelerator-Driven Systems" Proc. Accelerator Applications 2001 and ADTTA 2001 "Nuclear Applications in the New Millennium", Reno (USA). ANS (2001)

[22] Waclaw Gudowski, Jan Wallenius, Kamil Tucek, Marcus Eriksson, Johan Carlsson, Per Seltborg, J. Cetnar and R. Chakarova, "System and safety studies of accelerator driven transmutation" SKB Annual Report 2001, Stockholm April 2002 .

[23] J. E. Cahalan, A. M. Tentner, and E. E. Morris, "Advanced LMR Safety Anlaysis Capabilities in the SASSYS-1 and SAS4A Computer Codes," Proc. of the International Topical Meeting on Advanced Reactors Safety, Pittsburgh, April 17-21, 1994.

[24] R. N. Lyon, Ed., "Liquid Metals Handbook", NAVEXOS P-733(Rev.), U.S. Atomic Energy Commission and U.S. Department of the Navy, June, 1952.

[25] N. A. Nikol'skii, et al., "Thermal and Physical Properties of Molten Metals and Alloys", pp. 1-36, Problem of Heat Transfer , M. A. Mikheev, Ed.,Publishing House of the Academy of Sciences SSSR, Moscow, 1959. [Translated as USAEC Report AEC-tr-4511]

[26] D.I. Postone and H.R. Trellue, "User's Manual Version 2.0 for Monteburns, Version 1.0", Los Alamos National Laboratory report LA-UR-99-4999. September 1999.

[27] J. Cetnar, W. Gudowski and J. Wallenius, "Simulation of Nuclide Transmutations with Monte-Carlo Continuous Energy Burnup Code (MCB), Proc. Accelerator Applications 2001 and ADTTA 2001 "Nuclear Applications in the New Millennium", Reno (USA). ANS (2001)

[28] Byung-Chan Na, editor: "Comparison Calculations for an Accelerator-Driven Minor Actinide Burner", NEA-OECD report 2001, in preparation.

APPENDIX 2

J. Wallenius, Neutronic aspects of inert matrix fuels for application in ADS, Journal of Nuclear Materials, accepted for publication

Neutronic aspects of inert matrix fuels for application in ADS

J. Wallenius

Department of Nuclear and Reactor Physics
Royal Institute of Technology
AlbaNova University Centre
S-10691 Stockholm
Sweden

Abstract

Accelerator driven systems may operate on uranium or thorium free fuels. In order to guarantee the stability of such fuels at high temperatures, the use of inert matrices is foreseen. In the present study, safety parameters of 800 MWth ADS cores operating on oxide and nitride fuels with high americium content are investigated for a representative range of pin and core geometries. It is shown that among the inert matrices investigated, chromium yields the lowest void worth, hafnium nitride the highest fission probability for americium and magnesia the highest burnup potential.

Keywords: Inert matrix fuel, Accelerator Driven System, Void worth, Burnup potential

Introduction

In the Double Strata fuel cycle [Murata84, Salvatores97], the americium and curium produced in critical power reactors is supposed to be multi-recycled in dedicated minor actinide burners. An advantage of this approach is that handling of these highly active elements is constrained to a very small part of the nuclear power park. The poor reactivity coefficients of minor actinide based fuel, in conjunction with a very small effective fraction of delayed neutrons, however makes safe operation of critical dedicated cores questionable. The introduction of accelerator driven systems (ADS) for the purpose of minor actinide burning therefore appears adequate. The ADS core should operate on a fast neutron spectrum, in order to minimise production of strong neutron emitters like curium and californium. While a substantial part of the technology developed for fast breeder reactors is directly applicable to ADS, the fuel composition, form and state remains to be determined. In the present paper, safety parameters like void worths and coolant temperature coefficients of several fuel candidates are investigated. In addition an estimation of the relative burnup potential pertaining to each fuel type is given.

Core Model

A single zone ductless core model was used, in order to simplify the study of impact of fuel pin diameter and pin pitch on the safety coefficients. Table 1 summarises the parameters that were kept constant. A start-up core was considered, hence no curium in the fuel. The ratio of plutonium to americium was set to 40/60, in order to provide a minimum reactivity swing [Takizuka98]. Calculations were made for two liquid metal coolants: sodium and lead-bismuth eutectic. Radial steel reflectors were assumed in both cases. Two representative pin diameters were investigated, and the pin pitch was varied from P/D=1.25 to 2.25. The clad thickness was adjusted to allow for a maximum fission and helium gas pressure of 20 MPa, given a plenum height of 100 cm. In all cases, the fraction of inert matrix was adjusted to obtain a k-eigenvalue equal to 0.97. For oxide fuels a porosity of 10% was adopted, for nitride fuels 15%. Table 2 displays the average linear rating assumed for each fuel. A smaller rating corresponds to a larger

number of fuel pins in the core.

Method of Calculation

The continuous energy Monte Carlo code MCNP4C [Briesmeister00] in parallel mode was used to calculate neutron fluxes, k-eigenvalues and cross sections. The cross section data library used for the present work was ENDFB/VI-8. Each fuel pin was modelled explicitly, in order to obtain a correct leakage contribution to the void worth. A standard deviation of less than 40 pcm in the estimated k-eigenvalues was required, corresponding to calculation times of about two hours per core configuration (using eight Athlon 1.5 GHz processors). It should be noted that there is a considerable uncertainty in the inelastic cross section of lead [Embid98], which may lead to errors in the calculated void worths of LBE cooled cores. The magnitude of this uncertainty is of the order of 1000 pcm, but will not be critical for the conclusions of this study. Further, void worths in power flattened multiple zone cores will differ from single zone cores, as the radial leakage contribution to the neutron balance is suppressed in the latter case. Hence, the void worths here reported should be interpreted relative to one another, rather than in terms of absolute magnitude.

Inert matrix fraction

In Figure 1, the volume fraction of inert matrix required to obtain a k-eigenvalue of 0.97 is displayed as function of pin pitch for oxide fuels and LBE coolant. Since erosion concerns limits the velocity of heavy liquid metal coolants to about 2 m/s, the pin pitch must be increased to obtain a heat removal capacity similar to that of sodium. For an inner pin diameter of 5.0 mm and a clad thickness of 0.36 mm, the inert matrix fraction is found to range from 40 to 60 volume percent, with exception for the case of tungsten. Since fabricability may become a concern for smaller fractions of inert matrix, it seems like the absorption cross section of tungsten is a bit too high for this matrix to be compatible with the adopted Pu/Am ratio.

As the neutron mean free path in sodium is much higher than in LBE, the contribution of absorption in the plenum region to the neutron balance will be larger for identical geometries and fuel compositions. In order to compensate for this the fraction of inert matrix becomes 5 - 10 percent lower when adjusting the k-eigenvalue of the core to 0.97.

Increasing the pin diameter will enable a larger fraction of inert matrix to be used. In figure 2, the volume fraction of ZrN in nitride fuels is displayed. Increasing the inner clad diameter from 5.0 to 7.0 mm allows for an increase in ZrN fraction by 4 - 7%. It should be emphasized, that in none of the cases investigated, a volume fraction of inert matrix larger than 75% was obtained. If other boundary conditions (fabricability, safety) would require a larger matrix fraction, the Pu/Am ratio would have to be adjusted, with consequenses for reactivity management.

Void worths

The lack of a significant Doppler effect in ADS fuels implies that core configurations yielding prompt super-criticality should be avoided. The combination of MA-bearing fuel and liquid metal cooling will typically yield a positive coolant void worth. The choice of coolant, as well as the fuel design however have a significant impact on the magnitude of the void worth. Figure 3 shows sodium and LBE void worths (for voiding of core and upper plenum)as function of P/D for oxide fuels with zirconia and chromium matrices. As in the case of fast reactors, the void worth is lower for fuels having a high thermal conductivity. The reason for this is that a higher linear rating corresponds to a fewer number of fuel pins in the core and consequently a higher radial

leakage in the voided state. The drastic difference in void worth between sodium and LBE is due to the large amount of americium in the fuel. Though the difference is smaller for voiding of the core only, sodium has a clear disadvantage in terms of higher void worth in minor actinide burners.

In figure 4, the LBE void worth is compared for the five oxide fuel types investigated. Note that the Cr matrix offers an advantage in terms of a low void worth. The explanation is that chromium has its main inelastic scattering threshold at 1.2 MeV, in contrast to most other nuclides, which have thresholds at around 0.5 MeV. Chromium thus is inelastically transparent for a larger fraction newly born fission neutrons, yielding not only a harder spectrum, but also a smaller shift of spectrum during coolant voiding. Selecting inelastically transparent materials for the fuel matrix hence enables to obtain acceptable void worths for larger cores. The void worth for a nitride fuel in solid solution with ZrN varies with P/D between +1000 and +1500 pcm, much lower than its oxide counterpart. Thus it is mainly the poor thermal conductivity of zirconia that makes it usuitable as fuel matrix for ADS (low rating leading to larger number of fuel pins). Substituting ZrN with HfN increases the void worth by a factor of two.

Coolant temperature coefficients

While significant temperature feedbacks are not required for normal operation of an ADS, negative feedbacks remain useful in core disruptive accidents, as well as for minimising fluctuations in core power. The Doppler feedback of the ADS fuel is close to negligible, being about −0.05 pcm/K [NEA01]. Among the possible mechanisms to control the core, axial and radial expansion are still active in the ADS. Values of structural material expansion coefficients typically range from −0.2 to −0.5 pcm/K. The coolant temperature coefficient, on the other hand, ranges from +0.2 pcm/K to +1.0 pcm/K for certain fuels cooled by LBE, as shown in figure 5. For sodium cooled ADS cores, the temperature coefficient may be as large as +4 pcm/K, which hardly can be compensated by feedbacks from structural material expansion. Hence introduction of heavy liquid metals or helium gas as coolant for minor actinide burning ADS is well motivated.

Cross sections

The neutron spectrum of FBRs varies only marginally from one design to another, due to restrictions set by breeding and neutron economy. In ADS, one has a larger parameter space available for fuel matrix and core design. The less restrictive neutron economy allows for introduction of absorbing matrices, yielding a harder spectrum, or alternatively larger pin pitches, softening the spectrum. Table 3 shows spectrum averaged cross sections and fission probability for Am-241 as function of fuel matrix for the present core model. Note that hafnium nitride gives the highest probability for fission of americium, and consequently, the lowest build-up of curium.

Burnup potential

In fast neutron reactors, swelling of fuel cladding and wrapper tubes has been identified as the ultimate limitation to fuel burnup. Steels developed for the purpose of being swelling resistant have enabled to reach doses ranging from 150 DPA (austenitic steels) to 200 DPA (ferritic steels). In order to achieve high burnup of the ADS fuel, the design should provide a high ratio between fission and DPA rates. Since the minor actinides present in the fuel are fissionable by neutrons with energy above 1 MeV, it is of interest to minimise the presence of nuclides with large cross section for inelastic scattering in the fuel while simultaneously suppressing the flux that causes damage (neutrons with $E > 0.1$ MeV).

A simple estimation of the burnup potential B_p of a fuel can be found from the formula

$$B_p = 1 - \mathrm{Exp}[-\sigma_f \cdot t_{max}] \qquad (1)$$

where σ_f is the average fission cross section of fissionable nuclides, ϕ is the neutron flux, and t_{max} is given by

$$\phi_{fast}\, t_{max} = F_{max} \qquad (2)$$

Here, ϕ_{fast} is the flux of neutrons with energies above 0.1 MeV, i.e. the flux capable of causing radiation damage in the clad, and F_{max} is the fast fluence limit. For ferritic steels 200 DPA roughly corresponds to $F_{max} = 4.0*10^{23}$ n/cm^2 [Garner00]. The fuel averaged fission cross section and the corresponding burnup potential for the ADS fuel candidates here studied are listed in Table 4. These numbers may be compared to the average fission cross section of standard FBR oxide fuel, being 0.33 barn, yielding a burnup potential of 20%, if estimated by formula (1). The good agreement with the actual burnup limit may be coincidental, since equation (1) contains a bare minimum of physical information. However, the relative burnup potential of different fuels should be possible to predict using this approach.

Due to the comparatively low fission cross section of americium, the burnup potential does not increase in proportion to the fraction of removed U-238. Note that the burnup potential for the fuels with an MgO matrix is higher than for the other fuels. In general, it appears as the inert matrix fules here studied have a burnup potential ranging from 30 to 33%, which of course only may be realised in full extent if core management succeeds in levelling out power peaking factors.

Conclusions

The choice of fuel matrix has a significant impact on safety parameters in accelerator driven systems dedicated to minor actinide transmutation. An oxide fuel with chromium matrix appears to yield the lowest void worth among the fuel types studied in the present work. Strong neutron absorbers like tungsten and hafnium may be used to minimise production rates of curium, but have the disadvantage of increasing the void worth. Hafnium nitride on the other hand, yields the highest fission probability of americium.

The results of the present investigation indicate that chromium is an interesting inert matrix candidate for oxide fuels. It minimises the void worth, while retaining a high fission probability of americium and a reasonably high burnup potential. Fabricability and chemical compatibility do not appear to be major problems, but swelling at high neutron doses and phase separation at elevated temperatures may possibly be issues of concern.

Acknowledgements

This work was supported by the European Commission as part of the FUTURE and CONFIRM projects.

References

J.F. Briesmeister, editor, MCNP Version 4C, LA-13709-M, LANL (2000).
M. Embid et al, Proc. 5th IEM, EUR 18898 EN, page 505, OECD/NEA (1999).
F. Garner et al, J. Nuc. Mat. **276** (2000) 123.
H. Murata and T. Mukaiyama, Atomkernergie-Kerntechnik **45** (1984) 23.
NEA/NSC/DOC(2001)13, OECD/NEA (2001).
M. Salvatores, Nucl. Inst. Meth. A **414** (1997) 5.
T. Takizuka et al, Proc. 5th IEM, EUR 18898 EN, page 383, OECD/NEA (1999).

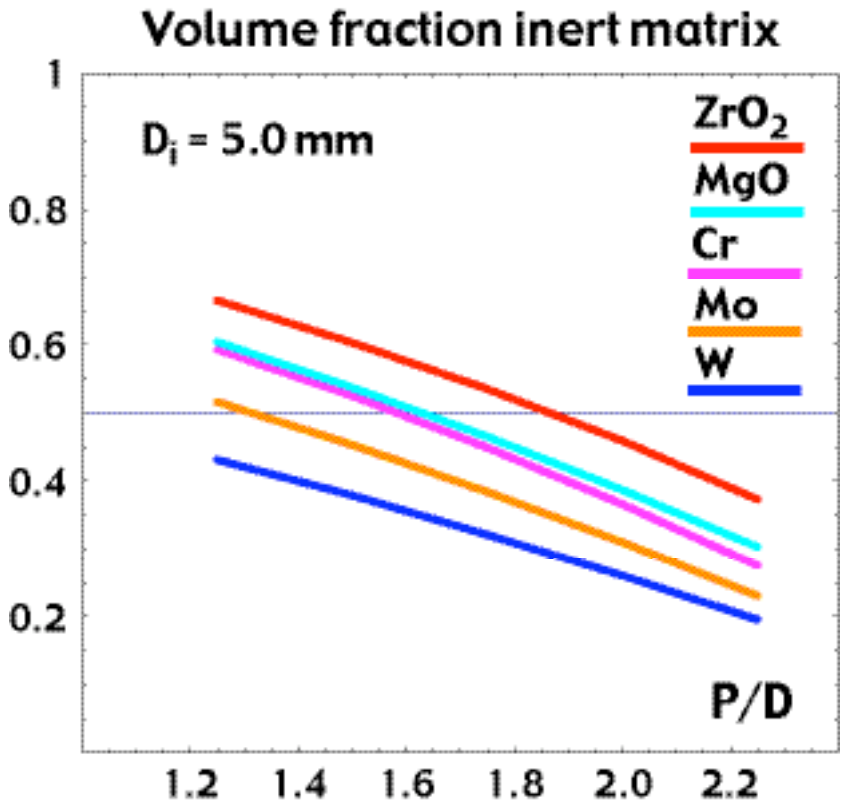

Figure 1: Volume fraction of inert matrix required to obtain a k-eigenvalue of 0.97 for oxide fuel and LBE coolant. 10% porosity was assumed.

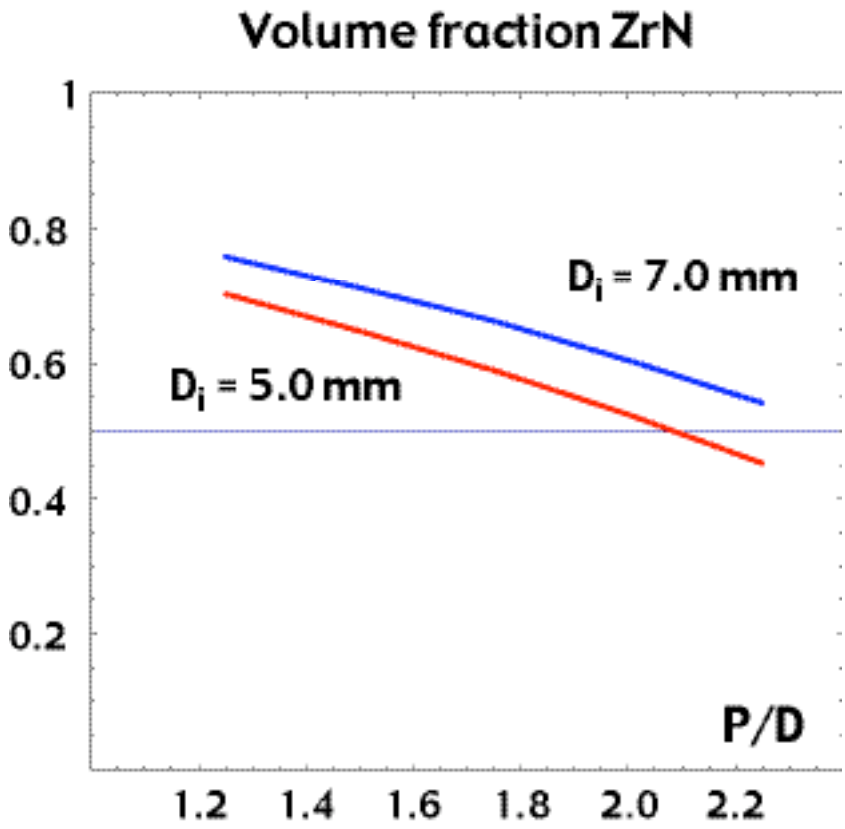

Figure 2: Volume fraction of ZrN required to obtain a k-eigenvalue of 0.97 for nitride fuel and LBE coolant. 15% porosity was assumed.

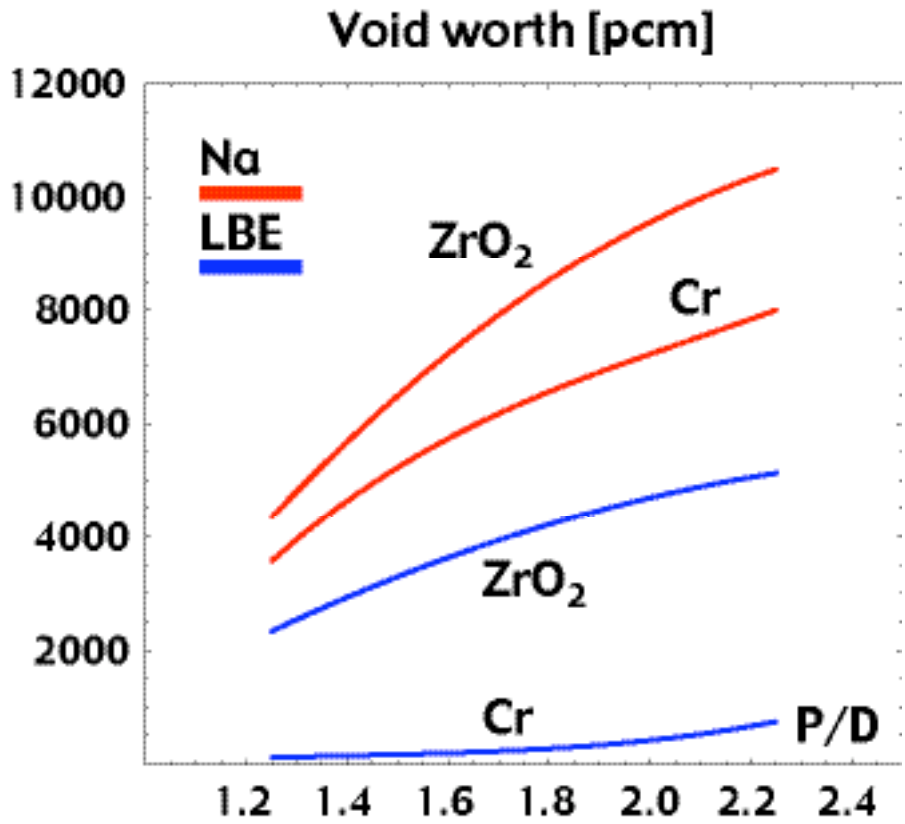

Figure 3: Void worths pertaining to oxide fuels with zirconia and chromium matrices. An inner clad diameter of 5.0 mm was assumed. The void worth was calculated by voiding the core and upper plenum from coolant. Due to uncertainties in the cross section of lead, the displayed values may be in (absolute) error by up to 1000 pcm.

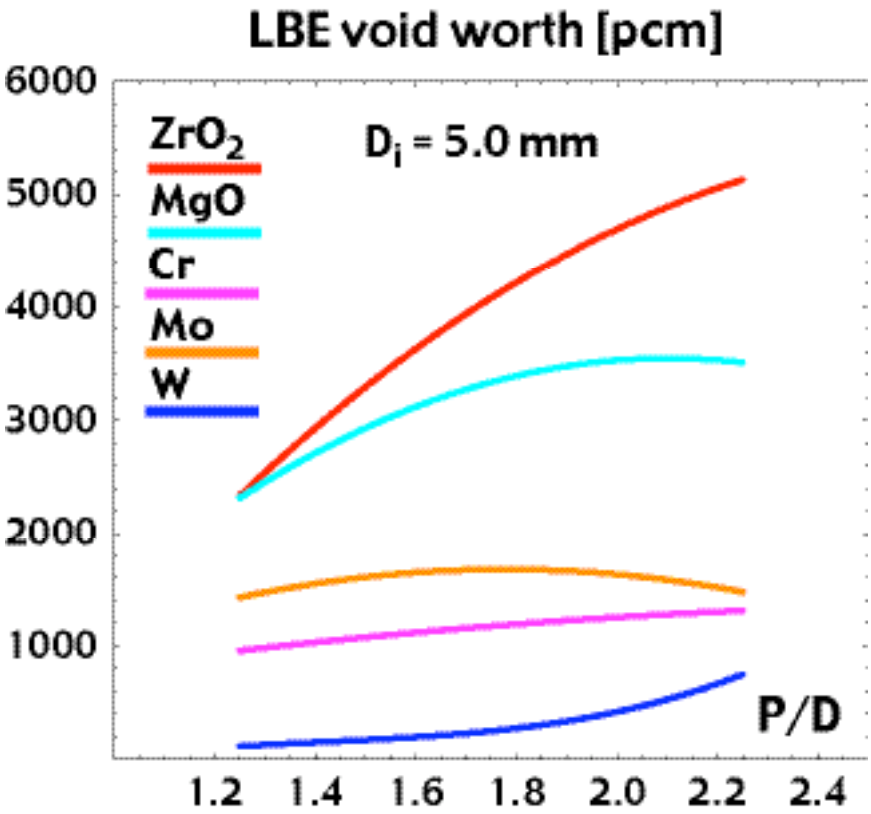

Figure 4: Void worths pertaining to oxide fuels with ceramic and metallic matrices. Due to uncertainties in the cross section of lead, the displayed values may be in (absolute) error by up to 1000 pcm.

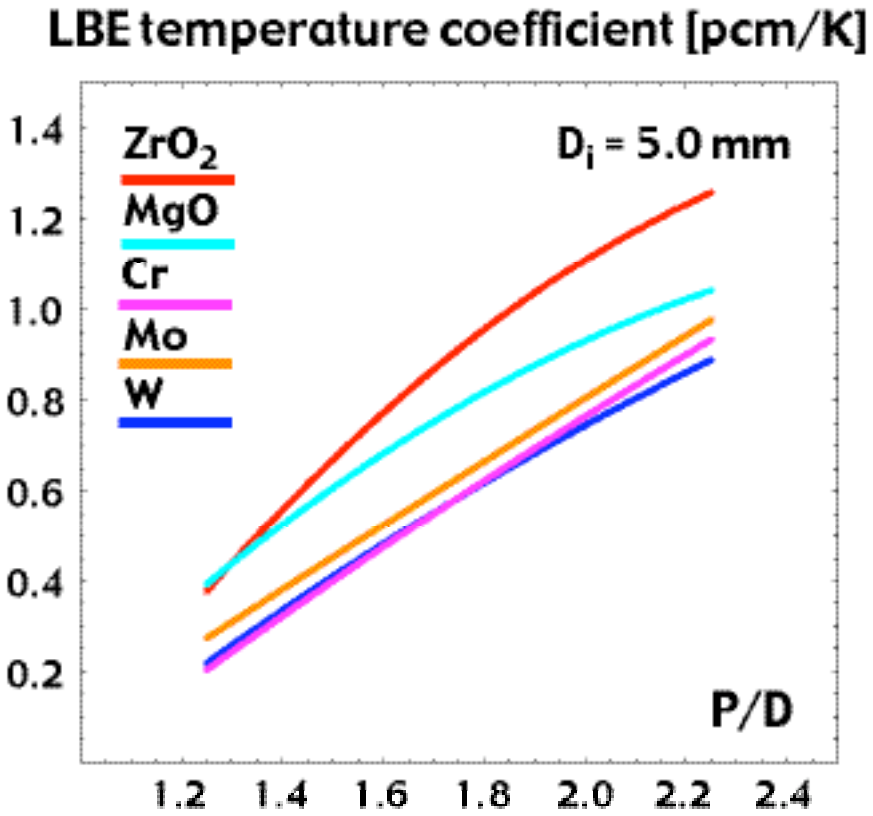

Figure 5: Lead-bismuth coolant temperature coefficient as function of P/D for oxide fuels.

Core power	800 MWth
Spallation target	LBE
Target radius	20 cm
Core height	100 cm
Pu/Am	40/60
k-eigenvalue	0.97

Table 1: ADS core parameters kept constant in the present study.

Composition	Matrix	Form	Rating
Oxide	ZrO_2	solid solution	15 kW/m
Oxide	MgO	composite	25 kW/m
Oxide	W	composite	35 kW/m
Oxide	Mo	composite	35 kW/m
Oxide	Cr	composite	35 kW/m
Nitride	ZrN	solid solution	35 kW/m
Nitride	HfN	solid solution	35 kW/m

Table 2: The uranium free fuels investigated here. "Rating" denotes average linear power density.

Fuel/Matrix	σ_f [b]	σ_c [b]	$\sigma_f / (\sigma_f + \sigma_c)$
Oxide/ZrO_2	0.31	1.34	0.19
Oxide/MgO	0.33	1.37	0.20
Oxide/W	0.33	1.10	0.23
Oxide/Mo	0.34	1.09	0.24
Oxide/Cr	0.34	1.17	0.22
Nitride/ZrN	0.35	1.18	0.23
Nitride/HfN	0.38	0.97	0.28

Table 3: Spectrum averaged cross sections and fission probabilities for Am-241 for the fuels here investigated. Values are given for LBE coolant, P/D = 1.75 and an inner clad diameter of 5.0 mm.

Fuel/Matrix	σ_f [b]	B_p [%]
Oxide/ZrO_2	0.64	32
Oxide/MgO	0.66	33
Oxide/W	0.63	30
Oxide/Mo	0.64	30
Oxide/Cr	0.65	31
Nitride/ZrN	0.66	31
Nitride/HfN	0.67	30

Table 4: Fuel and spectrum averaged fission cross section and burnup potential for the fuels here investigated. Values are given for LBE coolant, P/D = 1.75 and an inner clad diameter of 5.0 mm.

APPENDIX 3

J. Carlsson, H. Wider, Emergency Decay Heat Removal by Reactor Vessel Auxiliary Cooling System from an Accelerator-Driven System, Nuclear Technology Vol. 140, October 2002

Emergency Decay Heat Removal by Reactor Vessel Auxiliary Cooling System from an Accelerator-Driven System

Johan Carlsson * †

Royal Institute of Technology, Department of Nuclear and Reactor Physics, S-10691 Stockholm, Sweden

Hartmut Wider

Joint Research Center, Institute for Energy, NL-1755 ZG Petten, Netherlands

(4 September 2001)

Send invoice to:

Prof. Waclaw Gudowski

Department of Nuclear and Reactor Physics

Royal Institute of Technology

Stockholm Center for Physics, Astronomy and Biotechnology

Roslagstullsbacken 21

S-106 91 Stockholm

Sweden

Tel. +46 8 5537 82 00

Total number of pages in the preprint edition are 40.

*Email: johan@neutron.kth.se or johan.carlsson@jrc.nl

†Current address: Joint Research Center, Institute for Energy, NL-1755 ZG Petten, Netherlands

Contents

List of Tables

List of Figures

Abstract - *The passive emergency decay heat removal during severe cooling accidents in Pb/Bi-cooled 80MWt and 250MWt Accelerator-Driven System designs was investigated with the CFD code STAR-CD. For the 80MWt design, the calculations show that no structural problems occur when the accelerator proton beam is switched off immediately after accident initiation. A delay of the beam stop by 30 minutes after a combined Loss-Of-Heat-Sink and Loss-Of-Flow accident can be tolerated without reaching the fast creep temperature of the guard vessel (1173K). By using a melt-rupture disc on the vacuum pipe of the accelerator proton beam and by thus interrupting the beam at elevated temperatures in a passive way the grace time is increased from 30 minutes to 6 hours. An emergency decay heat removal design which would prevent radioactive release to the atmosphere even more reliably than the PRISM design was also investigated. For an ADS of 250MWt power with the same vessel as the 80MWt ADS, the maximum wall temperature reaches 745K after an immediate beam stop. This does not cause any structural problems either. The grace time until a beam stop is necessary for the 250MWt system was found to be about 12 minutes. To reduce elevated vessel temperatures more rapidly after a beam stop alternative cooling methods were investigated. For example the filling of the gap between the reactor and the guard vessel with liquid metal and the simultaneous use of water spray cooling on the guard vessel outside investigated. This decreases the coolant temperatures already within minutes after switching off the proton beam. The use of chimneys on the Reactor Vessel Auxiliary Cooling System, which increases the air flow rate lowers the maximum reactor vessel wall temperature only by about 20K. It can be concluded that the critical parameter for the emergency cooling of an ADS is the time delay in switching off the accelerator after an accident initiation.*

I. INTRODUCTION

The research described in this paper is aimed at investigating the emergency decay heat removal by a Reactor Vessel Auxiliary Cooling System (RVACS) of a Pb/Bi Accelerator-Driven System (ADS). The RVACS will be needed in Loss-of-Heat-Sink (LOHS) or Loss-of-Flow (LOF) accidents when the normal heat removal systems are not available, e.g. due to a station blackout (Loss-Of-Power, LOP). In the latter accident the accelerator is automatically switched off and the primary pumps stop running. However, as a worst case scenario it is conceivable that both the primary and secondary pumps loose their power supply, whereas the accelerator continues to operate.

The RVACS is a totally passive system, i.e. neither human operations nor mechanical-/electronical devices are necessary to start it. Only physical laws govern it, e.g. gravity and thermal expansion of the fluid. Consequently operational failures are extremely unlikely. Emergency decay heat removal by cooling of the outside of the guard vessel by natural air convection was already earlier planned for the Power Reactor Inherently Safe Module (PRISM) [1] and the Sodium Advanced Fast Reactor (SAFR) [2].

As the name implies, ADS are nuclear power plants driven by an accelerator proton beam. The core is sub-critical and Pb/Bi is considered as possible coolant. Other coolants that are considered are gas (helium) and sodium. The objective of the ADS is the transmutation of the waste from conventional nuclear power plants. The volume of the waste that needs storage could be reduced by one hundredth compared to direct storage [3]. The effective radioactive dose can similarly be reduced by one thousandth.

II. COMPARISON OF STAR-CD CALCULATIONS TO EXPERIMENTAL RESULTS FROM A NATURAL CONVECTION FLOW PROBLEM

The commercial Computational Fluid Dynamics (CFD) code STAR-CD [4] was tested against experimental data for buoyancy driven flows in the PASsive COntainment cooling

(PASCO) facility at Forschungszentrum Karlsruhe (FZK), Germany [5]. Figure 1 shows the PASCO facility.

Figure 1. Schematic view of the PASCO test channel.

The tests of STAR-CD considered both a detailed Two-Layer model with about 15 cells in the boundary layer as well as wall functions applied on a coarser mesh in the cell next to the wall. This means that a logarithmic function is used to model the velocity, and temperature profiles etc in the boundary layer. Different heat transfer correlations were investigated on the air-side in the wall function calculations; the correlation which lead to the most accurate results was developed at Argonne National Laboratory (ANL) [6], see Eq.1

$$Nu = 1.22 Re^{0.456} Pr^{0.4} \tag{1}$$

The experimental results from the PASCO facility gave a heat flux of 6500W and a mass flow of 0.34kg/s. The STAR-CD calculations using the Two-Layer model predicted a heat removal rate of 6700W and a mass flow of 0.37kg/s. Wall functions employed with the heat transfer correlation according to Eq.1 predicts a heat removal rate of 6600W and a mass flow rate of 0.355kg/s.

For the momentum, energy, and density equations a second order differencing scheme is employed. Turbulence is modelled with a linear $k - \epsilon$ turbulence equation.

III. PARAMETRIC STUDY

Parametrical studies were conducted on a simplified RVACS based on the PRISM and SAFR designs, see Fig.2.

Figure 2. Schematic view of PRISM's RVACS.

The parameters studied were the surface roughness, the fin pitch, the surface emissivity, the surface temperature, and the gap width between the guard vessel and collector wall [7]. All calculations except the surface roughness study used wall functions together with the

ANL heat transfer correlation, see Eq.1. The surface temperature and the surface emissivity were found to have the greatest impact on the heat removal rate from the guard vessel [8].

Figure 3 illustrates that the heat removal rate more than triples when the wall temperature rises from 573K to 973K. For the same temperature range, the mass flow increases moderately from 9.5kg/s to 12kg/s. Note the relatively greater contribution from thermal radiation at higher temperatures. This is due to the fact that the heat transfer rate from thermal radiation is dependent on the difference between the wall temperature to the fourth power subtracted by the surrounding temperature to the fourth power, i.e. $Q \propto T_a^4 - T_b^4$.

Figure 3. Heat removal rate with and without radiation as a function of wall temperature.

Investigations with vertical fins on the guard vessel bridging nearly the entire gap between the guard vessel and the collector wall, show that the optimal heat removal rate occurs at a fin pitch between 5 and 10cm [7]. This extensive use of fins leads to a doubling of the heat removal rate relative to the case without fins.

IV. NATURAL AIR CONVECTION COOLING OF AN 80MWT ADS

A. The Ansaldo Design

The integral investigations of this paper are based on the design of an 80MWt ADS demonstration facility by the Italian company Ansaldo [9]. See Fig.4 for an overview of this design.

Figure 4. Schematic view of the Ansaldo design.

The reactor vessel includes the heat exchanges and is thus a pool design. It is 8m tall and has an inner diameter of 6m. A guard vessel surrounds the reactor vessel. A cyclotron delivers a 3mA/600MeV proton beam current to a Pb/Bi target where spallation reactions occur. The neutrons released in these reactions sustain the fission process in the subcritical core.

The coolant flow is mainly driven by natural convection, and enhanced by the injection

of Argon bubbles above the core in order to lower the average density of the coolant in the riser. Thereby, the static pressure difference between the riser and the downcomer is increased, and thus, also the flow rate. The pressure drop over the core is only 20kPa at a mass flow rate of ∼5300kg/, corresponding to a coolant velocity of 0.42m/s in the core. The latter is rather small due to the large pitch to diameter ratio of 1.58 [9]. The remaining flow path has a pressure drop of only 9kPa at a flow rate of ∼5800kg/s. The difference in mass flow rate is due to the ∼500kg/s bypass flow through the dummy zone.

Since ADS and Light Water Reactors (LWR) have similar short lived fission products their decay heat generation is very much alike [10]. The following relation that was developed for a Boiling Water Reactor (BWR) and is used to model the decay heat generation in the present analysis, see Eq.2 [11].

$$P_d(t,T) = 0.062P_0(t^{-0.2} - (T+t)^{-0.2}) \tag{2}$$

where P_0 is normal operating power, t is the time after shutdown, and T is the period of time that the core has operated at normal power.

On the liquid metal coolant side, the heat transfer correlation used is Eq.3 [12].

$$Nu = 0.565Re^{0.5}Pr^{0.5} \tag{3}$$

As mentioned earlier, Eq.1 is used to calculate the heat transfer coefficient on the air-side.

B. Allowable Temperatures for Different Accident Conditions

The structural material in the reactor and guard vessel is assumed to be ferritic steel (AISI 316) as for the PRISM-S design. Maximum acceptable temperature limits for different accident conditions are shown in Tab I.

Table I

C. LOHS and LOF Accident with an Immediate Beam Stop using a PRISM Type RVACS

This scenario investigates a simultaneous LOHS and LOF accident in which the beam is switched off instantaneously after accident initiation, i.e. comparable to a classical station blackout or LOP accident.

In Fig.5, the Loss-of-Heat-Sink (LOHS) and Loss-of-Flow (LOF) accident begins after 3000 seconds or after almost 1 hour. Within seconds after the accelerator is switched off, the decay heat power generated in the core is reduced to about 6.2% of nominal power. One hour thereafter the decay heat is around 1% [17]. After the gas injection in the riser stops the flow rate declines. Thus, the temperature difference over the core grows and buoyancy forces will build up. Twenty minutes after shutdown, the flow in the riser reaches an equilibrium velocity of 1.6cm/s. Fourteen hours after accident initiation the coolant temperature above the core peaks at a maximum of 615K, which is actually lower than the core outlet temperature at nominal power.

Figure 5. Temperature and velocity evolution at core outlet in an 80MWth reactor.

The highest reactor vessel wall temperatures appear above the heat exchanger where the hot coolant coming from the riser hits the wall first. Hereafter, the coolant turns downwards and passes the heat exchanger (HX). The highest downward velocity below the HX is about 5cm/s at a distance of 1cm from the vessel wall, which is due to the increased density of the well-cooled Pb/Bi near the wall.

D. Verification of the 80MWt Calculation

1. Four Times Finer Mesh

To verify the results, examinations on a mesh four times finer than normal were carried out. The temperature evolution diverges to some extent both at the wall and the core outlet. Forty hours after accident initiation the differences are 5K and 8K, respectively. Apparently,

the coarse mesh calculation underestimates the heat removal rate by about 4% throughout the calculation. This can be partly explained by the different heat transfer models used next to the reactor vessel wall on the Pb/Bi side. Because the wall function approximation is no longer accurate on the finer mesh, the more detailed Two-Layer model had to be used. The velocity agrees very well in the two calculations.

2. Hand Calculation

The heat removal rate was also estimated with a hand calculation. The total thermal resistance, $\sum_{p=1}^{N} R_p$ can be described as the ratio between the overall temperature difference $\sum_{p=1}^{N} \Delta T_p$ to the heat flux used q, see Eq.4 [22].

$$\sum_{p=1}^{N} R_p = \frac{\sum_{p=1}^{N} \Delta T_p}{q} \tag{4}$$

where $\Delta T_p = T_p - T_{p+1}$ is the temperature between two facing walls or the temperature between two surfaces of the same wall. The resistance in the walls is calculated as Eq.5.

$$R = \frac{l}{k} \tag{5}$$

where l is the wall thickness and k is the wall conductivity.

The heat transfer between parallel walls is a combination of radiation and convection. Consequently the thermal resistance between two parallel walls is calculated according to Eq.6.

$$R^* = \frac{1}{\{Nu\frac{k}{l} + \frac{\epsilon\sigma}{2-\epsilon}(\theta_p^2 + \theta_{p+1}^2)(\theta_p + \theta_{p+1})\}} \tag{6}$$

where $Nu = \frac{hL}{\nu}$, ϵ surface emissivity, σ Stephan-Boltzmann constant, θ temperature in K.

For a natural convection between vertical plates the Nusselt number is calculated as Eq.7 [22].

$$Nu = 0.59(GrPr)^{1/4} \tag{7}$$

where $Gr = \frac{g\beta(T_s - T_\infty)L^3}{\nu^2}$ and $Pr = \frac{c_p \mu}{k}$.

The hand calculation predicts a heat removal rate, which differs by 20% from the STAR-CD results, see Tab II.

Table2

E. LOHS and LOF Accident with Immediate Beam Stop using an Ansaldo Type RVACS

The air circuit of the RVACS design is physically separated from the guard vessel [19], see Fig.6. The cooling air flows in 80 U-pipes of 15.2cm diameter positioned concentrically around the guard vessel.

Figure 6. Schematic view of the Ansaldo RVACS.

Compared to conventional RVACS the Ansaldo design is improved in the sense that in case of a rupture of both the guard and reactor vessel radioactive particles cannot be transported to the atmosphere. The heat removal capability is slightly impaired in comparison to a conventional RVACS. The temperature evolution in the reactor vessel wall for the case of an Ansaldo type RVACS can be seen in Fig.7.

Figure 7. Temperature evolution in the reactor vessel wall above the HX in a 80MWt reactor for PRISM and Ansaldo type RVACS.

F. LOHS and LOF Accident with a Delayed Beam Stop using a PRISM Type RVACS

This calculation assumes that the proton beam continues to operate for 30 minutes after the accident initiation, and the core power generation remains at normal operating power of 80MW during this period. However, this is a highly unlikely scenario since in case of a Loss-of-Power (LOP) accident the accelerator would loose its power supply too.

During these 30 minutes the average coolant temperature increases rapidly at about 1K per 4 seconds. The wall temperature will increase to 1123K, see Fig.8. Fast vessel creep does

not commence, but the ASME level D is exceeded for about 4 hours. The 30 minutes delay of beam stop will create a hot cloud in the upper part of the reactor vessel, which hinders the coolant to flow over the separating cylinder between the riser and the downcomer. Thus, the decay heat removal relies on conduction instead of convection until the hot cloud has dissolved about 2 hours after beam stop. Because of the blockage of the normal flow path, swirls develop in the remaining regions.

Figure 8. Temperature evolution when the beam stop is delayed by 30 minutes in an 80MWt reactor.

For a helium cooled ADS, the grace time would decrease to some tens of seconds in a severe cooling or depressurization accident because of the low heat capacity of the helium coolant [20].

G. LOF Accident with Immediate Beam Stop using a PRISM Type RVACS

A pure Loss-of-Flow accident was also examined on the Ansaldo reactor. For this design which does not have any mechanical pumps, a LOF accident means that the bubble injection above the core is interrupted. Thus the coolant is driven by natural convection only. The calculations showed that the Ansaldo design copes well with a LOF accident. The coolant flow rate remains more than half the steady state velocity due its to good natural circulation capability, e.g. the pressure drop through the core is very low. The temperature at the core outlet will increase only 80K, which will cause no problems for the structural materials, see Fig.9.

Figure 9. Temperature evolution in the reactor vessel above the heat exchanger and the coolant velocity evolution above the core after a LOF accident.

H. LOHS Accident with Immediate Beam Stop using a PRISM Type RVACS

Relative to a LOF accident, a Loss-of-Heat-Sink (LOHS) accident causes much more severe problems regarding elevated temperatures of structural materials, see Fig.10. This is

of course due to the fact that a large amount of energy is inserted into the coolant and much less is removed. Compared to the combined LOHS and LOF accident discussed earlier the reactor vessel wall temperature increases somewhat slower and decreases more rapidly due to the fact that the heat is distributed more evenly in the coolant, i.e. a hot cloud is not established in the upper part of the vessel.

Figure 10. Temperature evolution in the reactor vessel after a LOHS accident.

I. Use of a Passive Melt-Rupture Disc to Interrupt the Proton Beam in Case of a Delayed Beam Stop

A melt rupture disc can be inserted in the side of the vacuum pipe in order to switch off the accelerator proton beam once the coolant temperature exceeds a predesigned temperature limit. Hence, the beam pipe would be flooded with Pb/Bi and the impact point of the proton beam relocated from the core to the upper region of the vessel, only the three MW from the proton beam plus the decay heat generation from the core will be deposited in the coolant instead of 80MW. Thus, the melt rupture disc increases the grace time from 30 minutes to 6 hours before a total beam shut-off is needed.

A LOHS and LOF accident with a 3MW heat source in the upper part of the primary pool together with core decay heat in the lower section leads to a difficult natural circulation problem. Again, a hot cloud of Pb/Bi coolant is created in the upper region of the vessel, which disturbs the normal coolant flow path until the cloud is dispersed. After about 7 hours the wall temperature will surpass the fast creep limit, see Fig.11.

Figure 11. Temperature evolution in the reactor vessel wall above the HX with a melt rupture disc used on the vacuum pipe.

V. ENHANCED NATURAL AIR CONVECTION COOLING AND OTHER HEAT REMOVAL IMPROVING MEANS FOR A 250MWT ADS REACTOR

A. LOHS and LOF Accident with an Immediate Beam Stop using a PRISM Type RVACS

Investigations on the heat removal from a higher power ADS reactor were also performed. This is of interest since future ADS plants will have a higher power generation relative to the vessel surface area than the 80MWt Ansaldo design. According to the designers from Ansaldo, the power can be upgraded from 80MW to 250MW in the present vessel [21].

The accelerator proton beam is interrupted immediately after the LOF and LOHS accident initiation. Relative to the 80MW reactor the peak appears 18 hours later and at 127K higher temperature due to the greater heat generation to surface area ratio. The average coolant velocities above the core will stabilize at slightly more than 3cm/s. Figure 12 displays the reactor vessel wall temperature evolution.

Figure 12. Temperature and velocity evolution at core outlet 250MWt reactor.

B. LOHS and LOF Accident with an Immediate Beam Stop using a PRISM Type RVACS with 10m Tall Chimneys

A taller RVACS loop increases the static pressure difference between the riser and the downcomer due to the fact that gravity will act on a taller column of air. However, the increased length and the bends also increase the pressure drop, which has a negative effect on the heat removal. Chimneys will improve the heat removal only if the static pressure difference increase is greater than the pressure drop. Ten meter tall chimneys are accordingly only advantageous when the reactor vessel exceeds a temperature of about 700K. For an immediate beam stop of an 80MWt design the chimneys will have a negative effect on the heat removal rate, since the vessel temperature is relatively low. However, for the 250MWt reactor chimneys have a positive effect on the heat removal rate because of the higher coolant

temperatures. Straight 10m chimneys lower the maximum reactor vessel wall temperature by 18 degrees, whereas chimneys with step bends reduce the temperature by only 6 degrees, see Fig.13.

Figure 13. Temperature evolution in the reactor vessel wall above the HX in 250MW reactor. Calculations were performed with and without chimneys.

C. LOHS and LOF Accident with an Immediate Beam Stop and a Higher Emissivity of the Vessel Walls

The radiation heat transfer between the reactor and guard vessel is significantly improved if the emissivity is increased on their opposing wall surfaces. This is because a large fraction of the heat transfer between the vessels is by radiation. On a 250MWt reactor the maximum temperature of the reactor vessel wall is lowered by 34K as the emissivity is increased from 0.7 to 0.9, see Fig.14.

Figure 14. The temperature evolution in the reactor vessel wall above the HX. Calculations with 0.7 and 0.9 emissivity on the reactor and guard vessel wall.

Equation 8 describes the radiation heat transfer between infinite concentric cylinders [22], which gives an idea how the emissivity influence the radiation heat transfer between the vessels. A change of emissivity from 0.7 to 0.9 at $T_1 = 600K$ and $T_2 = 400K$ shows an increase of radiation heat transfer by a factor 50.

$$q_{12} = \frac{\sigma A_1 (T_1^4 - T_2^4)}{\frac{1}{\varepsilon_1} + \frac{1-\varepsilon_2}{\varepsilon_2}\left(\frac{r_1}{r_2}\right)^2} \tag{8}$$

where suffix 1 represent the inner vessel and suffix 2 the outer vessel.

D. LOHS and LOF Accident with an Immediate Beam Stop using Water Spray Cooling and Filling of the Gap Between the Vessels

To decrease the coolant temperatures rapidly in LOHS and LOF accident events, water spray cooling can be used on the guard vessel outside [23]. Since the evaporation process of

water droplets consumes large amounts of energy, spray cooling can be employed to boost the operation of conventional RVACS. This could be favorably utilized on larger power systems to decrease the temperatures of structural materials more rapidly.

In this examination, the heat removal from evaporation of water droplets is calculated analytically. The droplet size was chosen as 2mm diameter and the spray flow rate as 100kg/s. The heat transfer efficiency for these parameters is about 0.1 above 500K. At 500K the heat removal from the guard vessel is around 30MW. The heat transfer efficiency is basically defined as the ratio between the fraction of the droplet that is actually evaporated to the total energy needed to heat and evaporate an entire droplet, see Eq.9 [24]. As a conservative approach, the heat transfer efficiency is assumed to decay linearly to zero between 500K to 373K.

$$\varepsilon = \frac{Q}{m_d(h_{fg} + c_p \Delta T_{sub})N} \tag{9}$$

where Q is energy transferred to the spray, m_d mass of droplet, h_{fg} latent heat of vaporization, c_p specific heat, ΔT_{sub} subcooling temperature, and N is the number of droplets in a square plane.

To increase the heat transfer between the reactor and the guard vessel, the gap is filled with Pb/Bi coolant. Hence, good heat conduction between the reactor and guard vessel is accomplished, concurrently with effective heat removal through evaporation of droplets. As can be seen in Fig.15, the decay heat removal exceeds the decay heat generation within a few minutes after the LOHS and LOF initiation. The ASME level C is not exceeded for the reactor vessel wall.

Figure 15. The temperature evolution in the reactor vessel wall above the HX. Water spray cooling was used on the guard vessel surface and the gap between the vessels was filled.

E. LOHS and LOF Accident with Immediate Beam Stop in a Sodium Cooled Reactor

For reasons of comparison to traditional liquid metal coolants a calculation was performed with sodium (Na) instead of Pb/Bi. The density and specific heat of these two

coolants are very different. For Pb/Bi the conductivity, ρ, is 10234kg/m^3 and the specific heat, c_p, is 0.147kJ/(kg·K) at 644K, whereas for Na these are 860.2kg/m^3 and 1.30kJ/(kg·K), respectively, at the same temperature. The product of the density and the specific heat determines the heat capacity. The heat capacity turns out to be of the same order of magnitude, hence the temperature evolution after a LOHS+LOF accident is rather similar for these two coolants, see Fig.16.

Figure 16. Temperature evolutions in the reactor vessel wall above the HX in 250MWt sodium and Pb/Bi-cooled reactors.

F. LOHS and LOF Accident with Delayed Beam Stop using PRISM Type RVACS

The grace time until an accelerator beam stop is needed is naturally shorter for a 250MW reactor compared to an 80MW design. A beam stop delay of more than 6 minutes exceeds the ASME level C, whereas 12 minutes is the limit to avoid fast vessel creep (1173K). Figure 17 shows the temperature evolution in the reactor vessel at delays of beam stop for 6, 12 and 18 minutes.

Figure 17. The temperature evolution in the reactor vessel wall above the HX for different delays of beam shut-off.

VI. CONCLUSIONS

The calculations of the worst case cooling accidents in the 80MWth Ansaldo ADS show that an RVACS with air-cooling is a very attractive passive approach for lower power systems. For the 80MWt design a 30 minutes delay of the beam stop can be tolerated without getting into fast creep. A melt-rupture disc can be used on the vacuum pipe which will relocate the impact point of the proton beam if elevated coolant temperatures are reached. This increases the grace time from 30 minutes to 6 hours the accelerator should be definitely switched off.

Other measures for improving the RVACS performance were also evaluated for a 250MWt system in the same vessel. An increase in the emissivity between the guard and the reactor vessel will reduce the maximum reactor vessel wall temperature during the accident by 34K. The use of chimneys with and without bends lower the maximum vessel temperature by 6 and 24K, respectively. Water spray cooling on the guard vessel outside together with the filling of the gap between the reactor and the guard vessel with liquid Pb/Bi was investigated. It leads to a rapid cooling down of the ADS once the beam is switched off.

A general conclusion of this research is that the delay of the beam shut-off after a cooling accident initiation is the most critical parameter. For Pb/Bi systems the grace time is largest. For Na cooling and for helium cooling is particularly short.

VII. ACKNOWLEDGEMENTS

The European Commission funded this project and Prof Waclaw Gudowski made valuable comments.

REFERENCES

[1] , Van Tuyle, G.J., Slovik, G.C., Chan, B.C., Kennett, R.J., Cheng, H.S., Kroeger, P.G., "Summary of Advanced LMR Evaluations - PRISM and SAFR, Brookhaven National Laboratory", 87-91, (Oct. 1989)

[2] Baumeister, E.B., et al., "Inherent Safety Features and Licensing Plan of the SAFR plant", *Proc. Int. Conf. on Fast Breeder Systems, (Sept. 1987)*

[3] Delpech, M., "The Am and Cm transmutation - physics and feasibility", *Proc. Int. Conf. on Future Nuclear Systems, GLOBAL99* (1999)

[4] Computational Dynamics Ltd., *Methodology Volume 3.10a* (2000)

[5] Cheng, X., M*ü*ller, U., "Turbulent natural convection coupled with thermal radiation in large vertical channels with asymmetric heating", *Int. J. Heat Mass Transfer* **41**, 1681-1692 (1998)

[6] Hunsbedt, A., Magee, P.M., "Design and performance of the PRISM natural convection decay heat removal system", *Proc. Int. Topical Meeting on Safety of Next Generation Power Reactors*, 844-851, (1988)

[7] Karlsson J., "Decay Heat Removal by Natural Convection and Thermal Radiation from the Reactor Vessel", *3rd Int. Conf. on Accelerator Driven Transmutation Technologies and Applications* (1999)

[8] Hung, T-C., "The model development of a passive system and its application in residual heat removal", *Proc. of the 1994 International Mechanical Engineering Congress & Exposition*, 41-51, Chicago, USA (Nov. 1994)

[9] Cinotti, L., Corsini, G., *A proposal for enhancing the primary coolant circulation in an ADS*, ANSALDO Nucleare, unpublished (1999)

[10] , Buono, S., Rubbia, C., 1996, "Simulation of a Total Loss of Power accident in the

Energy Amplifier", *CERN/ET Internal note 96-015*, (1996)

[11] Pershagen, B., *Light Water Reactor Safety*, Pergamon Press, Oxford, England, pp.50 (1989), ISBN 0-08-035915-9

[12] Eckert, E.R.G., Drake, R.M., *Heat and Mass Transfer*, McGraw-Hill Book Company Inc., New York, USA, pp. 299 (1959)

[13] Rousanov, A.E., et al., "Design and study of cladding steels for fuel elements of NPP using heavy coolant", *Proc. Heavy Liquid Metal Coolants in Nuclear Technology, HLMC 98* (1998)

[14] Krieg, private communication to Wider H, (1999)

[15] Incropera, F.P., DeWitt, D.P., *Fundamentals of Heat and Mass Transfer*, John Wiley & Sons, New York, USA, pp.492-493 (1996)

[16] King, T.L., Landry, R.R., Throm, E.D., Wilson, J.N., *Preapplication, Safety Evaluation Report for the Sodium Advanced Fast Reactor (SAFR) Liquid-Metal Reactor*, U.S. Nucelar Regulatory Commission, 15-1 (1991)

[17] Pershagen, B., *Light Water Reactor Safety*, Pergamon Press, Oxford, England, pp.50 (1989), ISBN 0-08-035915-9

[18] Incropera, F.P., DeWitt, D.P., *Fundamentals of Heat and Mass Transfer*, John Wiley & Sons, New York, USA, pp.76-86 (1996)

[19] Cinotti, L., Corsini, G., *A proposal for enhancing the primary coolant circulation in an ADS*, ANSALDO Nucleare, unpublished (1999)

[20] Wider, H., Wilkening, H., Maschek, W., "Safety Advantages of Heavy Metal- Versus Gas-Cooled Accelerator Driven Systems", *3rd Int. Conf. on Accelerator Driven Transmutation Technologies and Applications* (1999)

[21] Cinotti, L., personal communication

[22] Incropera, F.P., DeWitt, D.P., *Fundamentals of Heat and Mass Transfer*, John Wiley & Sons, New York, USA, pp.739 (1996)

[23] Carluec B., Framatome, personal communication to H.Wider (1999)

[24] Delcorio, B., Choi, K-J., "Analysis of Direct Liquid-Solid Contact Heat Transfer in Monodispersed Spray Cooling", *J. of Thermophysics*, **5**, (1991)

Characteristic problem	**Temperature when problem occurs**
Corrosion of structural material	893K [13]
Creep of the reactor vessel	1173K [14]
Melting point AISI316	1670K [15]
ASME level C	922K [16]
ASME level D	977K [16]

TABLE I. Critical temperature limitations for structural materials and protective oxide layers.

Temperature coolant, [K]	**Hand calculation, [MW]**	**STAR-CD calculation, [MW]**
600	0.464	0.534
900	1.781	1.484

TABLE II. Hand calculation to verify the STAR-CD predictions.

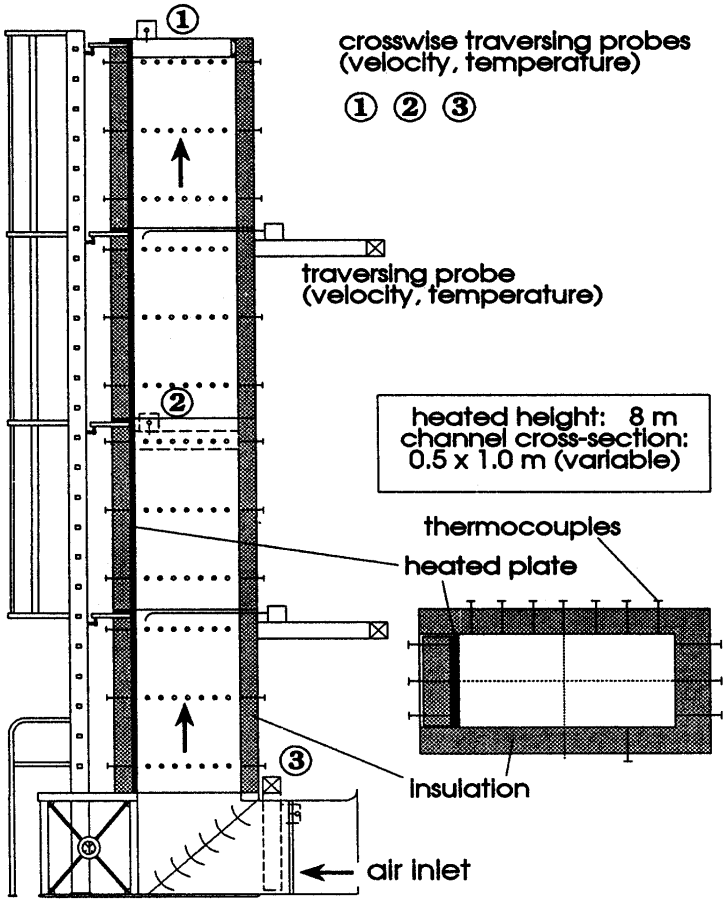

FIG. 1. Schematic view of the PASCO test channel.

FIG. 2. Schematic view of PRISM's RVACS.

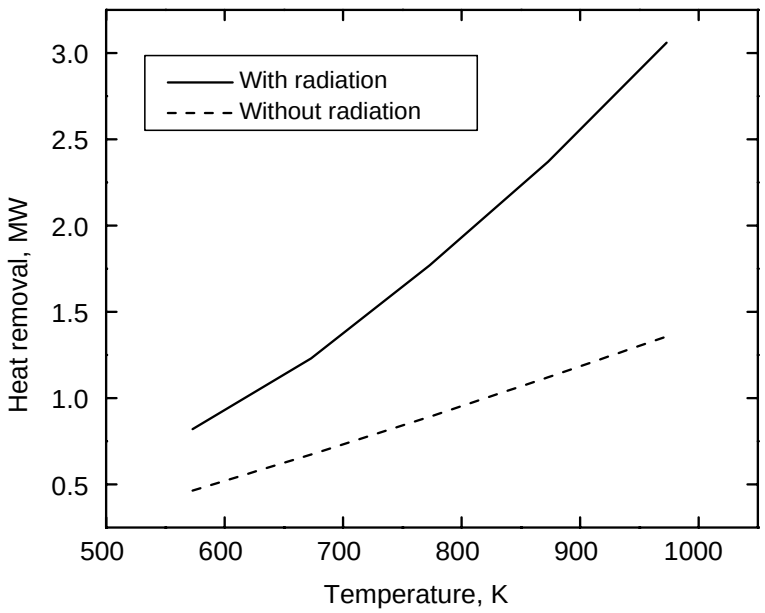

FIG. 3. Heat removal rate with and without radiation as a function of wall temperature.

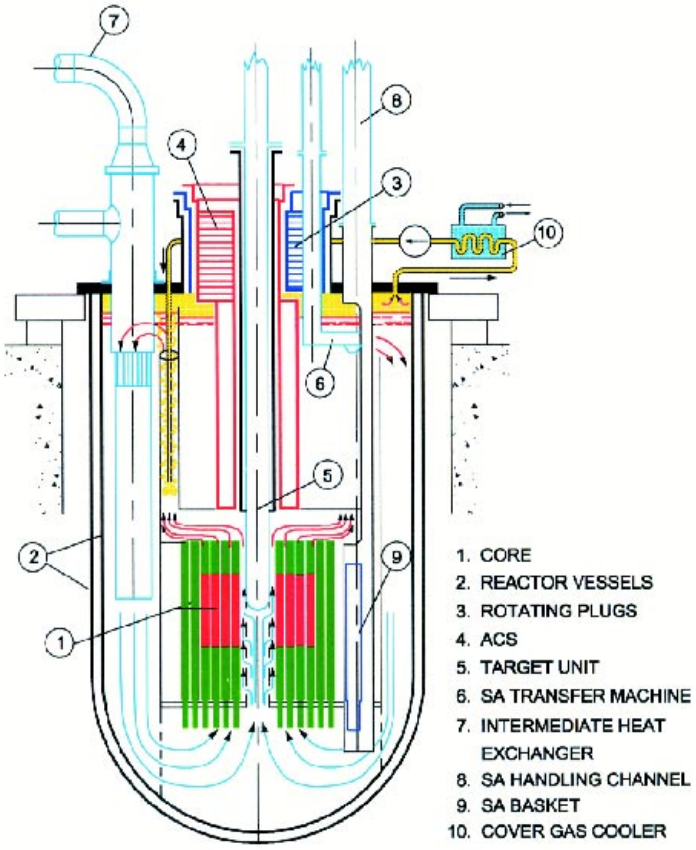

FIG. 4. Schematic view of the Ansaldo design.

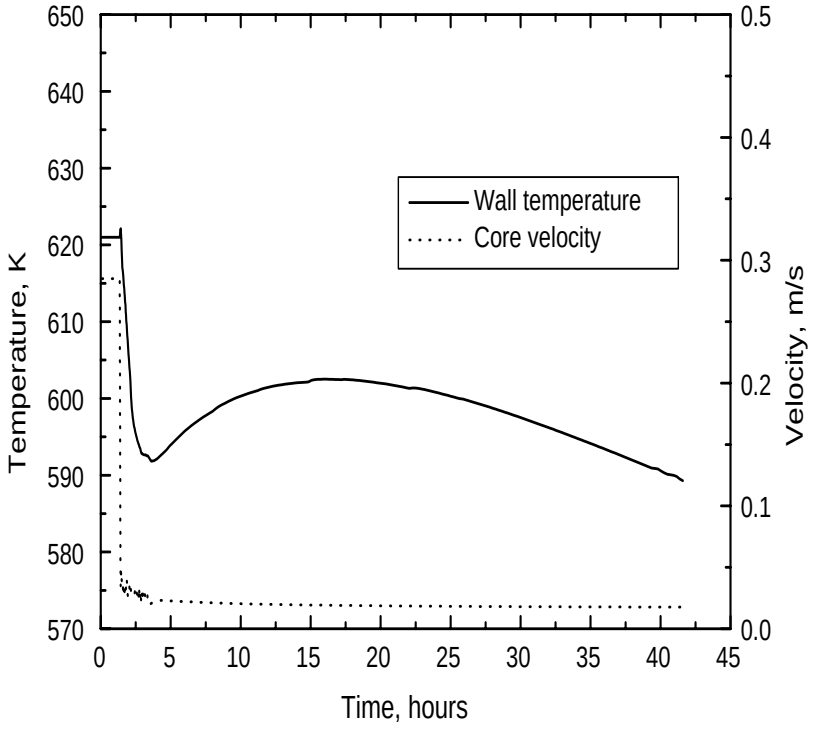

FIG. 5. Temperature and velocity evolution at core outlet in an 80MWth reactor.

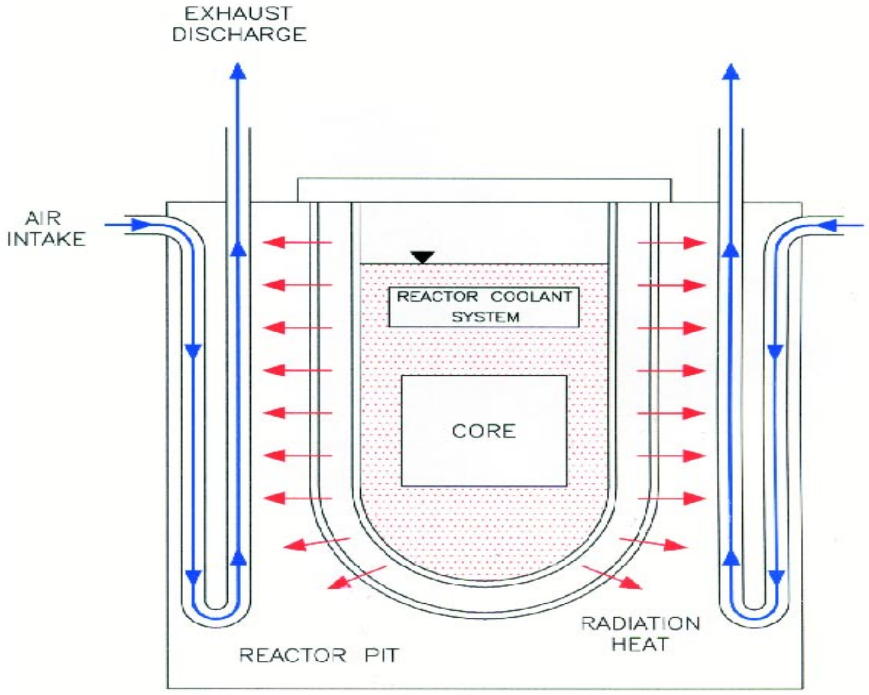

FIG. 6. Schematic view of the Ansaldo RVACS.

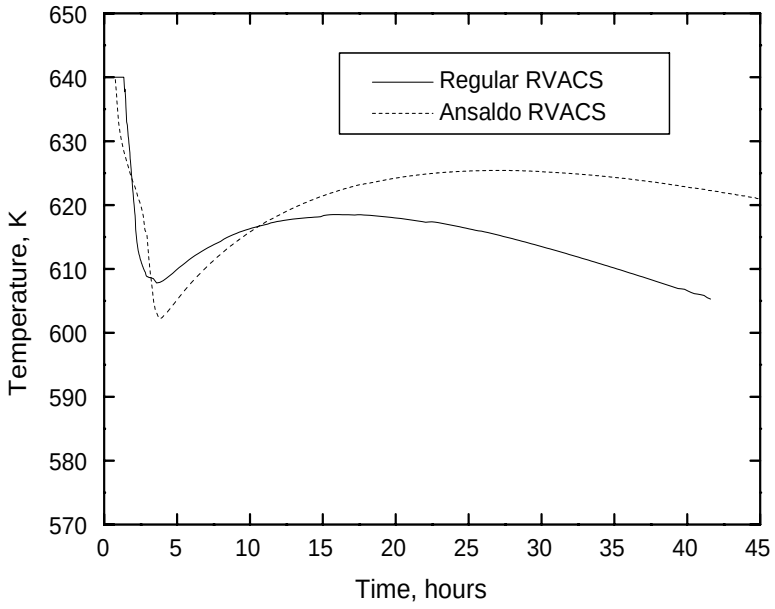

FIG. 7. Temperature evolution in the reactor vessel wall above the HX in a 80MWt reactor for PRISM and Ansaldo type RVACS.

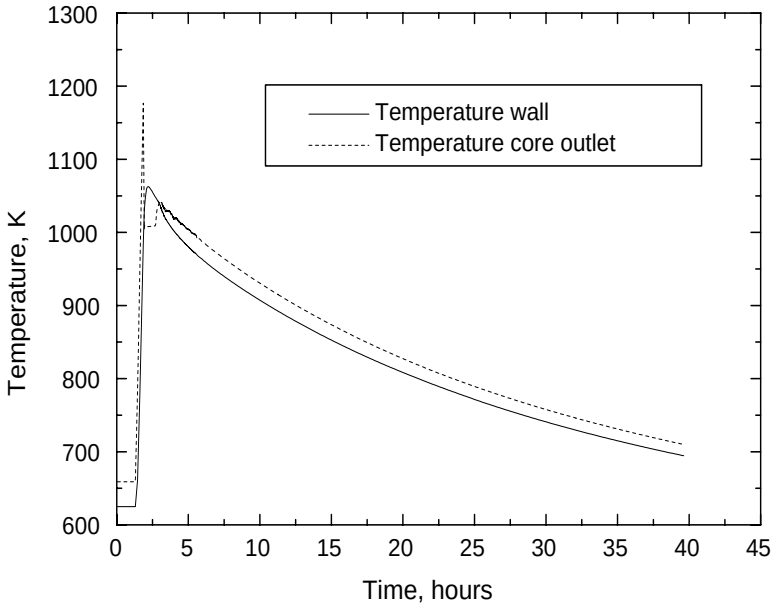

FIG. 8. Temperature evolution when the beam stop is delayed 30 minutes in an 80MWt reactor.

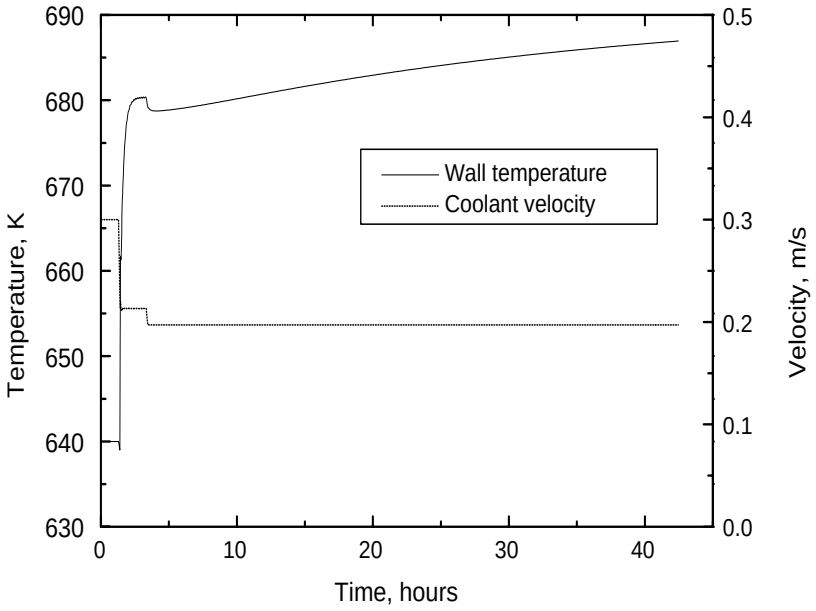

FIG. 9. Temperature evolution in the reactor vessel above the heat exchanger and the coolant velocity evolution above the core after a LOF accident.

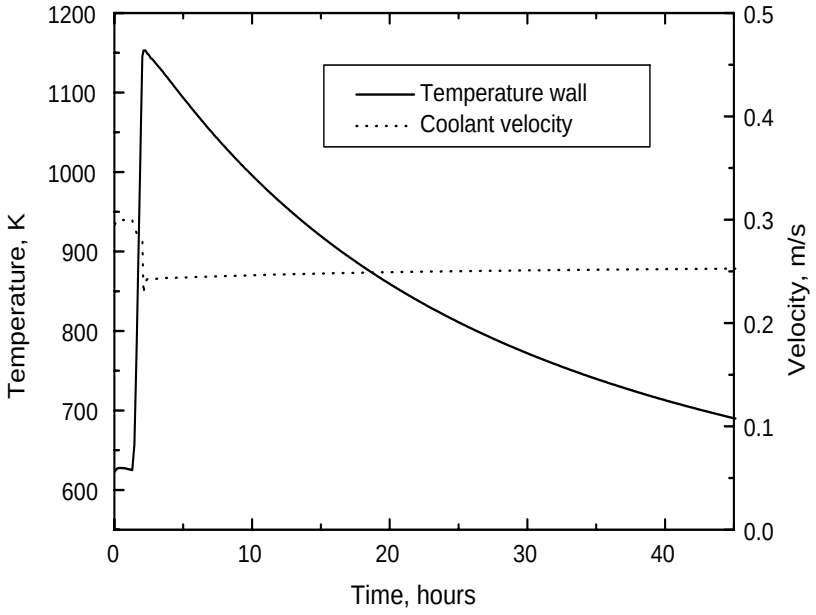

FIG. 10. Temperature evolution in the reactor vessel after a LOHS accident.

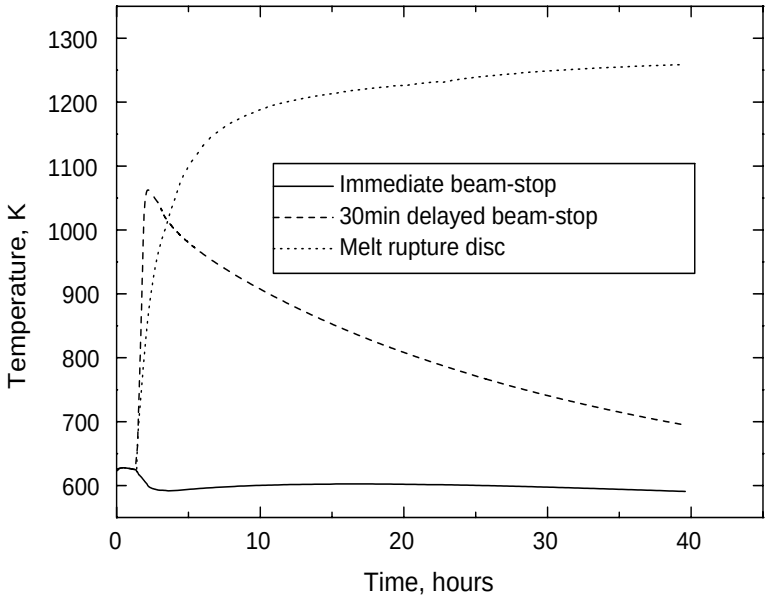

FIG. 11. Temperature evolution in the reactor vessel wall above the heat exchanger with a melt rupture disc used on the vacuum pipe.

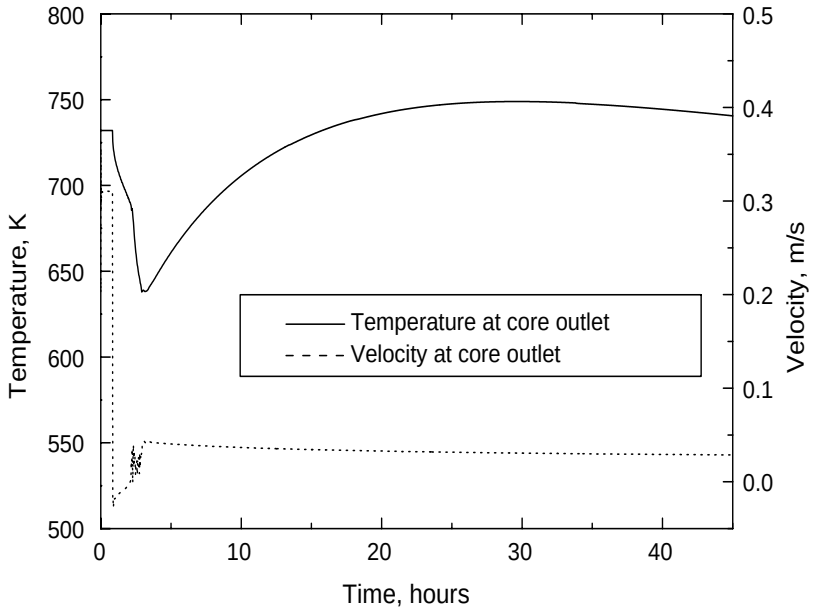

FIG. 12. Temperature and velocity evolution at core outlet of a 250MWt reactor.

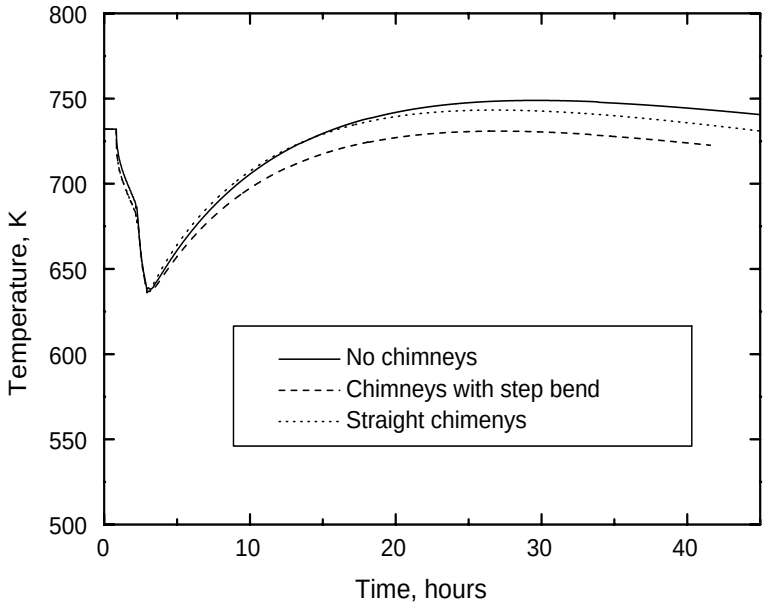

FIG. 13. Temperature and velocity evolution at core outlet of a 250MWt reactor.

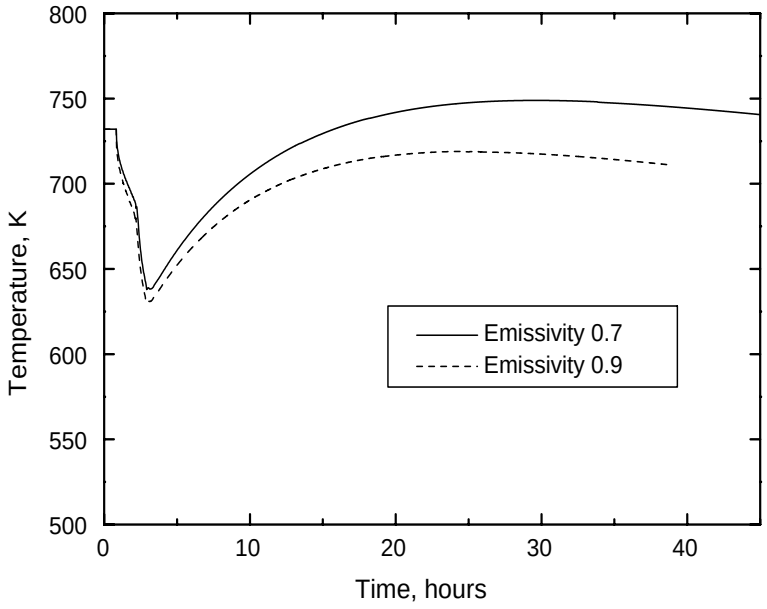

FIG. 14. The temperature evolution in the reactor vessel wall above the HX. Calculations with 0.7 and 0.9 emissivity on the reactor and guard vessel walls.

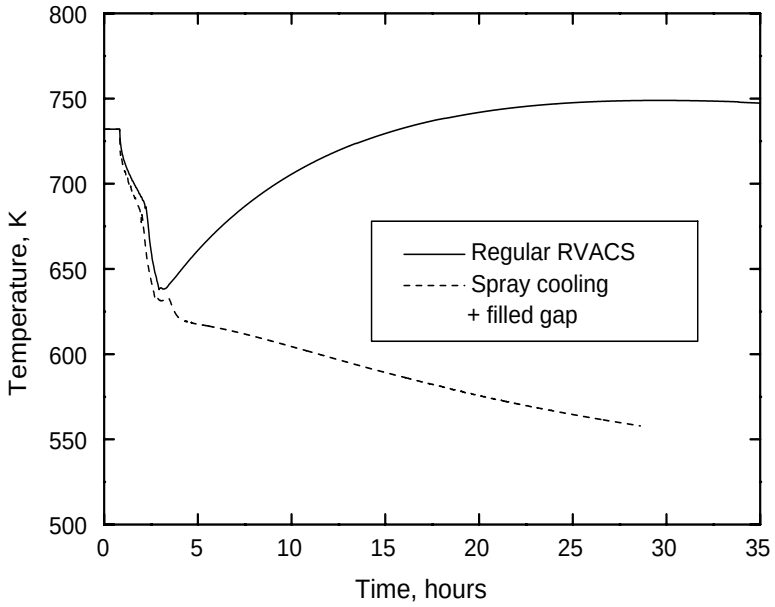

FIG. 15. The temperature evolution in the reactor vessel wall above the HX. Water spray cooling was used on the guard vessel surface and the gap between the vessels was filled.

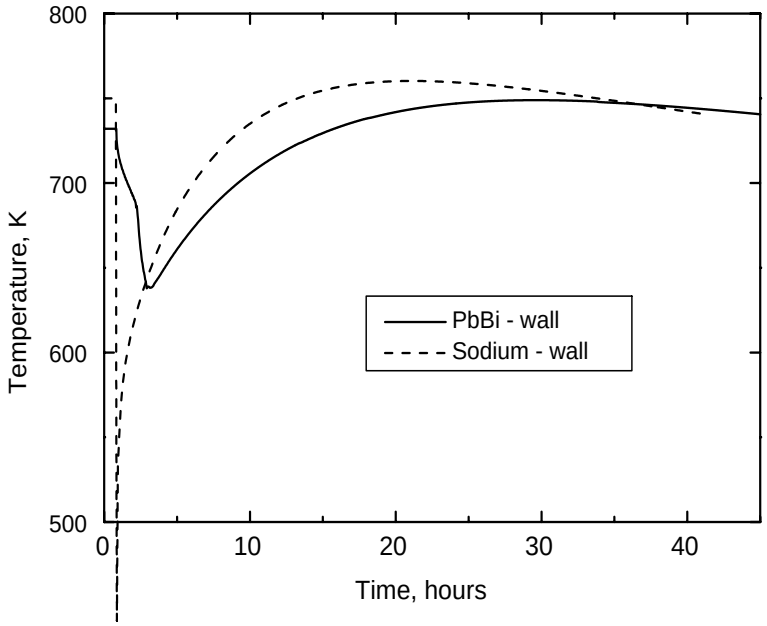

FIG. 16. Temperature evolution in the reactor vessel wall above the HX in a 250MWt sodium cooled reactor.

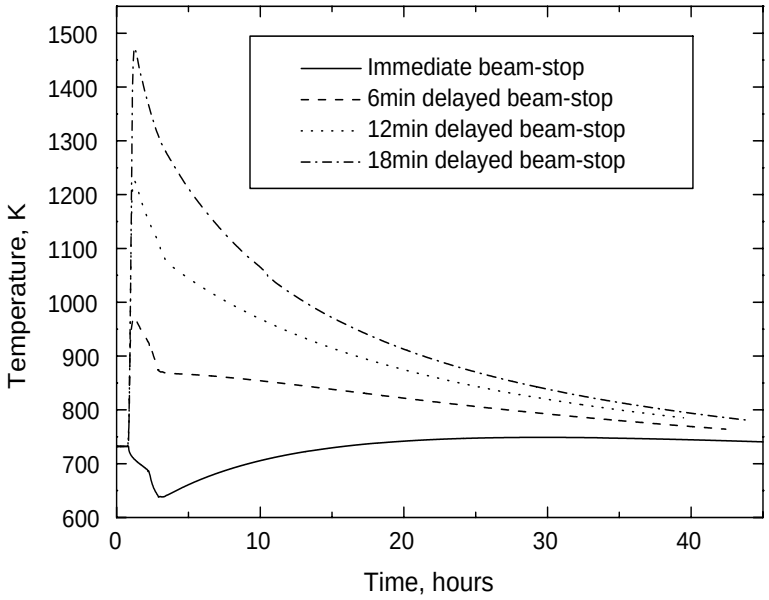

FIG. 17. The temperature evolution in the reactor vessel wall above the HX for different delays of beam shut-off.

APPENDIX 4

J. Carlsson, H. Wider, An investigation on locating the heat-exchangers in the riser of an Accelerator-Driven System' accepted for publication in the Annals of Nuclear Energy

An investigation on locating the heat-exchangers in the riser of an Accelerator-Driven System

Johan Carlsson *

Royal Institute of Technology, Department of Nuclear and Reactor Physics,

S-10691 Stockholm, Sweden

Hartmut Wider

Joint Research Center, Institute for Energy,

NL-1755 LE Petten, Netherlands

(22 October 2002)

Send invoice to:

Prof. Waclaw Gudowski

Department of Nuclear and Reactor Physics

Royal Institute of Technology

Stockholm Center for Physics, Astronomy and Biotechnology

Roslagstullsbacken 21

S-106 91 Stockholm

Sweden

Tel. +46 8 5537 82 00

Fax. +46 8 5537 84 65

E-mail. wacek@neutron.kth.se

Total number of pages in the preprint edition are 29.

*Email: johan@neutron.kth.se

Contents

List of Tables

List of Figures

Abstract - *The effect of locating the heat-exchangers in the risers of a 250 MW(thermal) accelerator-driven system was investigated. Apart from temperatures and velocities at normal operation, the accident scenarios loss-of-flow, loss-of-heat-sink, and a combined loss-of-flow and loss-of-heat-sink were examined. Assuming an immediate beam-stop after accident initiation, the loss-of-flow accident develops initially the highest core outlet temperatures of 1100 K after two minutes and 950 K after five minutes. The grace period before the accelerator proton beam should be shut off for a loss-of-heat-sink accident is ∼5 minutes. Flow guides and bypass routes were also incorporated in the design. The effect from these are evaluated in this paper and the results compared to a conventional design with the heat-exchangers in the downcomers. The computational fluid dynamics code STAR-CD was used in all calculations.*

I. INTRODUCTION

A general safety strategy for next generation nuclear power plants today is to increase their level of inherent and passive safety. This can be seen for example in the American Generation IV initiative [1] which states, "The evaluation of passive safety should be continued and passive safety measures incorporated into Generation IV nuclear energy systems whenever appropriate."... To incorporate passive safety measures is desirable for several reasons, first, the passive safety systems are very unlikely to fail since they depend on physical laws like for instance the thermal expansion of a fluid, second, the passive safety systems are in general less expensive than active systems since their construction is simpler and less supervision during operation is needed.

An inherent safety measure implemented for the Accelerator-Driven System with heat-exchangers in the risers (ADS-HXR) is, as the name implies, to locate the HX in the risers. In case of a leakage of steam from the secondary to the primary circuit, the buoyancy forces from the incoming low-density steam would work along the Pb/Bi-coolant flow direction instead of opposing it. The latter would be the case if the HXs are located in the downcomer.

A passive safety systems used on the ADS-HXR is the reactor vessel auxiliary cooling system (RVACS), which is the ultimate mean to remove decay heat in case the normal heat removal systems malfunction. RVACS were also planned for other designs like the power reactor inherently safe module (PRISM) [2] and the sodium advanced fast reactor (SAFR) [3]. The RVACS is a totally passive system, which is based on the principle of natural air convection around the guard vessel due to temperature differences in the riser and the downcomer of the RVACS.

A melt-rupture disc [4] is another passive safety system used on the ADS-HXR design. It is constructed on the accelerator vacuum beam pipe, where it is supposed to melt as the coolant temperature exceeds a certain predesigned limit. If melted, the coolant enters the vacuum pipe and hence the proton beam's impact point is relocated away from the core region. The core still generates decay heat and the proton beam inserts heat in the upper

part of the vessel, though, which has to be removed.

An Accelerator-Driven System (ADS) [5]is a type of nuclear power plant which is controlled by neutrons generated in a spallation process by an accelerator proton beam impacting on a heavy metal target. The core is sub-critical with a k_{eff} of normally about 0.93-0.97. The k_{eff} depends on for example parameters like the core design, on fuel type, coolant, and core life time. The ADS-HXR, uses Pb/Bi as coolant and moderator since it gives a hard neutron spectrum, good thermal properties, and generally good safety characteristics.

The main objective for the ADSs are their capability to reduce the amount of high-level nuclear waste by transmuting the transuranics (TRU; Pu, Ne, Cm and Am) and some of the most radiotoxic long-lived fission products (LLFP; ^{99}Tc, ^{129}I). By employing separation and transmutation the volume of the high-level waste could thus be reduced by about a factor of $\sim$100, and the effective radioactive dose from repository by a factor of $\sim$1000 [5,6]. Another positive consequence by employing ADS is the reduction of Pu inventory, which diminishes the risk of nuclear proliferation.

Section II describes the methodology used for this article. Section III presents the conceptual accelerator-driven system with the heat-exchangers (ADS-HXR) in the risers. In Sect IV are different accident scenarios are investigated for the ADS-HXR. The calculations are verified with hand calculations in Sect V. A comparison between a reactor where the HX are located in the risers with a reactor with the HX in the downcomers is performed in Sect VI. And, Sect VII investigates the importance of the flow guides and the by-pass routes. And finally, an investigation is done in Sect VIII performed on a reactor design of 800 MW(thermal).

II. METHODOLOGY

The investigations was initiated from the potential security enhancement by locating the HXs in risers instead of the downcomers of a Pb/Bi-cooled system. It was found that the natural convection was slightly impaired by locating the HXs in the risers after a LOF

accident, and hence countermeasures to reduce the pressure drops were examined. The influence from the usage of flow guides and bypass routes was investigated with regard to core velocities and core outlet temperatures during normal operation and accident events. Finally a comparison between locating the HXs in the risers and the downcomers was made.

The computational fluid dynamics (CFD) code STAR-CD was used for all calculations [7]. A second-order MARS scheme has been used to model the fluids' velocity, temperature, density, and viscosity. Time stepping was performed with a first-order implicit scheme. The calculations including the bypass route were three dimensional, whereas the remaining examinations were two dimensional.

The heat transfer correlation used on the air side was developed at the Argonne National Laboratory (ANL) within the American Liquid Metal Reactors' (ALMR) program, see Eq 1.

$$Nu = 1.22 \cdot Re^{0.456} Pr^{0.4} \tag{1}$$

The Nusselt number is defined as $Nu = hL/k$ where h is the heat transfer coefficient, L the characteristic length, and k the conductivity. Reynold's number is $Re = VL/v$ where V is the velocity in the bulk, and v the dynamic viscosity. The Prandtl number is $Pr = v/\alpha$ where α is the thermal diffusivity.

A correlation for liquid metals is used to calculate the heat transfer coefficient on the Pb/Bi coolant side, see Eq 2.

$$Nu = 0.565 Re^{0.5} Pr^{0.5} \tag{2}$$

III. THE CONCEPTUAL ACCELERATOR-DRIVEN SYSTEM WITH THE HEAT-EXCHANGERS IN THE RISERS

A. Design objectives

The incentive for placing the HXs in the risers was to increase ADS-HXR's level of inherent safety, see Sect III C. In general, inherent and passive safety was included where

it was seen as a safety enhancement for the ADS-HXR. For example, the ADS-HXR was designed to have a vessel with sufficiently large coolant heat capacity in relation to core power. The design margin was then examined for a LOF, a LOHS, or a TLOP accident, see Sect IV

B. Main characteristics

The ADS-HXR is a 250 MW(thermal) power reactor. The vessel is pool-type of 9 m height and 6 m diameter. A schematic drawing of the ADS-HXR can be seen in Fig 1 and the main design parameters can be found in Tab **??**.

Figure 1. Schematic view of the ADS-HXR.

Table I. Main characteristics of the ADS-HXR.

To reduce the risk for radioactive release or a loss-of-coolant accident (LOCA), a guard vessel encloses the reactor vessel. The vessel walls are made of steel AISI 316L. Also, the walls which separate the risers and the downcomers are assumed to be made of steel of the same properties. The temperature limits for structural materials and protective oxide layers are presented in Tab III B.

Table II. Critical temperature limitations for structural materials and protective oxide layers.

The coolant and the moderator of the ADS-HXR is Pb/Bi eutectic. Due to the heavy weight of the Pb/Bi atoms a relatively small amount of energy is lost in each collision between the neutrons and Pb/Bi. Thus the neutron spectrum is hard and has good transmutation potential for LLFPs and TRUs well. The Pb/Bi has good thermal properties, like for example high conductivity and a beneficial thermal expansion coefficient. Moreover, it is chemically stable and does not create violent chemical reactions with water nor air. However, eutectic Pb/Bi coolant is relatively corrosive and erodes structural materials. The corrosion can be mitigated by mixing the coolant with a specific amount of oxygen. The oxygen together with the ? will create ?, which act as a protective oxide layer on structural materials.

Hence their life time is increased significantly. Coolant velocities higher than 3m/s and coolant temperatures higher than 873K should be avoided in order to maintain the oxide layer [9,13].

Enhanced natural convection [8] is used instead of conventional pumps (this is not 100% sure) to regulate the flow rate in the ADS-HXR design. This means that argon gas is injected into the hotter region above the core in order to decrease the density further. Thus, the static pressure difference is increased between the riser and the downcomer and the circulation of coolant is increased. After passing the riser the gas exits via the the Pb/Bi coolant surface where it is collected and later re-injected into the riser [8]. The gas compressors are located outside the reactor vessel and are easily accessible for maintenance work.

The accelerator power needed for the SSC at BOL is ∼4.5M and at EOL ∼9MW. The proton beam impacts into a Pb/Bi target where endothermic nuclear reactions occur, thus about 75% of the initial accelerator power has to be removed, i.e. ∼7MW at EOL [14]. The target cooling is managed in a separate circuit.

Passive beam shut-off devices will be used to ensure interruption of the accelerator proton beam in case elevated temperatures are reached. The beam-stop device is a melt-rupture disc [4], would flood the accelerator vacuum pipe as a certain pre-designed temperature is exceeded. Passive devices that would shut-off the accelerator proton beam more quickly are under construction by the authors.

If the normal heat removal and safety systems fail, the ultimate mean to remove the decay heat generated in the core is the RVACS which functions by natural air circulation around the reactor vessel. The RVACS is totally passive and is driven by buoyancy forces in the air coming from the temperature differences between the riser and the downcomer of the RVACS, see Fig 2. The RVACS add to a parasitic loss of heat of about ?% during normal operation.

Figure 2. Schematic view of the RVACS of ADS-HXR.

C. The heat-exchanger positioned in the riser

The probability for a leakage of steam from the heat exchangers is between 10^{-1} to 10^{-2}. The consequence of such a leak depends of course on its size. A potential core cooling problem could be a larger steam leakage from the heat-exchangers (HX) when positioned in the downcomers'. This is due to the fact that the incoming steam would lessen the average density in the downcomer and thereby reduce the static pressure difference between the riser and the downcomer. To mitigate this effect from the inflowing steam the ADS-HXR's XSs are positioned in the riser of the vessel. Thus with regard to this accident scenario, a safety enhancement has been achieved in case steam leaks from the secondary circuit into the Pb/Bi coolant of the primary circuit.

In these investigations it was found that the pressure drop through the core and the HXs limit the coolant velocity quite severely during normal operation as well as during accident events. Even though the gas injection rate is 10 volume percent in the riser of the ADS-HXR design the flow rate at normal operation is $\sim$75% of the HXD design and gas injection rate of 4 volume percent.

D. Natural convection improvements

Lower pressure resistances are desirable because it means that less force is needed to drive the flow, regardless if this force is external or internal. During normal operation the power needed to maintain a certain flow rate would be reduced. Whereas during LOF accidents, the benefit from lower pressure drops is improved natural circulation and reduced core outlet temperatures.

Flow guides are introduced below and above the core, see Fig 1. The flow guide below the core turns the coolant smoothly upwards to the core. Similarly, after core outlet a circumferential S-bend guides the coolant past the Above Core Structures (ACS), see Fig 1. The reduction of pressure drop during normal operation is recognized as a velocity increase

of ?% through the core, see Sect VII for more information.

Since the coolant flow rate is impeded by the HXs, a low pressure drop BPR was constructed in parallel to the HXs. If the gas injection malfunctions, the coolant primarily chooses the BPR due to its lower pressure resistance. Thus the coolant velocities will become higher and decreases the temperature at core outlet compared to the design without BPRs.

To alleviate the natural convection flow after accidents, bypass routes (BPR) with low pressure drop were constructed in parallel with the HXs, see Fig 1. On the downcomer's side the BPR covers all the circumference by a ten centimeters passage next to the vessel wall. Argon gas is injected into the BPR also during normal operation in order to avoid backward flow, however, at a lower rate. The gas injection is balanced so that the velocities through the BPRs are as low as possible, due to that the main share should pass the HXs.

Since hot coolant passes the BPR during normal operation as well as in accident events, the heat removal by RVACS will work more efficiently. Another positive effect from the BPR is lower thermal stress on the reactor vessel wall is expected for a LOHS accident since the downcomer after the HX is physically separated from the reactor vessel. In a conventional design with the HX in the downcomers a rapid temperature transient appears in the reactor vessel below the HX if the pumps in the secondary system trips or the heat removal is stopped. This exerts the vessel for large thermal stresses [15]. The drawback of having hot coolant next to the reactor vessel wall also during normal operation is a larger parasitic loss. This could probably be solved by using a liner next to the reactor vessel wall. Coolant overflow of the liner would then appear in accident situations, after a certain thermal expansion of the coolant is attained. From there on the heat transfer is by convection instead of by conduction.

IV. EXAMINATION OF DIFFERENT ACCIDENT SCENARIOS FOR ADS-HXR

During normal operation the average velocity through the hottest channel is ? m/s and the temperature at core outlet is ? K.

A. Total-loss-of-power accident

A total-loss-of-power (TLOP) accident could be initiated by a station blackout. Thus, the normal heat removal systems stop to function, the argon gas injection stops, and the accelerator proton beam is off. Nevertheless, the core will generate decay heat of about ∼6.2% normal power immediately after the accident initiation and ∼1% of normal power after one hour. The reactivity feedbacks in this accident scenario have small influence on the power generation also when the proton beam is still on [4,16]. To ensure the integrity of the reactor components the decay heat has to be removed. For the ADS-HXR the ultimate emergency decay heat removal system is planned to be an RVACS.

The temperature and velocity evolution at core inlet and outlet after a TLOP accident can be seen in Fig **??**. The reactor vessel wall temperature can be seen Fig ?.

Figure 3. Temperature and velocity evolution at core outlet and in the reactor vessel wall after a TLOP accident.

A scenario with very low probability is that all systems stop except the accelerator proton beam. The grace period before the proton beam has to be shut off is ? minutes in order to avoid damages on structural materials, see Fig ?.

B. Loss-of-flow accident

During a loss-of-flow (LOF) accident the argon gas injection malfunctions, the enhanced circulation will gradually reduce until all argon gas has disappeared through the Pb/Bi surface. Twenty seconds after accident initiation the effect from the gas injection has more or less disappeared and the coolant flow relies on natural convection.

For a LOF accident the proton beam is assumed not to be interrupted and the core produces full power. Owing to the loss of enhanced convection the velocities in the core will be reduced severely, the temperature at core outlet peaks at 1150K after two minutes. At that point the buoyancy forces from the hot coolant starts to make a difference and 3 minutes later the temperature at core outlet has decreased to 950K. The reactor vessel temperature increases slower; it takes ?? minutes before the wall reaches critical limits. Figure **??** depicts the temperature evolution after a LOF accident.

Figure 4. Temperature evolution at core outlet and in the reactor vessel wall after a LOF accident.

In any case, to avoid damages on structural materials after a LOF accident, the accelerator proton beam should be shut down as soon as possible.

C. Loss-of-heat-sink accident

If the normal heat removal system fails whereas the core continues to operate at normal powers the average coolant temperature will on average increase by $\sim$1.4 K/s. Since the enhanced convection still functions and the coolant flows at high rate the heat is well distributed. As rapid temperature transient as for the LOF accident does not appear because the coolant velocities are maintained. Nevertheless, the coolant temperatures increase steadily and after about 5 minutes the accelerator proton beam should be shut off in order to avoid severe damage on structural materials. The temperature evolution at core outlet is displayed in Fig **??**.

Figure 5. Temperature and velocity evolution at core outlet and in the reactor vessel wall after a LOHS accident.

V. VERIFICATION OF THE 250MWT CALCULATION

A. Four Times Finer Mesh

As was presented in earlier articles [17], the STAR-CD code predicts natural air convection flows satisfactorily. A hand calculation is executed to validate the results, see Sect V B

B. Hand Calculation

The heat removal rate was also estimated by a hand calculation. The total thermal resistance, $\sum_{p=1}^{N} R_p$ can be defined as the ratio between the overall temperature difference $\sum_{p=1}^{N} \Delta T_p$ to the heat flux used q, see Eq.3 [**?**].

$$\sum_{p=1}^{N} R_p = \frac{\sum_{p=1}^{N} \Delta T_p}{q} \tag{3}$$

where $\Delta T_p = T_p - T_{p+1}$ is the temperature difference between two facing walls or between two surfaces of the same wall. The resistance in the walls is calculated from Eq.4.

$$R = \frac{l}{k} \tag{4}$$

where l is the wall thickness and k is the wall conductivity.

The heat transfer between parallel walls is a combination of radiation and convection. Consequently the thermal resistance between two parallel walls is calculated according to Eq.5.

$$R^* = \frac{1}{\{Nu\frac{k}{l} + \frac{\epsilon\sigma}{2-\epsilon}(\theta_p^2 + \theta_{p+1}^2)(\theta_p + \theta_{p+1})\}} \tag{5}$$

where $Nu = \frac{hL}{\kappa}$, ϵ surface emissivity, σ Stephan-Boltzmann constant, θ temperature in K [12].

For natural convection between vertical plates the Nusselt number is calculated from Eq.6 [12].

$$Nu = 0.59(GrPr)^{1/4} \tag{6}$$

where $Gr = \frac{g\beta(T_s - T_\infty)L^3}{\nu^2}$ and $Pr = \frac{c_p \mu}{k}$.

The hand calculation predicts a heat removal rate, which differs by ?% from the STAR-CD results, see Tab **??**.

Table III. Hand calculation to verify the STAR-CD predictions.

VI. COMPARISON BETWEEN LOCATING THE HX IN THE RISER AND THE DOWNCOMER

An investigation on coolant flow velocities and temperature was also performed with regard to the effect from locating the HXs in the risers instead of the downcomers of the reactor vessel. The reactor vessel and the core geometry was preserved in all calculations. Moreover, the cross-section and the length of the HXs were the same in all analyzes.

The reactor vessel with the HXs in the downcomers was shown to have better natural convection characteristics. This is mainly due the efficiency of the HX which determine the distance between the thermal centers of the core and the HXs. Moreover, the coolant velocities are more evenly distributed in the HXs of the downcomers, which reduce the pressure maximums.

A. Total-loss-of-power accident

The core outlet temperature differs ? K between the ADS-HXR and the design with the HXs in the downcomers. The temperature evolution at core inlet, and outlet after accident initiation is displayed in Fig. **??**. The velocity through the core is about ?% lower for the ADS-HXR design.

Figure 6. Temperature and velocity evolution at core outlet and in the reactor vessel wall after a TLOP accident.

B. Loss-of-flow and loss-of-heat-sink accidents

For the loss-of-flow accident their is a temperature spike of 1150K for ADS-HXR, whereas the Ansaldo design peaks at 920K. The reason for the spike in the ADS-HXR is that the velocity in the HXs drops quite rapidly and pressure build in the coolant thereafter needs some time to redirect the flow to the BPRs.

After ∼5 minutes the temperature difference at core outlet has stabilized at 40K, see Fig **??**.

Figure 7. Temperature and velocity evolution at core outlet and in the reactor vessel wall after a LOF accident.

C. Loss-of-heat-sink accident

For the loss-of-heat-sink accident the temperature right after accident initiation is about ?K higher for the ADS-HXR. Five minutes afterwards the difference is reduced to 40K. Figure **??** depicts the temperature evolution at core outlet for the ADS-HXR and the Ansaldo designs.

Figure 8. Temperature and velocity evolution at core outlet and in the reactor vessel wall after a LOHS accident.

VII. INVESTIGATION OF THE INFLUENCE FROM IMPROVED HYDRODYNAMICS

In order to estimate the improvement of the bypass routes and the flow guides were coolant velocities and temperatures examined both for normal operation and accident events, i.e. LOF, LOHS, and TLOP accident.

A. Bypass routes

The improvement from the BPRs is noticed after accident initiation. During normal operation the flow through the HXs is slightly impeded due to that some coolant passes the BPRs. The influence from the BPRs is studied for the LOF, LOHS, TLOP accidents which can be seen in Sect VII A 1 and .

1. Total-loss-of-power accident

The BPRs improve the circulation immediately after accident initiation compared to the case without BPRs. After 2 min the temperature difference at core outlet is about ? degrees, whereas after 1 hour the temperature difference is ? degrees. The temperature evolution at core inlet, outlet and the reactor vessel wall is displayed in Fig **??**. The coolant velocity at core outlet is ∼? m/s higher.

Figure 9. Temperature and velocity evolution at core outlet and in the reactor vessel wall after a TLOP accident.

2. Loss-of-flow and loss-of-heat-sink accidents

For a LOF accident the bypass route makes the most significant difference. The core outlet temperatures are ∼100 K lower compared to the case without BPRs. This is because higher coolant velocities can be maintained in the core region after accident initiation due to lower pressure resistance in the BPRs.

Figure 10. Temperature and velocity evolution at core outlet and in the reactor vessel wall after a LOF accident.

For a LOHS accident the argon gas injection would still function. Thus the BPRs makes no difference and the temperature evolution would be the same as for a design without BPRs.

B. Flow guides

The flow guides makes a difference during normal operation as well as during accidents with regard to the coolant flow rates. The flow speed through the core is increases by 5% and thus the temperature is reduced by 10K during normal operation.

Among the three accident scenarios (LOF, LOHS, TLOP), again the greatest improvement is noticed for the LOF accident. The temperature difference at core outlet is ∼100 K.

C. Neither bypass routes nor flow guides

Finally, a calculation on a design without bypass routes and flow guides was performed. Compared to the ADS-HXR the temperature difference at core outlet was ?K at normal operation. For the LOF accident a ? K difference at core outlet appears.

VIII. INVESTIGATION ON A 800 MW(THERMAL) ADS WITH THE HEAT-EXCHANGERS IN THE RISERS

Finally a study was made on a 800 MW(thermal) reactor with the heat-exchangers in the riser.

IX. CONCLUSIONS

To be written...

X. FUTURE WORK

The construction of the heat-exchangers will affect the static pressure difference between the risers and the downcomers, which would be interesting to do more research about.

Moreover, it is important to know better the mechanism of heat transfer in the HX when argon gas is injected in there.

XI. ACKNOWLEDGEMENTS

Footnotes

[1] Rupture of the protective oxide layer on structural components becomes severe.

[2] Fuel failures occur, but the reactor vessel can withstand this temperature for several hours.

[3] American Society of Mechanical Engineers

[4] Investment might be jeopardized, but fuel damage or radioactive release is unlikely.

[5] Endanger the plant from an investment standpoint, although significant fuel failures and radioactive releases are unlikely.

REFERENCES

[1] Generation IV Roadmap NERAC Subcommittee, "Technology Goals for Generation IV Nuclear Energy Systems", NERAC, (May 1 2001), http://gen-iv.ne.doe.gov/

[2] Van Tuyle, G.J., Slovik, G.C., Chan, B.C., Kennett, R.J., Cheng, H.S., Kroeger, P.G., "Summary of Advanced LMR Evaluations - PRISM and SAFR, Brookhaven National Laboratory", pp 87-91, (Oct. 1989)

[3] Baumeister, E.B., et al., "Inherent Safety Features and Licensing Plan of the SAFR plant", Proc. Int. Conf. on Fast Breeder Systems, Washington, USA (Sept. 1987)

[4] Wider H.U., Carlsson J., Jones A., "Beam Shut-Off in ADS Accidents - An Essential Requirement", GLOBAL 2001, Paris (2001)

[5] Rubbia, C., Buono, S., Kadi, Y., Rubio, J.A., "Fast Neutron Incineration in the Energy Amplifier as Alternative to Geologic Storage: The Case of Spain", CERN/LHC/97-01 (EET)

[6] Delpech, M., "The Am and Cm transmutation - physics and feasibility", Proc. Int. Conf. on Future Nuclear Systems, GLOBAL99, Jackson Hole, USA (1999)

[7] Computational Dynamics Ltd., Methodology Volume 3.10a (2000)

[8] Cinotti, L., Corsini, G., "XADS Pb-Bi Cooled Experimental Accelerator Driven System - Reference Configuration", Ansaldo Nucleare, unpublished (2001)

[9] Rousanov, A.E., et al., "Design and study of cladding steels for fuel elements of NPP using heavy coolant", Proc. Heavy Liquid Metal Coolants in Nuclear Technology, Obninsk, Russia (1998)

[10] King, T.L., Landry, R.R., Throm, E.D., Wilson, J.N., "Preapplication, Safety Evaluation Report for the Sodium Advanced Fast Reactor (SAFR) Liquid-Metal Reactor", U.S. Nucelar Regulatory Commission, 15-1 (1991)

[11] Shibli I A, European Creep Collaboration Committee (ECCC), ECCC coordination, ECCC Data Sheets (1999)

[12] Incropera, F.P., DeWitt, D.P., Fundamentals of Heat and Mass Transfer, John Wiley & Sons, New York, USA, pp.492-493 (1996)

[13] Novikova, N., Pashkin, Y., and Chekunov, V. "Some features of sub-critical blankets cooled with lead-bismuth", Int. Conf. on Accelerator Driven Technologies and applications, ADTTA99, 1999.

[14] Personal communication between Johan Carlsson and Jan Wallenius

[15] Ludwig, P.W.P.H., Verkooijen, A.H.M., "Thermal stresses in a core of a Fast Energy Emplifier cooled with lead under normal operating conditions including reactor scram and secondary pump trip", ICENES 2000, (2000)

[16] Eriksson, M., and J. Cahalan, "Inherent shutdown capabilities in accelerator-driven systems", Annals of Nuclear Energy, vol 29/14 pp 1689-1706, (May 2002)

[17] Carlsson, J., Wider, H., "Emergency decay heat removal by reactor vessel auxiliary cooling system from an Accelerator-Driven System", Nuclear Technology, vol. 140, no. 1, pp.28-40, 2002

[18] Wallenius, J., Tucek, K., Carlsson, J., Gudowski, W., "Application of Burnable Absorbers in an Accelerator-Driven System", Nuclear Science and Engineering, (2001)

Table I. Main characteristics of the ADS-HXR.

Plant Area	**Reference Solution**
Core power	250MW(thermal), k_{eff} 0.97 at BOL k_{eff} 0.94 at EOL
Accelerator power	3MW
Target unit	Pb-Bi eutectic, window type undecided
Fuel	U and Pu MOX
Coolant and moderator	Pb-Bi eutectic
Vessel height	9m
Vessel diameter	6m
Steel, reactor vessel	AISI 316L

Table II. Critical temperature limitations for structural materials and protective oxide layers.

Characteristic problem	**Temperature when problem occurs**
Corrosion of structural material	893K [9] [1]
ASME[2] level C	922K [10] [3]
ASME level D	977K [10] [4]
The limiting temperature to avoid creep failure in several hours under the given pressure conditions	1173K [11] [5]
Melting point AISI316	1670K [12]

Table III. Comparison between hand calculation and STAR-CD predictions.

Temperature coolant, [K]	**Hand calculation, [MW]**	**STAR-CD calculation, [MW]**
600	2.28	
900	5.95	

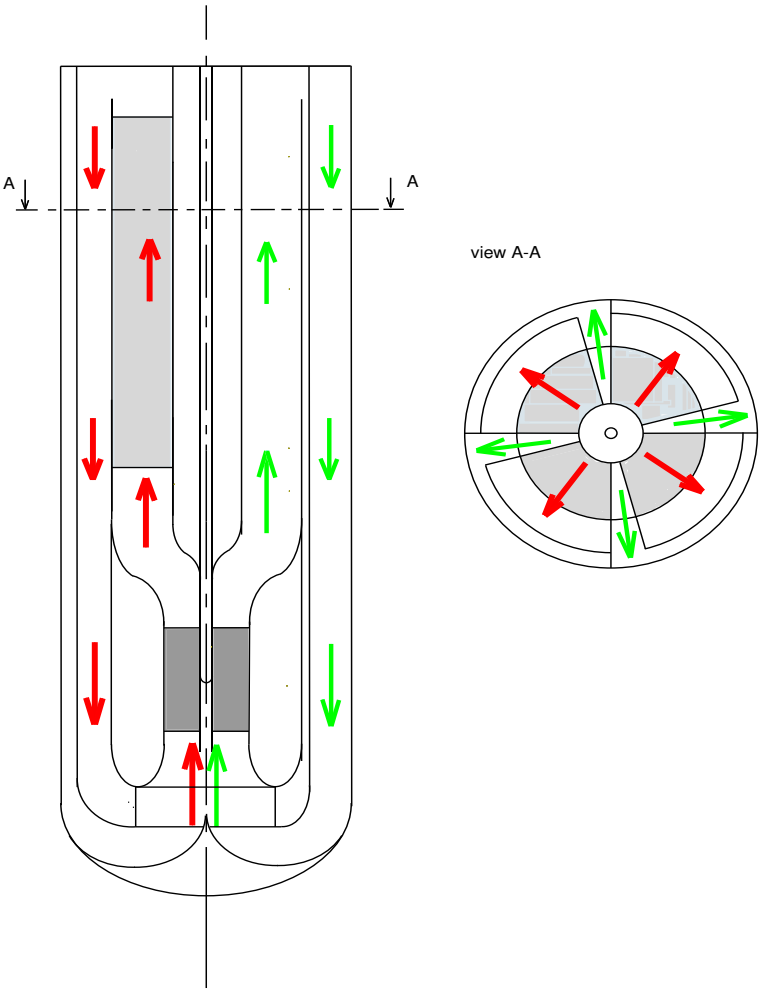

FIG. 1. Schematic view of the SSV.

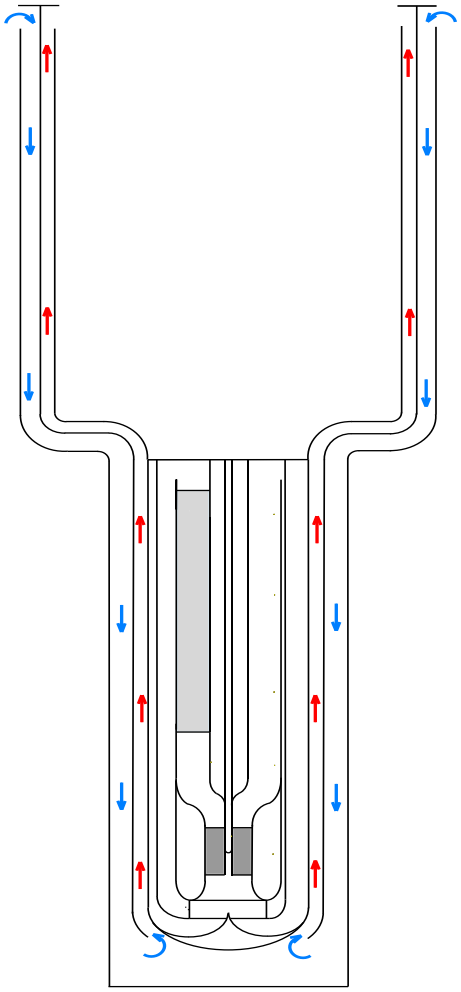

FIG. 2. Schematic view of RVACS of the SSV.

APPENDIX 5

P. Seltborg, J. Wallenius, K. Tuček, W. Gudowski, Definition and Application of Proton Source Efficiency in Accelerator Driven Systems, Nucl. Sci. Eng., accepted for publication.

Definition and Application of Proton Source Efficiency in Accelerator Driven Systems

Per Seltborg[*], Jan Wallenius, Kamil Tuček, Waclaw Gudowski
Department of Nuclear and Reactor Physics
Royal Institute of Technology, Stockholm, Sweden

Abstract *– In order to study the beam power amplification of an accelerator driven system, a new parameter, the proton source efficiency (ψ^*) is introduced. ψ^* represents the number of neutrons produced by fission in the core, relative to the eigenmode production, and is closely related to the neutron source efficiency (φ^*), which is frequently used in the ADS field. The main advantage with using ψ^* instead of φ^* is that the way of defining the source efficiency is unique.*

Numerical simulations have been performed with the Monte Carlo code MCNPX in order to study ψ^* as a function of different design parameters. It was found that, in order to maximize ψ^*, a target radius as small as possible should be chosen. For target radii smaller than about 30 cm, lead-bismuth is a better choice of coolant material than sodium, while for larger target radii the two materials are equally good. The optimal axial proton beam impact was found to be located approximately 20 cm above the core center. Varying the proton energy, ψ^*/E_p was found to have a maximum for proton energies between 1200 and 1400 MeV. Increasing the americium content in the fuel decreases ψ^* considerably, in particular when the target radius is large.

[*] E-mail: per@neutron.kth.se

I. INTRODUCTION

Accelerator Driven Systems (ADS) [1, 2, 3] are being investigated as a possible mean for reducing the long-term radiotoxicity of spent reactor fuel. In principle, the sub-criticality of ADS allows for dedicated cores with a much higher concentration of minor actinides than what is acceptable in critical reactors. Such dedicated cores enable multi-recycling of americium and curium, providing thus a potential for reducing the radio-toxicity by a factor of 50 to 100 [4].

In an ADS, a high-power particle accelerator is used to accelerate protons to energies of the order of 1000 MeV. The protons impinge on a heavy metal target, generating a large number of neutrons via spallation. The spallation neutrons leak out from the target, after different kinds of interactions with the target nuclei, and are subsequently multiplied in the surrounding sub-critical blanket.

An important factor when designing an ADS is to optimize the beam power amplification, given that the reactor is operating at a certain sub-critical reactivity (with sufficient safety margins to criticality). The neutron source efficiency parameter φ^* is sometimes used to study this quantity, since it is proportional to the number of fission neutrons produced in the core (which is closely related to the power produced in the core), by an average external source neutron.

However, calculating φ^* for an accelerator driven system introduces some complications, since the actual source particles are protons, and not neutrons. In order to determine φ^*, the external neutron source first has to be defined and then the efficiency of this neutron source can be determined. The main drawback with using φ^* is that this procedure can be done in several different ways, and the results are directly dependent on the choice of definition. Therefore, completely different values of φ^* are often observed [5, 6, 7], due to different choices of neutron source definition. Another complication associated to the neutron source efficiency is that, studying φ^* as a function of a certain design parameter might change the neutron source distribution and the number of neutrons produced per source proton. In this case, in order to represent (approximately) the beam power amplification, φ^* needs to be weighted with the number of source neutrons produced per source proton.

With the motivation of simplifying the concept of source efficiency, we introduce in this paper a new parameter ψ^*, representing the number of fission neutrons produced in the system by each source ***proton***. The main advantage with using the proton source efficiency instead of the neutron source efficiency is that there is no ambiguity in how to define it. Another benefit is that, using a coupled proton + neutron high-energy transport code (e.g. MCNPX [8]), the full source mode particle transport is performed in a single simulation. However, when the core calculations need to be divided into two separate simulations, ψ^* can be obtained from φ^*, independently of the choice of neutron source definition.

In this paper, ψ^* has been studied as a function of different design parameters, for a model of a nitride fuelled and lead-bismuth cooled ADS. First, the neutron source efficiency is defined and discussed (Section II) and then the proton source efficiency parameter is introduced (Section III). Section IV describes the reference model used in this study, and the modelling tool MCNPX. In Section V.A, ψ^* and φ^* are studied as functions of the target radius and coolant material. In the following sections, ψ^* is studied as a function of the axial proton beam impact (V.B) and the proton beam energy (V.C). Finally, an americium based fuel has been compared with the plutonium based reference fuel (V.D).

II. NEUTRON SOURCE EFFICIENCY φ^*

II.A. *Definition of the Neutron Source Efficiency*

The neutron source efficiency, usually denoted φ^*, represents the relative efficiency of external source neutrons and it is defined as the average importance (in the fundamental mode) of the external source neutrons over the average importance (in the fundamental mode) of the fission neutrons (φ^* for an average fission neutron is 1) [9].

The neutron flux distribution ϕ_s in a sub-critical core is the solution to the inhomogeneous steady-state neutron transport equation

$$\boldsymbol{A}\phi_s = \boldsymbol{F}\phi_s + S_n \tag{1}$$

where **F** is the fission production operator, **A** is the net neutron loss operator and S_n is the external source. The neutron source efficiency φ^* is defined according to Eq. (2), using the adjoint flux ϕ_0^* [10, 11]

$$\varphi^* = \frac{\dfrac{<\phi_0^*, S_n>}{<S_n>}}{\dfrac{<\phi_0^*, \boldsymbol{F}\phi_s>}{<\boldsymbol{F}\phi_s>}} \tag{2}$$

where ϕ_0^* is the adjoint flux (the everywhere positive solution of $\boldsymbol{A}^*\phi_0^* = \frac{1}{k_{eff}}\boldsymbol{F}^*\phi_0^*$) which provides a measure of neutron importance, $<\mathbf{F}\phi_s>$ is the total production of neutrons by fission and $<S_n>$ is the total production of neutrons by the external source. In the above formula, the brackets imply integration over space, angle and energy.

As some of the integrals in Eq. (2) cannot be directly calculated with MCNPX, another procedure was sought to compute φ*. By using the neutron balance equation (Eq. 1), the properties of the adjoint flux ϕ_0*, the **A**, **F** operators and their adjoints **A***, **F***, the source efficiency can be expressed equivalently as

$$\varphi^* = \left(\frac{1}{k_{eff}} - 1 \right) \cdot \frac{< \boldsymbol{F}\phi_s >}{< S_n >} \qquad (3)$$

Eq. (3) is a simple formula relating the total fission neutron production $<\mathbf{F}\phi_s>$ to the external source, φ* and the reactivity $(1 - 1/ k_{eff})$. It shows that, for given values of k_{eff} and $<S_n>$, the larger φ* the larger the fission power produced in the system.

The quantities on the right hand side of Eq. (3) are standard outputs from MCNPX.

II.B. *Definition of the External Neutron Source*

Since the actual source particles in an accelerator driven system are protons and not neutrons, it is not obvious which is the best way to define the neutron source. The procedure to calculate φ* needs to be divided into two steps – the first generating the source neutrons, produced from the proton beam interacting with the target, and the second one determining the efficiency of these source neutrons. Different source definitions are possible and they will result in different values and meanings of φ*. A brief summary of four different definitions of the external neutron source that have been used in the ADS field is given in [12]. Among these, the two most frequently used definitions, the target neutron leakage source and the energy cut-off source, will be discussed in the two following sections. The two other definitions are the fission source, consisting of the first generation of fission neutrons, and the primary neutron source, which is the collection of neutrons that are created directly from proton induced spallation (primary spallation neutrons) [7].

II.B.1. The Target Neutron Leakage Source

This approach uses the neutrons that leak out radially from the target as source neutrons [5, 13]. The method consists of, in the first step, transporting the high-energy protons and the secondary particles that they produce in the target. Only the target is present in the first step. The neutrons that leak out from the target are defined as the source, and their properties, in terms of position, direction and energy, are written to a source file. In the second step, the leakage neutrons are reemitted as fixed source neutrons in a separate run and the efficiency (φ*) of them is determined. Since the target neutron leakage spectrum includes a high-energy tail, both step 1 and 2 need to be simulated with a high-energy transport code (not limited to the energy range of cross-section data libraries).

Since the neutron source is generated by a proton beam/target simulation, the distribution of the source neutrons is dependent on the target properties and the proton beam properties. This might induce complications when trying to optimize φ* and the beam power amplification, by varying different design parameters. If a change in the studied design parameter changes the distribution of the source neutrons, φ* has to be weighted by the number of neutrons produced per source proton. With the target neutron leakage definition, examples of these parameters are the target dimension, the proton beam energy or the axial proton beam impact position. Other design parameters, such as the core coolant material, the fuel composition or the core dimensions, are independent of the target region and do not affect the neutron source.

II.B.2. The Energy Cut-off Neutron Source

The other way to define the neutron source is to collect the neutrons that fall below a certain cut-off energy (usually 20 or 150 MeV) [6, 14, 15]. In the first step, a high-energy code is used to transport the accelerated protons and the secondary high-energy particles. The neutrons that are produced are either killed if they are born below the cut-off energy or transported until they fall below this energy. The properties of the killed neutrons are written to a source file. In the second step, the killed neutrons are reemitted as fixed source neutrons in a separate run and φ* is determined.

An advantage of this approach is that the second step can be simulated with a low-energy transport code. The cut-off energy is set to the upper energy of the cross section library that will be used in second step calculation. This is desirable since many reactor codes systems are limited to the upper energy limit of the cross-section data library (e.g. 20 or 150 MeV).

It has been shown in [6] that, in contrast to the target neutron leakage source, the neutron source distribution in this case is rather insensitive to changes in the target radius. However, substituting the coolant material or changing the fuel composition will affect the distribution of the neutron source.

III. PROTON SOURCE EFFICIENCY ψ*

III.A. *Introduction of the Proton Source Efficiency*

In order to simplify the concept of source efficiency, a new parameter, called "proton source efficiency" and denoted ψ*, which represents the product of φ* and the number of source neutrons generated per source proton

(S_n/S_p), is introduced in this paper. We thus have the following relation between the ***proton*** source efficiency ψ* and the ***neutron*** source efficiency φ*:

$$\psi^* = \varphi^* \cdot \frac{< S_n >}{< S_p >} \quad (4)$$

This parameter could also, in analogy with φ*, be expressed in terms of k_{eff} and the total number of neutrons produced by fission in the core, for each source ***proton***. Inserting Eq. (3) in Eq. (4) it is expressed in the same way as φ*, only with the replacement of S_n by S_p

$$\psi^* = \left(\frac{1}{k_{eff}} - 1 \right) \cdot \frac{< \boldsymbol{F}\phi_s >}{< S_p >} \quad (5)$$

$<\mathbf{F}\phi_s>/<S_p>$ is the total production of neutrons by fission over the total number of source protons.

Investigating ψ* and φ* as functions of the target radius and of coolant material illustrates the discussion in the previous section about which design parameters that affect and do not affect the neutron source distribution. Using the target neutron leakage definition of the external neutron source and changing the coolant material, S_n/S_p does not change, so ψ* and φ* vary in exactly the same way. When varying the target radius, on the other hand, S_n/S_p changes, so ψ* and φ* varies in different ways.

Consequently, if one wants to use the neutron source efficiency parameter φ*, it needs to be weighted with S_n/S_p when it is studied as a function of the target radius, whereas this is not necessary when comparing different core coolant materials. However, with the introduction of the proton source efficiency and always referring to ψ*, none of this has to be considered, and the procedure is simplified.

III.B. *Relationship between ψ* and Core Power*

The total power produced by fission in the core (P_f) can be expressed as the product of the total number of fission events and the average available energy released in a fission ($\overline{E}_f$), according to the following relation:

$$P_f = \frac{< \boldsymbol{F}\phi_s >}{\overline{\nu}} \cdot \overline{E}_f \quad (6)$$

For a given fuel composition, $\overline{E}_f$ and $\overline{\nu}$ can, for the purpose of this study, be considered to be constant. Even though there are high-energy neutrons entering into the fuel (the neutron yield is not constant with respect to neutron energy), the fraction of fissions in the core that are induced by high-energy neutrons is very small. Therefore, a change in the neutron yield for these fission events will have very little impact on $\overline{\nu}$. The variations of $\overline{E}_f$ and $\overline{\nu}$ have been calculated for the series of different studies presented in this paper and were found to be much smaller than the statistical errors in the simulations (except in the case where the fuel composition was modified). We therefore obtain (using Eq. 5) that ψ* is approximately proportional to P_f.

If we further make the approximation that the energy produced by fission is proportional to the total power produced in the core ($P_f \propto P_{tot}$), ψ* is also proportional to the total power, according to

$$P_{tot} \propto \frac{k_{eff}}{1 - k_{eff}} \cdot \psi^* \quad (7)$$

However, this approximation is only valid to a reasonable accuracy for a fixed fuel composition, which should be kept in mind in Section V.D, where two different fuels are compared.

IV. SYSTEM MODELING

A homogenized model representing a nitride fuelled and lead-bismuth cooled ADS (maximum 800 MWth) has been studied. The height of the active core in the reference model (Fig. 1) is 100 cm and the outer radius is 70 cm. The inner radius is 20 cm, which is also the boundary of the lead-bismuth target. The accelerator tube has a radius of 15 cm and the axial position of the proton beam impact is 25 cm below the top of the core. The radius of the radially uniform 1000 MeV proton beam is 7.5 cm. Above and below the active zone of the core, plena for accommodation of gas release are included, having lengths of 100 and 50 cm, respectively. The radial reflector is assumed to consist of 90 % steel and 10 % lead-bismuth.

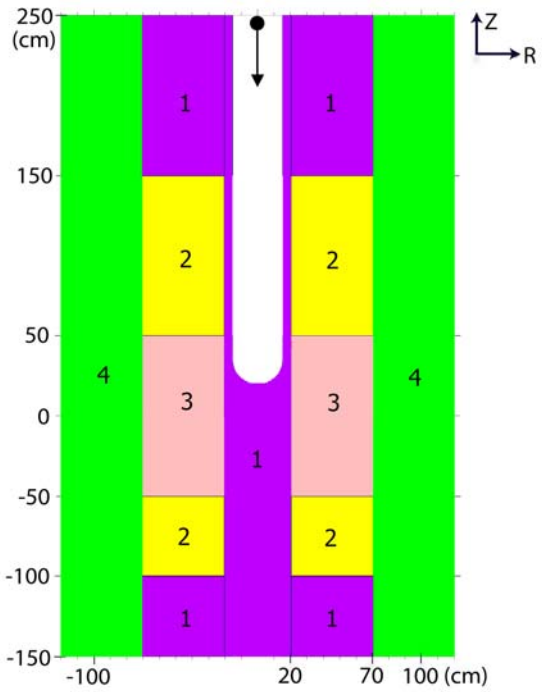

Fig. 1. RZ-view of the homogenised reference model. The 1000 MeV protons are guided through the accelerator tube and impinge on the Pb-Bi target. The different regions in the model are pure Pb-Bi (1), the plena (2), the active core (3) and the reflector (4)

The relative fraction of fuel, cladding and coolant material used in the homogenized model correspond to a pin radius of 2.5 mm and a pin pitch of 1.72. The nitride actinide fuel is in solid solution with ZrN. The volume fraction of ZrN was adjusted to 83 %, in order to obtain a k_{eff} of about 0.95. The fuel consists of 80% plutonium and 20% americium (the actinide vectors are listed in Table I). The spallation target and the core coolant consist of lead-bismuth eutectic and the fuel pin cladding of 10% chromium and 90% iron.

TABLE I

Relative Fraction of Actinides in the Reference Fuel. The Pu vector corresponds to that of spent LWR MOX fuel after 7 years of cooling and the Am vector to a mixture of spent UOX and MOX fuel.

Plutonium	**80 %**	**Americium**	**20 %**
Pu-238	5 %	Am-241	67 %
Pu-239	38 %	Am-243	33 %
Pu-240	30 %		
Pu-241	13 %		
Pu-242	14 %		

The Monte Carlo code MCNPX (Version 2.3.0), in coupled neutron and proton mode, was used for all simulations, relying on the evaluated nuclear data library ENDF/B-VI.8 (limited to 20 MeV). The Intranuclear Cascade model used by MCNPX was the Bertini package [16].

V. THE PROTON SOURCE EFFICIENCY AS A FUNCTION OF DIFFERENT DESIGN PARAMETERS

The proton source efficiency ψ^* has been studied as a function of a number of design parameters, such as the target radius, coolant material, axial proton beam impact position, proton beam energy and fuel composition. The starting point for each parameter study is the reference model.

V.A. *ψ^* as function of Target Radius*

In this section, ψ^* has been computed for different target radii for the reference lead-bismuth cooled core and for a sodium cooled core. The neutron source efficiency φ^*, using the target neutron leakage definition, has also been determined. k_{eff} was kept constant at about 0.95 by adjusting the outer radius of the core.

Since changing the geometry of the core might affect the results, ψ^* has also been studied as a function of the outer core radius, varying from 60 to 90 cm. It was found that an increase of the core radius leads to a slight increase of ψ^*, on average 0.26% per cm. The reason for this is that the radial neutron leakage into the reflectors decreases as the core radius increases. This dependence of ψ^* (rather small but not automatically negligible) on the core radius should be kept in mind in the parameter studies where the core radius is varying.

V.A.1. The Lead-Bismuth Cooled Reference Model

ψ^* was computed for the reference model for different target radii, both as the product of φ^* and S_n/S_p (Eq. 4) and directly according to Eq. (5), in order to verify the consistency between the two different expressions. φ^* was calculated using the target neutron leakage definition. The results are listed in Table II and we see that they are in good agreement, the differences being within the statistical uncertainty. Hence, using a two-step simulation procedure, ψ^* can be obtained according to Eq. (4), independently of the choice of neutron source definition. If MCNPX is used, ψ^* is obtained directly according to Eq. (5). ψ^*, φ^* and S_n/S_p are also plotted as functions of target radius in Fig. 3 and Fig. 4.

TABLE II

Computation of ψ* according to Eq. (4) and Eq. (5) (1σ-error ~ 0.75 %). For the 10 cm target radius, the radius of the accelerator tube was decreased to 10 cm. The results are also plotted in Fig. 3 and Fig. 4.

Target Radius	φ^*	$\frac{<S_n>}{<S_p>}$	$\varphi^* \cdot \frac{<S_n>}{<S_p>}$	ψ^*
10	1.81	21.9	39.8	39.6
20	1.35	26.8	36.3	35.9
30	1.13	29.0	32.9	32.4
40	0.99	30.0	29.6	29.5
50	0.89	30.2	26.7	27.0

Concerning the dependence on target radius, we see that ψ* decreases considerably when the radius increases. There are mainly two reasons for this behaviour. One of them is the softening of the neutron leakage spectrum (the spectrum of the neutrons that enter into the fuel), when the target is enlarged. The probability to induce fission for the source neutrons strongly decreases with decreasing energy, especially when the core is loaded with even-neutron number actinides, as will be shown below. Lower neutron energy also inhibits other possible neutron multiplication reactions, such as (n,xn)-reactions and secondary spallation. The mean energy of the neutron leakage spectrum decreases by a factor of four when the target radius is increased from 20 cm to 50 cm and the fraction of neutrons above 20 MeV is only 0.5% for a radius of 50 cm, while 3.2% for a 20 cm radius. The radial neutron leakage spectra for different target radii are plotted in Fig. 2 and the fraction of leakage neutrons above some energy thresholds are listed in Table III.

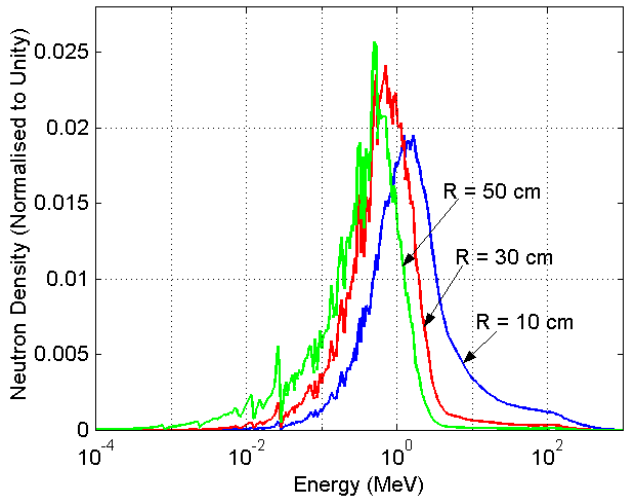

Fig. 2. Radial target neutron leakage spectra for different target radii.

TABLE III

Fraction of Neutrons Leaking out Radially from the Target that have Energies above 1, 7, 20 and 150 MeV.

Target Radius	>1 MeV	>7 MeV	>20 MeV	>150 MeV
10	62.4%	13.4%	6.9%	1.1%
20	45.2%	6.1%	3.2%	0.45%
30	31.0%	3.0%	1.7%	0.22%
40	20.7%	1.6%	0.9%	0.12%
50	13.5%	0.8%	0.5%	0.07%

The other reason for the decrease in ψ* is that the axial neutron leakage increases significantly with increasing target radius. The fraction of axial leakage neutrons relative to the total number of neutrons exiting the target is approximately 5 % for the 20 cm radius target while about 28 % for the 50 cm radius target. The major part of the axial leakage is in the backward direction, through the accelerator tube.

Increasing the target radius, on the other hand, increases the neutron multiplication inside the lead target, which leads to a higher number of neutrons created per source proton (S_n/S_p increases from 26.8 for r=20 cm to 30.2 for r=50 cm). The multiplicative effect of (n,xn)-reactions and secondary spallation in the lead target enhances the proton source efficiency. Consequently, with increasing target radius, there are more neutrons for each source proton that enter into the fuel, though the efficiency of these neutrons is strongly reduced. Accordingly, we see in Table II that ψ* decreases less rapidly than φ* with increasing target radius, due to the increase in S_n/S_p. These two competing factors in ψ* are thus well represented by Eq. (4).

We conclude that, in order to optimize the proton source efficiency, a target radius as small as possible should be chosen (increasing the radius from 20 cm to 50 cm decreases ψ* by about 25%). These results are in good agreement with other similar studies [6]. However, it has also been shown that, reducing the target radius has some undesirable effects, for instance higher fluence/burnup ratio (lower maximum burnup) and more severe high-energy damages. Further, for a large-scale ADS, the target must be sufficiently large to be able to remove the heat from the high-power accelerator beam. It is thus clear that, in order to optimally design a cost-efficient ADS with high fuel performances, a trade-off between several different aspects arises.

V.A.2. A Sodium Cooled Model

Replacing the lead-bismuth coolant with sodium reduces the reactivity by about 5000 pcm, so in order to maintain a k_{eff} of 0.95, the outer core radius was increased

by 11 cm. As is shown in Fig. 3, the proton efficiency for small target radii is lower for the sodium cooled core than with the lead-bismuth coolant (approximately 7% lower for r = 20 cm).

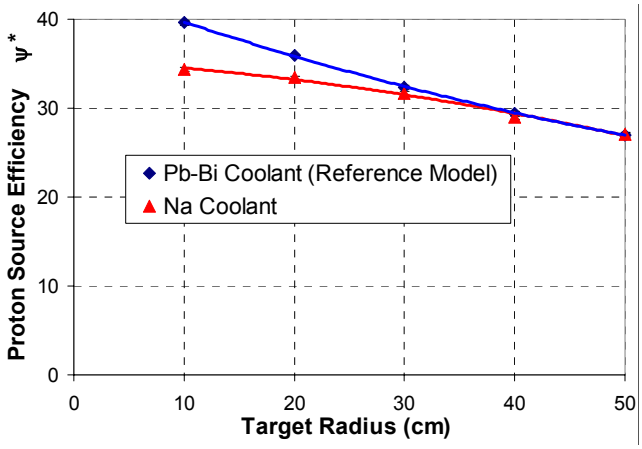

Fig. 3. Proton source efficiency ψ* versus target radius for a Pb-Bi cooled and a Na cooled model (1σ-error ~ 0.75 %)

The reason for this is that there is no neutron multiplication in the sodium coolant, in contrast to lead-bismuth. The differences between the two curves indicate that the contribution from (n,xn)-multiplication in the Pb-Bi coolant is significant for target radii smaller than about 30 cm. As long as there is a fraction of neutrons with energy higher than about 7 MeV (the (n,2n)-threshold in lead) there will be (n,xn)-neutron multiplication in lead. When the target radius is small, this high-energy fraction is rather high (6.1% have energies higher than 7 MeV for r=20 cm compared to 0.8% for r=50 cm). When the target radius increases, the fraction of high-energy neutrons decreases, and at radii above 40 cm the ψ* values are essentially the same. Another difference between the two coolant materials is that lead-bismuth has better spallation-neutron production characteristics. This enhances ψ* for small target radii, in which cases there are still a significant fraction of very high-energy neutrons leaking out into the fuel region. The difference between the Pb-Bi and the Na coolant are further illustrated in Fig. 4, where the neutron source efficiencies are compared.

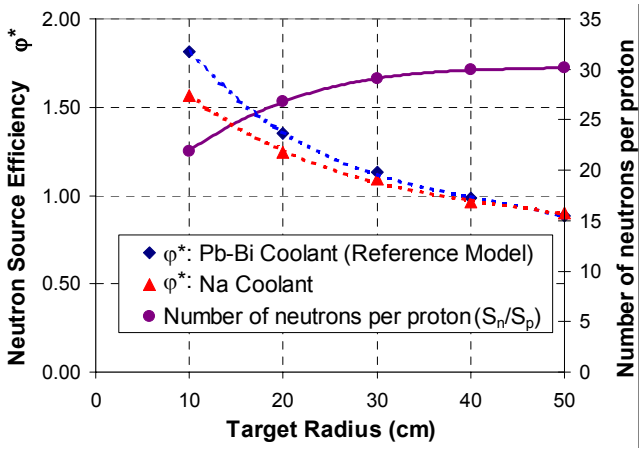

Fig. 4. Neutron source efficiency φ* (according to the target neutron leakage definition) versus target radius for the Pb-Bi cooled and the Na cooled model (1σ-error ~ 0.75 %), and number of neutrons per source proton (S_n/S_p).

V.B. *ψ* as function of Axial Beam Impact Position*

The proton source efficiency has been studied as a function of the axial beam impact position, varying from the center of the core (z = 0) to the top of the core (z = 50 cm). It is seen in Fig. 5 that, for the reference model (with an accelerator tube radius of 15 cm) the maximum in ψ* is obtained at about 20 cm above the core center. Moving away from the optimum impact position, ψ* decreases, due to increasing axial neutron leakage.

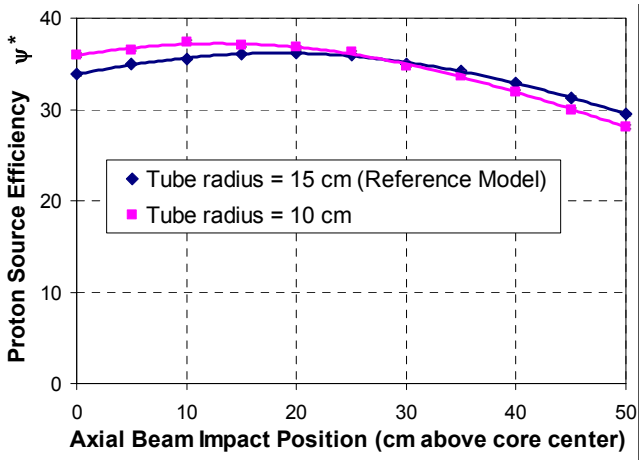

Fig. 5. Proton source efficiency ψ* versus axial beam impact position (cm above the core center) for a tube radius of 15 cm and of 10 cm (1σ-error ~ 0.50 %)

As is seen in Fig. 5, ψ* and its dependence of the axial beam impact is rather sensitive to the accelerator tube radius. For a tube radius of 10 cm, the beam impact position

that maximizes ψ* is moved downwards in the core, with the optimum at about 13 cm above the core center. The maximum value of ψ* also increases somewhat (~ 3%) when the tube radius is changed from 15 cm to 10 cm.

When the tube radius decreases there are mainly two effects appearing. One is that the axial neutron leakage in the backward direction decreases (increasing ψ*) and the other one is that the energy spectrum of the neutrons entering into the fuel is softened (decreasing ψ*). When the beam impact is close to the core center, the impact of the leakage on the neutron balance is more pronounced than the softening of the neutron spectrum. On the contrary, when the beam impact is close to the top of the core, the softening effect is dominant and ψ* is lower for the 10 cm tube radius.

An accidental scenario that has been considered in an ADS is that the accelerator tube is filled (partially or fully) with the target material [17], which would increase k_{eff}. For the reference model, filling the tube from 20 cm above the core center till the top of the core, this increase is about 600 pcm. For an initial reactivity level of k_{eff} = 0.95, and not taking the variations in ψ* into account, this would increase the core power by 14 %. For the 10 cm tube radius, the change in k_{eff} is smaller and also the effect on the power. However, the rapid decrease in ψ* above z = 20 cm will tend to reduce the core power. Adding these two opposite effects together, according to Eq. (7), it is found that the core power decreases when the tube channel is filled with lead-bismuth coolant. Filling the tube from z = 20 cm to z = 50 cm decreases the core power by 7 % for the 15 cm tube radius and by 20 % for the 10 cm tube radius.

However, if the reactor is operating at a reactivity level closer to criticality, the effect on the core power from a reactivity insertion will be higher and might be more important than the decrease in ψ*. One way to increase the safety margins to prompt criticality, is to set the proton beam impact at the top of the core (z = 50 cm). However, the loss in proton source efficiency by moving the impact from the optimal position to the top of the core would be large - about 18 % for the 15 cm tube radius and 24 % for the 10 cm tube radius.

V.C. *ψ* as function of Proton Beam Energy*

The proton source efficiency was calculated for different proton beam energies, varying from 400 MeV to 2.5 GeV, for a 20 cm and a 50 cm radius target. The ψ* values divided by the proton energy (ψ^*/E_p) are displayed in Fig. 6.

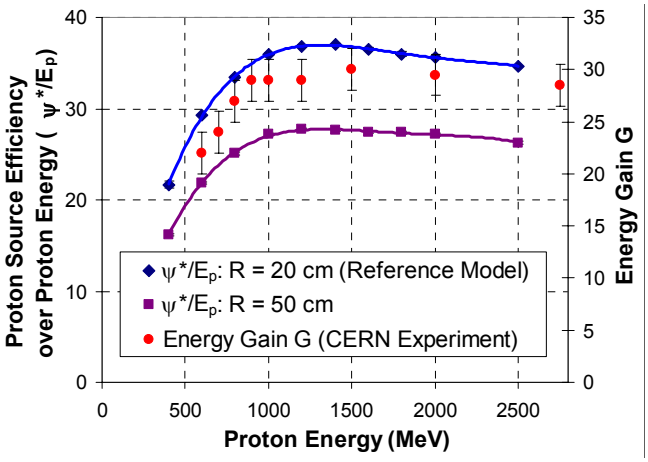

Fig. 6. Proton source efficiency per proton energy in GeV (ψ^*/E_p) versus proton beam energy, for a target radius of 20 cm and 50 cm (1σ-error ~ 0.50 %). Energy gain G from CERN experiments [18] for a set-up configuration of k_{eff} = 0.895.

As expected, ψ* is higher for the 20 cm radius than for the 50 cm radius, for all proton energies. However, the shape of the two curves is very similar. ψ^*/E_p increases strongly with increasing proton energy up to about 1000 MeV. The maximum is reached at about 1200-1400 MeV. Above 1400 MeV the curves decrease slightly. The reason for this is that the range of the protons increases with increasing energy and a larger fraction of the spallation induced neutrons will be created far away from the center of the core (or even below the core). This increases the axial neutron leakage in the downward direction. For instance, the range of 1 GeV protons impinging on a lead target is about 53 cm, while about 95 cm for 2 GeV protons [17]. The distance from the top of the target to the bottom of the core was 75 cm (Fig. 1).

The proton source efficiency divided by the proton energy (ψ^*/E_p) is closely related to the energy gain (beam power amplification) of a source driven sub-critical system. The energy gain (G), as defined in [18], represents the total power produced in the core over the accelerator power

$$G = \frac{P_{tot}}{P_{acc}} = \frac{G_0}{1 - k_{eff}} \tag{8}$$

where G_0 relates to the efficiency of the spallation regime. Similarly, using Eq. (7), P_{tot}/P_{acc} can be expressed as

$$\frac{P_{tot}}{P_{acc}} = \frac{P_{tot}}{< S_p > E_p} \propto \frac{k_{eff}}{1 - k_{eff}} \cdot \left(\psi^* / E_p \right) \tag{9}$$

Hence, for given k_{eff}, ψ^*/E_p is proportional to the energy gain G. In the experiments performed at CERN [18], the

energy gain was studied as a function of the proton beam energy. The results are re-plotted in Fig. 6. We see in the figure that the MCNPX simulated values of ψ* have similar relative dependence on the proton energy, as the results from the CERN experiments. This comparison confirms that the ψ* parameter represents well the beam power amplification of an ADS.

The k_{eff} of the sub-critical assembly in the CERN experiments was 0.895. In order to obtain G for $k_{eff} = 0.95$, the values have to be multiplied by (1-0.895)/(1-0.95). For $E_p = 1000$ MeV the energy gain becomes 61.

V.D. *ψ* for an Americium Based Fuel*

Finally, ψ* has been studied for an americium based fuel (40% Pu and 60% Am), as a function of the target radius. The results are displayed, together with the results for the reference model, in Fig. 7. We see that the introduction of americium decreases the source efficiency significantly.

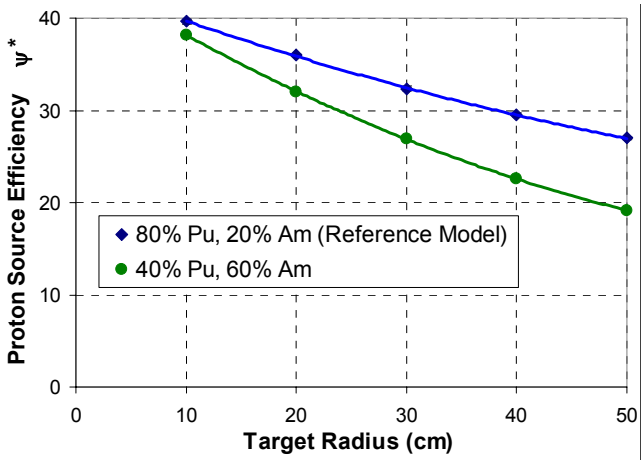

Fig. 7. Proton source efficiency ψ* versus target radius for an americium based fuel, compared with the plutonium based reference model (1σ error ~ 0.75 %).

This is expected, since the fission cross-section of Am-241 and Am-243 decreases rapidly for neutron energies below 1 MeV. Fig. 8, where the fission cross-section over the absorption cross section is plotted for Am-241 and Pu-239, shows that the fission probability of Am-241 is very sensitive to neutron energies between 0.1 and 1 MeV, whereas for Pu-239, it is high everywhere in this energy range. Above 1 MeV the fission probability for plutonium and americium are of the same order of magnitude. The other even-neutron number actinides, Pu-238, Pu-240, Pu-242 and Am-243, have similar cross-section dependence as Am-241, while the Pu-241 cross-section is similar to that of Pu-239.

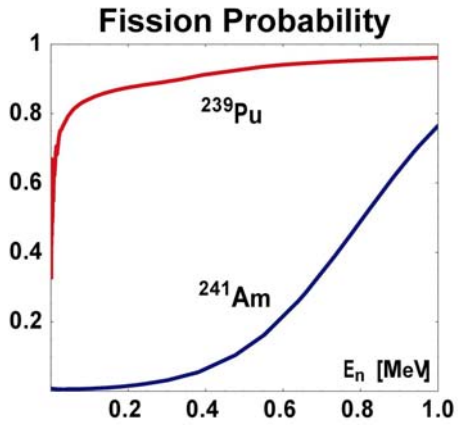

Fig. 8. Fission cross-section over absorption cross-section for Pu-239 and Am-241 (ENDF/B-VI).

Hence, the neutrons entering into the fuel with energy below 1 MeV will have less probability to induce fission in the fuel, when the core is loaded mainly with americium. As was shown in Fig. 2 and in Table III, the energy distribution of the leakage neutrons is very sensitive to the target radius. For a 10 cm radius, only 38% of the leakage neutrons are below 1 MeV and ψ* is not so sensitive to the americium/plutonium ratio, which is also seen in the Fig. 7. However, with increasing target radius, the fraction of neutrons above 1 MeV decreases rapidly, with a corresponding loss in proton source efficiency. Thus, increasing the americium concentration from 20% to 60%, reduces ψ* by 11% for the 20 cm target radius and by 29% for the 50 cm target radius.

In Section III.B, it was shown that, for a fixed fuel composition, ψ* is approximately proportional to the core power. However, increasing the fraction of americium in the fuel slightly increases $\bar{\nu}$ (by about 5 %). Therefore, since ψ* is directly proportional to the number of neutrons produced by fission, normalising to the same core power, the difference between the two curves would be slightly larger than in Fig. 7.

VI. CONCLUSIONS

Instead of using the neutron source efficiency parameter φ* in order to study the optimisation of the beam power amplification, a new parameter ψ*, representing the efficiency of the source protons, has been introduced. ψ* is proportional to the number of neutrons produced by fission in the system (which in its turn is approximately proportional to the core power). By introducing ψ*, ambiguities in defining the external neutron source when calculating φ* are avoided. If MCNPX is used, only one simulation is required for the source mode calculations,

whereas using the neutron source efficiency, the procedure needs to be divided into two separate simulations. However, the main advantage with ψ^* is that it is independent of the calculation method. The one-step procedure and the two-step procedure (irrespective of the neutron source definition) give the same result.

Studying the radius of the spallation target, it was found that ψ^* decreases strongly with increasing target radius (by 25% when the radius is changed from 20 cm to 50 cm). The two main reasons for this behaviour is that, the axial neutron leakage increases and that the energy spectrum of the neutrons that enter into the fuel is softened, when the target is enlarged. These effects are only partly compensated by the increased neutron multiplication inside the target. Hence, in order to maximize the beam power amplification, a target radius as small as possible should be chosen, without exceeding the limits determined by other target-core characteristics (e.g. high-energy particle fuel damages and beam power heat removal). Substituting the lead-bismuth coolant by sodium decreases ψ^* for target radii smaller than 30 cm, whereas for larger target radii, the two coolant options perform equally good.

The axial position of the proton beam impact that maximizes ψ^* was, for the reference model (tube radius = 15 cm), located approximately 20 cm above the core centre. However, the dependence of ψ^* on the impact position is sensitive to the accelerator tube radius, and for a tube radius of 10 cm, the maximum was found at about 13 cm above the core centre. Reducing the tube radius from 15 to 10 cm also increases the maximum of ψ^* by 3 %.

Investigating the proton source efficiency per proton energy (ψ^*/E_p) as a function of the proton energy showed that a maximal accelerator amplification is obtained for proton energies of about 1200 to 1400 MeV, but with rather small changes between 1000 and 2000 MeV. Finally, increasing the americium content in the fuel from 20% to 60%, decreases ψ^* considerably, especially for larger target radii. Due to the sharp decrease in fission cross-section below 1 MeV, americium is more sensitive than plutonium to the softening of the energy spectrum of the neutrons that enter into the fuel.

ACKNOWLEGDEMENTS

This work was financially supported by the Swedish Centre for Nuclear Technology, SKB AB (Swedish Nuclear Fuel and Waste Management Co) and the European Commission (Project MUSE: FIKW-CT-2000-00063). The authors would like to thank J. Cetnar, R. Klein Meulekamp and R. Jacqmin for useful discussions.

REFERENCES

1. M. SALVATORES et al., ”Long-Lived Radioactive Waste Transmutation and the Role of Accelerator Driven (Hybrid) Systems,” *Nucl. Instrum. Methods A*, **414**, 5 (1997).

2. D. G. FOSTER et al., ”Review of PNL Study on Transmutation Processing of High Level Waste,” LA-UR-74-74, Los Alamos National Laboratory (1974).

3. T. TAKIZUKA et al., “Conceptual Design of Transmutation Plant,” Proc. Specialist Mtg. Accelerator Driven Transmutation Technology for Radwaste, LA-12205-C, p. 707, Los Alamos National Laboratory (1991).

4. M. DELPECH et al., “The Am and Cm Transmutation – Physics and Feasability,” *Proc. Int. Conf. Future Nuclear Systems, GLOBAL’99,* August 30-September 2, 1999, Jackson Hole, Wyoming, American Nuclear Society (1999).

5. J. WALLENIUS et al., Application of burnable absorbers in an accelerator driven system”, Nuclear Science and Engineering, 96, 137 (2001)

6. W. S. YANG, L. MERCATALI et al., ”Effects of Buffer Thickness on ATW Blanket Performances”, *Int. Meeting Accelerator Applications/Accelerator Driven Transmutation Technology and Applications* ADTTA/AccApp’01, November 11-15, 2001, Reno, Nevada, USA (2001).

7. P. SELTBORG, R. JACQMIN, “Spallation Neutron Source Effects in a Sub-Critical System,” *Int. Meeting Accelerator Applications/Accelerator Driven Transmutation Technology and Applications,* ADTTA/AccApp’01, November 11-15, 2001, Reno, Nevada, USA (2001).

8. L. S. WATERS, “MCNPX™ User´s Manual – Version 2.1.5,” Los Alamos National Laboratory, November 14, (1999).

9. M. SALVATORES, “Accelerator Driven Systems (ADS), Physics Principles and Specificities,” J. Phys. IV France 9, pp. 7-17 –7-33 (1999).

10. R. SOULE, M. SALVATORES, R. JACQMIN, “Validation of Neutronic Methods Applied to the Analysis of Fast Sub-Critical Systems: The MUSE-2 Experiments,” GLOBAL’97, page 639 (1997).

11. G. ALIBERTI et al., “Analysis of the MUSE-3 Subcritical Experiment”, Int. Conf. Global 2001, France, Paris, September (2001).

12. R. KLEIN MEULEKAMP, A. Hogenbirk, ”The Neutron Source in ADS applications”, PDS-XADS D23 App. D, NRG report /I 20782 / 02.50727, Petten (2002).

13. K. TUCEK et al., “Source Efficiency in an Accelerator-Driven System with Burnable Absorbers,”, *Int. Conf. on Back-End of the Fuel Cycle: From Research to Solutions, GLOBAL 2001*, Paris, France (2001).

14. S. ATZENI et al., “Statistical Fluctuations in Montecarlo Simulations of the Energy Amplifier,” CERN/LHC/97-12 (EET), CERN (1997).

15. K. W. BURN, “A Decoupled Approach to the Neutronics of subcritical configurations: Evaluating the Neutron Source”, RT/ERG/99/2, ENEA, Bologna, Italy (1999)

16. H. W. BERTINI, Phys. Rev. 131, 1801, (1969).

17. L. MONSANT et al., ”Proposed Sub-criticality level for an 80 MWth Lead-Bismuth Cooled ADS, 7th IEM, Jeju, Korea (2002).

18. S. ANDRIAMONJE et al., ”Experimental determination of the energy generated in nuclear cascades by a high energy beam”, Physics Letters B 348, 697-709 (1995).

19. S. BUONO, “Beam Target Design in Accelerator Driven Systems”, Frederic Joliot/Otto Hahn Summer School ‘2002, August 21-30, 2002, Cadarache, France (2002).

APPENDIX 6

A. V. Ignatyuk, V. Lunev, Yu. Shubin, E. Gai, N. Titarenko, W. Gudowski, Neutron And Proton Cross Section Evaluations For ^{232}Th up to 150 MeV, Nuclear Science and Technology, Volume 142, Number 2, October 2002.

Nuclear Science and Technology, Volume 142, Number 2, October 2002.

NEUTRON AND PROTON CROSS SECTION EVALUATIONS FOR ^{232}TH UP TO 150 MeV

A. V. Ignatyuk, V. P. Lunev, Yu. N. Shubin, E.V. Gai, N. N. Titarenko

Institute of Physics and Power Engineering, 249020 Obninsk, Russia

W.Gudowski [1]

Royal Institute of Technology, 100-44 Stockholm, Sweden

No. of pages : 32

No. of tables : 4

No. of figures: 22

[1] E-mail address: wacek@neutron.kth.se
Postal address: Royal Institute of Technology, Stockholm Center for Physics, Astronomy and Biotechnology, Dept. of Nuclear and reactor Physics, 106 91 Stockholm , Sweden

Nuclear Science and Technology, Volume 142, Number 2, October 2002.

NEUTRON AND PROTON CROSS SECTION EVALUATIONS FOR ^{232}TH UP TO 150 MeV

A. V. Ignatyuk, V. P. Lunev, Yu. N. Shubin, E.V. Gai, N. N. Titarenko

Institute of Physics and Power Engineering, 249020 Obninsk, Russia

W.Gudowski

Royal Institute of Technology, 100-44 Stockholm, Sweden

Abstract: Investigations aimed at the development of neutron and proton cross section evaluations for ^{232}Th at intermediate energies in the range of 0 – 200 MeV are described. The coupled-channels optical model has been used to calculate the neutron total, elastic and reaction cross sections and the elastic scattering angular distributions. Evaluations of the neutron and charged particle emission cross sections and of the fission cross sections have been obtained on the basis of the statistical description that includes direct, pre-equilibrium and equilibrium mechanisms of nuclear reactions. The Kalbach parametrization of angular distributions has been used to describe the double-differential cross sections of emitted neutrons and charged particles in ENDF/B-VI format.

I. INTRODUCTION

Recent development of accelerator-driven transmutation systems (ADS) and their relevance for nuclear waste management has created a new interest in high quality nuclear data for fissile isotopes, structural materials and fission products. In practice, the energy interval from thermal energies to a few thousand MeV should be covered in order to properly model ADS [1]. The status of available nuclear data differs strongly for the energy regions below and above of 20 MeV. Huge efforts have been made in the past to create libraries of evaluated neutron data (ENDF/B, JENDL, JEF, BROND, etc.) for the low energy region, which meet requirements of the conventional nuclear reactors. In spite of some differences between the evaluations, most data in this region satisfy needs of major current applications. In contrast, for energies higher than 20 MeV data are rather scarce and are not yet systematized.

Both neutrons and protons in the energy range between 20 MeV and a few hundred of MeV play non negligible role in accelerator-driven systems and transport of these particles should be simulated with a better precision than allowed by available data today.

A lack of experimental data has to be compensated for by the development of reliable calculation methods. Various methods are used to get the required data: both systematics with parameters selected from comparison with experimental data and models based on various assumptions.

The codes based on the intranuclear cascade model combined with the evaporation model have been successfully applied for energies above a few hundred MeV [2-4]. At lower energies, however, nuclear structure effects are so prominent that their description requires more detailed consideration of competitive reaction mechanisms. Therefore, special attention should be put to this energy region, and the evaluated data files for energies from 20 to 150 MeV should be prepared in the same manner as for the energy region below 20 MeV [1] for the most important structural and fissile materials. Some valuable efforts have been already made by the Los Alamos group [5] and the evaluated data files for more than 40 of the most important structural and shielding materials were extended up to 150 MeV in the ENDF/B-VI library. Also some attempts to prepare similar evaluations for actinides were made by this group [6], but their evaluations were limited to neutron elastic scattering and neutron production cross sections, mainly for energies below 100 MeV. Fission cross sections, charged-particle yields, and fission-neutron yields were discussed in [6] but were not included

in the files prepared on the basis of the evaluations. Moreover, these evaluations suffer of some unrealistic fluctuations obtained in the neutron production cross sections.

The renewed interest in the thorium fuel cycle for ADS and advanced conceptual designs of transmutation systems with conventional U-Pu fuels need reliable data at least for the isotopes of thorium, uranium and plutonium. Evaluation of intermediate energy data for all these nuclides is under intensive development now. The main results of experimental data analysis and evaluations for the intermediate energy neutron and proton data files for ^{232}Th are presented below.

II. INCIDENT NEUTRON ENERGIES BELOW 20 MeV

Below 20 MeV the combination of the BROND-2 and ENDF/B-VI evaluations was used. Data on the number of neutrons per fission, delayed neutron data and number of prompt neutrons per fission and also resonance parameters up to 50 keV were taken from BROND-2, the other data were taken from ENDF/B-VI evaluations with corrections of inelastic scattering cross sections to the first three levels above 2.5 MeV. It was shown in the recent analysis [7,8] that the differences between various evaluations are essential for many data but nowadays we have not enough experimental data to considerably improve current evaluations.

III. INCIDENT NEUTRON ENERGIES ABOVE 20 MeV

Evaluations above 20 MeV are based on nuclear model calculations, whose parameters are to be adjusted to the available experimental data. A coupled-channel optical model has been used to calculate the transmission coefficients for neutrons and charged particles, and to evaluate the angular distributions for neutron and proton scattering as well. The coupled channels calculations were carried out using code ECIS-88 [9] with traditional potential shape based on the Woods-Saxon form for volume real and imaginary parts and with derivative Woods-Saxon for surface peaked imaginary part. Real Tomas spin-orbit interaction was not deformed. The GNASH code [10] was used to calculate the integral and double differential cross sections and to prepare data in ENDF/B-VI format. The level density description for all channels was obtained with the Gilbert-Cameron approach fitted to experimental data on the density of low-lying discrete levels and neutron resonances. The phenomenological systematics of the level density parameters developed in the framework of the RIPL project [11] was applied to the fission channels and to nuclei for which the corresponding experimental information does not exist.

III A. Total and scattering cross sections

Evaluations of neutron total cross sections are based on coupled-channel optical model calculations with potential parameters fitted to experimental data. The analysis of such data was performed in many laboratories, and the deformed optical model parameters obtained were used for the neutron cross section evaluations of heavy nuclei and actinides [7,12-16]. These sets of parameters give approximately the same total cross sections. However, the calculated neutron absorption cross sections differ significantly for various sets. Discrepancies between the absorption cross section evaluations are essential at neutron energies above 10 MeV, and their effects appear in the evaluated cross sections of (n,xn), fission and other reactions.

Among different sets of optical model parameters, mentioned above, only paper [15] by Young suggests parameters for ^{238}U valid for neutron energy up to 100 MeV, and paper by Ignatyuk et al. [7] for neutron energies up to 150 MeV. As was shown in paper [7] the parameters from [15] enable to reproduce experimental total cross-section for neutron energies below 20 MeV rather well, but overestimate it in the energy region 50-150 MeV. The parameters suggested in [12] for neutron scattering on ^{232}Th reproduced experimental angular distributions data of Smith [26] as well as total neutron cross section of Iwasaki et al. [24] surprisingly well. But this set of parameters is valid for neutrons only and for the restricted energy range up to 20 MeV. We made attempts to develop the consistent set of parameters for neutrons and protons in frame of the Lane approach.

For the ^{232}Th nuclei we started from the parameters suggested in paper [7] for ^{238}U, but included into consideration besides data for neutron total cross sections [19-25] and experimental data on neutron angular distributions elastically scattered with the energies from 4.5 up to 10 MeV [26], the experimental data on angular distributions of elastically and inelastically scattered protons with the energies of 20, 26, 35 and 65 MeV [29-33] also. The extending experimental data base for the optical model parameters search leads to the different values of parameters and their dependence on incoming particle energies in comparison with ones from paper [7], in which the main goal was the high energy parameter search, reproducing neutron total and proton inelastic cross-sections only. The inclusion into consideration the experimental data on angular distributions for protons results in the dependence of geometrical parameters on incoming particle energy.

The suggested set of parameters enables to reproduce well the total cross section experimental data of Poenitz et al. [25], which lay a little higher than the data of Iwasaki et al. [24] in the region from 0.5 to 20 MeV. The angular distributions of elastically scattered neutrons with the energies of 4.5-10 MeV [26], and the energy near 14.5 MeV [13,27,28] are reproduced well. Moreover the angular distributions of elastic and inelastic scattered protons with the energies 20 and 26 MeV [29,30], 35 MeV [31,32] and 65 MeV [33] are described rather well.

Therefore an optimal set of optical model parameters has been estimated from the analysis of experimental data on neutron total cross sections, angular distributions for neutron and proton elastic and inelastic scattering, and proton absorption cross sections. These parameters, shown in Table I, differ only a little from those used in our previous evaluations of intermediate energy neutron data on ^{238}U [7].

The total cross section calculated with the parameters given above is compared in Fig. 1 with available experimental data and other calculations. Below 20 MeV there are many experimental data and only some of them are presented in Fig. 1. A reasonable agreement of our calculations with the Barashenkov's systematics [18] and experimental data [19-25] is obtained for all energies above 20 MeV.

The corresponding calculations of neutron and proton absorption cross sections are shown in Fig. 2, upper part and lower part, respectively. There are no direct measurements of these cross sections at high energies. However, a reasonable estimation is given by Barashenkov's systematics, based mainly on proton induced reaction data [18]. The experimental data available for heavy nuclei are also shown in Fig. 2 in comparison with the systematics [18] and our optical model calculations. The optical model calculations reproduce well the proton absorption cross section in the whole energy region from the Coulomb barrier to 200 MeV, and at high energies they are in a reasonable agreement with the Barashenkov's evaluations for both proton and neutron induced reactions. The calculated absorption cross sections for ^{232}Th differ slightly from the similar ones estimated for ^{238}U [7] by a small factor proportional to the ratios of the corresponding geometrical cross sections ($\sim A^{2/3}$). Therefore, the present evaluation of the absorption cross sections above 50 MeV appears to be consistent with all available experimental data.

The coupled-channel model makes it possible to calculate also the angular distributions for elastic and inelastic scattering of neutrons and protons to the low-lying collective levels. In Fig. 3 the calculated cross sections are compared with experimental data on neutron elastic scattering angular distributions at energies below 10 MeV [26].

Experimental data on neutron elastic scattering angular distributions at incident neutron energy of 14.5 MeV [13,27,28] are compared with our calculations in Fig. 4. The contributions of the lowest collective levels, 2^+, 4^+ and 6^+, to inelastic scattering are shown, too. These levels are to be taken into account because their excitation energies are much smaller than the energy resolution in the experimental data of elastic scattering. The quasi-elastic scattering angular distribution including the contributions of the low-lying collective levels is represented by the thick solid curve in Fig. 4.

The results of our calculations of elastic and inelastic neutron (dashed lines) and proton (solid lines) scattering cross sections are compared with experimental data on elastic and inelastic scattering of protons to the low-lying collective levels [29-33] in Figs. 5-8 at proton energies of 20, 26, 35 and 65 MeV.

The reasonable agreement of calculations with experimental data has allowed us to apply the optical model with the parameters obtained to evaluate the elastic and inelastic scattering angular distributions for both neutron and protons over the whole energy range.

III B. Fission cross sections and fission prompt neutrons

The fission cross section above 10 MeV has been measured by several groups [34-49]. In our opinion, the experimental data of Pankratov [41] for incident neutrons in the energy region from 20 to 40 MeV, as well as the data of Kudo et al. [46] and Szerypo et al. [48] for the incident protons at energies about 20 MeV seem too high and contradict data of other groups and were ignored in subsequent analysis. Data of Donets et al. [35] has a preliminary status and it should be taken into consideration only after the complete processing of measurement results.

The calculated neutron induced fission cross sections were fitted to the BROND-2 evaluation at energies below 20 MeV in order to estimate the fission barrier parameters. For higher energies, the effects of nuclear viscosity were included in the calculations of the fission widths of highly excited compound nuclei [50]. As the observed fission cross section at high energies is determined by the contributions of more than a dozen residual nuclei, which undergo fission after emission of neutrons or protons, an estimate of the fission barriers for all nuclei is a rather cumbersome task. Taking into account the damping of shell effects at high energies the calculations have been confined by fitting the liquid drop barriers only. The final evaluation of the fission cross sections for energies above 20 MeV was obtained in the frame of a statistical approximation with rational functions of the available experimental data and

theoretical model curves. The result of this approach is shown in Fig. 9 together with the experimental data and the evaluation of INPE group [51]. It should be noted that an accurate description of the fission cross sections is very important for consistent evaluation of multiple emission of neutrons and charged particles.

The ^{232}Th(p,f) reaction cross section in the energy region from 10 to 200 MeV was estimated on the basis of rational approximation of experimental data up to 303 MeV. Below 6.5 MeV the evaluated cross section was determined on the basis of calculations with GNASH as a renormalised penetrability of the Coulomb barrier. In the energy region from 6.5 to 14 MeV the cross section was calculated with GNASH. Beginning from 12 MeV the calculations and all experimental data above 20 MeV were used. The evaluated ^{232}Th(p,f) reaction cross section is shown in the lower part of Fig. 9 together with the corresponding experimental data.

The results of our evaluation for $<\nu>$, the average number of prompt neutrons per fission, are shown in the lower part of Fig. 10 in the energy region up to 150 MeV for neutrons and protons, together with the experimental data of Howe [52] and the INPE evaluation for the incident neutron energies below 50 MeV [51]. Our evaluations are based mainly on the cascade evaporation fission model calculations fitted to the experimental data below 50 MeV. In the upper part of Fig. 10 the corresponding temperatures of the Maxwellian fission neutron spectrum are shown as a function of the incident particle energies.

III C. Neutron production cross sections and spectra

Evaluations of particle emission spectra and corresponding production cross sections have been performed in accordance with the rules of the ENDF/B-VI format for the double-differential cross sections, by using the Kalbach representation of such data [53]. Differential cross sections are described in this approach by the integral production cross section for the corresponding emitted particle multiplied by a normalised angular distribution function of the following form

$$f(\mu_b, E_a, E_b) = f_0(E_a, E_b)\left\{\frac{a(E_a, E_b)}{\sinh a(E_a, E_b)}\left[\cosh\left(a(E_a, E_b)\mu_b\right) + r(E_a, E_b)\sinh\left(a(E_a, E_b)\mu_b\right)\right]\right\},$$

where E_a is the incident particle energy in the laboratory system, μ_b - cosine of the scattering angle of the emitted particle b and E_b is its energy in the center-of-mass system. $f_0(E_a,E_b)$ is

the normalised spectrum of the emitted particle; $r(E_a,E_b)$ is the pre-compound fraction of this spectrum, and $a(E_a,E_b)$ is the simple function proposed in [53]. The function $a(E_a,E_b)$ depends mainly on the center-of-mass emission energy E_b and, to a lesser extent, on particle type and incident energy at higher values of E_a . Consequently, the two energy-dependent functions $f_0(E_a,E_b)$ and $r(E_a,E_b)$ completely determine (together with $a(E_a,E_b)$) the shape of emitted particle spectra and the anisotropy of the corresponding angular distributions, respectively.

Neutron emission is a dominant reaction that competes with nuclear fission. The calculated neutron production cross sections for both incident neutrons and protons are shown in Fig. 11. For incident neutron energies below 20 MeV, the calculations agree reasonably well with the evaluations of the (n,2n), (n,3n) reactions based on experimental data and included in the BROND-2 evaluation. Above 20 MeV there are no direct experimental data on neutron emission cross sections or on the multiplicity of secondary neutrons.

For incident protons some experimental data on the ^{232}Th(p,xn) in the proton energies below 30 MeV are available too [54,55]. However, these data are not sufficient to estimate the total neutron production cross section, the contributions of ^{232}Th(p,xnf) reactions are required for each step of neutron evaporation. The available experimental data on the cross section of (p,n)+(p,2n)+(p,3n) reactions are shown in Fig. 12 and they well reproduced by our calculations. The calculated cross section of the sum of (p,nf)+(p,2nf)+(p,3nf) reactions is shown also together with the calculated total neutron production cross section. Agreement between calculated (p,xn) cross sections and experimental data may be considered as a partial confirmation of a reasonable estimation of the neutron production cross section for incident protons.

The calculated spectra of emitted neutrons for several energies of incident neutrons and protons are shown in Fig. 13. The pre-equilibrium components of spectra become larger with increasing incident particle energy, while the soft equilibrium components change only a little. The calculated r-factors, which define the anisotropy of secondary neutron angular distributions, are compared for incident neutrons and protons in Fig. 14.

III D. Charged particle emission cross sections and spectra

In order to calculate the transmission coefficients for protons, the same potential as for neutrons, with the corresponding Lane components has been used. The calculated absorption cross section for such a potential agrees reasonably well with Barashenkov's systematics of the proton induced reaction cross sections at high energies [18], but, at the present time, the

experimental data are not accurate enough to test such calculations for energies close to the Coulomb barrier.

The proton production cross section calculated with transmission coefficients mentioned above, is shown in Fig. 15. The corresponding normalized proton spectra and r-factors are presented in Figs. 16 and 14 (lower part), respectively.

For similar calculations of deuteron, triton and α-particle yields, which should be lower than the proton yields, the spherical optical model has been used with the parameters from [56-58] presented in Tables II-IV. The same parameters were applied before for the analogous evaluations of the neutron induced reactions on ^{238}U [7].

Some deficiencies of the pre-equilibrium model used in the GNASH code were demonstrated in the analysis of production cross sections of deuterons and heavier charged particles [17,59,60]. To get more accurate evaluations of deuteron, triton and α-particle yields, the modified ALICE-IPPE code [60] was used. This code describes the cluster emission on the basis of the Ivamoto-Harada model [59] with parameters adjusted to the available experimental data on cluster yields and spectra in proton induced reactions. Deuteron emission was calculated using the quasi-direct and pick-up mechanisms. For triton emission the pick-up processes were taken into account, and for α-particles the knock-out, pick-up and multiple pre-equilibrium emission were included into consideration.

The calculated cross sections for the ^{232}Th(n,xd), ^{232}Th(p,xd), ^{232}Th(n,xt), ^{232}Th(p,xt), ^{232}Th(n,xα), and ^{232}Th(p,xα) reactions are shown in Figs. 17, 18 and 19. The experimental data [61-67] on the yields of the same charged particles in the proton induced reactions on ^{209}Bi and ^{232}Th, the heaviest studied targets, are shown for the comparison. Undoubtedly, uncertainties of such estimations of light cluster production cross sections are rather large, maybe several tens of percent, but at a present time there is not enough experimental data to improve significantly the theoretical description. On the other hand, all of these cross sections are much smaller than the neutron production cross sections, and big uncertainties for these cross sections are probably acceptable for most applications related to the development of accelerator-driven systems.

To evaluate the spectra and angular distributions of emitted charged particles we returned, nevertheless, to the GNASH calculations and Kalbach presentation, but the main parameters of the pre-equilibrium model were changed for each cluster channel in order to obtain the same production cross sections as with the ALICE-IPPE code. The calculated spectra of deuterons, tritons and α-particles are shown in Figs 20, 21 and 22, respectively.

IV. SUMMARY AND CONCLUSIONS

The major components of the intermediate-energy neutron and proton data evaluations for ^{232}Th up to 150 MeV have been described in the present work. Evaluations are based on the coupled-channel model and the statistical model of pre-equilibrium and equilibrium particle emission, with theoretical model parameters adjusted to the available experimental data. The evaluated cross sections are consistent with the well-tested neutron data files below 20 MeV. Complete evaluations have been produced in ENDF/B-VI format. This data enhances capabilities of the high-energy transport codes to simulate more adequately neutron and proton transport in the energy range up to 150 MeV.

Acknowledgements.
This work was partially supported by European Commission in the frame of IABAT-project (FI4I-CT96-0012). The authors acknowledge also support of SKB AB - Swedish Nuclear Fuel and Waste Management Ltd.

REFERENCES

1. A.J. Koning, "Requirements for an Evaluated Nuclear Data File for Accelerator Based Transmutation," Report NEA/NSC/DOC(93)6 and ECN-C-93-005; "Nuclear Data Evaluation for Accelerator-Driven Systems," in: *Proc. Second International Conference on Accelerator-Driven Transmutation Technologies and Applications*, Kalmar, Sweden, June 3-7, 1996, Vol. 1, p. 438, H. Condé, Ed., Gotab, Stockholm, Sweden (1997).
2. H.W. Bertini, "Intranuclear-Cascade Calculation of the Secondary Nucleon Spectra from Nucleon-Nucleus Interactions in the Energy Range 340-2900 MeV and Comparison with Experiment," *Phys.Rev.,* **188,** 1711 (1969).
3. V.S. Barashenkov, V.D.Toneev, Interactions of High Energy Particles with Nuclei, (Atomizdat, Moscow, 1972).
4. R.E. Prael, H. Lichtenstein, "Users Guide to the LAHET Code System," Report LA-UR-89-3014, Los Alamos National Laboratory (1989).
5. M.B. Chadwick, P.G. Young, S. Chiba, S.C. Frankle, G.M. Hale, H.G. Hughes, A.J. Koning, R.C. Little, R.E. MacFarlane, R.E. Prael, and L.S. Waters, "Cross-Section Evaluations to 150 MeV for Accelerator-Driven Systems and Implementation in MCNPX," *Nucl. Sci. Eng.,* **131**, 293 (1999).
6. P.G. Young, E.D. Arthur, M. Bozoian, T.R. England, G.M. Hale, R.J.LaBauve, R.C. Little, R.E. MacFarlane, D.G. Madland, R.T. Perry, and W.B. Wilson, "Transport Data Libraries for Incident Proton and Neutron Energies to 100 MeV," Report LA-11753-MS, Los Alamos National Laboratory (1990).
7. A.V. Ignatyuk, V. P. Lunev, Yu. N. Shubin, E.V. Gai, N.N. Titarenko, A. Ventura, W. Gudowski, "Neutron Cross Section Evaluations for ^{238}U up to 150 MeV," *Nucl. Sci. Eng.,* **131**, 340 (2000).
8. B.D. Kuzminov, V.N. Manokhin, "Status of Nuclear Data for Thorium Fuel Cycle," in: Voprosy Atomnoi Nauki i Tekhniki (VANT), ser. Yadernye Konstanty, № 3-4, 41, (1997) (In Russian).
9. J. Raynal, "Coupled-Channel Calculations and Computer Code ECIS," in: "Workshop on Applied Nuclear Theory and Nuclear Model Calculations for Nuclear Thechnology Applications" Trieste, Italy, Feb. 15 – March 18, 1988, (Trieste 1988), M.K.Mehta and J.J.Schmidt Editors. World Scientific, (1989) p. 506.
10. P.G. Young, E.D. Arthur, M.B. Chadwick, "Comprehensive Nuclear Model Calculations: Theory and Use of the GNASH Code," in: *Proc. IAEA Workshop on Nuclear Reaction*

Data and Nuclear Reactors. Trieste, Italy, 15 April - 17 May 1996, Vol. 1, p. 227, A.Gandini and G.Reffo Editors, World Scientific, Singapore (1998)

11. A.V. Ignatyuk, "Level Densities," In: Reference Input Parameter Library for Nuclear Model Calculations – Handbook, IAEA – TECDOC-1034, Vienna, 1998, ch. 5.
12. Ch. Lagrange, "Results of coupled channels calculations for the neutron cross sections of a set actinide nuclei," Report NEANDC(E) 228"L", INDC (FR) 56/L (1982).
13. L.F. Hansen, B.A. Pohl, C. Wong, R.C. Haight, Ch. Lagrange, "Measurements and Calculation of Neutron Scattering in Actinide Region," *Phys. Rev.,* **C34**, 2075 (1986).
14. V.A. Konshin, "Calculations of Neutron and Proton Induced Reaction Cross Sections for Actinides in the Energy Region from 10 MeV to 1 GeV," Report JAERI-Research-95-036, Japan Atomic Energy Research Institute (1995).
15. P.G. Young, "Optical Model Parameters," in Reference Input Parameter Library for Nuclear Model Calculations – Handbook, IAEA–TECDOC-1034, Vienna, 1998, ch. 4.
16. H. Vonach, A. Pavlik, M.B. Chadwick, R.C. Haight, R.O. Nelson, S.A. Wender, and P.G. Young, "$^{207, 208}$Pb(n,xn) Reactions for Neutron Energies from 3 to 200 MeV," *Phys. Rev.,* **C50**, 1952 (1994).
17. M.B. Chadwick, P.G. Young, "GNASH Calculations of the Neutron and Proton Induced Reactions for Lead Isotopes and Benchmarking of Results," Report T-2-96, Los Alamos National Laboratory (1996).
18. V.S. Barashenkov, Cross Sections of Particle and Nucleus Interactions with Nuclei (Russian), JINR, Dubna, 1993.
19. R.H. Hildebrand, C.E. Leith, "Total Cross Sections of Nuclei for 42-MeV Neutrons," *Phys. Rev*., **80**, 842 (1950).
20. G. Deconninck, A. Gonze, P. Macq, J.P. Meulders, "Total Cross-Sections for 28.4 MeV Neutrons," *Journal de Physique – Colloquia,* **22,** 652 (1961).
21. J.L. Leroy, F.C. Berthelot, E. Pomelas, "Measurement of Sodium, Thorium And Uranium Cross Sections for Neutrons with Energies Between 2 and 10 MeV," *Journal de Physique – Colloque,* **24**, 826 (1963).
22. U. Fasoli, D. Toniolo, G. Zago, L. Zuffi, "Total Neutron Cross Section For 90-Th-232 in the Energy Region 1.5 - 8.5 MeV," *Nucl.Phys.,* **A151,** 369 (1970).
23. D.G. Foster Jr., D.W. Glasgow, "Neutron Total Cross Sections, 2.5 - 15 MeV," *Phys. Rev.,* **C3,** 576 (1971).

24. T. Iwasaki, M. Baba, K. Hattori, K. Kanda, S. Kamata, N. Hirakawa, "Measurements of Neutron Total Cross Section for Th-232", in: *Specialists' Meeting on Fast Neutron Scattering on Actinide Nuclei*. NEANDC(J)-75, (1981)
25. W.P. Poenitz, J.F. Whalen, "Total Neutron Cross Sections Measurements in the Energy Region from 47 keV to 20 MeV," Report ANL-NDM-80 (1983).
26. A.B. Smith and S. Chiba, "Neutron Scattering from Elemental Uranium and Thorium," *Annals of Nuclear Energy*, **23**, 459 (1996).
27. Ju.V. Dukarevich, A.N. Djumin, "Elastic Low Angle Scattering of Fast Neutrons," *ZET (Journal of Experimental and Theoretical Physic)*, **44(1),** 130 (1963).
28. C.I. Hudson Jr., W.S. Walker, S. Berko, "Differential Elastic Scattering of 15.2-MeV Neutrons by Ta, Bi, Th, U," *Phys. Rev*., **128,** 1271 (1962).
29. L.F. Hansen, I.D. Proctor, and D.W. Heikkinen, V.A. Madsen, "Nuclear deformation in the actinide region by proton inelastic scattering," *Phys. Rev.,* **C25,** 189 (1982).
30. L.F. Hansen, S.M. Grimes, C.H. Poppe, and C. Wong, "Charge exchange (p,n) reactions to isobaric analogue states of high Z nuclei: $73 < Z < 92$," *Phys. Rev.,* **C28,** 1934 (1983).
31. C.H. King, G.M. Crawley, J.A. Nolen, Jr., and J. Fink, "Extraction of deformation parameters from inelastic proton scattering," *J. Phys. Soc. Japan,* **44** Suppl., 564 (1978).
32. C.H. King, J.E. Finck, G.M. Crawley, J.A. Nolen Jr., and R.M. Ronningen, "Multipole moments of ^{154}Sm, ^{176}Yb, ^{232}Th, and ^{238}U from proton inelastic scattering," *Phys. Rev.,* **C20,** 2084 (1979).
33. Y. Takeuchi, H. Skaguchi, M. Nakamura, T. Ichichara, M. Yosoi, M. Ieri, and S. Kobayashi, "Quadrupole and hexadecapole moments of ^{232}Th and ^{238}U from inelastic scattering of 65 MeV polarised protons," *Phys. Rev.,* **C34,** 493 (1986).
34. R.V. Babcock. EXFOR12294 (1961)
35. A.Yu. Donets, A.V. Evdokimov, A.V. Fomichev, T. Fukhahori, A.B. Laptev, G.A. Petrov, O.A. Shcherbakov, Yu.V. Tuboltsev, A.S. Vorobyev, "Neutron-Induced Fission Cross-Sections of U233, U235, U238, Th232, Pu239 and Np237 in the energy range 1 - 200 MeV," in: *Proceedings of the VII International Seminar on Interaction of Neutrons with Nuclei, ISINN-7*. Dubna , May 25-28, 1999, JINR Report E3-98-212, W.I. Furman Editor, Dubna, 1999. p.p.357-362. Status of the data is preliminary.
36. V.P. Eismont, A.P. Korobkin, A.V. Prokofyev, A.N. Smirnov, J. Blomgren, H. Conde, K. Elmgren, N. Olsson, J. Rahm, E. Ramstrem, "Neutron-Induced Fission Cross Section Measurements for 232Th, 235U and 238U in the Intermediate Energy Region," in: *Proc.*

of the International Conference Nuclear Data for Science and Technology. Trieste, Italy, 19-24 May 1997 G. Reffo, A. Ventura and C. Grandi Editors, (1997) p.p. 494-496.

37. A.V. Fomichev, I.V. Tuboltseva, A.Yu. Donets, A.B. Laptev, O.A. Shcherbakov, G.A. Petrov, "Measurement of neutron induced fission cross section ratios," in: *Proc. of the International Conference Nuclear Data for Science and Technology,* Julich, Germany, 13-17 May 1991, S.M. Qaim Editor, Springer-Verlag 1992, p.p.734-736.
38. P.W. Lisowski et al., in: *Proc. Symp. On Neutron Cross-Sections from 10 to 50 MeV*, Brookhaven National Laboratory, Upton, NY, USA, 12-14 May 1980, **v. 1** (1980) p.301.
39. P.W. Lisowski et al., in: *Proc. Specialists' Meeting on Neutron Cross-Sections Standards for the Energy Above 20 MeV*, Uppsala, Sweden 21-23 May 1991, p.178 (1991)
40. V.M. Pankratov, N.A. Vlasov, B.V. Rybakov, "Cross Sections for the Fission of Th-232, U235 and U238 Induced by 10-22 MeV Neutrons," *Atomnaya Energiya,* **9**, 399 (1960) (In Russian).
41. V.M. Pankratov, "Fission Cross Sections of Th232, U233, U235, Np237, U238 for 5-37 MeV Neutrons," *Aomnaya Energiya*, **14**, 177 (1963) (In Russian).
42. B.A. Bochagov, V.S. Bychenkov, I.D. Dmitriev, S.P. Maltsev, A.I. Obukhov, N.A. Perfilov, V.A. Udod, O.E. Shigaev, "Determination of fission cross sections in irradiation of ^{238}U, ^{235}U, ^{209}Bi, $^{208\text{-}206}$Pb, ^{197}Au ^{181}Ta, Yb and Sm with 1 GeV protons," *Yadernaya Fizika*, **28,** 572 (1978) (In Russian).
43. V.P. Eismont, A.V. Prokofyev, A.N. Smirnov, "Cross sections of intermediate energy proton induced fission of heavy nuclei and fissility of excited nuclei," in: *Proc. of the International Conference Nuclear Data for Science and Technology,* Gatlinburg, Tennessee, USA, May 9-13, 1994, J.K. Dickens Editor, (1994) pp. 397-399.
44. V.A. Konshin, E.S. Matusevitch, V.I. Regushevsky, "Cross-section for the fission of ^{181}Ta, Re, Pt, ^{197}Au, Pb, ^{209}Bi, ^{232}Th, ^{235}U and ^{238}U by protons in the energy 150-660 MeV," *Yadernaya Fizika*, **2,** 682 (1965) (in Russian).
45. W. Kurzewicz, J. Szerypo, P. Hornshoj, N. Rud, Z. Zelazny, W. Reisdorf, "Fission of ^{232}Th Induced by 4 - 11 MeV Protons," *Z. Physik,* **A306,** 99 (1982).
46. H. Kudo, H. Muramatsu, H. Nakahara, K. Miyano, I. Kohno, "Fission fragment yields in the fission of ^{232}Th by protons of energies 8 to 22 MeV," *Phys. Rev.,* **C25,** 3011 (1982).
47. H. Steiner, J.A. Jungerman, "Proton-induced fission cross sections for ^{238}U, ^{235}U, ^{232}Th, ^{209}Bi, and ^{197}Au," *Phys. Rev.,* **101,** 807 (1956).
48. J. Szerypo, B. Szweryn, P. Hornshoj, H. Loft Nielsen, M. Luontama, "Radiative Capture of Protons by the Deformed Nuclide ^{232}Th," *Z. Physik,* **A323,** 97 (1986).

49. H. Tewes, "Excitation functions for some Proton-induced reactions of Thorium," *Phys. Rev.,* **98,** 25 (1955).
50. A.V. Ignatyuk, G.A. Kudyaev, A.R. Junghans, M. deJong, M.G. Clerc, and K.H.Schmidt, "Analysis of dissipation effects in nuclear fission observed in the fragmentation of ^{232}Th projectiles," *Nucl. Phys*., **A593**, 519 (1995).
51. Yu.A. Korovin, A.Yu. Konobeyev, V.P. Lunev, P.E. Pereslavtsev, A.Yu. Stankovsky, *INPE MATERIAL 9032* incident neutron data file for Th-232 (Eval-SEP96) Obninsk 1996.
52. R.E. Howe, "Measurement of fission neutron multiplicities for Thorium-232 and uranium-235 with incident neutron energies to 49 MeV," *Nucl. Sci. Eng.,* **86**, 157 (1984).
53. C. Kalbach, "Systematics of Continuum Angular Distributions," *Phys. Rev.,* **C37,** 2350 (1988).
54. A. Celler, M. Luontama, J. Kantele, J. Zylicz, "Cross section of Th-232(p,xn+yn) reactions at energy of protons 6.8 to 20.2 MeV," *PhysicaScripta,* **24,** 930 (1981).
55. H. Kudo, H. Muramatsu, H. Nakahara, K. Miyano, I. Kohno, "Fission fragment yields in the fission of ^{232}Th by protons of energies 8 to 22 MeV," *Phys. Rev.,* **C25,** 3011 (1982).
56. J. Bojowald, H. Machner, H. Nann, W. Oelert, M. Rogge, and P. Turek, "Elastic deuteron scattering and optical model parameters at energies up to 100 MeV," *Phys. Rev.,* **C38,** 1153 (1988).
57. F.D. Becchetti Jr., and G.W.Greenlees, Ann. Rep. J.H. Williams Lab., Univ. Minnesota (1969).
58. V. Avrigeanu, P.E. Hodgson, and M. Avrigeanu, "Global Optical Potentials for Emitted Alpha Particles," *Phys.Rev.,* **C49,** 2255 (1994).
59. A. Iwamoto, K. Harada, "Mechanism of Cluster Emission in Nucleon-Induced Pre-equilibrium Reactions," *Phys. Rev.,* **C26,** 1821 (1982).
60. A.I. Dityuk, A.Yu. Konobeyev, V.P. Lunev, Yu.N. Shubin. "New Advanced Version of Computer Code ALICE-IPPE," Report INDC(CCP)-410, IAEA, Vienna (1998).
61. F.E. Bertrand and R.W. Peelle, "Complete Hydrogen and Helium Particle Spectra from 30 to 60 MeV Proton Bombardment of Nuclei with A=12 to 209 and Comparison with Intranuclear Cascade Model," *Phys. Rev*., **C8**, 1045 (1973).
62. J.R. Wu, C.C. Chang , H.D. Holmgren, "Charged particle spectra: 90 MeV Protons on ^{27}Al, ^{58}Ni, ^{90}Zr, and ^{209}Bi," *Phys. Rev*., **C19,** 698 (1979).
63. M. Lefort, G.N. Simonoff, X. Tarrago, R. Bibron, " Production de Tritium dans le Thorium par des Protons de 135 MeV," *J. Phys. Radium*, **20**, 959 (1959).

64. C. Brun, M. Lefort, X. Tarrago, "Contribution a l'Etude du Double Pick-up Indirect Mesure de la Production de Tritium par des Protons de 82 et 105 MeV dans Diverses Cibles," *J. Phys. Radium,* **23,** 167 (1962).
65. M. Lefort, J.P. Cohen, H. Dubost, and X. Tarrago, "Evidence for Nucleon Clustering from High-Energy Reactions," *Phys. Rev.,* **139 B**, 1500 (1965).
66. H. Gauvin, M. Lefort, and X. Tarrago, "Emission d'Helions dans les Reactions de Spallation," *Nucl. Phys.,* **39**, 447 (1962).
67. H. Dubost, M. Lefort, J. Peter, and X. Tarrago, "^{4}He and ^{3}He Particles from Au, Bi and Th Nuclides Bombarded by 157-MeV Protons," *Phys. Rev.,* **136 B**, 1618 (1964).

TABLE I. Optical potential parameters for neutrons and protons on ^{232}Th*

Well depth, MeV	Energy Range, MeV	Geometry, fm
$V_r = 51.5 \pm 16\eta - 0.242E + \Delta_c$	$0 < E < 40$	$r_v = 1.21,\ a_v = 0.7$
$V_r = 50.58 \pm 16\eta - 0.219E + \Delta_c$	$40 < E < 100$	$r_v = 1.21,\ a_v = 0.7$
$V_r = 49.34 \pm 16\eta - 0.2066E + \Delta_c$	$100 < E < 150$	$r_v = 1.21,\ a_v = 0.7$
$\Delta_c = 0.4Z/A^{1/3}$		$r_{coul} = 1.26$
$W_d = 2.079 \pm 5\eta + 0.686E - 2.12 10^{-2}E^2$	$0 < E < 20$	$r_d = 1.455 - 2.81 10^{-2}E + 7.625 10^{-4}E^2$, $a_d = 0.621 + 8.61 10^{-3}E$, E<15 MeV $a_d = 0.75$, E>15 MeV
$W_d = 9.619 \pm 5\eta - 0.123E + 4.0 10^{-4}E^2$	$20 < E < 150$	$r_d = 1.2$, $a_d = 0.75$, E>15 MeV
$W_V = 0.0$	$0 < E < 14.2$	
$W_v = -1.708 + 0.122E - 2.2 10^{-4}E^2$	$14.2 < E < 100$	$r_v = 1.26$, $a_v = 0.35 + 1.8 10^{-3}E$
$W_v = 0.692 + 0.098E - 2.2 10^{-4}E^2$	$100 < E < 150$	$r_v = 1.26$, $a_v = 0.35 + 1.8 10^{-3}E$
$V_{so} = 6.18$	$0 < E < 150$	$r_{so} = 1.16,\ a_{so} = 0.667$

*Here $\eta = (A-2Z)/A$; $\beta_2 = 0.196$, $\beta_4 = 0.07$ and the scheme of 0^+-2^+-4^+-6^+coupled levels is adopted.

TABLE II. The optical potential parameters for deuterons [56]

Well depth, MeV	Energy range, MeV	Geometry, fm
$V_r = 81.32 - 0.24E + \Delta_c$		$r_v = 1.18,\ a_v = 0.636 + 0.035A^{1/3}$
$\Delta_c = 1.43Z/A^{1/3}$		$r_{coul} = 1.30$
$W_v = 0.0$	E< 45	$r_{wv} = 1.27, a_{wv} = 0.768 + 0.021A^{1/3}$
$W_v = 0.132(E-45)$	E> 45	
$W_d = \max(0; 7.80 + 1.04A^{1/3} - 0.712W_v)$		$r_{wd} = 1.27$, $a_{wd} = 0.768 + 0.021A^{1/3}$
$V_{so} = 6.00$		$r_{so} = 0.78 + 0.038A^{1/3}$ $a_{so} = 0.78 + 0.038A^{1/3}$

TABLE III. The optical potential for tritons [57]

Well depth, MeV	Energy Range, MeV	Geometry, fm
$V_r = 165.0 - 0.17E - 6.4(A-2Z)/A$		$r_v = 1.200,\ a_v = 0.720$
		$r_{coul} = 1.30$
$W_v = 46.0 - 0.33E - 110(A-2Z)/A$	E< 40 MeV	$r_{wv} = 1.40,\ a_{wv} = 0.840$
$W_v = 32.8 - 110(A-2Z)/A$	E> 40 MeV	
$V_{so} = 2.5$		$r_{so} = 1.200,\ a_{so} = 0.720$

TABLE IV. The optical potential parameters for α-particles [58]

Well depth, MeV	Energy range, MeV	Geometry, fm
V_r= 101.1-0.248E+Δ_c		r_v= 1.245, a_v=0.817-0.0085$A^{1/3}$
Δ_c= 6.051Z/$A^{1/3}$		R_{coul}=1.245
W_V= 12.64+0.2E -1.706$A^{1/3}$ W_V= 26.82+0.006E -1.706$A^{1/3}$	E<73 E>73	r_{wv}= 1.57, a_{wv}= 0.692-0.02$A^{1/3}$

FIGURE CAPTIONS

Fig. 1. Comparison of different calculations of the total neutron cross section with experimental data: Hildebrand et al. [19]; Deconninck et al. [20]; Leroy et al. [21]; Fasoli et al. [22], Foster et al. [23], Iwasaky et al. [24], Poenitz et al. [25]. The solid curve represents the current work, dashed line is the Barashenkov's systematics, dot-dashed is the INPE evaluation up to 50 MeV.

Fig. 2. Comparison of the calculated neutron and proton absorption cross sections with experimental data and Barashenkov systematics from [18].

Fig. 3. Comparison of the calculated elastic scattering neutron cross section with the available experimental data for energies below 10 MeV [26]. Each calculated curve is shifted relative to the data at the energy 10 MeV by factor 10, successively.

Fig. 4. Comparison of the calculated elastic scattering neutron cross section at 14.5 MeV with experimental data. The scattering cross sections for the ground and collective low-lying levels are shown by solid and dot-dashed curves respectively. The thick solid curve is the sum of the cross sections for the ground and collective low-lying levels; experimental data from: Dukarevich et al. [27], Hudson et al. [28], Hansen et al. [13]. The calculated elastic scattering cross section for 14.5 MeV protons is shown by the dashed curve.

Fig. 5. Comparison of the calculated elastic and inelastic scattering proton (solid lines) and neutron (dashed lines) cross sections at 20 MeV with experimental data [29]. For the elastic scattering the ratio to the corresponding Rutherford scattering cross section is shown for protons.

Fig. 6. The same as in Fig. 5 for the proton energy 26 MeV. Experimental data from [29,30].

Fig. 7. The same as in Fig. 5 for the proton energy 35 MeV. The experimental data are taken from [31,32].

Fig. 8. Comparison of the calculated elastic and inelastic scattering proton cross sections (the solid curves) at 65 MeV with experimental data [33]. The calculated cross sections for incident neutrons are shown by the dashed curves.

Fig. 9. Evaluated fission cross section for neutron and protons in comparison with the experimental data [34-49] and INPE evaluation [51].

Fig. 10. Evaluated prompt fission neutron numbers and fission neutron spectra temperatures for incident neutrons (solid curves) and protons (dashed curves) in comparison with the available above 20 MeV experimental data [52] and the previous evaluation [51].

Fig. 11. Evaluated neutron production cross sections for incident neutrons from the (n,xn) reactions (solid curve) and protons from the (p,xn) reactions (dashed curve) in comparison with the IPNE evaluation [51] and experimental data of Celler et al., [54] and Kudo et al., [55].

Fig. 12. Low-energy part of calculated neutron production cross sections (dashed curve) in comparison with the available experimental data on the (p,xn) cross sections and the calculated (p,xnf) cross section (dot-dashed curve). The calculated (p,xn) cross section is shown by the dotted curve. Experimental data of Celler et al. [54] and Kudo et al., [55].

Fig. 13. Normalised secondary neutron spectra for the incident neutrons (solid curves) and protons (dashed curves) at the incident particle energies 20, 50, 100 and 150 MeV.

Fig. 15. Evaluated proton production cross sections for incident neutrons (solid curve) and protons (dashed curve). Experimental data from [61,62].

Fig. 16. Normalised secondary proton spectra for the incident neutrons (solid curves) and protons (dashed curves) at the incident particle energies 20, 50, 100 and 150 MeV.

Fig. 14. Preequilibriuim components of the neutron (solid curves) and proton (dashed curves) spectra for the incident neutron energies 20 MeV, 50 MeV, 100 MeV, and 150 MeV .

Fig. 17. The deuteron production cross section evaluated on the basis of statistical calculations and experimental data by Bertrand et al. [61] and Wu et al. [62].

Fig. 18 The triton production cross section evaluated on the basis of statistical calculations and experimental data by Bertrand et al. [61], Wu et al. [62], Lefort at al. [63,65], and Brun et al. [64].

Fig. 19. The α-production cross section evaluated on the basis of statistical calculations and experimental data by Bertrand et al. [61], Wu et al. [62], Gauvin et al. [66], and Dubost at al. [67].

Fig. 20. Normalized secondary deuteron spectra for the incident neutron (solid curves) and protons (dashed curves) at the incident particle energies 20, 50, 100 and 150 MeV.

Fig. 21. Normalized secondary triton spectra for the incident neutron (solid curves) and protons (dashed curves) at the incident particle energies 20, 50, 100 and 150 MeV.

Fig. 22. Normalized secondary α-particle spectra for the incident neutron (solid curves) and protons (dashed curves) at the incident particle energies 20, 50, 100 and 150 MeV.

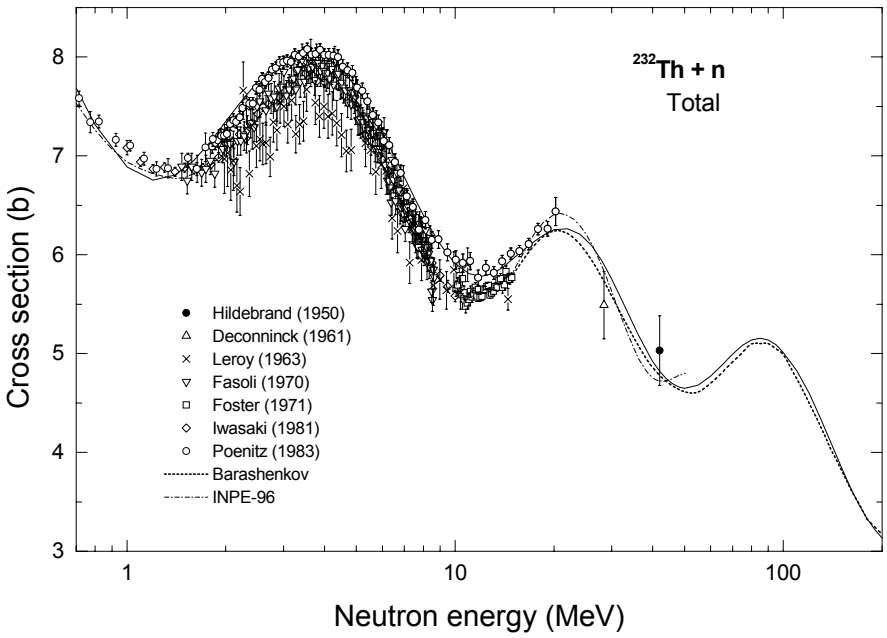
232Th + n
Total
Hildebrand (1950)
Deconninck (1961)
Leroy (1963)
Fasoli (1970)
Foster (1971)
Iwasaki (1981)
Poenitz (1983)
Barashenkov
INPE-96
Cross section (b)
Neutron energy (MeV)

Fig.1.

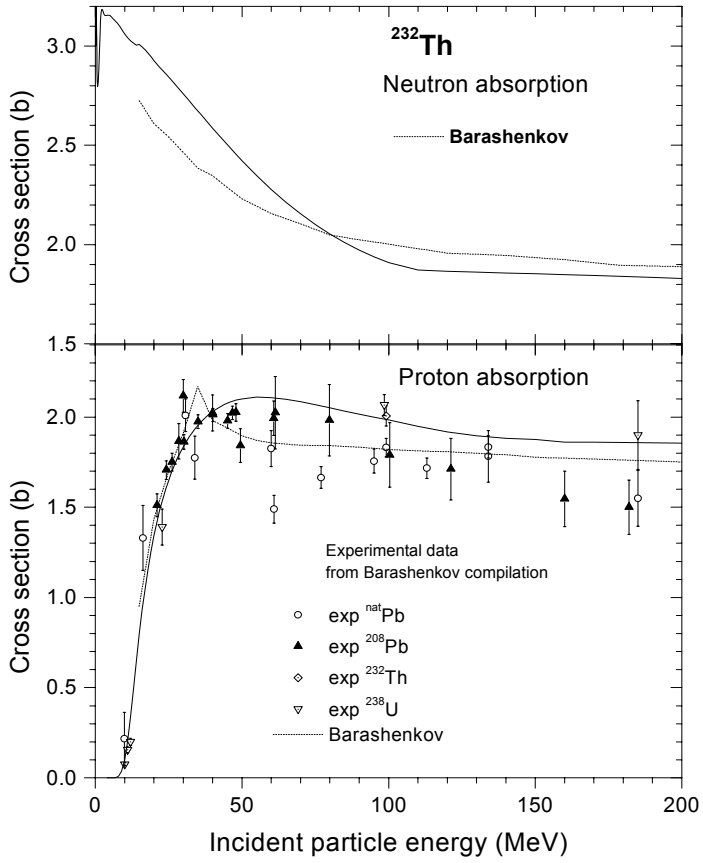
232Th
Neutron absorption
Barashenkov
Proton absorption
Experimental data
from Barashenkov compilation
exp natPb
exp 208Pb
exp 232Th
exp 238U
Barashenkov
Cross section (b)
Incident particle energy (MeV)

Fig.2.

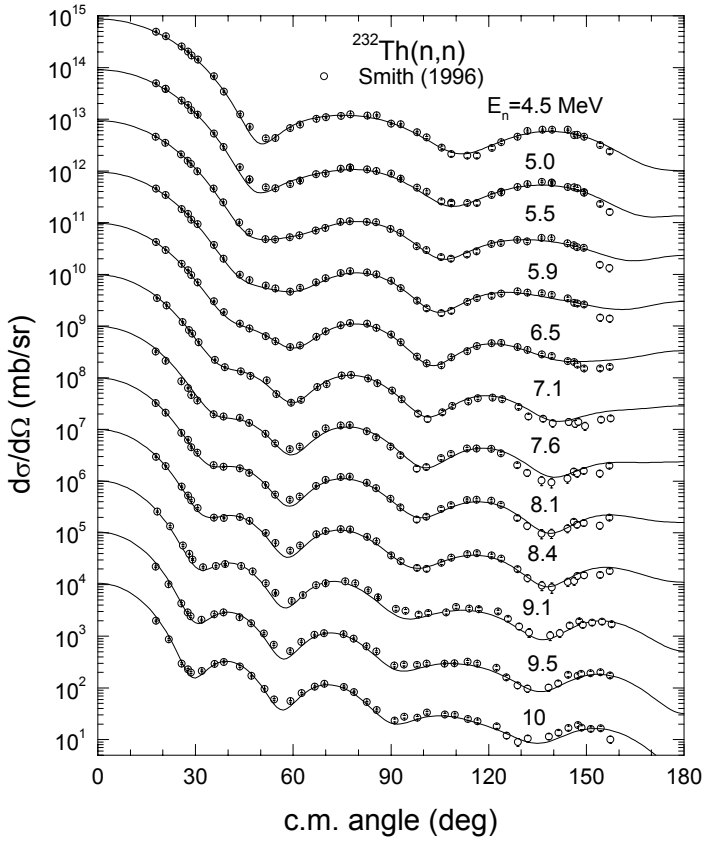
^{232}Th(n,n)
Smith (1996)
E_n=4.5 MeV
5.0
5.5
5.9
6.5
7.1
7.6
8.1
8.4
9.1
9.5
10
dσ/dΩ (mb/sr)
c.m. angle (deg)

Fig.3.

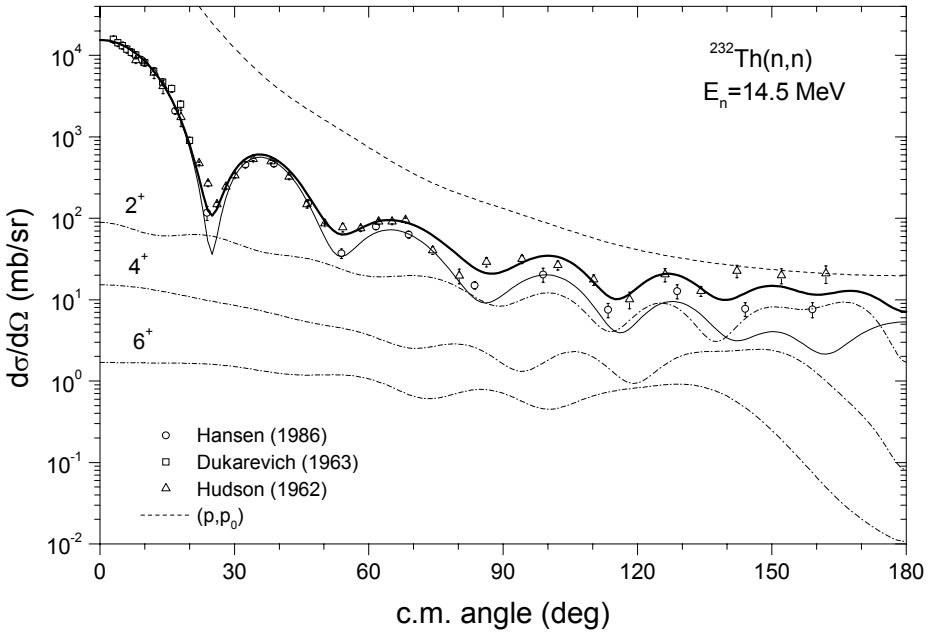
^{232}Th(n,n)
E_n=14.5 MeV
2^+
4^+
6^+
Hansen (1986)
Dukarevich (1963)
Hudson (1962)
(p,p_0)
dσ/dΩ (mb/sr)
c.m. angle (deg)

Fig.4.

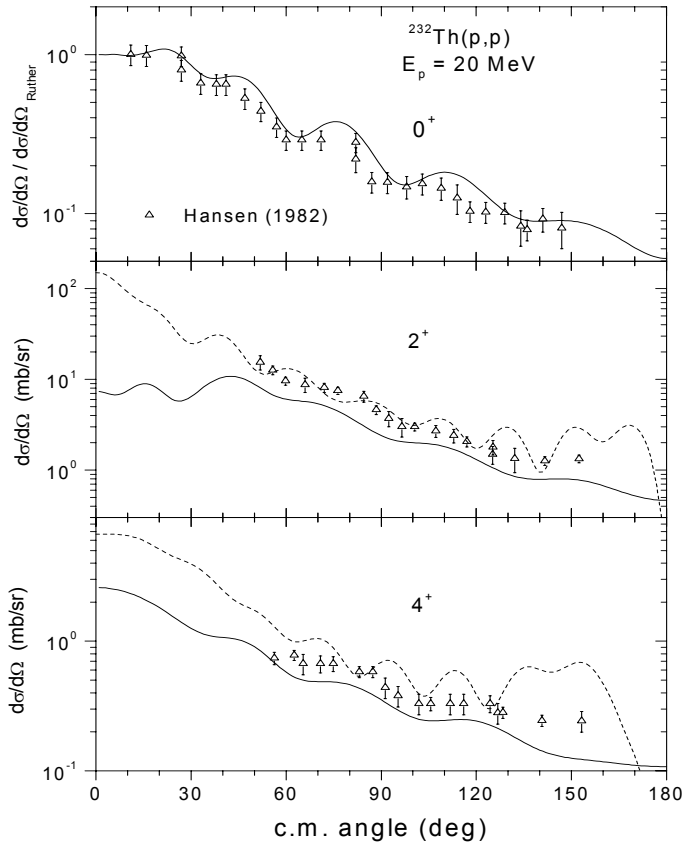
^{232}Th(p,p)
E_p = 20 MeV
0^+
Hansen (1982)
2^+
4^+
dσ/dΩ / dσ/dΩ Ruther
dσ/dΩ (mb/sr)
c.m. angle (deg)

Fig.5.

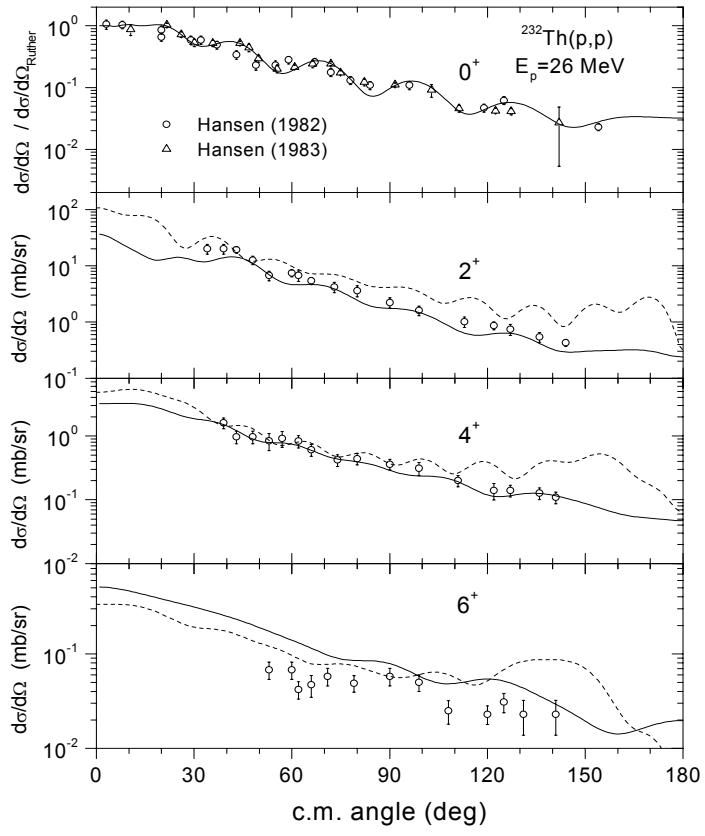
^{232}Th(p,p)
E_p=26 MeV
0^+
Hansen (1982)
Hansen (1983)
2^+
4^+
6^+
dσ/dΩ / dσ/dΩRuther
dσ/dΩ (mb/sr)
c.m. angle (deg)

Fig.6.

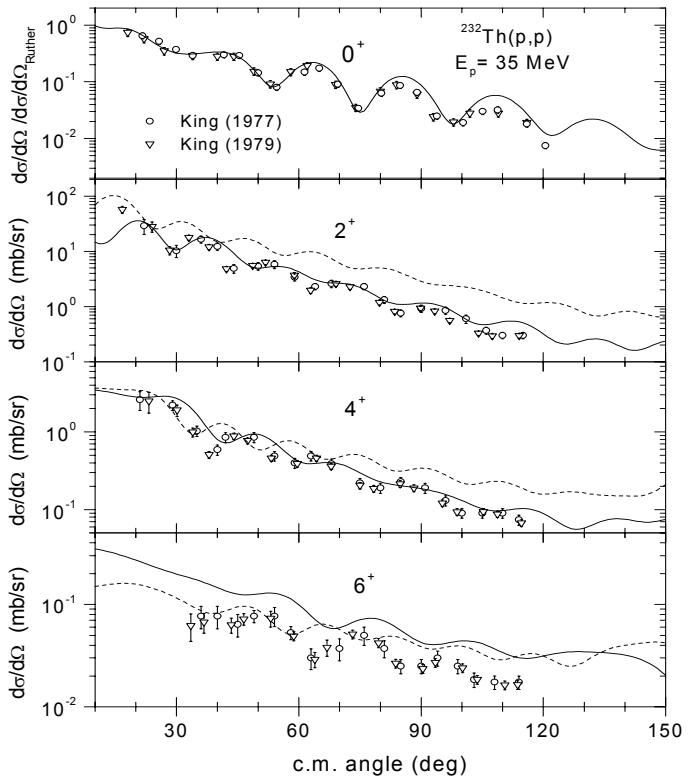
^{232}Th(p,p)
E_p= 35 MeV
0^+
2^+
4^+
6^+
King (1977)
King (1979)
dσ/dΩ /dσ/dΩ$_{Ruther}$
dσ/dΩ (mb/sr)
c.m. angle (deg)

Fig.7.

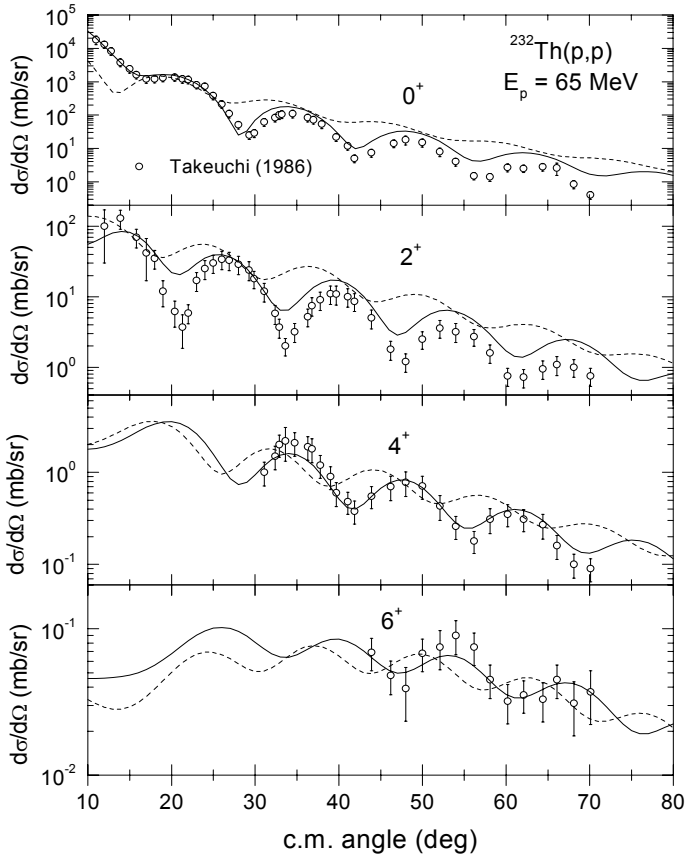
^{232}Th(p,p)
E_p = 65 MeV
0^+
2^+
4^+
6^+
Takeuchi (1986)
dσ/dΩ (mb/sr)
c.m. angle (deg)

Fig.8.

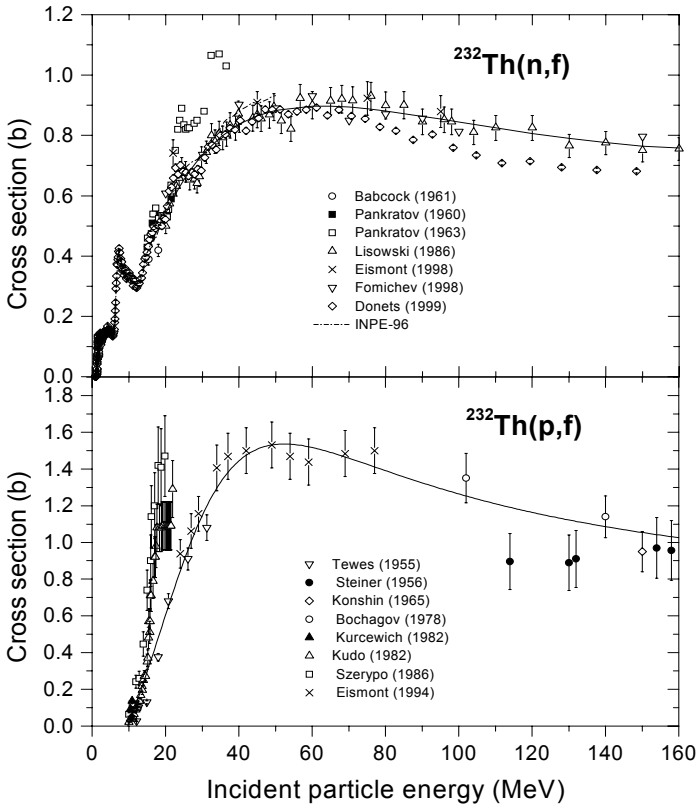
232Th(n,f)
Babcock (1961)
Pankratov (1960)
Pankratov (1963)
Lisowski (1986)
Eismont (1998)
Fomichev (1998)
Donets (1999)
INPE-96
232Th(p,f)
Tewes (1955)
Steiner (1956)
Konshin (1965)
Bochagov (1978)
Kurcewich (1982)
Kudo (1982)
Szerypo (1986)
Eismont (1994)
Cross section (b)
Incident particle energy (MeV)

Fig.9.

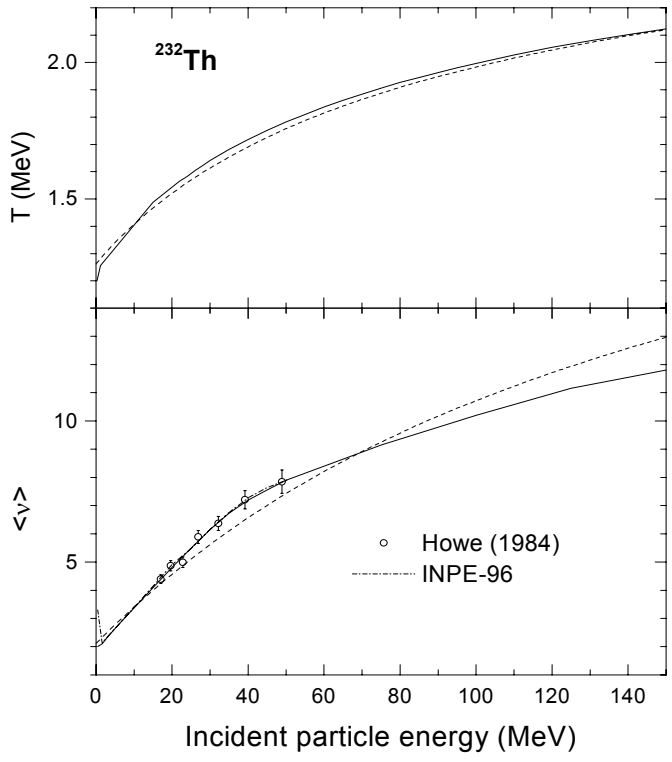
232Th
T (MeV)
<ν>
Howe (1984)
INPE-96
Incident particle energy (MeV)

Fig.10.

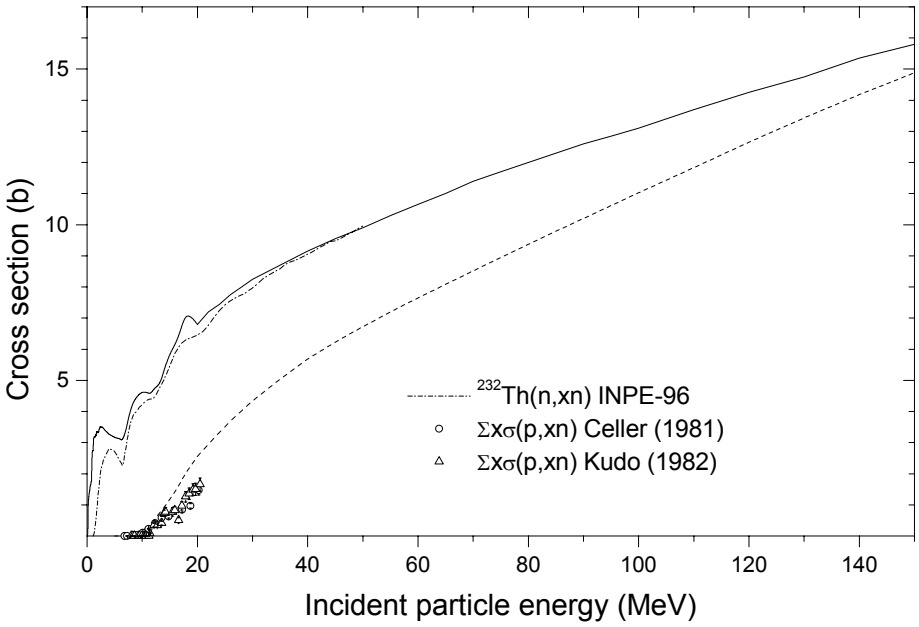
Cross section (b)
Incident particle energy (MeV)
^{232}Th(n,xn) INPE-96
Σxσ(p,xn) Celler (1981)
Σxσ(p,xn) Kudo (1982)

Fig.11.

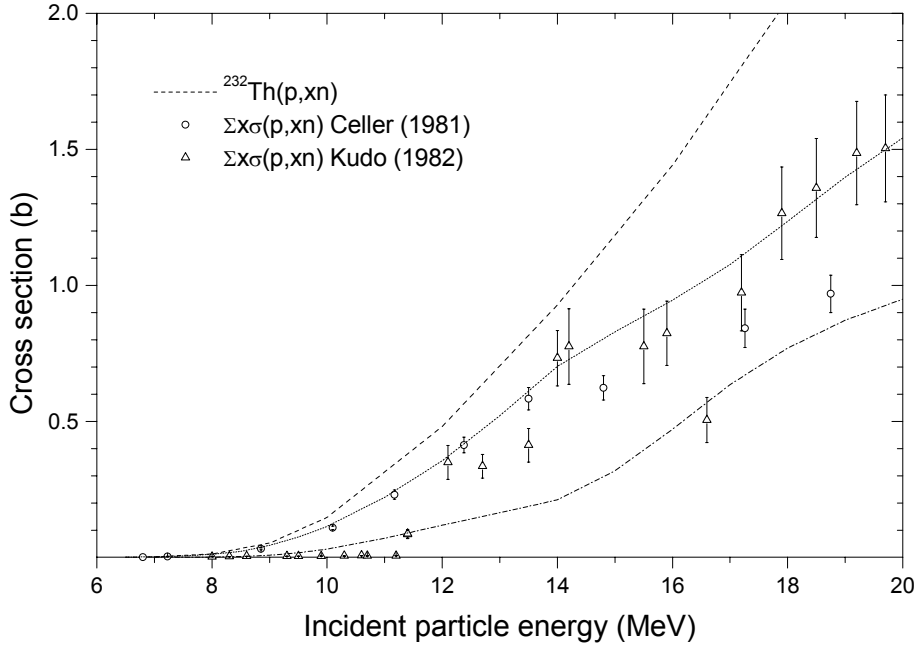
Cross section (b)
Incident particle energy (MeV)
^{232}Th(p,xn)
Σxσ(p,xn) Celler (1981)
Σxσ(p,xn) Kudo (1982)

Fig.12.

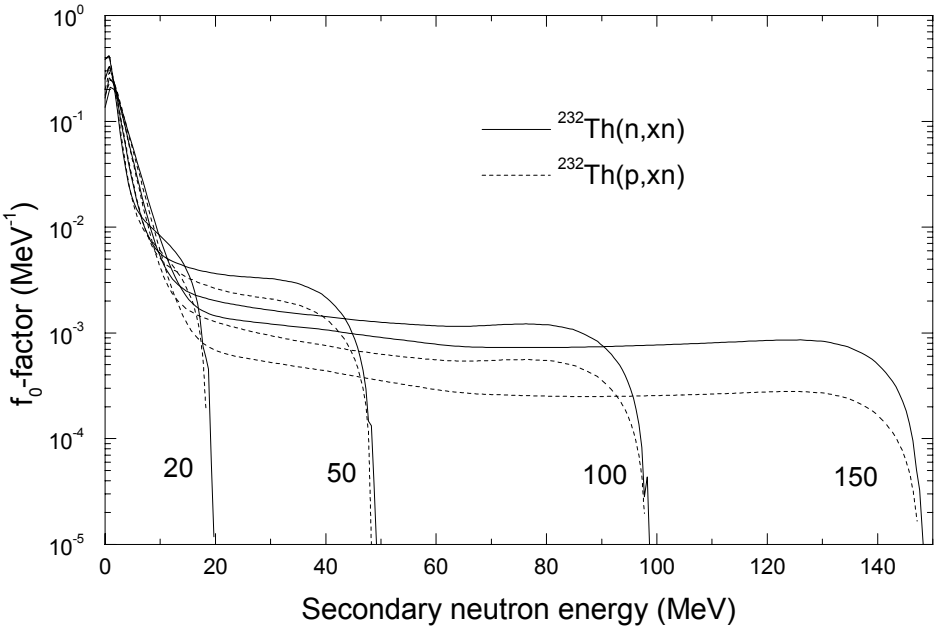
10^0
10^{-1}
10^{-2}
10^{-3}
10^{-4}
10^{-5}
f_0-factor (MeV^{-1})
^{232}Th(n,xn)
^{232}Th(p,xn)
20
50
100
150
0
20
40
60
80
100
120
140
Secondary neutron energy (MeV)

Fig.13.

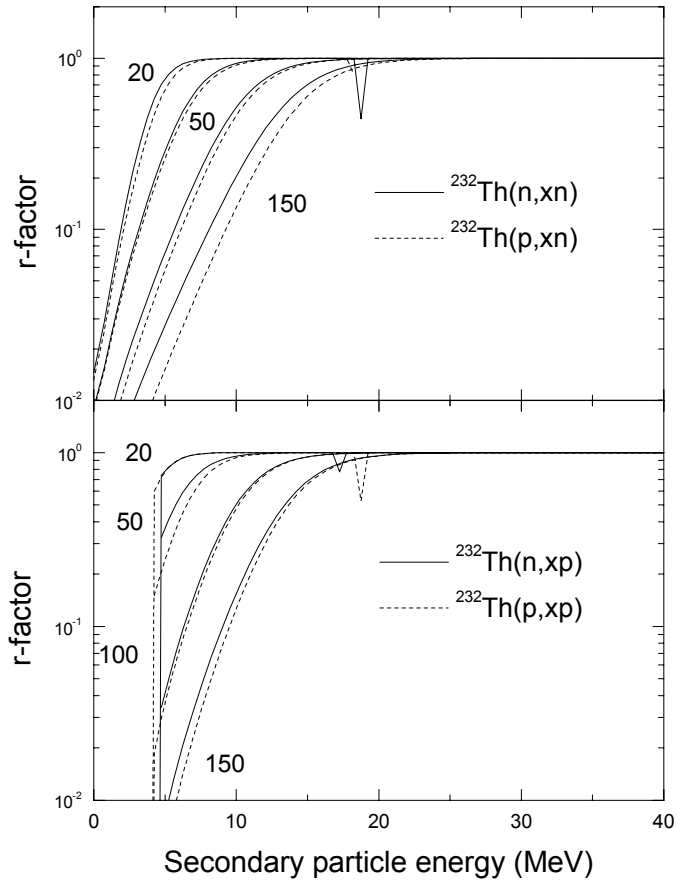
r-factor
10^0
10^{-1}
10^{-2}
20
50
150
^{232}Th(n,xn)
^{232}Th(p,xn)
r-factor
20
50
100
150
^{232}Th(n,xp)
^{232}Th(p,xp)
0
10
20
30
40
Secondary particle energy (MeV)

Fig.14.

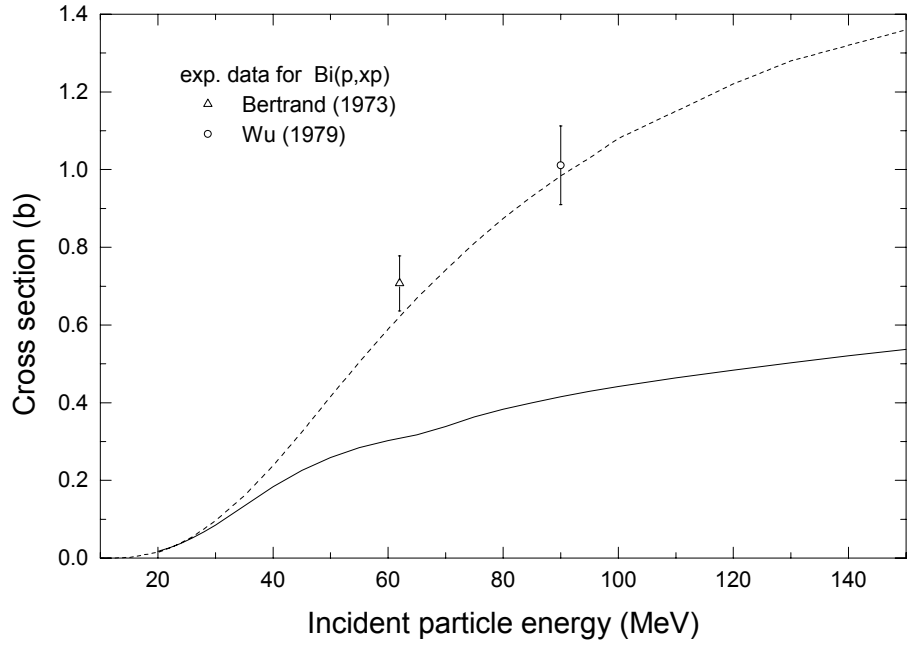
exp. data for Bi(p,xp)
Bertrand (1973)
Wu (1979)
Cross section (b)
Incident particle energy (MeV)
0.0
0.2
0.4
0.6
0.8
1.0
1.2
1.4
20
40
60
80
100
120
140

Fig. 15.

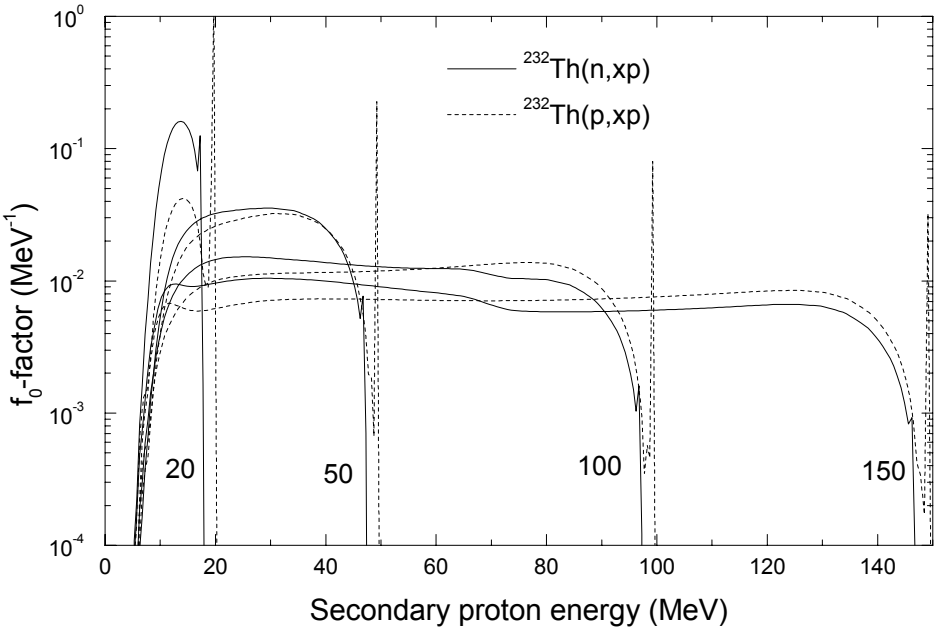
232Th(n,xp)
232Th(p,xp)
f0-factor (MeV-1)
Secondary proton energy (MeV)
20
50
100
150
10^0
10^-1
10^-2
10^-3
10^-4
0
20
40
60
80
100
120
140

Fig.16.

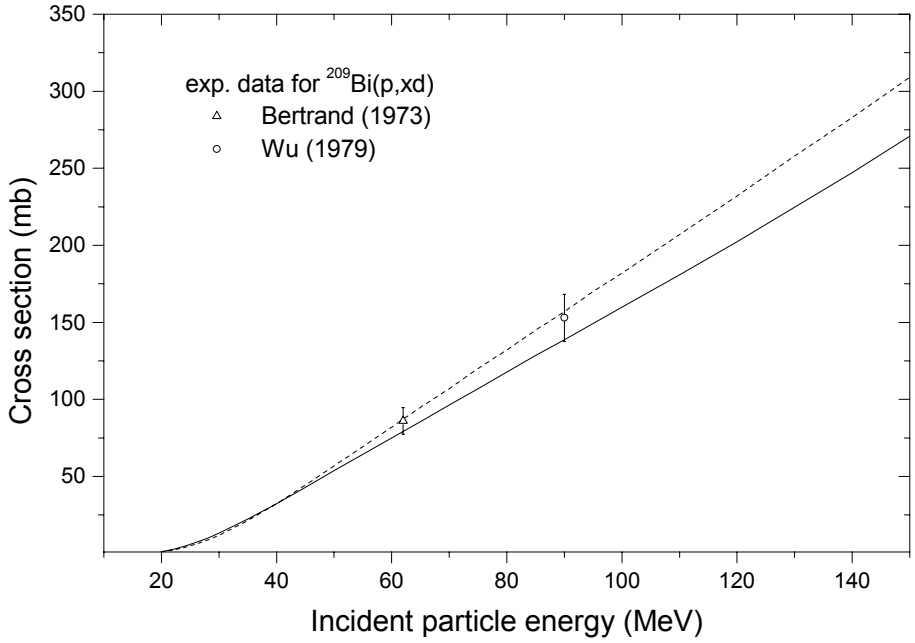
exp. data for ^{209}Bi(p,xd)
Bertrand (1973)
Wu (1979)
Cross section (mb)
Incident particle energy (MeV)
350
300
250
200
150
100
50
20
40
60
80
100
120
140

Fig.17.

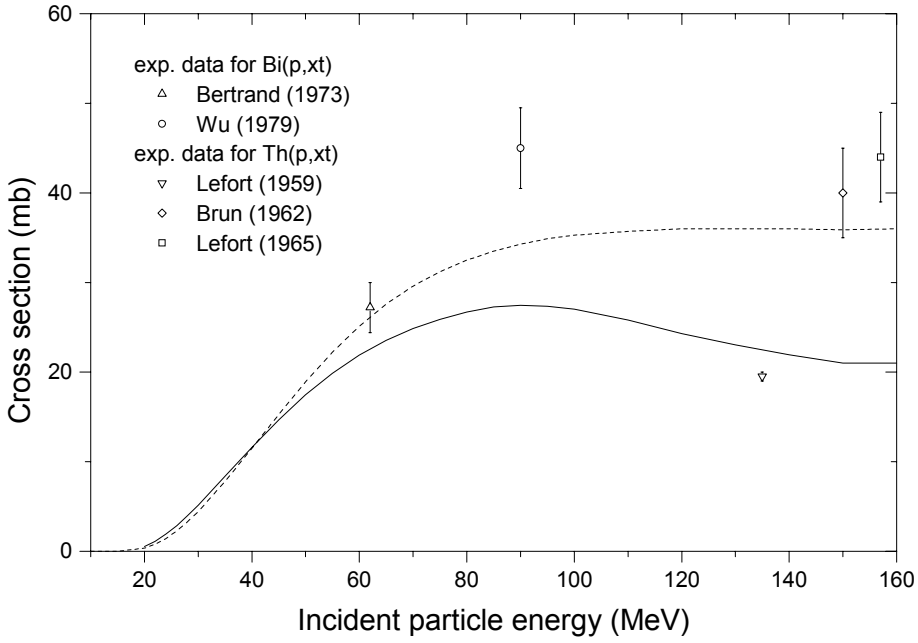
exp. data for Bi(p,xt)
Bertrand (1973)
Wu (1979)
exp. data for Th(p,xt)
Lefort (1959)
Brun (1962)
Lefort (1965)
Cross section (mb)
Incident particle energy (MeV)
60
40
20
0
20
40
60
80
100
120
140
160

Fig.18.

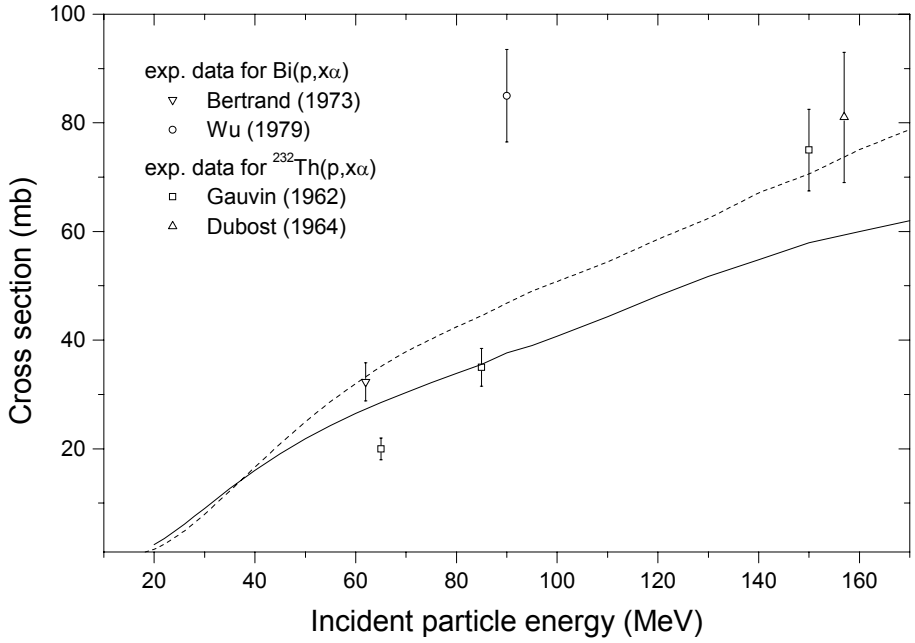
exp. data for Bi(p,xα)
Bertrand (1973)
Wu (1979)
exp. data for 232Th(p,xα)
Gauvin (1962)
Dubost (1964)
Cross section (mb)
Incident particle energy (MeV)

Fig.19.

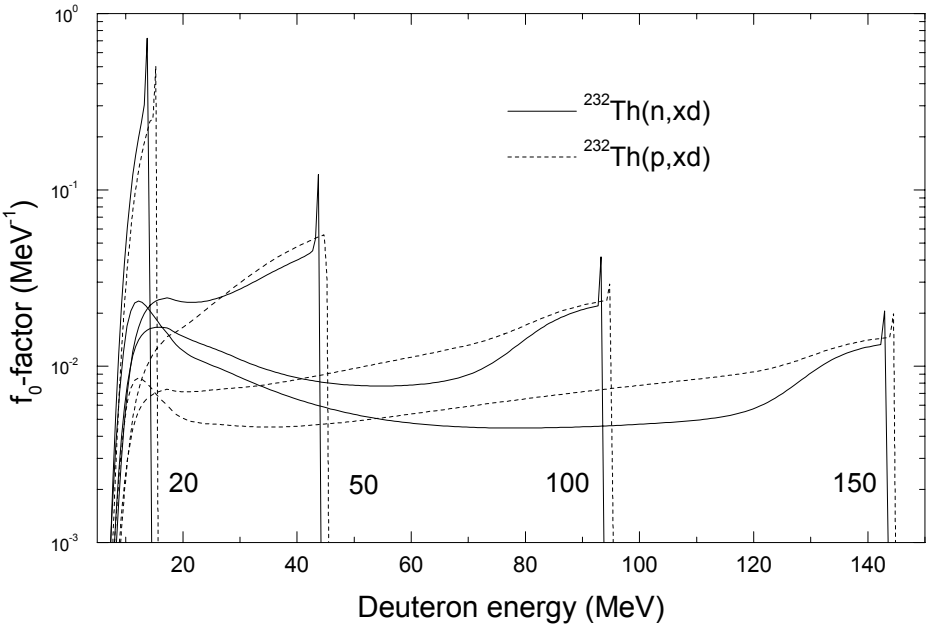
232Th(n,xd)
232Th(p,xd)
20
50
100
150
f0-factor (MeV-1)
Deuteron energy (MeV)

Fig.20.

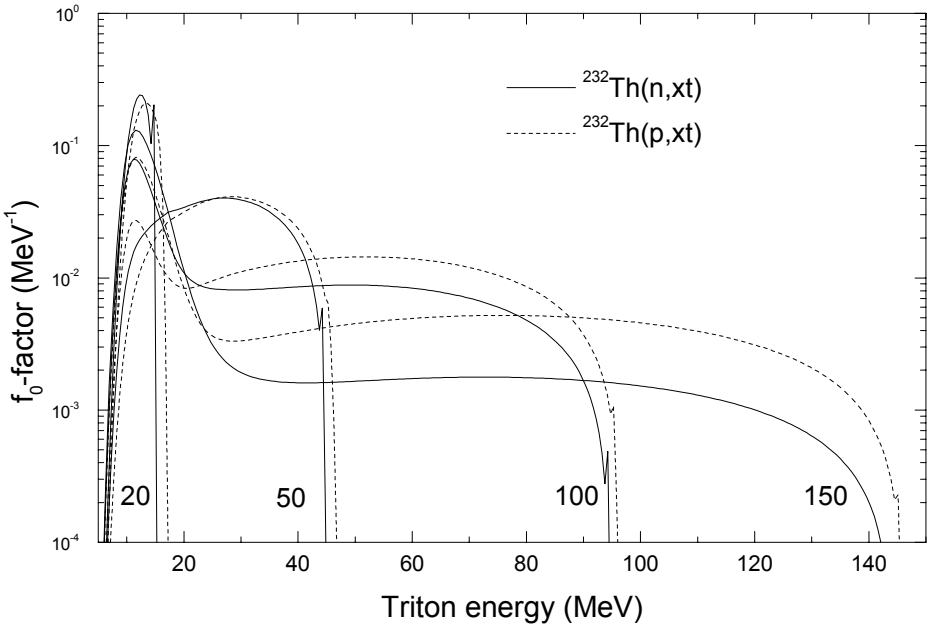
^{232}Th(n,xt)
^{232}Th(p,xt)
20
50
100
150
f_0-factor (MeV^{-1})
Triton energy (MeV)

Fig.21.

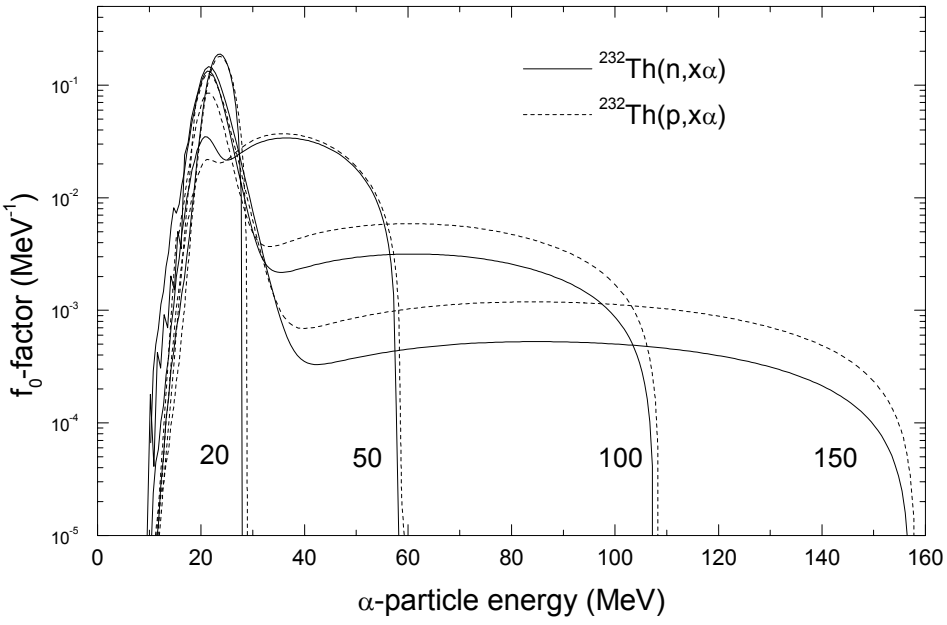
^{232}Th(n,xα)
^{232}Th(p,xα)
20
50
100
150
f_0-factor (MeV^{-1})
α-particle energy (MeV)

Fig.22.

APPENDIX 7

I. Gudowska, W. Gudowski, M. Kopec, Monte Carlo Evaluation of Neutron Contamination in High-Energy Photon Therapy Beams, Proc. of The Biennial Topical Meeting of the Radiation Protection and Shielding Division(RPDS) of the American Nuclear Society(ANS), Santa Fe, New Mexico, USA, 14-18 April 2002

Monte Carlo Evaluation of Neutron Contamination in High-Energy Photon Therapy Beams

Irena Gudowska
Dept. of Medical Radiation Physics
Karolinska Institutet and Stockholm University
Box 260, S-171 76 Stockholm
Sweden
tel. +46 8 517 75447
E-mail: irena@radfys.ks.se

Waclaw Gudowski
Nuclear and Reactor Physics
Royal Institute of Technology
Stockholm Center for Physics, Astronomy and Biotechnology
Roslagstullsbacken 21, S - 106 91 Stockholm, Sweden
tel. +46 8 5537 82 00
E-mail: wacek@neutron.kth.se

Mariusz Kopeć
Department of Theoretical and Computational Physics
Faculty of Physics and Nuclear Techniques
University of Mining and Metallurgy
al. Mickiewicza 30, 30 059 Kraków, Poland
tel. +48 12 617 3778
E-mail: mariusz@hp715.ftj.agh.edu.pl

SUMMARY

Evaluations of the photoneutron production, photoneutron fluences and absorbed dose to tissue have been performed for a clinical photon beam of 50 MV from the MM50 racetrack accelerator at Karolinska Hospital, Stockholm. Simulations were performed using the Monte Carlo code MCNP4C2 for the electron-photon-photoneutron production and transport in the treatment room and separately for the photoneutrons generated in the soft tissue only. The Monte Carlo calculated photoneutron fluence in the treatment room of the MM50 racetrack microtron and photoneutron absorbed dose to tissue are compared to the measurements using the ^{235}U fission chamber and the results evaluated by a combined MC-numerical method respectively.

I. BACKGROUND

Photonuclear reactions in the treatment room and within the treated volume of the patient during radiation therapy with high energy photon beams are a source of particles of high linear energy transfer (LET), characterized by a high relative biological effectiveness (RBE). The photonuclear radiation field around medical electron accelerators is dominated by photoneutrons from the primary source in the accelerator head, generated mainly through (γ,xn) reactions, and hence transported and scattered inside the machine and the treatment room. These neutrons together with the photoneutrons produced directly in the tissue deliver small but significant dose to the patient. As they are transported through the whole body of the patient the healthy tissues are exposed to undesirable doses.

The measurements of the photoneutron radiation in the high energy, intense photon field and hospital environment are troublesome and difficult to perform, thus a development of the calculation methods allowing evaluation of photoneutron production and neutron absorbed dose to patient is of high interest.
The aim of this work is to calculate the photoneutron fluence in the treatment room and absorbed dose to patient using the MCNP4C2 code and validate these results by comparison to the experimental data[1] (ref. SSIrep85) and the evaluations using a combined MC-numerical method[2] (ref. PMB99).

II. APPROACH

A Monte Carlo code MCNP4C2 (Ref) has been used to simulate electron-photon-photoneutron transport inside the treatment room for the 50 MV photon therapy beam from the MM50 racetrack microtron installed at the Karolinska Hospital, Stockholm.

A. Accelerator and Treatment Room Geometry

The MM50 racetrack microtron provides electron and photon beams with maximum energies in the range 2 - 52 MeV. The accelerator is equipped with an electron and photon beam scanning system instead of conventional flattening filters (Brahme 1982). Large homogenous or intensity modulated fields are produced using different scanning matrices for the narrow elementary electron and photon beams.

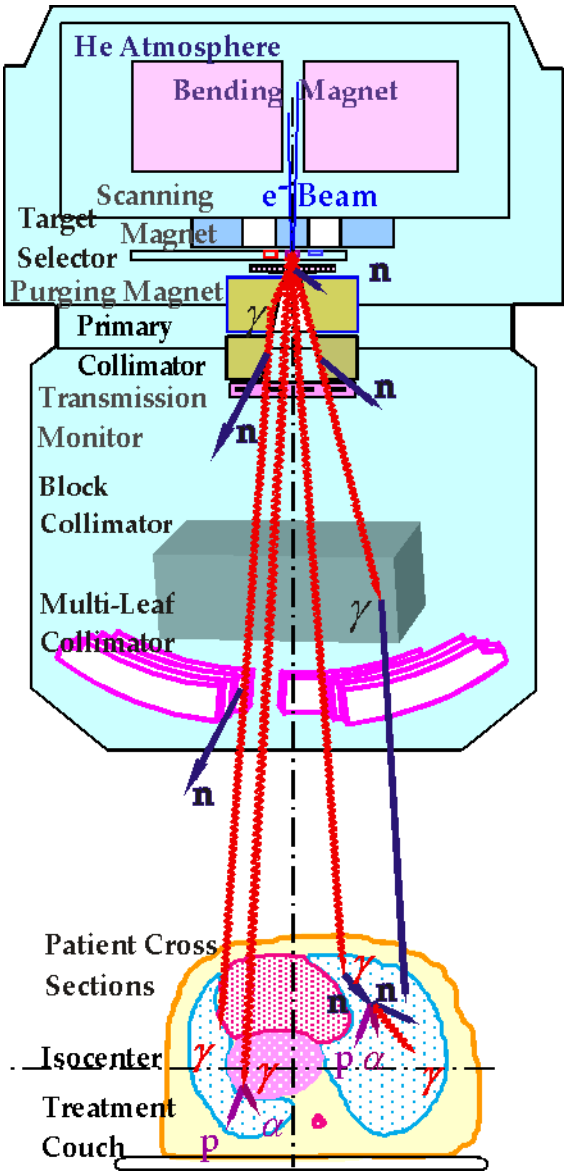

Figure 1. Schematical view of the treatment head of the MM50 racetrack microtron.

In the present studies a pencil electron beam of 50 MeV perpendiculary incident on a composite target 5.5 mm tungsten + 6.5 mm copper (5.5W6.5Cu) is used. The radiation field of 10 x 10 cm^2 at 1 m source-to surface distance (SSD) was achieved by the primary variable collimators of lead and the double focused multileaf collimator with tungsten leaves.

The design of the treatment head of the 50 MV racetrack microtron and the physical processes simulated in this work are schematically shown in figure 1.

The geometry and material composition of the accelerator and the treatment room used in the MCNP4C2 simulations follow the detailed technical description, supplied by the Scanditronix Medical AB. The geometry of the bremsstrahlung target was simulated with the accuracy of ± 0.1 mm whereas the other parts of the gantry like collimators and shielding within ± 3 mm.

The treatment head and the phantom were divided into cells of different geometrical shape and size in order to optimize the calculation time and to be able to use different variance reduction techniques.

Figure 2 shows a part of the treatment room as simulated in the MCNP4C2 calculations.

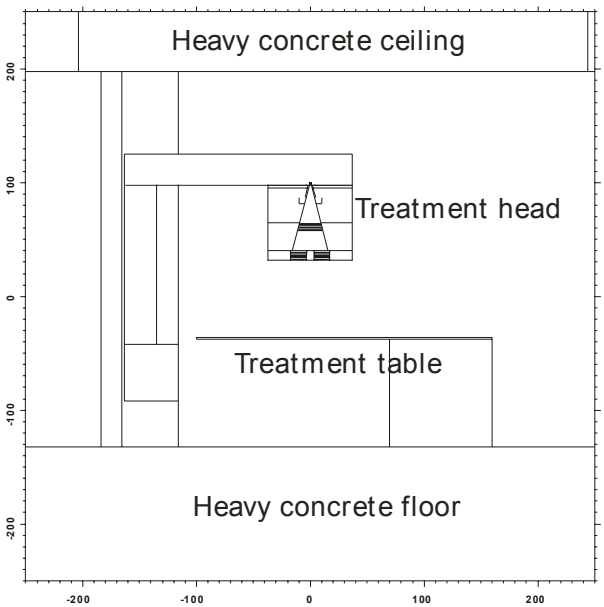

Figure 2. Schematic drawing of the treatment room geometry used in the MC calculations.

A. Photoneutron Cross Section

The cross sections for photonuclear production in heavy elements of the treatment head and room have been used from the LA150.G library evaluated at LANL (ref.IAEA –TECDOC). For the light elements as carbon and oxygen constituting the soft tissue the same LA150.G library was used.
For nitrogen, the photoneutron cross section data, missing in the LANL library, have been substituted by the data for oxygen following the evaluation of the integrated photonuclear cross sections as discussed by Gudowska et al (ref 2). The photonneutron reactions in the rare elements of the soft tissue have been neglected in these studies.

III MEASURED DATA

///

A. Measurements of the photoneutron fluence with the fission chamber

//Ref. SSI rapport
Detector calibration with the 252Cf source
252Cf source spectrum vs neutron spectrum under the treatment head.
Calibration in the thermal neutron pile – Grenoble
Calibr. Factor – thermal neutron fluence, Fi ther/count.//

A. Fission chamber method.

The photoneutron fluences inside the treatment room of the MM50 racetrack microtron at the Karolinska Hospital were measured using a small ionisation chamber with a thin layer of fissile material ^{235}U. The measurement method and the experimental results are described elsewhere (Ref Gudowska SSI rapport.)
This chamber has been used as an 'on - line' detector both inside and outside the photon beam. The bare ^{235}U fission chamber is very sensitive to thermal neutrons ($_{ther}$ = 583 b). In order to measure fast neutrons the detector was put inside a polyethylene cylinder of the 15.5 diameter and 15.5 cm height. To improve the counting technique for fast neutron measurements inside the photon beam a special lead block, 3x3x12 cm^3, was applied on the moderator to screen the detector from primary photon and lepton radiation (ref 5). The 'pile-up' effect in the detector for these measurement conditions has been estimated to be about 10% and the correction due to thermal neutron diffusion through the moderator was about 6%.
For the fast neutron measurements the detector has been calibrated using neutrons from a ^{252}Cf source at the Dosimetry Laboratory of the Swedish Radiation Protection Institute [5]. The bare ^{235}U fission chamber has been calibrated foil against thermal neutrons in the isotropic thermal neutron fluence in the SCE pile at the Centre d' Etudes Nucleaires de Grenoble, France [5].
The measured neutron fluence has been normalized per photon absorbed dose at the depth maximum. The accuracy of the measured neutron fluence using the ^{235}U fission chamber is about 20% taking account statistical and systematic uncertainties of the measurements and calibration. The fast neutron fluences measured by the ^{235}U fission chamber were compared to the results using a passive method, activation of the In foils placed inside the polyethylene moderator. The agreement between these two measurements method is within about 15% ? (Ref 5)

B. Photoneutron Production in the Detector System with ^{235}U Fission Chamber

A photoneutron production in the fission chamber, the lead filter and the polyethylene moderator has been evaluated using the MCNP4C2 code. The geometry of the detector system has been simulated as shown on the figure 3, including a careful simulation of the fission chamber. The fission reaction rate in the ^{235}U layer has been calculated for the electron-photon-photoneutron transport through the whole treatment head and treatment room. Additionally, the reaction rate in the fission layer of the detector has been calculated for the case when the bremstrahlung photons were stored on the surface source under the treatment head for the geometry as shown on the figure 3, thus giving the contribution from the photoneutrons produced in the detector system only,

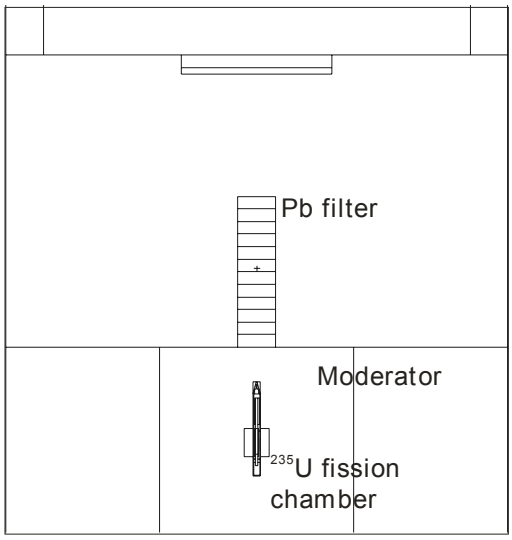

Figure 3. Simulated geometry of the detector system using ^{235}U chamber for the measurements inside the photon beam.

Comparison of these two results of the reaction rate in the fission layer yielded in the photoneutron production in the detector system of about 16% of the total photoneutrons measured.

IV MC SIMULATION – RESULTS

BB. Sim

The Monte Carlo calculated photon absorbed dose delivered to soft tissue at a depth of 5.5 cm on the central axis has been compared to measured absorbed dose to water at the same depth for the same scanning pattern of the photon beam using the similar method as discussed by Gudowska et al (ref PMB)
Both the calculated and measured absorbed doses were normalized to the number of electrons hitting the target. The Monte Carlo calculated absorbed dose to soft tissue for the 50 MeV pencil electron beam was 6.79 x 10^{-15} Gy/electron, agree with the experimental determination of absorbed dose to water was 6.63 x 10^{-15} Gy/electron within 3% (ref Gud. PMB99).

C. Simulation of the detector system

Comparison with the experimental data.
- results: count rate
- Fluence rate

Simulation with the detector
Simulation with the air cells.

We have tested several problems/tasks concerning photoneutron production that can be verified by the experiments and other calculation methods.
In all cases we get the discrepancies between results from MCNP4C2 and experimental data by a factor ~2 dependent on the problem.

WCu target, 50 MeV, 10x10cm2, stationary beam

count rate - detector
- fluence rate - air
- conversion factor Dg/el – MC vs Measurements
- gamma-n detector , with Pb shield,only polyethylene moderator,
- Photon source-surface
- results: whole room vs only gantry scattering from the walls, roof etc.

We also prepared an input where a detailed detector – ^{235}U fission chamber is simulated. This detector is in principle sensitive only to thermal neutrons.

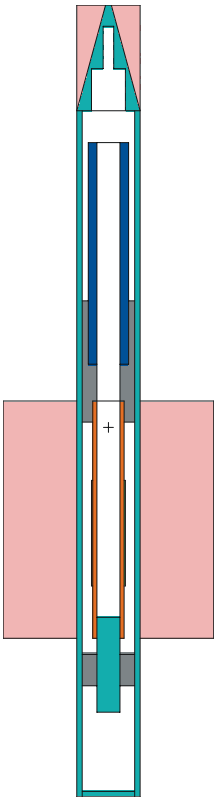

Figure 3b. Simulated geometry of the detector system using ^{235}U chamber.

By estimating reaction rate (or thermal neutron fluence close to the chamber) and using calibration factor from the calibration in the known thermal neutron field we can make more accurate comparison to the measured data (to the number of counts in the detector).
Again from this test we get the same discrepancies by a factor ~ 2.

b) are the cells large enough that local deposition of the energy is valid?

We use cells of the volume 25 cm^3 for the track length estimate of the neutron fluence in the air. Also other cell sizes were tested.

Several tests using MCNP4C2 have been done to check the conversion factors used in our problems.

Moreover photoneutron production in the detector was simulated. The number of neutrons produced inside the

detect or system compared to the total number of neutrons produced in the whole machine looks reasonable if we evaluate the fraction in %..

D. RESULTS

Comparison with the experimental data.

- results: count rate
- Fluence rate

WCu target, 50 MeV, 10x10cm2, stationary beam

Simulation with the detector
Simulation with the air cells.

We have tested several problems/tasks concerning photoneutron production that can be verified by the experiments and other calculation methods.

In all cases we get the discrepancies between results from MCNP4C2 and experimental data by a factor ~2 dependent on the problem.

count rate - detector

- fluence rate - air
- conversion factor Dg/el – MC vs Measurements
- gamma-n detector , with Pb shield,only polyethylene moderator,
- Photon source-surface
- results: whole room vs only gantry scattering from the walls, roof etc.

The photonuclear simulations were performed with the geometries first including only the gantry and then with the whole treatment room. The differences between these two cases do not exceed 30% (higher neutron fluence at the isocenter for the whole room geometry) and are in agreement with the other published results for similar set-ups.

V. PHOTONEUTRON PRODUCTION IN TISSUE

A. MCNP4C2 simul. in the Soft tissue

.

C. Photoneutron production in the patient.

Soft tissue – comparison to method described in publication PMB (ref)
Photon source on the surface.

B. Photonuclear reactions in tissue.

Photonuclear cross section in tissue:

Gamma-n in the light elements, cross section data 14N replaced by 16O data, neglected rare elements

through the air between the gantry window and the phantom, and subsequently through the phantom. The latter was simulated by a 30x40x40 cm^3 cubic phantom whose surface was placed at a distance of 100 cm from the target. The settings of the collimator and irradiated volume corresponded to a radiation field of 10x10 cm^2 at the phantom surface. The composition of the phantom material is assumed to be average soft tissue in an adult male, ICRU-44 (ICRU 1992).

Another important and interesting test has been performed to compare the photoneutron production and the photoneutron absorbed dose inside the tissue equivalent phantom (light target elements) evaluated by a method combining MC (for electron-photon transport), numerical evaluations of the photoneutron production and again MC evaluation of the photoneutron transport and absorbed dose (tally fm4) . In this case we have used photon source saved on the surface. Since MCNP4C2 doesn't want to calculate energy deposition (tally 6) when the source has to be taken from the surface, we have been forced to use the tally fm to evaluate photoneutron energy deposition in the tissue.
These calculation have been done to make an comparison to the published work, see, publication:
7. I. Gudowska, A. Brahme, P. Andreo, W. Gudowski and J. Kierkegaard, "Calculation of absorbed dose and biological effectiveness from photonuclear reactions in a bremsstrahlung beam of end point 50 MeV", Physics in Medicine and Biology, 44 (1999) pp. 2099-21

I have prepared an input to test exactly the same example as published by me in PMB 1999.
Since in this work I discuss only gamma-n in patient (tissue), to avoid contribution from neutrons
produced in the gantry I prepared a photoneutron source on the surface below the gantry.

So I run MCNP4C2 with a photon source on the surface (cut off energy in the source 5 MeV).
I put also a cut off energy of 10 MeV for the photons transported through the phantom since the thresholds
for gamma-n reactions in the used light elements are above 10 MeV.
In this case MCNP4C2 doesn't want to calculate tally F6:n (bug in the code) ,
we were forced to calculate energy deposition by tally multiplier Fm4.
I have checked by the other example (without using a surface source) that F6:n is giving the same
result and tally multiplier fm4.
This calculations give a difference by about factor 2 (higher from MCNP4C) when compare to neutron
energy deposition in the cells inside the tissue phantom evaluated in the work published in PMB 99.

However these discrepancies by factor 2 appear only in the tallies (energy and track length fluxes F4:n).

When I compare the total number of photoneutrons produced in the tissue phantom normalized to primary electron
as calculated for work PMB 99 it agrees within about 30% with the weighted number of the source neutrons calculated by MCNP4C2.
This discrepancies by 30% can be explained by differences in the cross section data for light elements (for example: differences
in the Los Alamos model when compared to the experimental data) . From private communication with Mark Chadwick,there is about
30% higher cross section for gamma-n in oxygen in Los Alamos library if compared to the experimental data.

B. Results :
, discussion , models

Also in this case the discrepancies by factor about 2 have been found.

When I compare the total number of photoneutrons produced in the tissue phantom normalized to primary electron
as calculated for work PMB 99 it agrees within about 30% with the weighted number of the source neutrons calculated by MCNP4C2.
This discrepancies by 30% can be explained by differences in the cross section data for light elements (for example: differences
in the Los Alamos model when compared to the experimental data) . From private communication with Mark Chadwick,there is about
30% higher cross section for gamma-n in oxygen in Los Alamos library if compared to the experimental data.

On summary of the neutron balance we get:

neutron creation tracks weight energy
>
>photonuclear 229319 1.4332E-02 2.5120E-02
>Having 8 000 000 starting electrons I assume that weight per source is
>nothing else then the number of photoneutrons/number of original electrons
>
>Making this division we get: 2.866E-02 - EXACTLY TWICE AS MUCH AS IS GIVEN
>IN WEIGHT!!
>As long as we have a confidence that WEIGHT given by MCNP is correct (it
>agrees with our experiments!!!) - we have DOUBLE NUMBER OF PHOTONEUTRONS
>in MCNP simualtions!!
>And I presume that this DOUBLE NUMBER OF NEUTRONS is used in tally
>normalisation giving overestimation of tallies just by a factor of 2!!
>
>MCNP is rather consistent in DOUBLE COUNTING of photoneutrons

VI. DISCUSSION - TESTS

Comparison with the experimental data.
- results: count rate
- Fluence rate

Simulation with the detector
Simulation with the air cells.

We have tested several problems/tasks concerning photoneutron production that can be verified by the experiments and other calculation methods.
In all cases we get the discrepancies between results from MCNP4C2 and experimental data by a factor ~2 dependent on the problem.

WCu target, 50 MeV, 10x10cm2, stationary beam

count rate - detector
- fluence rate - air
- conversion factor Dg/el – MC vs Measurements
- gamma-n detector , with Pb shield,only polyethylene moderator,
- Photon source-surface
- results: whole room vs only gantry scattering from the walls, roof etc.

AA.

Furthermore we are quite comfortable with the **MCNP simulations of the electron-photon transport** through the gantry of the 50 MV Racetrack microtron.

We did careful calculations of the bremsstrahlung production in the target, transport through the gantry and the tissue equivalent phantom. All these MC results have been compared to the experimental data of the radial and depth dose profiles for different photon beams. The obtained discrepancies between MCNP calculations and measurements are within 2-10%.
Also, MC calculations of the factor: photon absorbed dose to water (at maximum) to the number of electrons hitting target (electron current on the target) were performed for different
operation modes of the 50MV Racetrack and compared to the measurements. Again good agreement beetwen MCNP and experimental results, within 3-5% was obtained.
See, published works:
6. I. Gudowska, B. Sorcini and R. Svensson, "Evaluation of a 50 MV Photon Therapy Beam from a Racetrack Microtron Using MCNP4B Monte Carlo Code", In "Advanced Monte Carlo for Radiation Physics, Particle Transport Simulation and Applications", Proc. of the Monte Carlo 2000 Conference, Lisbon, 23-26 October 2000, pp. 317-322,

calculation of the photon fluence, differential in energy and angle, in the tissue using the electron - photon transport mode of MCNP for the bremsstrahlung production in the target and photon transport from the target to the patient

We did careful calculations of the bremsstrahlung production in the target, transport through the gantry and the tissue equivalent phantom. All these MC results have been compared to the experimental data of the radial and depth dose profiles for different photon beams.

The bremsstrahlung productions, photon transport and the radial and depth photon dose distributions for 50 MeV electron beams impinging on different targets of the MM50 racetrack microtron simulated using MCNP4B code were discussed elsewhere (Ref Gud. MC2000). The comparison with the experimental data – good agreement was obtained.
The calculations using the MCNP4C2 code (version) gave the similar results.

A. Sensitivity study

- tests different geometry of the gantry
- different materials in the gantry
- simulation whole room vs gantry only
- different operation modes (different scan matrices)

The photonuclear simulations were performed with the geometries first including only the gantry and then with the whole treatment room.

B. MC optional modes

- analog vs biased
- cut off energies
- no force collision
- imp: =1

The treatment head and the phantom were divided into cells of different geometrical shape and size in order to optimize the calculation time and to be able to use different variance reduction techniques;
these have been cell-dependent energy cut-off, geometry splitting with Russian roulette and forced collision to increase the sampling of collisions in specified cells.
General electron and photon cut-off energies were 0.75 MeV.
Photon forced collisions were applied in the target cells, and photon and electron transport in the gantry were limited to cells that contributed

substantially to primary and secondary particle production.
To obtain improved electron transport the bremsstrahlung target 9Be6W was divided into several layers in order to break the electron path into many small steps.
//Increased sampling of interactions within the regions of the target was achieved dividing the 9 mm beryllium region into two layers of 4 mm and 5 mm thickness and the tungsten region into six 1 mm thick layers. To insure detailed multiple scattering, step parameters for Be and W were taken equal to 25 and 12 respectively.//

C. Uncertainties

experiment, MC statistical and systematic uncertainties

C. Problems
Computing time
Bugs
Cross section tables
Models

VIII. SIGNIFICANCE

IX. CONCLUSIONS

MCNP4C2 simulations of the neutron contamination originated from photonuclear reactions in the 50 MV photon beam from the racetrack microtron encountered serious discrepancies compared to the experimental results and the evaluations using a combined MC-numerical method. The total number of the source photoneutrons produced in the tissue phantom obtained from the weighthed number of the generated photoneutron tracks agrees reasonably with results using a combined MC-numerical method within 10-30% ((accuracy)). Unfortunately, all the results extracted from the tally f4:n (neutron track length fluence) with the tally multipliers calculating the neutron energy deposition and consistently the results of tally f6:n give an overestimation of the results obtained by MC-numerical method by the factor about 2. The similar discrepancies, by factor about 2 (1.7 – 2.1), are obtained if the MCNP4C2 results are compared to the experimental results of the neutron fluences measured in the patient plane for the 50 MV pencil photon beam.
There are indications that these discrepancies may be caused by a normalization error in MCNP4C2. The weighted number of tracks for the source photoneutrons given in the MCNP4C2 output multiplied by the number of primary electrons gives the absolute number of the produced photoneutron tracks which is different than the one given in the same output data. The difference of the factor of 2 (exactly) obtained for the “biased” photonuclear simulations could be easily explained by the artifact of the biasing procedure of the photoneutron creation. However, the “analog” simulations give the same discrepancy – number of the source photoneutrons given by the MCNP4C2 output is over factor of 2 higher than the product of weigted number of photoneutron tracks multiplied by the number of primary electrons (nps).
Extensive sensitivity studies showed that the simplifications in the geometry and/or material composition of the simulated therapy unit account for maximum 20-30% differences in the results. Moreover, the different variance reduction techniques give the consistent results within the statistical error and are excluded as a sources of the found discrepancies.
Before final conclusions are drawn about the quality of the photonuclear simulations in MCNP4C2 it is absolutely necessary to verify if this normalization peculiarity is not biasing tally results.

ACKNOWLEDGMENTS

REFERENCES

1. I. Gudowska, "Measurements of the Neutron Absorbed Dose from Medical Accelerators" Internal Report, Dept. of Radiation Physics, The

Karolinska Institute, Stockholm, RI 1984-04, 1-87 (1984).
2. I. Gudowska, "Neutron Fluence and Dose Equivalent Measurements around Medical Accelerators using Foil Activation and a ^{235}U Fission Chamber, Internal Report Dept. of Radiation Physics, The Karolinska Institute, Stockholm, RI 1985-02, 1-65 (1985).
3. I. Gudowska, "Photonuclear processes in the treatment room and patient during radiation therapy with 50 MV photons" SSI Report P858, 1-54 (1996).
4. I. Gudowska and A. Brahme "Neutron radiation from high-energy X-ray medical accelerators" Nukleonika, Vol. 41, No. 2, 99-112 (1996).
5. I. Gudowska, "Measurements of Neutron Radiation Around Medical Electron Accelerators by Means of ^{235}U Fission Chamber and Indium Foil Activation", Radiation Protection Dosimetry Vol. 23 No. 1/4 pp. 345-348 (1988).
6. I. Gudowska, B. Sorcini and R. Svensson, "Evaluation of a 50 MV Photon Therapy Beam from a Racetrack Microtron Using MCNP4B Monte Carlo Code", In "Advanced Monte Carlo for Radiation Physics, Particle Transport Simulation and Applications", Proc. of the Monte Carlo 2000 Conference, Lisbon, 23-26 October, 317-322, eds. A. Kling et al, Springer (2000).
7. I. Gudowska, A. Brahme, P. Andreo, W. Gudowski and J. Kierkegaard, "Calculation of absorbed dose and biological effectiveness from photonuclear reactions in a bremsstrahlung beam of end point 50 MeV", Physics in Medicine and Biology, 44, 2099-2125 (1999).
8. Reference to MCNP4C2 version
9. Handbook on photonuclear data for applications, Cross sections and spectra, IAEA-TECDOC-Draft No 3, March 2000, (Ref. ??)
10. M.B. Chadwick, P.G. Young, R.E. MacFarlane, M.C. White, R.C. Little, "Photonuclear physics in radiation transport: I. Cross-sections and spectra" Nucl.Sci.Eng. (2000 submitted).

d) to what accuracy do you think you measured it

The accuracy of the measured neutron fluence is about 20% taking account statistical and systematic uncertainties of the measurements and calibration.

Uncertainty of the measured neutron fluence using the ^{235}U chamber method is about 12% taking into account: errors of the fission fragment pulse counting, the noise of the electronic system, fluctuations of the photon dose rate during the measurements and errors during calibration procedure [5].

---

1. Second-level Subheadings. This level of sub-heading is Arabic-numbered, flush left, and initial capital style ending with a period. Text continues on the same line as the second-level subheadings.

1. Figures and Tables. Both Figures and Tables should be numbered sequentially with Arabic numbers, should be placed in the text closely following the first reference to their contents, and should have an appropriate caption in bold type.

Table 1. ADMT-456 Preliminary Data

Description	One	Two	Three
Cfhdljfd8	123.5	8.76	0.645
Dfjkjicj nmks	146.3	8.98	0.454
Wsf mkdfsi	133.3	9.68	0.543
Kjdejit ji uj	110.4	9.56	0.510

Note the different styles for table and figure captions. Table captions (above the table and centered) have first-letter capitalization and no period. Figure captions (below the figure and centered) resemble a regular sentence with a period.

All photographs, figures, and illustrations will be published in black and white only and should be inserted in the manuscript electronically.

Table 2. ADMT-456 Final Data

Description	One	Two	Three
Cfhdljfd8	128.5	8.66	0.649
Dfjkjicj nmks	147.3	8.58	0.458
Wsf mkdfsi	136.3	9.48	0.547
Kjdejit ji uj	115.4	9.36	0.516
